



**NTNU – Trondheim**  
Norwegian University of  
Science and Technology

# Thrust gas bearing analytical tool development

**David Rondon**

Natural Gas Technology

Submission date: June 2014

Supervisor: Tor Bjørge, EPT

Norwegian University of Science and Technology  
Department of Energy and Process Engineering





**NTNU – Trondheim**  
Norwegian University of  
Science and Technology

# Thrust gas bearing analytical tool development

David Rondon

Master of Science in Natural Gas Technology

Submission date: June 2014

Supervisor: Tor Bjørge

Co-supervisor: Carlo Mazzali, Statoil

Norwegian University of Science and Technology  
Department of Energy and Process Engineering



EPT-M-2014-98

**MASTER THESIS**

for

Student David Rondon

Spring 2014

Thrust gas bearing analytical tool development

*Utvikling av beregningsverktøy for aksielle gasslager***Background and objective**

Statoil has been focusing on the design and development of gas bearing technology for more than 10 years. This type of bearing should allow for a simplification and CAPEX reduction of the compression unit with respect to traditional oil lubricated or magnetic bearings.

Statoil has issued two related patents (US2011/0052375, US2012/0163742): the working principle is the same, but one is related to a radial gas bearing type and the other to an axial type. More specifically this technology consists of a tapered textured surface (fixed to the stator) facing a cylindrical plain surface on the shaft, in other words a traditional textured surface seal with convergent geometry. The textured surfaces can be envisioned to be the typical hole pattern or honeycomb type as per traditional high pressure cylindrical seals. Part of the compressed process fluid is conveyed through the resultant tapered annular channel and, thanks to the dynamic effects generated, stiffness and damping capacities are created. The concept therefore leverage on the axial pressure differential created across the convergent annulus to generate lifting and damping capacities to the magnitude required to lift the rotor and keep it run in a stable manner. Hence we speak about a combined gas bearing/seal technology.

Statoil has started investigating the capability and performances of the combined thrust gas/bearing by performing CFD simulations. Those simulations provide an extensive understanding about the phenomena occurring within the bearing, but they are quite costly and time consuming, not suitable for feasibility studies or quick screening as typically requested at the early design stage of a new project.

For this reason a program was started in cooperation with the Norwegian University of Science and Technology (NTNU) with the goal of developing an analytical tool to predict the rotor dynamic performances of a honeycomb/hole pattern convergent axial gas seal/bearing and to validate them through CFD simulations.

At present time a semester project has been completed (“Estimation of honeycomb/hole pattern thrust gas bearing using the bulk-flow theory” by David Rondon).

**The following tasks are to be considered:**

The scope of the master thesis will be to further develop the analytical tool presented in the above project to predict static and dynamic performances of the Statoil patented axial gas seal/bearing, with the possibility to validate them versus CFDs results.

More specifically the master thesis shall investigate the following subjects:

1. Influence and sensitivity of different integration methods
2. Zero order equations sensitivity analysis vs main parameters (i.e. entrance and exit loss coefficients, different friction factors definition, adiabatic vs isothermal flow, geometry, pressure and pressure differentials, etc.)
3. Laminar vs turbulent model
4. 1st order equations and sensitivity to pre-swirl and other boundary conditions

-- " --

Within 14 days of receiving the written text on the master thesis, the candidate shall submit a research plan for his project to the department.

When the thesis is evaluated, emphasis is put on processing of the results, and that they are presented in tabular and/or graphic form in a clear manner, and that they are analyzed carefully.

The thesis should be formulated as a research report with summary both in English and Norwegian, conclusion, literature references, table of contents etc. During the preparation of the text, the candidate should make an effort to produce a well-structured and easily readable report. In order to ease the evaluation of the thesis, it is important that the cross-references are correct. In the making of the report, strong emphasis should be placed on both a thorough discussion of the results and an orderly presentation.

The candidate is requested to initiate and keep close contact with his/her academic supervisor(s) throughout the working period. The candidate must follow the rules and regulations of NTNU as well as passive directions given by the Department of Energy and Process Engineering.

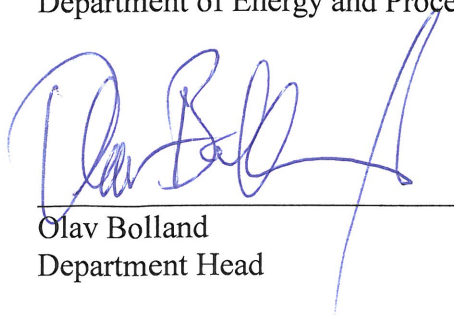
Risk assessment of the candidate's work shall be carried out according to the department's procedures. The risk assessment must be documented and included as part of the final report. Events related to the candidate's work adversely affecting the health, safety or security, must be documented and included as part of the final report. If the documentation on risk assessment represents a large number of pages, the full version is to be submitted electronically to the supervisor and an excerpt is included in the report.

Pursuant to "Regulations concerning the supplementary provisions to the technology study program/Master of Science" at NTNU §20, the Department reserves the permission to utilize all the results and data for teaching and research purposes as well as in future publications.

The final report is to be submitted digitally in DAIM. An executive summary of the thesis including title, student's name, supervisor's name, year, department name, and NTNU's logo and name, shall be submitted to the department as a separate pdf file. Based on an agreement with the supervisor, the final report and other material and documents may be given to the supervisor in digital format.

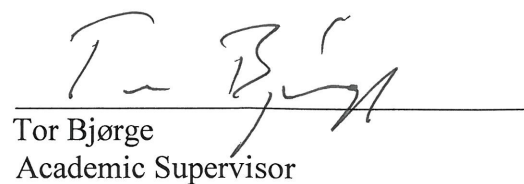
- ☐ Work to be done in lab (Water power lab, Fluids engineering lab, Thermal engineering lab)  
☐ Field work

Department of Energy and Process Engineering, 14. January 2014



---

Olav Bolland  
Department Head



---

Tor Bjørge  
Academic Supervisor

Research Advisor:

Carlo Mazzali, Statoil





## **Preface**

This work has been carried out at the Department of Energy and Process Engineering of the Norwegian University of Science and Technology (NTNU) in collaboration with Statoil ASA. The objective of this thesis is to develop a reliable analytical tool to predict the rotordynamic performance of a thrust gas bearing designed and patented by Statoil ASA using honeycomb/hole-patterned surfaces.

First and foremost, I owe my deepest gratitude to my supervisors Carlo Mazzali and Tor Bjørge from Statoil ASA for giving me the opportunity to realize this work and their instructive guidance. Throughout our regular meetings, expert advice and encouragement I learned many valuable lessons.

I would also like to express my gratitude to Professor Tor Ytrehus, his corrections and advices allowed the development of this work. I have also been fortunate of being assisted by Professor Dara Childs at Texas A&M University, his contribution by sharing vital information is greatly appreciated.

Further, I would like to thank Olimpia Magliulo and Achim Wick for their invaluable contribution to the progress of this thesis. To Eydis, Daniel, Alexandra, Lisbeth, Rachelle, Mariangel, Maribel, Yeraldin, Andres, Alberto, Celine and my friends around the world: thank you for your support and patience!

Last but not least, I am very grateful to my parents and family in Venezuela, without their moral and financial support I could have never taken my master degree.

**David Rondon**

**Trondheim, Norway. June, 2014**



## Abstract

Looking for a cheaper and low maintenance alternative to magnetic bearings, Statoil patented a new design for thrust gas bearings with honeycomb/hole-patterned surface. Honeycomb/hole-pattern surface on annular seals have been extensively studied, as a good seal it reduced leakage of systems previously using labyrinth seals, there is low temperature increase and provides better rotordynamic stability, qualities highly desirable for thrust bearings.

Statoil wants to develop an analytical tool to predict leakage, thrust force, damping and stiffness of axial bearings. The results from the tool must be compared to the results from Computational Fluid Dynamics (CFD) simulations before planning experiments and this tool must be reliable. A similar tool (ISOTSEAL) has been developed for annular seals by Texas A & M University in the United States and its results were validated with some experiment. Using a similar approach as in ISOTSEAL, the development of this analytical tool starts by using the “Bulk-Flow” theory to simplify the system from three-dimensional to one-dimensional. Two set of equations considered, the zeroth-order equations for steady-state solutions (leakage and thrust force) and the first-order equations for dynamic solutions (stiffness and damping).

The values for leakage are within 10% deviation from the CFD simulations carried out. But the thrust force results are not satisfactory. A sensitivity test was carried out and the results reflected that the entrance loss coefficient and the friction model were the most sensitive parameters. Later, calculations using different friction models were carried out, but there has been no much improvement since data from previous works is limited. The results for damping and stiffness showed considerable deviations from the CFD results, mainly due to the influence of the results from the zeroth-order equations, as they are also influenced by the friction model. In conclusion the analytical tool does not give reliable results; the model is highly dependent on the friction model and the conditions at the entrance. Another important factor is the ratio of the area of holes and the area of the surface and it affects directly the calculations for stiffness and damping.



## List of Content

	Page
<b>1 Introduction</b>	<b>1</b>
<b>2 Literature review</b>	<b>5</b>
<b>3 Geometry and considerations</b>	<b>11</b>
<b>4 Bulk-flow model</b>	<b>17</b>
<b>5 Friction model</b>	<b>23</b>
<b>6 Numerical Solution</b>	<b>29</b>
6.1 Zeroth-Order Equations.....	29
6.2 First-Order Equations.....	30
6.3 MATLAB Solver.....	31
<b>7 Results using Zeroth Order equations</b>	<b>33</b>
7.1 Parameters.....	33
7.1.1 Geometrical parameters.....	33
7.1.2 Thermodynamic parameters.....	34
7.2 Simulations using the coefficients from ISOTSEAL.....	34
7.3 Sensitivity test.....	40
7.3.1 Case A.....	41
7.3.2 Case B.....	44
7.4 Sensitivity test using different friction-factor models.....	48
7.4.1 Case A.....	48
7.4.2 Case B.....	50
7.5 Simulations for diverse cases.....	52
<b>8 Results using First Order equations</b>	<b>55</b>
8.1 Case A: Centered position.....	55
8.2 Case A: Offset position.....	57
8.3 Case B: Centered position.....	60
8.4 Case B: Offset position.....	62
<b>9 Discussions</b>	<b>65</b>
9.1 Static Solutions.....	65
9.2 Dynamic Solutions.....	68
<b>10 Conclusions</b>	<b>73</b>
<b>Bibliography</b>	<b>75</b>

Appendix A	i
Appendix B	xiii
Appendix C	xvii
Appendix D	xix
Appendix E	xxvii
Appendix F	xliii
Appendix G	lxxii
Appendix H	lxxv

## List of Figures

	Page
2.01 Hole-patterned annular seal (Shin, 2005).....	5
2.02 One-control-volume for annular seals (Nelson, 1984).....	6
2.03 Shrouded impeller surface geometry (Gupta, 2005).....	6
2.04 Two-control-volume analysis (Shin,2005).....	7
2.05 Response of a spring-mass system for stable performance (API, 2010).....	9
2.06 Response of a spring-mass system for unstable performance (API, 2010).....	9
3.01 Distribution of the holes in the hole-patterned surface (Lloyd's Register, 2012).....	11
3.02 Case A at centered position.....	12
3.03 Case B at centered position.....	12
3.04 Case A with 50% offset.....	12
3.05 Case B with 50% Offset.....	13
3.06 Representation of the spring-damper system for both sides of the thrust bearing.....	13
3.07 Pressure drop for a system (Hassini & Arghir, 2013).....	14
3.08 Illustration of Coriolis and centrifugal forces (Persson, 2005).....	15
3.09 T-P diagram for real gases showing the inversion line (Sonntag & Van Wylen, 1991).....	16
4.01 The two control volumes(Rondon, 2013).....	17
4.02 The system of coordinates for the two control volumes.....	18
5.01 Friction-factors as function of the Reynolds number for honeycomb seals for two clearances (D'Souza & Childs, 2002).....	26
6.01 Schematic view of the shooting method (Cambridge Press, 2007).....	30
6.02 The solver's algorithm for stiff system of ordinary differential equations.....	31
7.01 Pressure of the flow along the radius for case A at centered position with 8,59% mean percentage error.....	36
7.02 Temperature of the flow along the radius for case A at centered position with 4,45% mean percentage error.....	36
7.03 Radial Velocity of the flow along the radius for case A at centered position.....	37
7.04 Circumferential velocity of the flow along the radius for case A at centered position.....	37
7.05 Pressure of the flow along the bearing for case B at centered position with 2,05% mean percentage error.....	38

7.06	Temperature of the flow along the bearing for case B at centered position with 1,53% mean percentage error.....	39
7.07	Radial Velocity of the flow along the bearing for case B at centered position.....	39
7.08	Circumferential Velocity of the flow along the bearing for case B at centered position.....	40
7.09	The leakage variation with entrance loss coefficient for case A for centered and offset position.....	41
7.10	The thrust force variation with entrance loss coefficient for case A at offset position.....	42
7.11	The leakage variation with ns for case A at centered and offset position.....	42
7.12	The thrust force variation with ns for case A at offset position.....	43
7.13	The leakage variation with nr for case A at centered and offset position.....	43
7.14	The thrust force variation with nr for case A at offset position.....	44
7.15	The leakage variation with entrance loss coefficient for case B at centered and offset position.....	45
7.16	The thrust force variation with entrance loss coefficient for case B at offset position.....	45
7.17	The leakage variation with ns for case B at centered and offset position.....	46
7.18	The thrust force variation with ns for case B at offset position.....	46
7.19	The leakage variation with nr for case B at centered and offset position.....	47
7.20	The thrust force variation with nr for case B at offset position.....	47
7.21	Friction factor for the different models that depend on the Reynolds number.....	48
7.22	Leakage and the errors for case A at centered position.....	49
7.23	Leakage and the errors for case A at offset position.....	49
7.24	Thrust force and the errors for case A at offset position.....	50
7.25	Leakage and the errors for case B at centered position.....	51
7.26	Leakage and the errors for case B at offset position.....	51
7.27	Thrust force and the errors for case B at offset position.....	52
7.28	Error for leakage at different cases.....	53
7.29	Errors for thrust force at different configurations.....	53
8.01	Stiffness of the bearing when the area ratio 1 for case A at centered position.....	55
8.02	Stiffness of the bearing when the area ratio 0,56 for case A at centered position....	56
8.03	Damping of the bearing when the area ratio 1 for case A at centered position.....	56
8.04	Damping of the bearing when the area ratio 0,56 for case A at centered position....	57
8.05	Stiffness of the bearing when the area ratio 1 for case A at offset position.....	58
8.06	Stiffness of the bearing when the area ratio 0,56 for case A at offset position.....	58
8.07	Damping of the bearing when the area ratio 1 for case A at offset position.....	59
8.08	Damping of the bearing when the area ratio 0,56 for case A at offset position.....	59
8.09	Stiffness of the bearing when the area ratio 1 for case B at centered position.....	60
8.10	Stiffness of the bearing when the area ratio 0,56 for case B at centered position....	61
8.11	Damping of the bearing when the area ratio 1 for case B at centered position.....	61
8.12	Damping of the bearing when the area ratio 0,56 for case B at centered position....	62
8.13	Stiffness of the bearing when the area ratio 1 for case B at offset position.....	62



8.14	Stiffness of the bearing when the area ratio 0,56 for case B at offset position.....	63
8.15	Damping of the bearing when the area ratio 1 for case B at offset position.....	63
8.16	Damping of the bearing when the area ratio 0,56 for case B at offset position.....	64
9.01	Effect of the area ratio in the model for first-order equations.....	69

## List of Tables

	Page
5.01 Friction models and/or friction coefficients for the simulations with zeroth-order equations.....	27
5.02 Friction coefficients for the simulations with First-order equations.....	28
7.01 Results for leakage at case A centered.....	34
7.02 Results for leakage at case A 50% offset.....	34
7.03 Results for Thrust force at case A 50% offset.....	35
7.04 Results for leakage at case B centered.....	35
7.05 Results for leakage at case B 50% offset.....	35
7.06 Results for Thrust force at case B 50% offset.....	35

# Nomenclature

## Roman Letters

Symbol	Name	Dimension
$C$	Damping	N.s/m
$C_r$	Average clearance	m
$C_e$	Clearance at the entrance	m
$C_x$	Clearance at the outlet	m
$c$	Nondimensional average clearance	-
$d$	Amplitude of eccentric clearance	-
$D$	Transfer function	N/m
$D_h$	Hydraulic diameter	m
$e$	Energy	N.m
$e_r$	Roughness	m
$f$	Frequency ratio	-
$f_f$	Friction-factor	-
$f_r$	Friction factor at the rotor	-
$f_s$	Friction factor at the stator	-
$g$	constant	-
$H$	Clearance	m
$H_d$	Cell-depth	m
$h$	Nondimensionalized clearance	-
$h_d$	Nonimensionalized cell-depth	-
$ID$	Inlet radius	m
$j$	Imaginary unit, $\sqrt{-1}$	-
$K$	Stiffness	N/m
$M$	Mass	Kg
$MW$	Molecular weight	kg/kmol
$nr, mr$	Friction coefficients at the rotor	-
$ns, ms$	Friction coefficients at the stator	-
$OD$	Outlet radius	m
$P$	Pressure	N/m <sup>2</sup>
$P_c$	Critical pressure	N/m <sup>2</sup>
$P_r$	Reservoir pressure	N/m <sup>2</sup>

$P_s$	Sump pressure	N/m <sup>2</sup>
$p$	Nondimensionalized pressure	-
$p_s$	Nondimensionalized sump pressure	-
$\mathbf{p}$	Nondimensionalized sump pressure in complex numbers	-
$R$	Radius	m
$r$	Nondimensionalized radius	-
$Re$	Reynolds number	-
$Re_r$	Reynolds number at the rotor	-
$T$	Temperature	K
$t$	Time	s
$U$	Velocity	m/s
$\bar{u}$	Nondimensionalized velocity	-
$\mathbf{\bar{u}}$	Nondimensionalized velocity in complex numbers	-
$Z_c$	Compressibility factor	-

## Vectors

Symbol	Name
$\vec{n}$	Normal vector
$\vec{V}$	Velocity vector

## Greek Letters

Symbol	Name	Dimension
$\gamma$	Heat capacity ratio	-
$\varepsilon$	Entrance loss coefficient	-
$\epsilon$	Excentricity ratio	-
$\zeta$	Exit recovery factor	-
$\theta$	Angle	rad
$\mu$	Dynamic viscosity	N.s/ m <sup>2</sup>
$\mu_T$	Joule-Thomson coefficient	K. m <sup>2</sup> /N
$\mathcal{V}$	Volume	m <sup>3</sup>
$\rho$	density	kg/ m <sup>3</sup>
$\rho_r$	Reservoir density	kg/ m <sup>3</sup>
$\bar{\rho}$	Nondimensionalized density	-
$\mathbf{\bar{\rho}}$	Nondimensionalized density in complex numbers	-
$\tau$	Nondimensionalized time	-
$\tau_{r\theta}$	Shear stress at the rotor in circumferential direction	N/ m <sup>2</sup>
$\tau_{s\theta}$	Shear stress at the stator in circumferential direction	N/ m <sup>2</sup>
$\tau_{rR}$	Shear stress at the rotor in radial direction	N/ m <sup>2</sup>
$\tau_{sR}$	Shear stress at the stator in radial direction	N/ m <sup>2</sup>
$\tau_w$	Shear stress at the wall	N/ m <sup>2</sup>
$\phi$	Axial frequency of the rotor	rad/s
$\omega$	Rotational speed	rad/s

$\Omega$	frequency	rad/s
----------	-----------	-------

### Subscripts

Symbol	Name
$i$	inner
$o$	outer
$R$	Radial direction
$\theta$	Circumferential direction
$Z$	Axial direction
$r$	Relative to rotor
$s$	Relative to stator
0	Zeroth-order
1	First-order

### Abbreviations

BDF	Backward Differentiation Formulae
CFD	Computational Fluid Dynamics
JTE	Joule-Thompson Effect



# Chapter 1

## Introduction

Rotating equipment needs axial and radial support to work efficiently. For radial support there is a wide variety of radial bearings. For axial support there are devices called thrust bearings and they also come in different configurations, such as ball bearings, roller bearings, fluid bearings and magnetic bearings. In general a good bearing has low friction, thus low power losses. Each type of bearing has its specification, for some applications rolling-element bearings are better for supporting the rotor. Fluid film bearings generally have lower friction and longer lifespan than mechanical bearings and require little or no maintenance. Another important feature of fluid bearings is that they add damping to the system, attenuating the vibrations at certain frequencies. Using gas instead of oil can enhance benefits of fluid films bearings. In fact, due to lower viscosity, friction is lower and there is no need for lubricants, making them better suited for high-speed applications. Gas has substituted liquids in industrial applications due to stability and environmental concerns especially for low load and high speed applications.

Regarding seals, there are many types of seals in the industry; some of them are dry while other requires a lubrication fluid. A good seal is considered to allow low temperature increase and low leakage, one type of seals largely popular in the industry is the labyrinth seal, which fulfills those requirements. Unfortunately there are other issues that must be taken into account, such as the excessive destabilizing forces that under some circumstances these seals exert on the rotor due to development of high cross coupled stiffness and low direct damping. Therefore honeycomb/hole-patterned seals have been used for replacing labyrinth seals in some particular applications, especially when subjected to high differential pressure. These types of seals consist in many small pockets of the shape of honeycomb or simple holes uniformly distributed over a surface. Not only they reduce the leakage from older type of seals and reportedly present less than 5% temperature increase or decrease, but also reduce swirl (responsible for increasing cross-coupled stiffness) and increase direct damping, attenuating the destabilizing effects. There are also setbacks for these types of seals; the most noticeable are related to their high sensitivity of their dynamic coefficients versus the tapering of their geometry.

Statoil has patented a thrust bearing that uses a honeycomb/hole-patterned surface. This new design brings the positive aspects of honeycomb/hole-patterned seals into the axial bearing configuration, such as high static force, low leakage and positive damping. This type of bearing are significantly cheaper than magnetic bearings in terms of cost and manufacturability. For that reason the company wants to develop an analytical tool to predict the leakage, thrust force, damping and stiffness of axial bearings. The results must be compared to Computational Fluid Dynamics (CFD) simulations before planning experiments.

Several studies have been developed for annular seals, equations and friction models. A tool called ISOTSEAL was developed by the Turbolab at the Texas A&M University in the United States and its results were validated with some experiments. However for some pressure ratios higher than a certain value the tool is not able to predict any result.

Developing a similar tool to ISOTSEAL is requested, meaning that the user must input the boundary conditions such as pressure at the inlet and outlet, temperature and the gas properties. In return the tool must deliver the leakage, thrust force and damping and stiffness for different axial frequencies of the rotor.

To accomplish the task, this study worked using the “Bulk-Flow” theory developed by G.G. Hirs in 1973 for lubricant films but adapted to the use of gas. The Bulk-flow theory has not only being applied on analyzing seals but it is used for analyzing the flow through shrouded impellers for liquid and gas, and it has successfully predicted the leakage and rotordynamic coefficients for seals and impellers. For those reasons there are other algorithms beyond ISOTSEAL that apply the Bulk-flow theory. With some assumptions made on the governing equations, the problem was simplified in a 1D problem. Two sets of equations are considered from the model. One determines the leakage and thrust force assuming steady and axisymmetric flow, while the other defines the stiffness and damping. This study does not take into account the tilting of the rotor, therefore cross-coupled stiffness and cross-coupled damping were not considered.

The results were compared to the ones from CFD simulations ordered to another company. The criterion for comparison is that leakage, thrust force, damping and stiffness from the algorithm must be a reasonable error relative to the CFD simulations (i.e. 10%). There are previous studies showing different friction models and the use of coefficients that show the losses at the inlet of the bearing due to sudden contraction. Having many parameters that influence the accuracy of the results requires a sensitivity test to determine the most critical ones; also other cases besides the ones mentioned in the CFD simulation report were used for comparison.

Some restrictions must be considered. Firstly numerical integration using computational tools involves their numerical errors due to computational resources (floating point and truncation, among others). Another obstacle is the nonexistence of experimental results to which the results from the analytical tool can be compared; even the CFD simulations used have not been validated yet.

The following chapters will provide the answers to the reader’s questions regarding phenomena, procedures and analysis of the findings in this thesis. A literature review of the previous work in



annular gas seal and shrouded impellers in addition to a review in rotordynamics can be found in chapter 2. In chapter 3 the geometry of the thrust bearing that will be analyzed is presented with insights of the phenomena involved. The bulk-flow is developed in chapter 4. The following chapter shows the different friction models available at the moment and the models employed on this thesis. The numerical methods are discussed in chapter 6. The last three chapters of this thesis show the different results for leakage, thrust force, stiffness and damping and the consequent conclusions.



## Chapter 2

### Literature review

Hirs (1973) introduced the “Bulk-flow theory” that contributed to the theory of turbulent thin films in journal bearings and seals. In Storteig(1999) it is argued that the theory “does not consider fluctuations in local velocities due to turbulence or the shape of the velocity profiles when relating average fluid velocity to wall shear stresses” (Storteig, 1999)

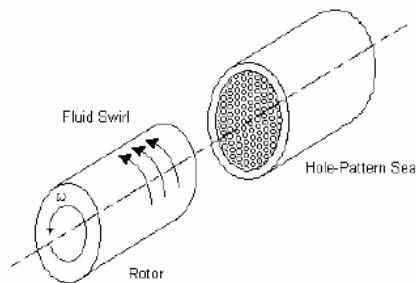


Figure 2.01. Hole-patterned annular seal (Shin, 2005).

This theory is a simplified mathematical modelling of seals, and though it was proposed for lubricant films it has been used for gas seals as well. However, the equations must be adapted. The compressibility effect must be counted in the equations by adding the energy equation and an equation of state, such as ideal gas for example.

Nelson (1984,1985) developed a computational model using Hirs' Bulk-flow theory to model a system of smooth-rotor/roughened-stator. This model predicted that honeycomb seals would decrease cross-coupled stiffness, which is beneficial to the stability of the system. It was also predicted that convergent seals developed higher direct stiffness than constant clearance seals.

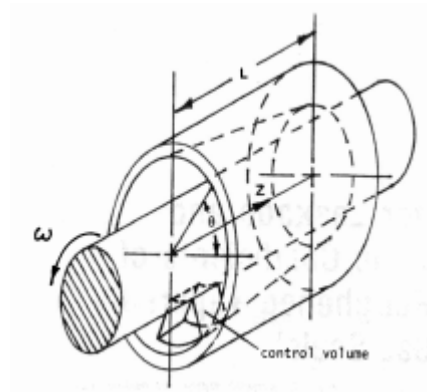


Figure 2.02. One-control-volume for annular seals (Nelson, 1984).

Childs (1991) developed a model for shroud impellers adapting the Bulk-Flow theory to determine the axial forces developed on a pump impeller shroud. The procedure is the same as in previous work, but differs in the coordinate system.

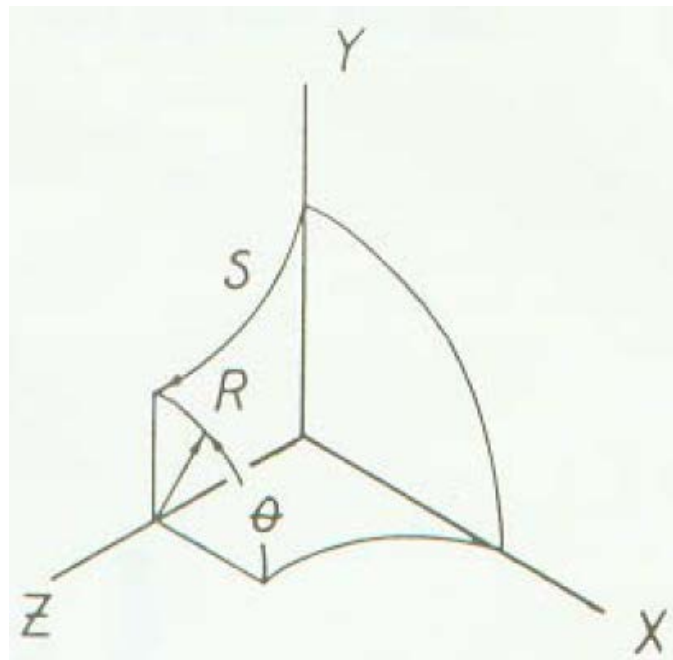


Figure 2.03. Shrouded impeller surface geometry (Gupta, 2005).

Before Ha & Childs (1996), the Bulk-Flow theory was considered for one-control-volume models. Ha & Childs (1996) developed a two-control-volume model, which improved the predictions for direct stiffness and damping, and cross-coupled stiffness.

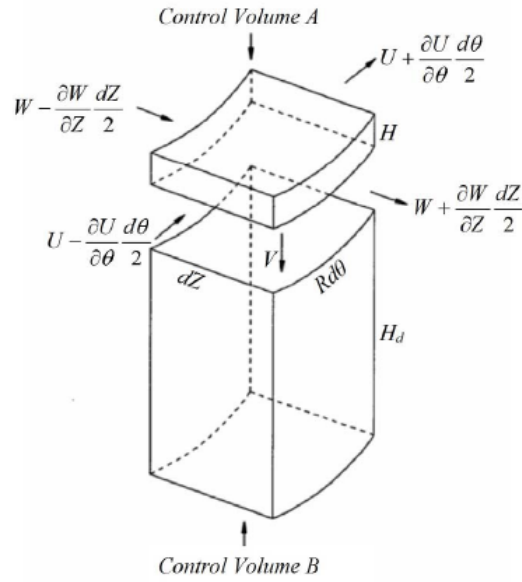


Figure 2.04. Two-control-volume analysis (Shin,2005).

Kleynhans & Childs (1997) showed that the cell of honeycomb seals reduce the effective acoustic velocity of the flow within the seals and they demonstrated that “the acoustic influence of cell depth caused frequency depended rotordynamic characteristic”, which means that the modeling of seals required an acoustic model as well.

The bulk-flow model is highly dependent on the friction models, specially the friction-factor models. D’Souza & Childs(2002) compared predictions for rotordynamic coefficients using three different friction-factor models and found that except for cross-coupled coefficients, the three models predict the same rotordynamic coefficients. It was discussed as well about the dependency of the friction-factor on cell depth, clearance, cell width and the Reynolds number among other parameters.

Gupta (2005) presented the analysis for shrouded centrifugal compressor impellers, which adapted the equations for pump impellers using the equation of state for gases. This work included the centrifugal and Coriolis effects on the analysis and solution of the equations.

In Shin (2005) the equations for annular seals were adapted to add the energy equation for attempts to predict the compressibility effects on the seal. Before that, the gas in the annular seals and shrouded impeller were considered to follow an isothermal process. This study revealed that real gas properties moderately affected the dynamic coefficients, especially for high pressure gas application.

In general the reaction forces acting on one-degree-of-freedom systems can be modeled as:

$$-F = M\ddot{x} + C\dot{x} + Kx \quad 2.01$$

In equation 2.01,  $x$  represents the axial displacement relative to the stator and  $F$  represents the reaction force action on the rotor. The rotordynamic coefficients are the stiffness  $K$  and damping  $C$ .  $M$  represents the added mass, but for gases the inertial effects are negligible.

$$M\ddot{x} = 0 \quad 2.02$$

Stiffness is a mechanical system in charge of opposing and resisting external dynamic forces (Muszynska, 2005). It represents the rigidity of a system. Stiffness is associated to the ratio of an applied dynamic force to the dynamic response of a mechanical device as in equation 2.03.

$$K = \frac{F}{x} \quad 2.03$$

Equation 2.03 also describes the function of springs, which react with an opposite force when being pulled or pushed. However, for springs the energy remains constant.

Damping creates forces that oppose motion by dissipating the energy of the movement. In general, the dissipation can occur in three main forms of damping (Crawford, 1992):

- Friction damping: it happens when two parts of a system slide against each other.
- Viscous damping: it comes from the resistive force against a body moving through a viscous fluid.
- Hysteresis damping: it is due to the slipping and sliding of internal lanes when a material is bent.

For systems of one degree of freedom (one direction of motion is allowed) when damping is positive, it means a decay in the amplitude of vibrations, which keeps the system as “stable” whereas negative damping is responsible for a grow in the amplitude of vibrations in time, this response is unstable (API, 2010).

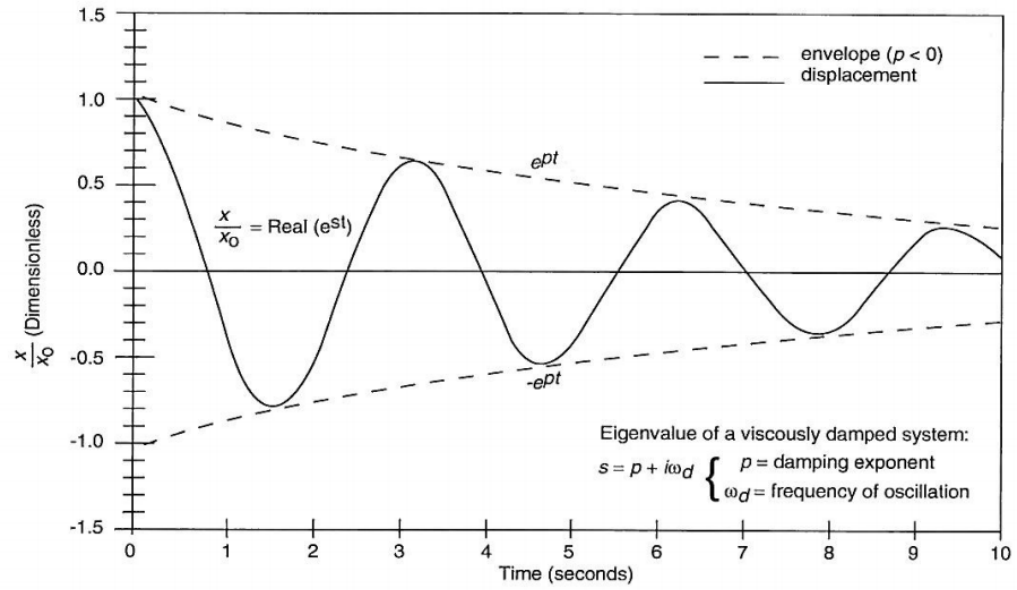


Figure 2.05. Response of a spring-mass system for stable performance (API, 2010).

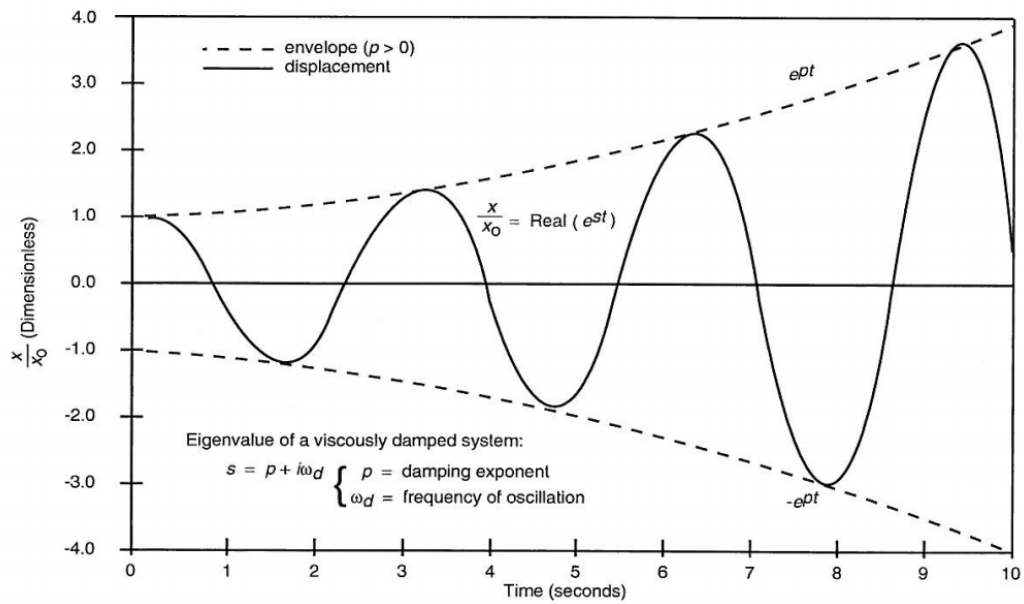


Figure 2.06. Response of a spring-mass system for unstable performance (API, 2010).





## Chapter 3

### Geometry and considerations

The model for thrust gas bearing is described by Underbakke et al.(2012) explaining the functionality of such device. For this thesis it is necessary to describe the geometry of the bearing as well as some important considerations when simplifying the governing equations employing the bulk-flow theory.

The thrust bearing consist in two tapered textured surfaces that face a smooth disk similar to a balance drum from the rotor. The surfaces of the bearing have some orifices uniformly distributed as illustrated in figure 3.01.

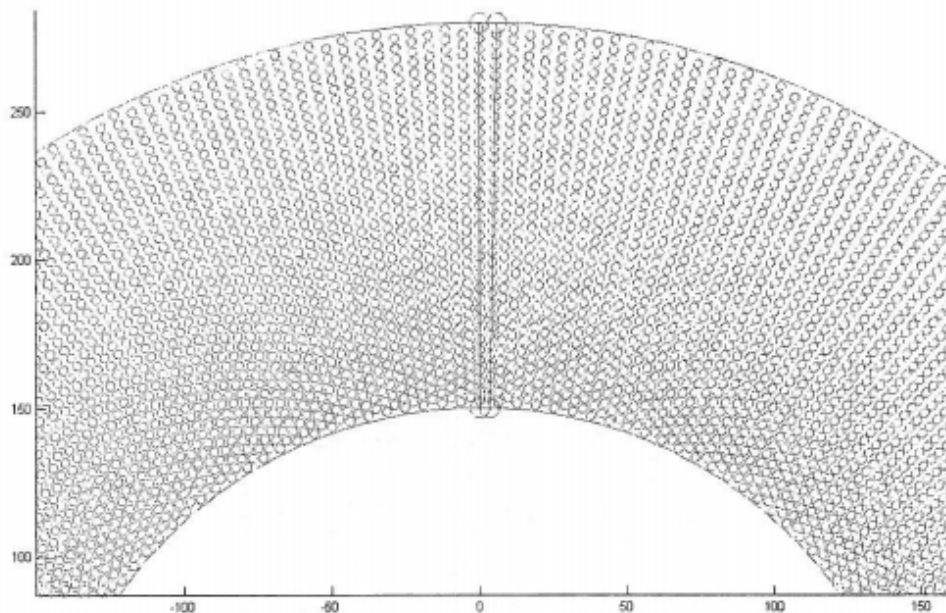


Figure 3.01. Distribution of the holes in the hole-patterned surface (Lloyd's Register, 2012).

Two base cases are taken in consideration in this thesis, case A as in figure 3.02 and case B as in figure 3.03. Those figures show cases A and B at centered position, meaning that at both sides of the bearing the clearance distribution is the same. The simulations were also carried out at offset position. An offset position of 50% means that the smallest clearance will be reduced by 50% in one side by moving the rotor that same distance towards that side and the other side will have 50% more clearance, as illustrated in figures 3.04 and 3.05.

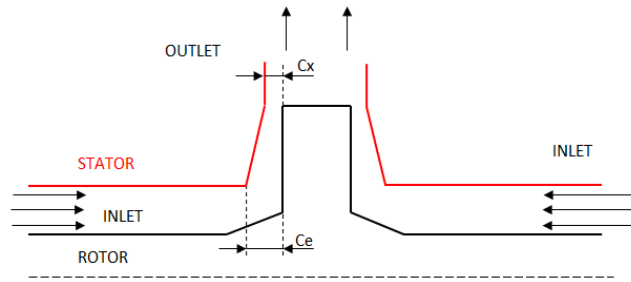


Figure 3.02. Case A at centered position.

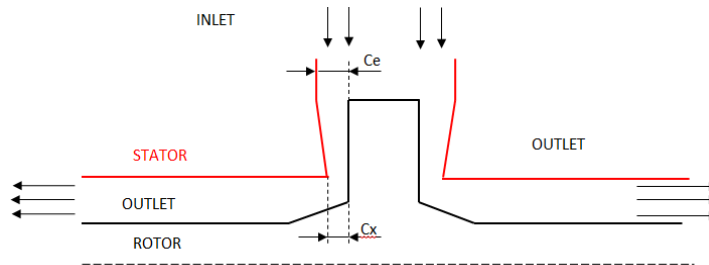


Figure 3.03. Case B at centered position.

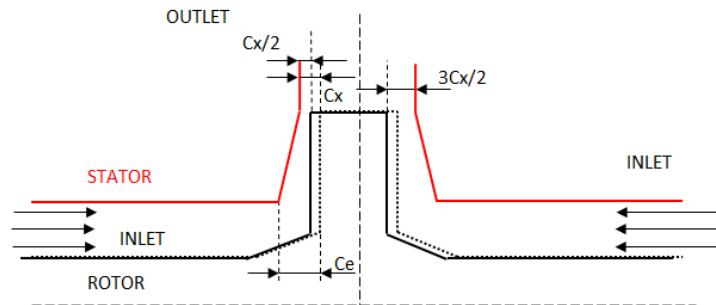


Figure 3.04. Case A with 50% offset.

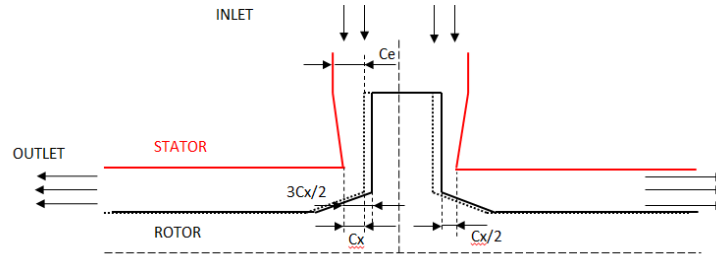


Figure 3.05. Case B with 50% Offset.

The fluid acts at both sides of the rotor, producing stiffness and damping in the system. For the thrust bearing, this is equivalent of having two set of springs and dampers working in parallel as seen in figure 3.06.

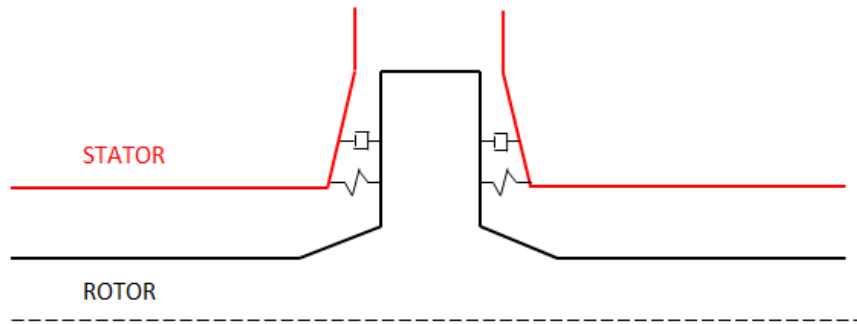


Figure 3.06. Representation of the spring-damper system for both sides of the thrust bearing.

To calculate the equivalent stiffness and damping for two springs and dampers in parallel, equations 3.01 and 3.02 can be used:

$$K_{equivalent} = K_1 + K_2 \quad 3.01$$

$$C_{equivalent} = \frac{1}{\frac{1}{C_1} + \frac{1}{C_2}} \quad 3.02$$

To account all the possible effects involved in the Bulk-Flow model for thrust bearings in chapter 4, it is important to define some phenomena and terms:

- Entrance loss coefficient: the entrance loss coefficient counts all the losses at the entrance due to a sudden contraction. This coefficient was used to model the losses due to local separation and impacts at the inlet for annular seals and as a consequence affecting the pressure and density distribution at the inlet. The loss of momentum due to sudden contraction will apply for case B, but for case A it should account the losses due to impact and change in flow direction. If the coefficient is “0” no losses due to sudden contraction are assumed.
- Exit Recovery factor: it has been studied in Childs (1993) the possibility of a greater pressure downstream the bearing than the pressure immediately inside the bearing. In Childs (1993) it has been noted as well that the exit-recovery phenomenon increases a seal’s direct stiffness. When the exit recovery factor is “1”, no recovery of pressure is implied.

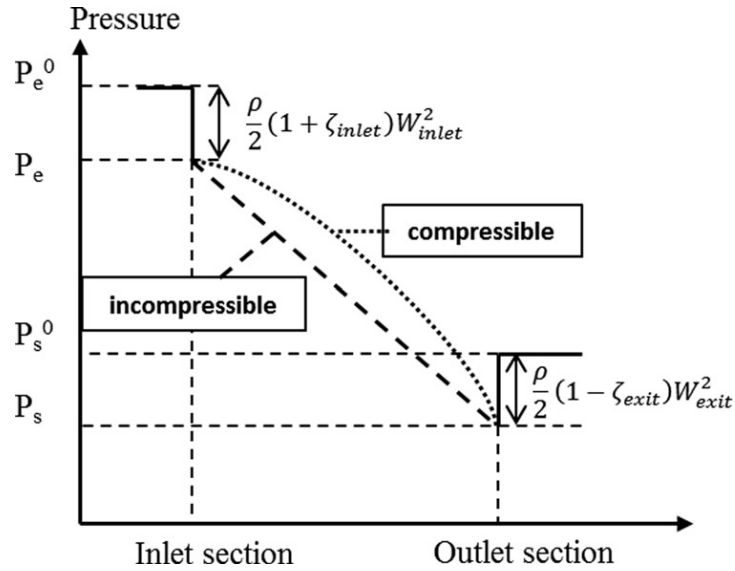


Figure 3.07. Pressure drop for a system (Hassini & Arghir, 2013).

- Coriolis Effect and centrifugal effect: these two effects are not present in the calculations for annular seals due to the assumption of zero radial velocities. They are both inertial forces viewed in a rotating reference frame. They are both proportional to the mass of the fluid but differ in the proportionality of the velocities. The Coriolis Effect describes the apparent deflection of a particle when moving relative to a rotating system, the force is described as  $F = -2m\Omega \times U_r$  where  $m$  is the mass,  $\Omega$  is the rotating speed of the system and  $U_r$  the relative velocity. The centrifugal effect is the apparent force that draws a particle away from its rotating axis; it can be described as  $F = m \frac{U_\theta^2}{r}$  where  $U_\theta$  is the tangential velocity (Persson, 2005).

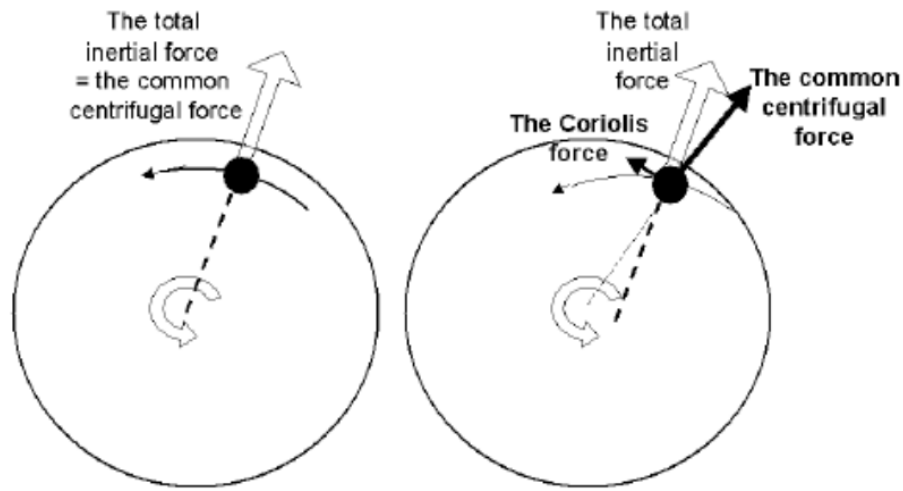


Figure 3.08. Illustration of Coriolis and centrifugal forces (Persson, 2005).

- **Joule-Thomson Effect.** The Joule-Thomson effect (JTE) is normally referred to when analyzing the performance of the fluid through a valve. It describes for real gas the effect on temperature as a result of pressure drop in an adiabatic process, keeping the enthalpy approximately constant. This is called throttling. The Joule-Thomson coefficient ( $\mu_T$ ) describes the behavior of temperature of the fluid during a throttling process and it is defined in equation 3.03. For ideal gases the Joule-Thomson coefficient is zero because the enthalpy is solely a function of the temperature, and therefore pressure drop do not cause a temperature change. Nonetheless for real gases the temperature may increase or decrease and it depends on the position of the process on a T-P diagram as in figure 3.09. The line that passes through the points of zero slopes in the enthalpy lines is called the inversion line, at the right side of the inversion line temperature increases when throttling and at the left side the temperature increases when throttling (Sonntag & Van Wylen, 1991).

$$\mu_T = \left( \frac{\partial T}{\partial P} \right)_h \quad 3.03$$

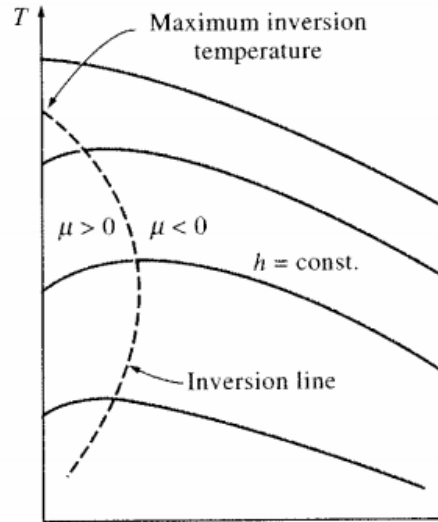


Figure 3.09. T-P diagram for real gases showing the inversion line (Sonntag & Van Wylen, 1991).

- Friction: Friction appears as the force that opposes the motion development at the interface of two bodies relatively moving to each other (Cengel & Boles, 1993). The energy supplied is converted into heat during the process; therefore there is a temperature rise at the interface. This friction does not involve solely two solid bodies in contact. It can be encountered between fluid and solid or between the layers of a fluid moving at different velocities. In fluid mechanics, friction is directly related to viscosity as it is a measure of fluid's resistance to flow, which relates local stresses in a moving fluid to the strain rate of the fluid element (White, 2011). There have been plenty of friction models to predict the friction in a system. Hirs (1973) proposed adopting a Blasius-type pipe friction factor model while in Childs (1993) it was defined a Fanning friction model like in equation 3.04, where  $\tau$  is the shear stress at the wall,  $f$  the friction factor,  $\rho$  the density and  $v$  the fluid velocity relative to the wall.

$$\tau_w = \frac{f_f \rho U^2}{2} \quad 3.04$$

## Chapter 4

### Bulk-flow model

In this chapter the work from Rondon (2013) will be expanded to introduce some terms related to Coriolis and Centrifugal effects. The integral forms of the bulk-flow governing equations using the control volumes illustrated in figure 4.01 are:

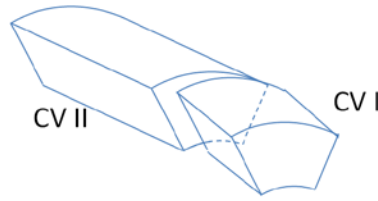


Figure 4.01. The two control volumes(Rondon, 2013).

Continuity

$$\frac{\partial}{\partial t} \left( \iiint \rho d\mathcal{V} \right) + \oint \rho \vec{\nabla} \cdot \vec{n} dA = 0 \quad 4.01$$

Circumferential momentum

$$\frac{\partial}{\partial t} \left( \iiint \rho U_{\theta} d\mathcal{V} \right) + \oint \rho U_{\theta} \vec{\nabla} \cdot \vec{n} dA = \sum F_{\theta} \quad 4.02$$

Radial momentum

$$\frac{\partial}{\partial t} \left( \iiint \rho U_R d\mathcal{V} \right) + \oint \rho U_R \vec{\nabla} \cdot \vec{n} dA = \sum F_R \quad 4.03$$

$$\frac{\partial}{\partial t} \left( \iiint \rho e dV \right) + \iint (\rho e + p) \vec{\nabla} \cdot \vec{n} dA = -R\omega\tau_{r\theta} \quad 4.04$$

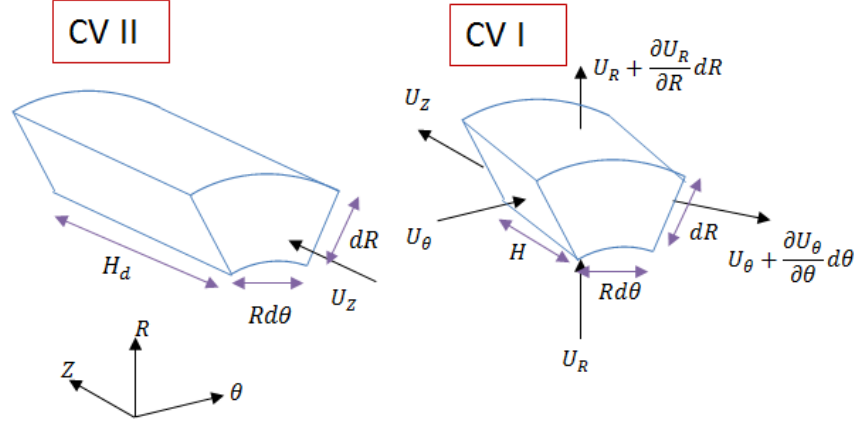


Figure 4.02. The system of coordinates for the two control volumes.

Adiabatic flow was assumed for the energy equation and it is only affected by the friction caused by the rotor. It has been assumed adiabatic flow because in the CFD simulations the temperature increased over 13% contrary to the temperature increase for seals reported by Kleynhans and Childs (1997) which was less than 5% which was the reason for assuming isothermal flow.

Continuity equation for control Volume A:

$$\frac{\partial}{\partial t}(\rho H) + \frac{1}{R} \frac{\partial}{\partial R}(\rho U_R H R) + \frac{1}{R} \frac{\partial}{\partial \theta}(\rho U_\theta H) + \rho U_z = 0 \quad 4.05$$

Continuity Equation for control volume B:

$$H_d \frac{\partial \rho}{\partial t} = \rho U_z \quad 4.06$$

Circumferential momentum equation

$$\frac{\partial}{\partial t}(\rho U_\theta H) + \frac{1}{R} \frac{\partial}{\partial \theta}(\rho U_\theta^2 H) + \frac{1}{R} \frac{\partial}{\partial R}(\rho U_\theta U_R H R) + \rho H \frac{U_\theta U_R}{R} + \rho U_\theta U_z + \tau_{r\theta} + \tau_{s\theta} = -\frac{H}{R} \frac{\partial P}{\partial \theta} \quad 4.07$$



Where the term  $\rho H \frac{U_\theta U_R}{R}$  is the Coriolis term in the equation 4.07.

Radial momentum equation

$$\frac{\partial}{\partial t}(\rho U_R H) + \frac{1}{R} \frac{\partial}{\partial \theta}(\rho U_\theta U_R H) + \frac{1}{R} \frac{\partial}{\partial R}(\rho U_R^2 H R) + \rho U_R U_Z + \tau_{rR} + \tau_{sR} - \rho H \frac{U_\theta^2}{R} = -H \frac{\partial P}{\partial R} \quad 4.08$$

Where the term  $\rho H \frac{U_\theta^2}{R}$  is the centrifugal term in equation 4.08.

Energy equation for control volume A:

$$\frac{\partial}{\partial t}(\rho H e) + \frac{1}{R} \frac{\partial}{\partial \theta}((\rho e + p) U_R H R) + \frac{1}{R} \frac{\partial}{\partial \theta}((\rho e + p) U_\theta H) + (\rho e + p) U_Z = -R \omega \tau_{r\theta} \quad 4.09$$

Energy equation for control volume B:

$$\frac{\partial}{\partial t}(\rho H_d e) = (\rho e + p) U_Z \quad 4.10$$

Where,

$$e = \frac{P}{Z_c(\gamma - 1)\rho} + \frac{U_\theta^2}{2} + \frac{U_R^2}{2} \quad 4.11$$

The variable  $U_Z$ , described as the transient axial velocity from control volume A to control volume B, can be eliminated by substituting  $U_Z$  from equation 4.06 into equations 4.05, 4.07 and 4.08, and equation 4.10 into equation 4.09.

For the energy equation, it is assume that the flow is adiabatic and therefore bi heat flow rate terms appear.

The shear stresses are expressed as:

$$\tau_{r\theta} = \frac{\rho f_r U_r (U_\theta - R\omega)}{2} \quad 4.12$$

$$\tau_{s\theta} = \frac{\rho f_s U_s U_\theta}{2} \quad 4.13$$

$$\tau_{rR} = \frac{\rho f_r U_r U_R}{2} \quad 4.14$$

$$\tau_{sR} = \frac{\rho f_s U_s U_R}{2} \quad 4.15$$

Where relative velocities are:

$$U_r = \sqrt{U_R^2 + (U_\theta - R\omega)^2} \quad 4.16$$

$$U_s = \sqrt{U_R^2 + U_\theta^2} \quad 4.17$$

The friction factors are determined by the friction-factor model. The loss due to sudden contraction at the inlet is modeled in equation 4.18 when the inlet is at the inner radius and equation 4.19 when the inlet is at the outer radius:

$$P_r - P_{(R_i)} = \frac{(1 + \varepsilon)\rho_{(R_i)}U_{R(R_i)}^2}{2} \quad 4.18$$

$$P_r - P_{(R_o)} = \frac{(1 + \varepsilon)\rho_{(R_o)}U_{R(R_o)}^2}{2} \quad 4.19$$

Assuming an isentropic relationship between the conditions before and after the inlet, equation 4.20 when the inlet is at the inner radius and 4.21 when the inlet is at the outer radius are written:

$$\frac{P_{(R_i)}}{P_r} = \left(\frac{\rho_{(R_i)}}{\rho_r}\right)^\gamma \quad 4.20$$

$$\frac{P_{(R_o)}}{P_r} = \left(\frac{\rho_{(R_o)}}{\rho_r}\right)^\gamma \quad 4.21$$

And the exit recovery is modeled in equation 4.22 when the outlet is at the outer radius and in 4.23 when the outlet is at the inner radius:

$$P_s - P_{(R_o)} = \frac{(1 - \zeta)\rho_{(R_o)}U_{R(R_o)}^2}{2} \quad 4.22$$

$$P_s - P_{(R_i)} = \frac{(1 - \zeta)\rho_{(R_i)}U_{R(R_i)}^2}{2} \quad 4.23$$

To solve similar equations for seals and impellers, Nelson (1984,1985) and later Childs (1991,1993) propose to use the “perturbation theory”. This theory consists on finding an approximate solution

for mathematical problems that cannot be solved exactly by adding small terms to the description (Vanden-Eijnden, n.d.). The solution of the problem  $A$  is expressed as a power series of small parameters as in equation 4.24. The term  $A_0$  corresponds to the solution of the problem when it is simplified, while the rest of terms are approximation or deviations from that solution, which are higher-order terms.

$$A = A_0 + \epsilon A_1 + \epsilon^2 A_2 + \dots \quad 4.24$$

When the perturbation's value  $\epsilon$  is rather small, equation 4.24 can be simplified into equation 4.25.

$$A = A_0 + \epsilon A_1 \quad 4.25$$

For this thesis, the solvable term  $A_0$  refers to zeroth-order equations and the assumptions must be steady axisymmetric flow to simplify the problem. The term  $A_1$  refers to first-order equations and to solve these equations axisymmetric flow with fixed axial motion of the rotor is needed. Leakage and thrust force, also called static solutions are calculated using the zeroth-order equations and, stiffness and damping are calculated using the first-order equations.

The procedure to solve the zeroth and first order perturbation governing equation is given in appendix A. Once the solution is obtained, the first order perturbation pressure is integrated to get perturbation reaction force. The general transfer function on two-control-volume is,

$$-F_{(j\Omega)} = D_{(j\Omega)} X_{(j\Omega)} \quad 4.26$$

The frequency of the axial movement of the rotor is  $\Omega$ ,  $F(j\Omega)$  is the reaction force and  $Z(j\Omega)$  is the displacement of the rotor. In terms of frequency dependent rotordynamic coefficients, the model is,

$$-F_{(\Omega)} = K_{(\Omega)} X + C_{(\Omega)} \dot{X} \quad 4.27$$

Therefore,

$$D_{(j\Omega)} = K_{(\Omega)} + jC_{(\Omega)} \quad 4.28$$



## Chapter 5

### Friction model

There have been many models proposed to approximate the experimental values of the friction factor to apply them in the bulk-flow theory. Hirs (1973) first based his theory on using friction model for pipes in a similar way as the renowned Blasius type:

$$f = n(Re)^m \quad 5.01$$

Where  $f$  is the friction factor,  $n$  and  $m$  are the friction-factor coefficients and  $Re$  is the Reynolds number that is defined as:

$$Re = \frac{\rho U D_h}{\mu} \quad 5.02$$

The hydraulic diameter is defined as:

$$D_h = \frac{4Area}{Perimeter} \quad 5.03$$

For Bulk-flow applications, the hydraulic diameter is defined as:

$$D_h = 2H \quad 5.04$$

Resulting in a definition of the Reynolds number for this case as:

$$Re = \frac{2\rho UH}{\mu} \quad 5.05$$

Where  $\mu$  is the dynamic viscosity of the gas and  $U$  is the velocity of the flow relative to the wall. The coefficients “ $n$ ” and “ $m$ ” are empirically determined from experimental data.

In chapter 4 it has been discussed the existence of two surfaces taken into account in the bulk-flow model. A rotating surface and a stationary surface are considered in the model and that's the reason for the existence of two friction factors, different from each other due to the different surfaces, the rotating part is considered smooth while the honeycomb/hole-patterned surface lays in the stationary part.

The relative velocities of the flow are:

$$U_s = \sqrt{U_R^2 + U_\theta^2} \quad 5.06$$

$$U_r = \sqrt{U_R^2 + (U_\theta - R\omega)^2} \quad 5.07$$

Where sub-indexes s and r refer to the stationary and rotating parts respectively.

Hirs(1973) proposed to use the Blasius model with constant friction-factor coefficients to the flow at each surface. For ISOTSEAL, as default, it was considered the following friction-factors equation 5.08 for the stator (honeycomb/hole-patterned) and equation 5.09 for the rotor (smooth surface):

$$f_s = 0,0785(Re)^{-0,1101} \quad 5.08$$

$$f_r = 0,0586(Re)^{-0,217} \quad 5.09$$

On the other hand Ha & Childs(1994) adopted different models for each surface. For the rotating part, a moody friction-factor model was proposed because the authors considered it a good model for smooth surface:

$$f_r = 0,001375 \left[ 1 + \left( 10^4 \frac{e_r}{H} + \frac{10^6}{Re_r} \right)^{1/3} \right] \quad 5.10$$

Where  $e_r$  is the roughness of the rotor and  $Re_r$  is the Reynolds number at the rotor, using  $U_r$  as the velocity of the fluid.

For a honeycomb (as well as hole-patterned) surfaces it was found a correlation using the results from a set of experiments using flat plates:

$$f_s = c_1 + \frac{H}{H_d} \left( \frac{c_2}{\left( \frac{P}{P_c} \right)} + c_3 Ma^{c_4} \right) \quad 5.11$$

Where  $P_c$  is the critical pressure of the gas, Ma is the Mach number of the flow and the constants' value  $c_1$ ,  $c_2$ ,  $c_3$  and  $c_4$  are 0,0045; 0,0023; 0,1664 and 0,2663, respectively.

Ha and Childs (1994) noted several characteristics that support the use of equation 5.11, such as:

1. The friction-factor is approximately constant as Reynolds numbers increases, but shows a better correlation to the Mach number,
2. The friction-factor decreases as the inlet pressure increases,
3. The friction-factor is sensitive to the changes in clearance,
4. The friction-factor is also sensitive to the change in the ratio of clearance to honeycomb cell width.

On the other hand, Al-Qutub et al. (2000) pointed out that there are experiments proving that the Mach number has little effect on the friction-factor. The Reynolds number is set back to be the primary source of change in the friction-factor for both the rotor and the stator. Al-Qutub et al. (2000) also noted that the friction-factor is sensitive to the change in the ratio of clearance to cell width as it can be seen in the following equations:

$$f_s = 0,081(Re)^{-0,215} \quad 5.12$$

$$f_r = \left[ 0,05126 + 0,5569 \left( \frac{H}{H_d} \right) \right] Re^{-0,096} \quad 5.13$$

In D'Souza & Childs (2002) a comparison was made between three different friction-factor models, among them are the models considered in Ha and Childs (1994) and Al-Qutub et al. (2000). A third model is considered based on the following characteristics of the friction-factor from experimental data:

1. It is sensitive to changes in the clearance,
2. Depends strongly on the cell width, cell depth and clearance,
3. The ratio of clearance to honeycomb cell width and the ratio of cell depth to cell width are important parameters
4. Depends on the Reynolds number

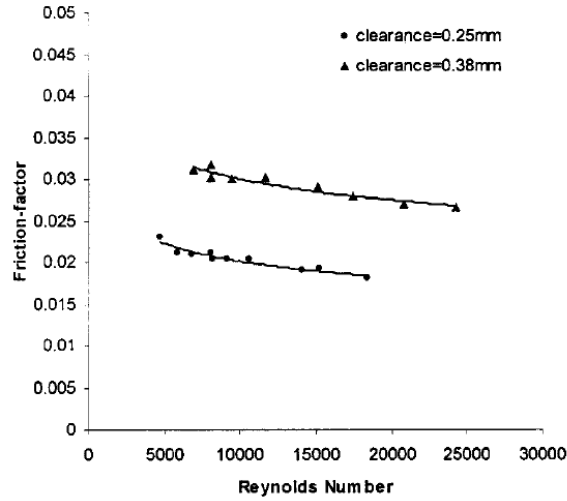


Figure 5.01. Friction-factors as function of the Reynolds number for honeycomb seals for two clearances (D'Souza & Childs, 2002).

Figure 5.01 shows measured friction-factor data at clearances 0,25mm and 0,38mm. D'Souza & Childs (2002) used the test data using different clearances and obtained the following equations based on the Blasius model:

At 0,25 mm clearance,

$$f = 0,0776 Re^{-0,1465} \quad 5.14$$

And at 0,38mm clearance,

$$f = 0,0973 Re^{-0,1277} \quad 5.15$$

Thus the coefficients will be considered as functions of the clearance in the following forms:

$$ns = a_0 + a_1 H \quad 5.16$$

$$ms = b_0 + b_1 H \quad 5.17$$

Using ns and ms from equations 5.14 and 5.15, the equations 5.14 and 5.15 transform into:

$$ns = 151,54H + 0,0397 \quad 5.16$$

$$ms = 144,62H - 0,1827 \quad 5.17$$



However there are a couple of issues to take into consideration:

- For liquid seals (the first case considered by the authors) the Reynolds number depends on the average clearance because it was first considered for constant clearance seals.
- It was found in 40% of the cases that the friction factor abruptly increases with increasing Reynolds numbers (Reynolds number in the order of 20.000 or higher).

After presenting the different friction models that were considered by many authors, for the numerical integration of the zeroth order equations these are the friction models that were used:

Table 5.01. Friction models and/or friction coefficients for the simulations with zeroth-order equations.

<b>Simulation</b>	<b>Rotor side</b>	<b>Stator side</b>
<b>1</b>	Blasius model nr=0,0586 , mr=-0,217	Blasius model ns=0,0785 , ms=-0,1101
<b>2</b>	Al-Qutub et al. (2000)	Al Qutub et al. (2000)
<b>3</b>	Ha & Childs	Ha & Childs
<b>4</b>	Blasius model nr=0,0586 , mr=-0,217	D'Souza & Childs. (2002)
<b>5</b>	Blasius model nr=0,0586 , mr=-0,217	Blasius model ns=0,0776 , ms=-0,1465
<b>6</b>	Blasius model nr=0,0586 , mr=-0,217	Blasius model ns= 0,0973, ms=-0,1277
<b>7</b>	Blasius model nr=0,0586 , mr=-0,217	Blasius model ns= 0,0586, ms=-0,217
<b>8</b>	Blasius model nr=0,0586 , mr=-0,217	Blasius model ns= 0,1247, ms=-0,047
<b>9</b>	Blasius model nr=0,0586 , mr=-0,217	Blasius model ns= 0,0612, ms=-0,044
<b>10</b>	Blasius model nr=0,0586 , mr=-0,217	Blasius model ns= 0,032, ms=0,077

For the numerical integration of the first order equations, model used the friction coefficients from table 5.02:

Table 5.02. Friction coefficients for the simulations with First-order equations.

<b>Simulation</b>	<b>Rotor side</b>	<b>Stator side</b>
<b>1</b>	Blasius model nr=0,0586 , mr=-0,217	Blasius model ns=0,0785 , ms=-0,1101
<b>2</b>	Blasius model nr=0,0586 , mr=-0,217	Blasius model ns=0,0776 , ms=-0,1465
<b>3</b>	Blasius model nr=0,0586 , mr=-0,217	Blasius model ns= 0,0973, ms=-0,1277
<b>4</b>	Blasius model nr=0,0586 , mr=-0,217	Blasius model ns= 0,0586, ms=-0,217
<b>5</b>	Blasius model nr=0,0586 , mr=-0,217	Blasius model ns= 0,1247, ms=-0,047
<b>6</b>	Blasius model nr=0,0586 , mr=-0,217	Blasius model ns= 0,0612, ms=-0,044
<b>7</b>	Blasius model nr=0,0586 , mr=-0,217	Blasius model ns= 0,032, ms=0,077

The reason behind choosing different friction coefficients for cases 5 to 10 for the zeroth-order and 2 to 7 for first-order equations is due to testing different friction models and their effect on the results from the algorithm due to the importance of the friction model in the bulk-flow theory.

## Chapter 6

### Numerical Solution

#### 6.1 Zeroth-Order Equations

To solve the zeroth-order equations listed in Appendix A, 4 boundary values are needed. At the inlet of the bearing three values are known: pressure, circumferential velocity and density. At the outlet of the bearing there are two possible conditions: if the flow is choked, the Mach number is the boundary value, and if the flow is unchoked, the pressure at the outlet must be given.

As stated before, 4 boundary values are known but not at the same border. This situation is referred as Boundary Value Problem, because the system of ordinary differential equations (ODEs) is required to satisfy boundary conditions at more than one value of the independent variable” (Cambridge Press, 2007).

Solving a Boundary Value Problem requires to employ the Shooting Method. For this method consistent values must be chosen for all the dependent variables at one limit in the shooting method. The ODEs are integrated using those values, arriving at the other boundary. In figure 6.01, discrepancies can be found from the desired boundary values leading to a multidimensional root-finding problem, which can be solved by using the Newton-Raphson Method or the Bisection Method.

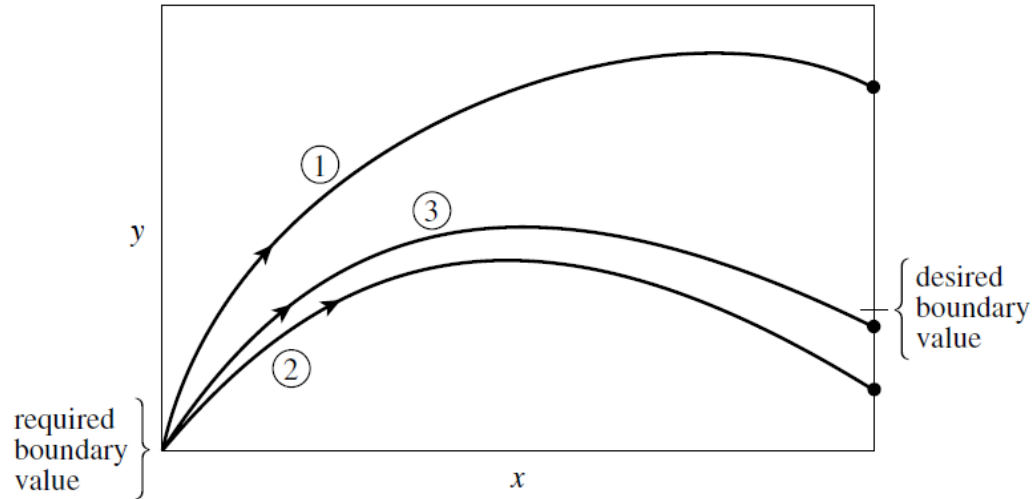


Figure 6.01. Schematic view of the shooting method (Cambridge Press, 2007).

The density, pressure and radial velocity at the bearing's inlet depend on the Mach number, which is the guessed value as stated in Appendix A. To adjust the Mach number at the inlet to match the other boundary value, in this case the pressure at the outlet, the bisection method had to be employed. The procedure is guessing two values for the Mach number at the inlet in order to get two values for the pressure, the difference between them and the desired value must produce a crossover. Interpolating using this function produces another value of the Mach number to evaluate the function with, replacing the values of the boundaries.

## 6.2 First-Order Equations

Once the values for the dependent variables are obtained as a result of solving the zeroth order equations, they will be needed for solving the first order equations. The equations only depend on the nondimensional radius as explained in Appendix A.

The procedure to integrate the first order equation is different than in the first step. The shooting method will not be necessary to guess the initial values as it was needed for the first set of equations. Using the procedure described by Childs (1993), the first step is obtaining the transfer matrix by using the equations at different initial values, then the initial values for the specific problem have to be calculated using the transition matrix. The procedure is summarized in appendix A.

### 6.3 MATLAB Solver

The zeroth and first order equations have been described as “stiff” by Gupta (2005) and Rondon (2013). Due to the nonlinearity of the equations, Rondon (2013) stated that explicit methods cannot be used to solve stiff problems. Gupta (2005) proposed an automatic stepsize adjust algorithm.

In MATLAB there is a tool called “ode15i” which is capable of solving stiff systems of equations. Ode15i is used for solving fully implicit differential equations using the “Backward Differentiation Formulae”. Backward Differentiation Formulae (BDF) consist on many different implicit multistep methods for numerically integrating ordinary differential equations. The BDF methods are implemented together with a modified Newton method to “solve the nonlinear system at each time step” (Ascher & Petzold, 1998).

ODE15i is a function that requires several inputs. It first needs consistent initial conditions: pressure, density, radial and circumferential velocities and their derivatives, for that reason it is required to use the function “decic” that calculates these derivatives. After using “decic”, those new values will be used by “ode15i” as indicated in figure 6.02.

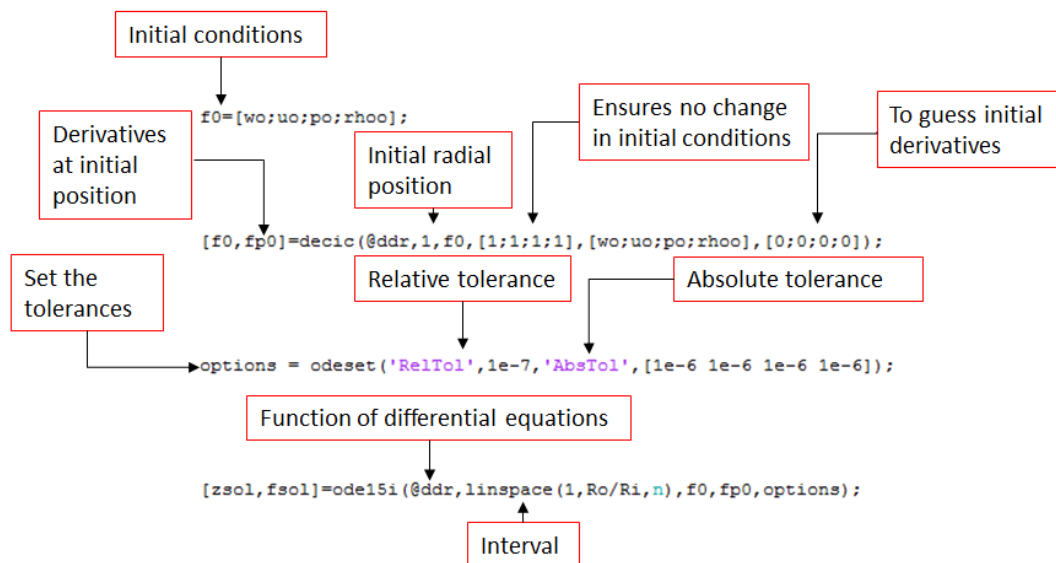


Figure 6.02. The solver’s algorithm for stiff system of ordinary differential equations.



## Chapter 7

### Results using Zeroth Order equations

The results for the static solution are compared to the results from the CFD simulations using the same conditions. First, the simulations were compared using the friction coefficients used in ISOTSEAL, then a sensitivity test was carried out varying thermodynamic parameters and physical parameters, and finally the simulations were carried out for different friction-factor models. The leakage and thrust force are of importance and therefore were compared at each simulation.

#### 7.1 Parameters

The different parameters are classified in the following categories:

##### 7.1.1 Geometrical parameters

For case A:

- $ID = 300 \text{ mm}$
- $OD = 560 \text{ mm}$
- $H_d = 3 \text{ mm}$
- $\gamma_c = 0,56$

For case B:

- $ID = 560 \text{ mm}$
- $OD = 300 \text{ mm}$
- $H_d = 3 \text{ mm}$
- $\gamma_c = 0,56$

### 7.1.2 Thermodynamic parameters

- $P_R = 120 \text{ bar}$
- $P_S = 60 \text{ bar}$
- $T_R = 120 \text{ Celsius}$
- $MW = 19,85 \text{ kg/kmol}$
- $\gamma = 1,319$
- $Z_c = 0,95$
- $\mu = 1,679 \times 10^{-5} \text{ Pa.s}$

The heat capacity ratio, compressibility factor and dynamic viscosity were calculated with the average result between inlet and outlet conditions from the CFD simulations using HYSYS with the Lee-Kesler-Plocker equation of state package.

### 7.2 Simulations using the coefficients from ISOTSEAL

The simulations were carried out assuming that the fluid does not have any circumferential velocity at the inlet. For the friction model the coefficients that were used are the same as in ISOTSEAL. Table 7.01 through table 7.06 illustrate the equations the two cases at centered and 50% offset position.

Table 7.01 Results for leakage at case A centered.

Leakage [kg/s]	Error [%]
9,64	$\pm 6,53$

Table 7.02 Results for leakage at case A 50% offset.

Leakage [kg/s]	Error [%]
9,91	$\pm 4,95$



Table 7.03 Results for Thrust force at case A 50% offset.

<b>Thrust Force</b> <b>[N]</b>	<b>Error</b> <b>[%]</b>
197800	$\pm 27,83$

Table 7.04 Results for leakage at case B centered.

<b>Leakage</b> <b>[kg/s]</b>	<b>Error</b> <b>[%]</b>
6,65	$\pm 5,50$

Table 7.05 Results for leakage at case B 50% offset.

<b>Leakage</b> <b>[kg/s]</b>	<b>Error</b> <b>[%]</b>
6,91	$\pm 9,73$

Table 7.06 Results for Thrust force at case B 50% offset.

<b>Thrust Force</b> <b>[N]</b>	<b>Error</b> <b>[%]</b>
55100	$\pm 171$

These were the results for adiabatic flow. The results for isothermal flow are shown in appendix H.

Figure 7.01 through figure 7.04 represent the pressure, temperature, radial and circumferential velocity along the radius for case A at centered position. In figure 7.01 there is discrepancy in the initial pressures, showing that there are important losses in pressure not been taken care of. Figure 7.02 shows the temperature of the gas along the bearing, showing again a discrepancy between both results, from the algorithm and from the CFD simulations.

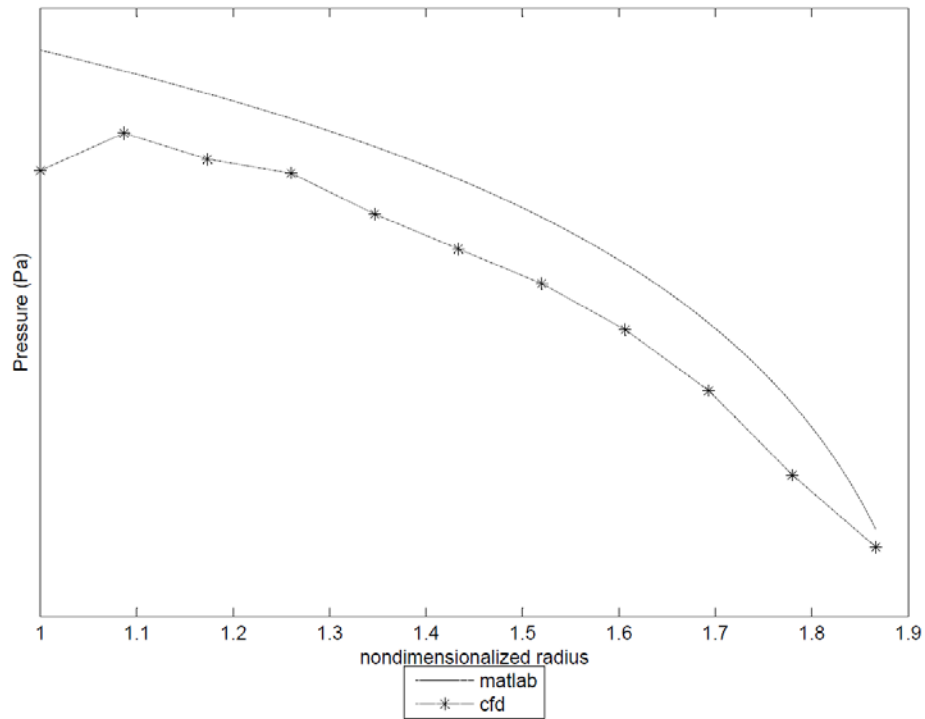


Figure 7.01. Pressure of the flow along the radius for case A at centered position with 8,59% mean percentage error.

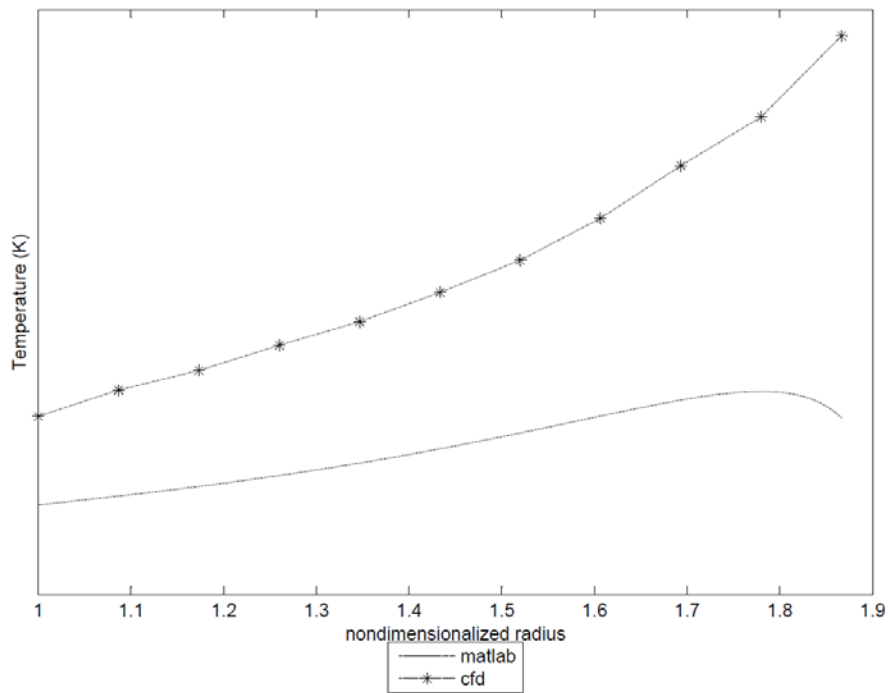


Figure 7.02. Temperature of the flow along the radius for case A at centered position with 4,45% mean percentage error.

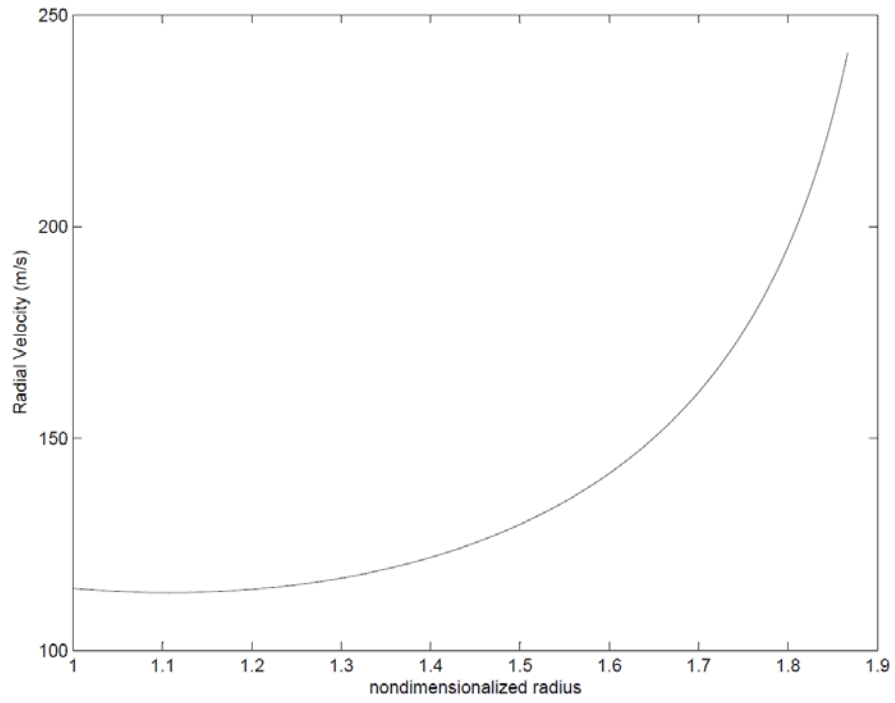


Figure 7.03. Radial Velocity of the flow along the radius for case A at centered position.

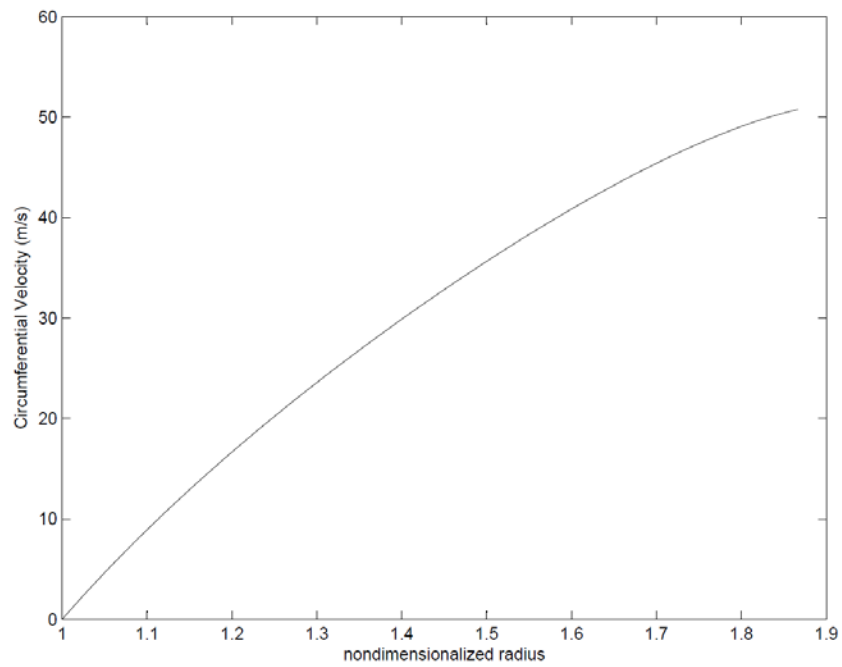


Figure 7.04. Circumferential velocity of the flow along the radius for case A at centered position.

For case B at centered position the same variables are shown in figure 7.05 through 7.08. The pressure shown in figure 7.05 is closer than the pressure distribution for case A. The same trend can be seen in appendix D for the offset position.

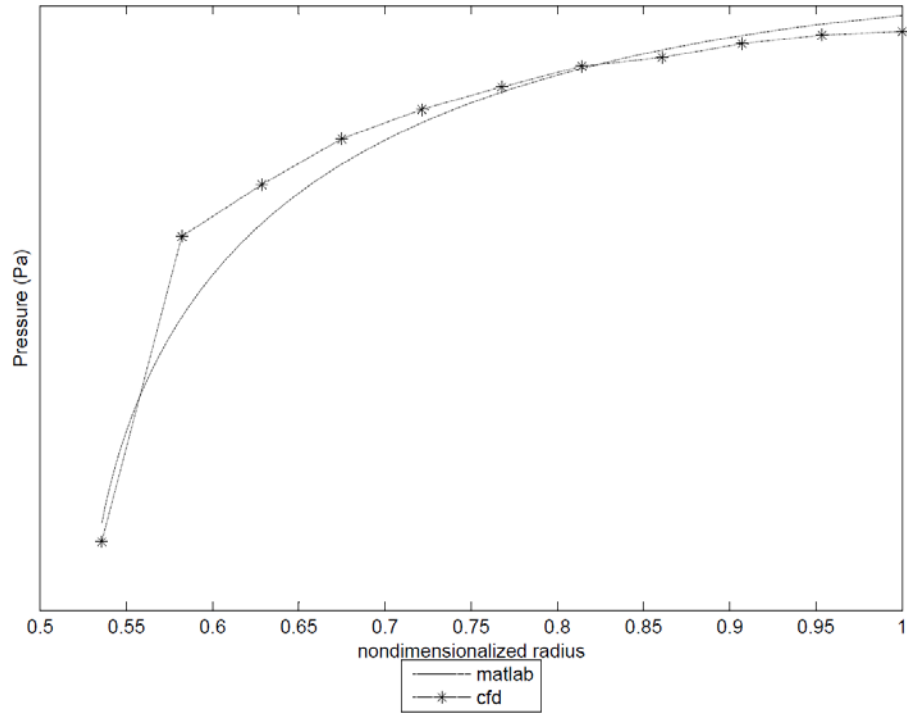


Figure 7.05. Pressure of the flow along the bearing for case B at centered position with 2,05% mean percentage error.

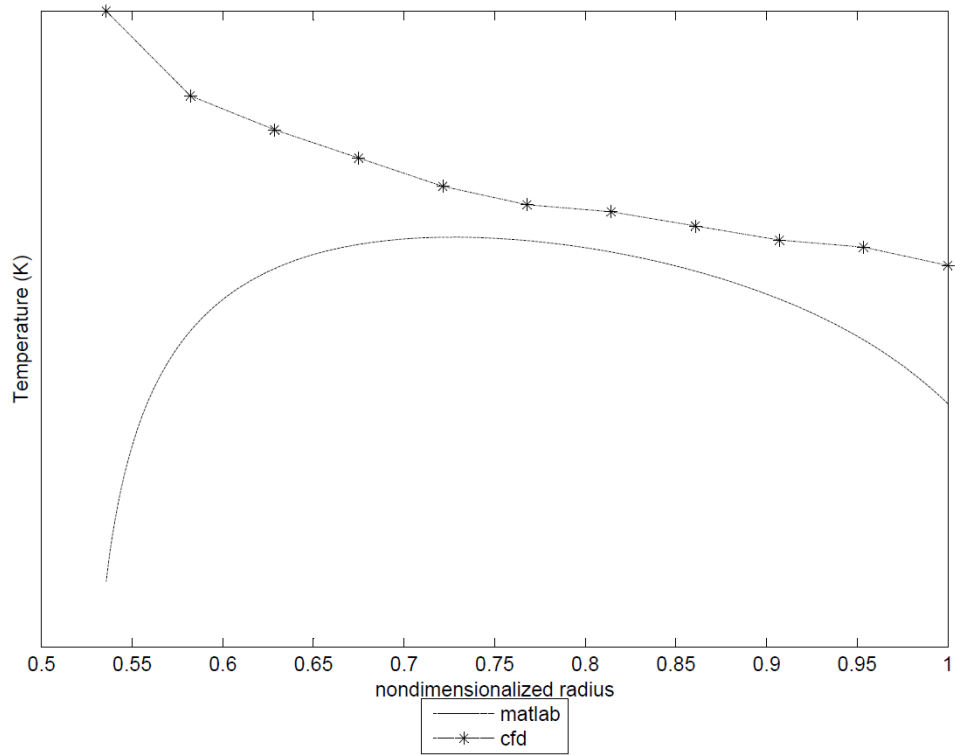


Figure 7.06. Temperature of the flow along the bearing for case B at centered position with 1,53% mean percentage error.

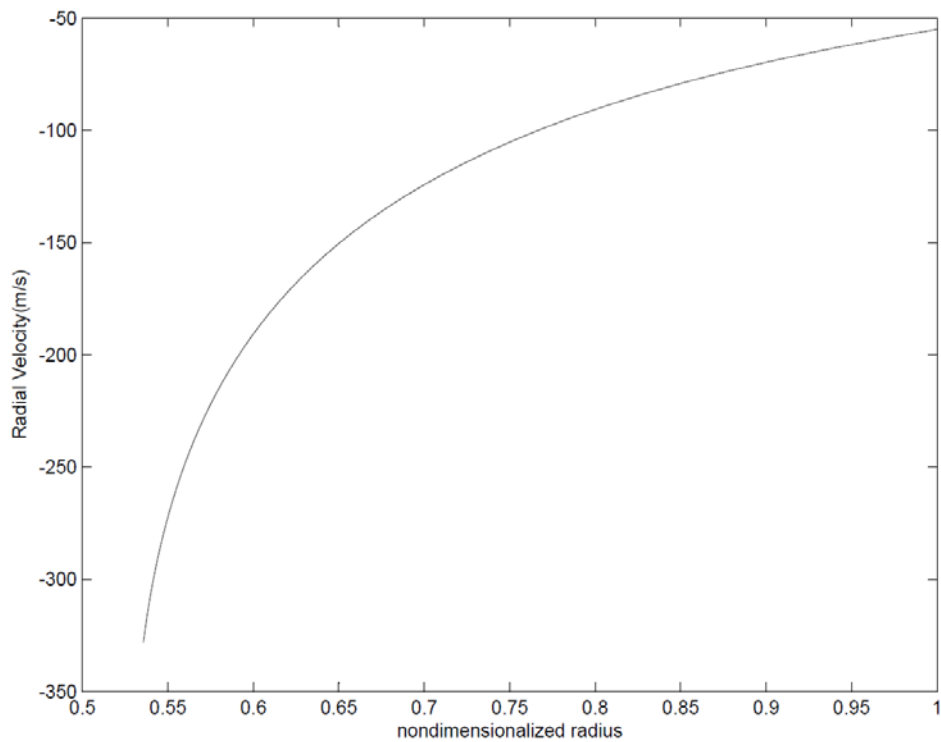


Figure 7.07. Radial Velocity of the flow along the bearing for case B at centered position.

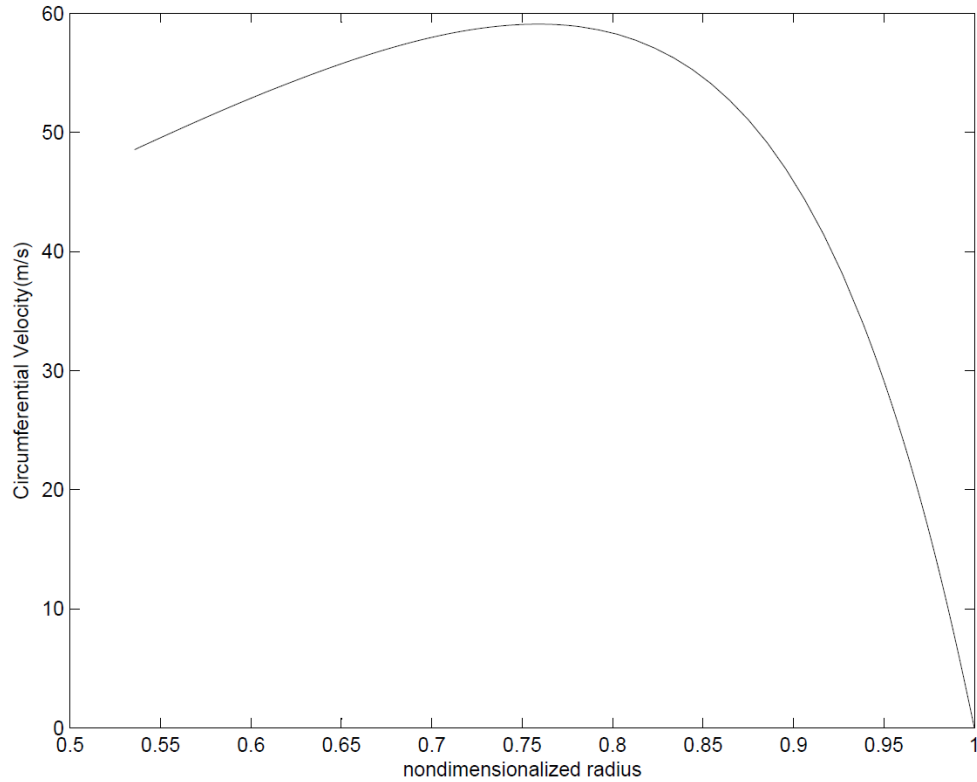


Figure 7.08. Circumferential Velocity of the flow along the bearing for case B at centered position.

### 7.3 Sensitivity test

A sensitivity test was applied in Shin (2005) because the values for the predicted leakage were not in accordance to the experiments. The friction coefficients were adjusted to fit the experimental results. For this thesis several parameters were varied, including:

- Compressibility factor
- Heat capacity ratio
- Entrance loss coefficient
- Preswirl
- $ns$
- $nr$

The entrances loss coefficient and the friction coefficients  $ns$  and  $nr$  provided the highest variation for the thrust force and the leakage and are shown in this chapter while the other parameters are presented in appendix E.

### 7.3.1 Case A

Figure 7.09 through 7.10 show the leakage and thrust force for case A varying the entrance loss coefficient, it can be seen that the leakage decreases while increasing the entrance loss coefficient, while for the thrust force it happens the opposite.

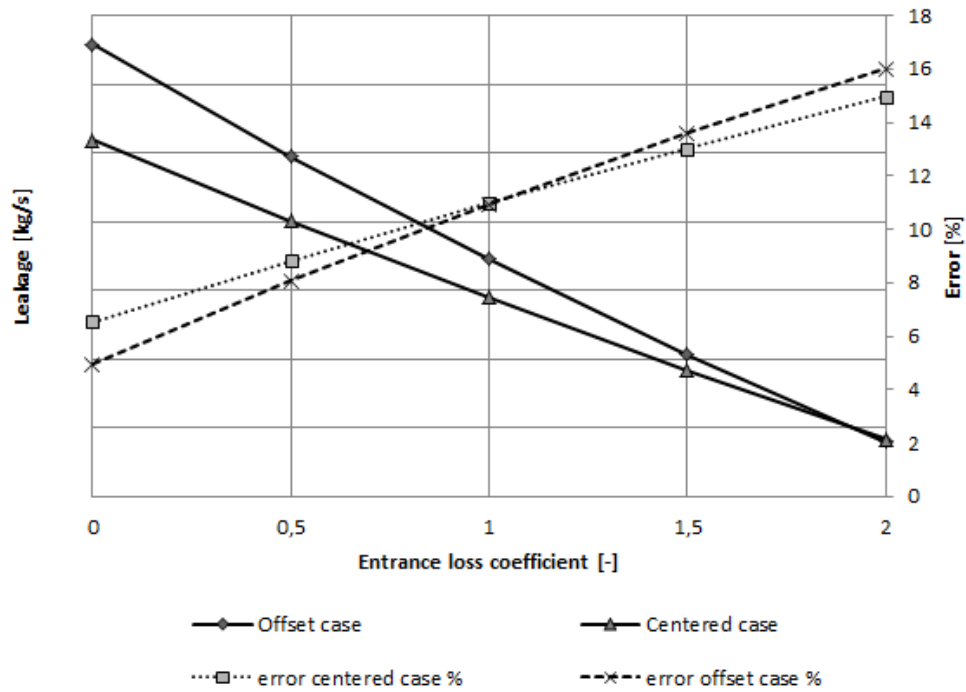


Figure 7.09. The leakage variation with entrance loss coefficient for case A for centered and offset position.

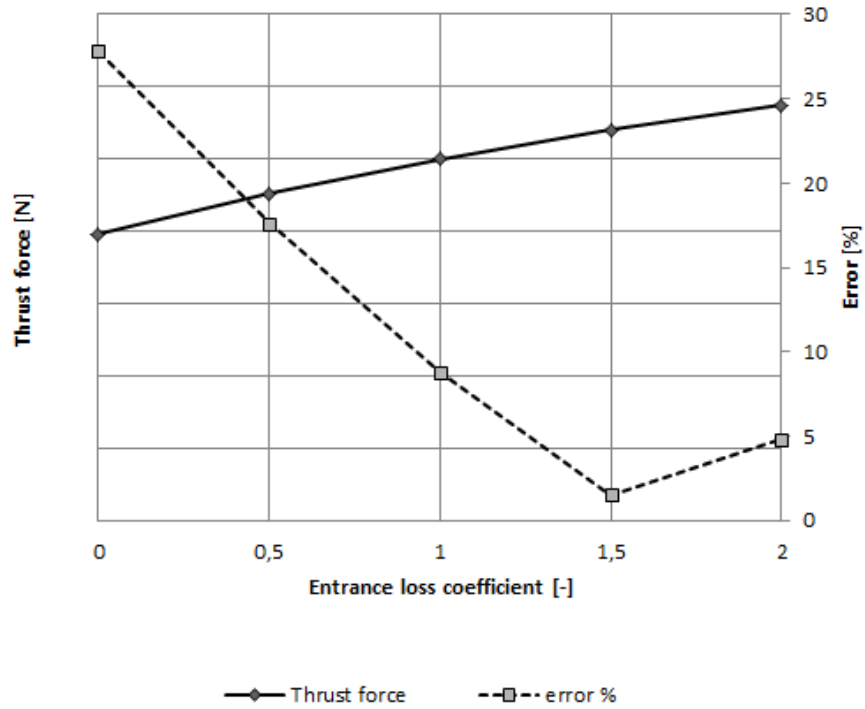


Figure 7.10. The thrust force variation with entrance loss coefficient for case A at offset position.

Figures 7.11 and 7.12, show the variation of the leakage and thrust force with variation  $ns$ . Decreasing  $ns$  from the coefficient used in ISOTSEAL increases the error for leakage but decreases the error for thrust force.

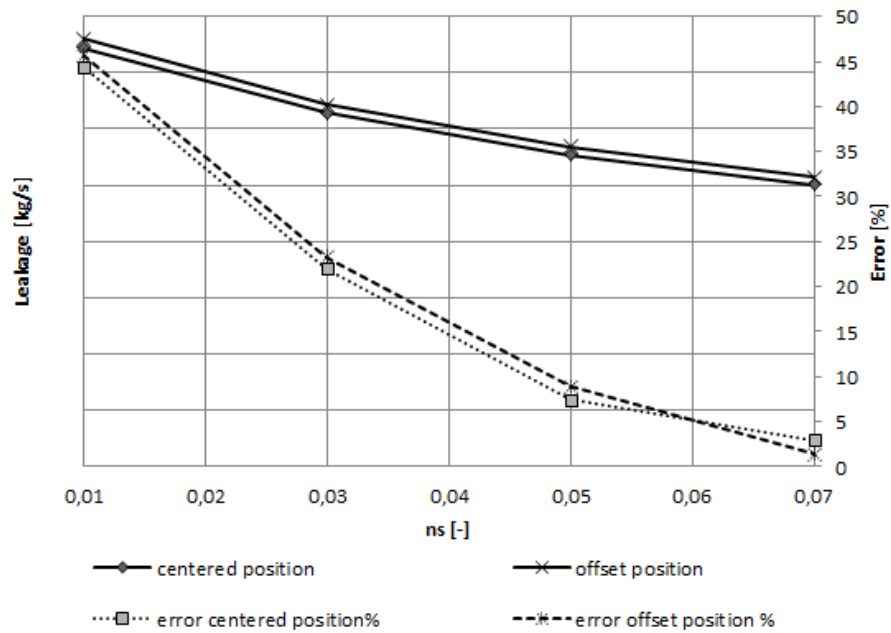


Figure 7.11. The leakage variation with  $ns$  for case A at centered and offset position.



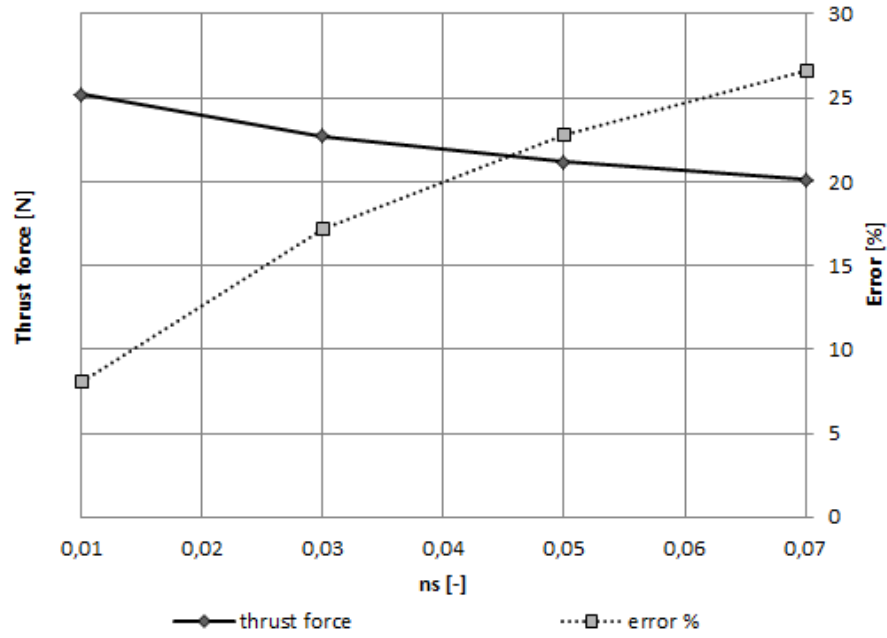


Figure 7.12. The thrust force variation with ns for case A at offset position.

Figures 7.13 and 7.14 show the variation for case A in leakage and thrust force with nr. Decreasing nr seems to be beneficial for the errors for both cases, especially for leakage.

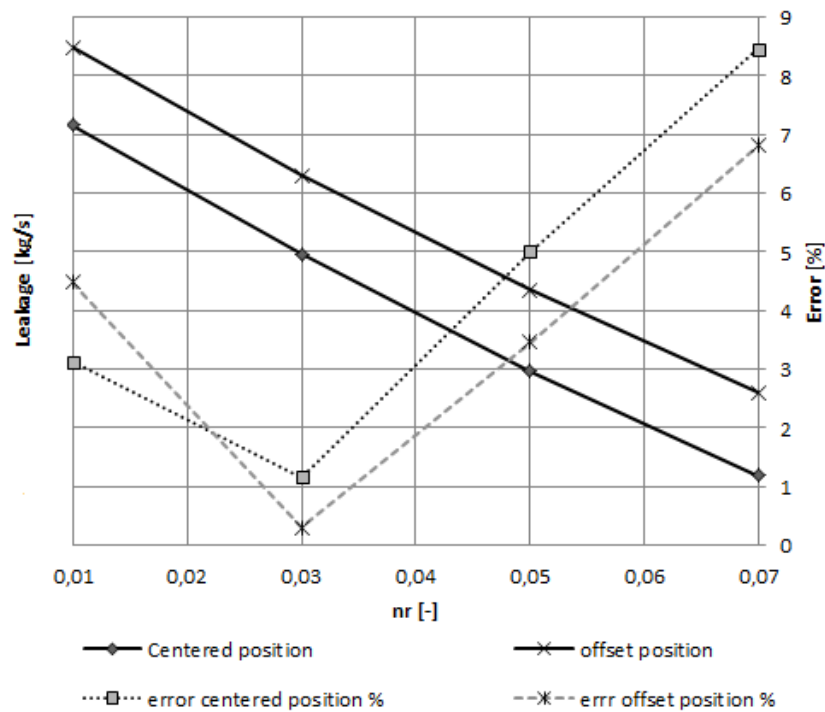


Figure 7.13. The leakage variation with nr for case A at centered and offset position.

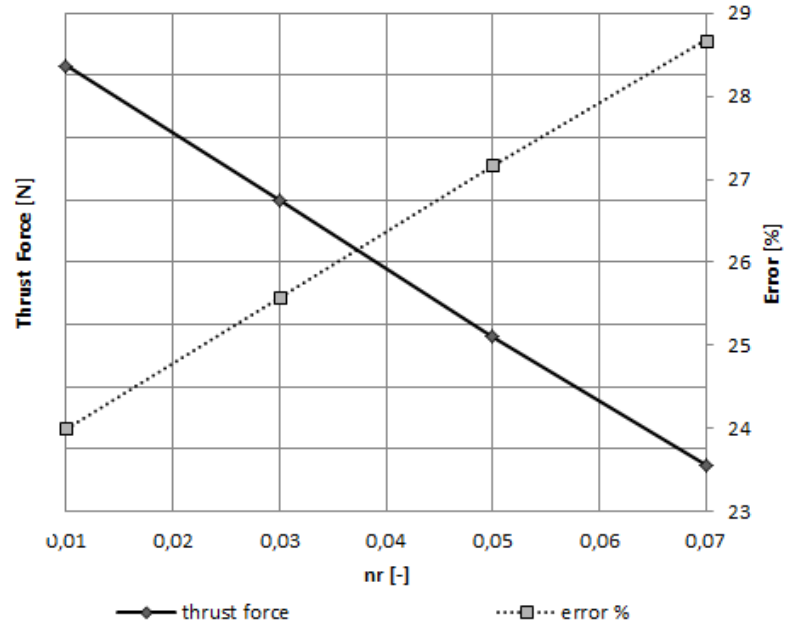


Figure 7.14. The thrust force variation with nr for case A at offset position.

### 7.3.2 Case B

Figures 7.15 and 7.16 shows the effect of varying the entrance loss coefficient on leakage and thrust force. Error for leakage decreases as this coefficient increases but it is the opposite for the thrust force.

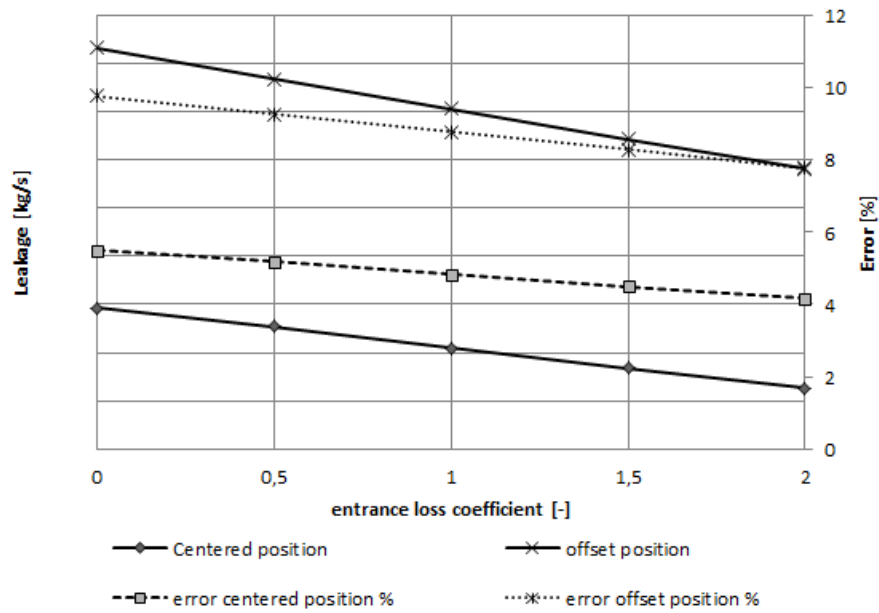


Figure 7.15. The leakage variation with entrance loss coefficient for case B at centered and offset position.

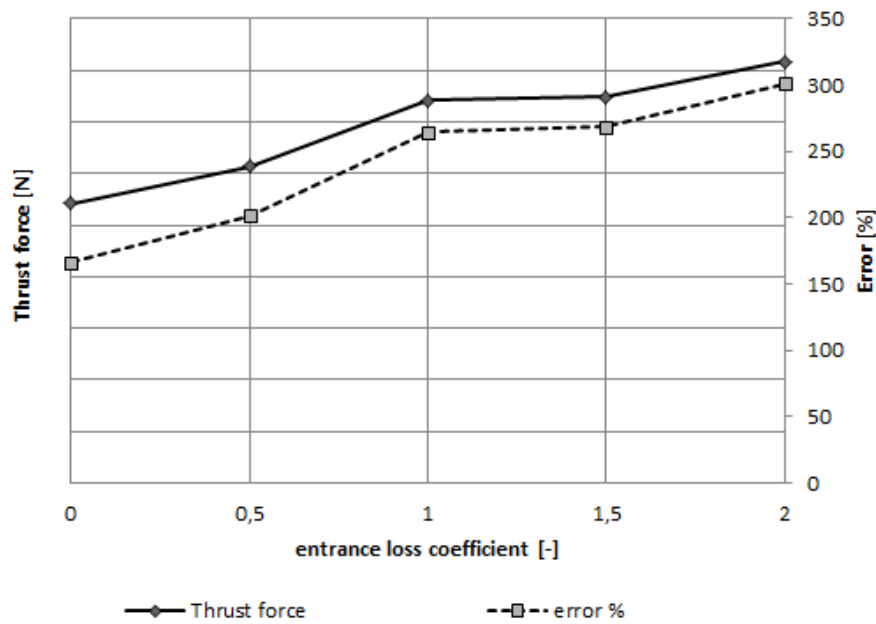


Figure 7.16. The thrust force variation with entrance loss coefficient for case B at offset position.

The effect of varying  $n_s$  and  $n_r$  on the leakage and thrust force for case B can be seen in figure 7.17 through figure 7.20.

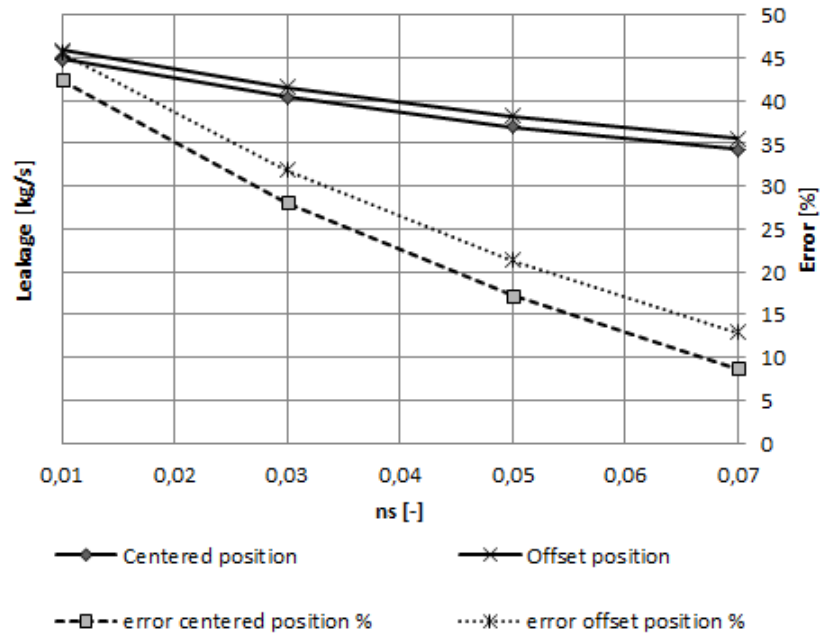


Figure 7.17. The leakage variation with ns for case B at centered and offset position.

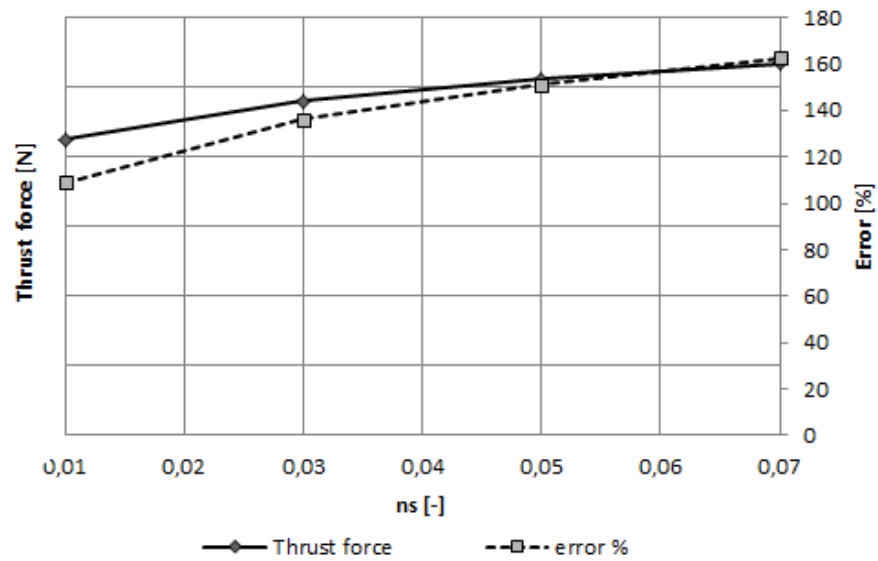


Figure 7.18. The thrust force variation with ns for case B at offset position.

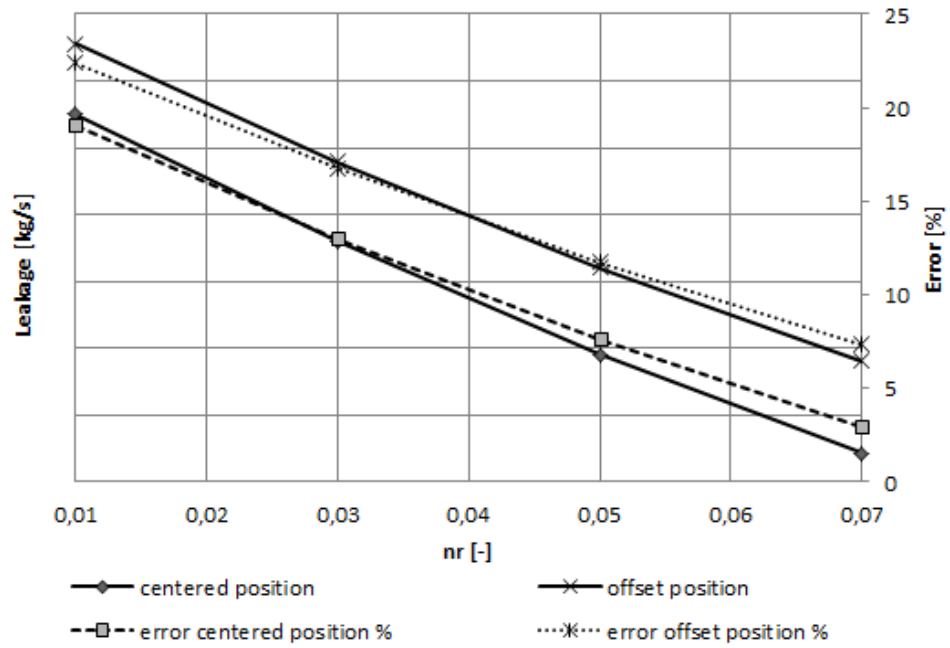


Figure 7.19. The leakage variation with nr for case B at centered and offset position.

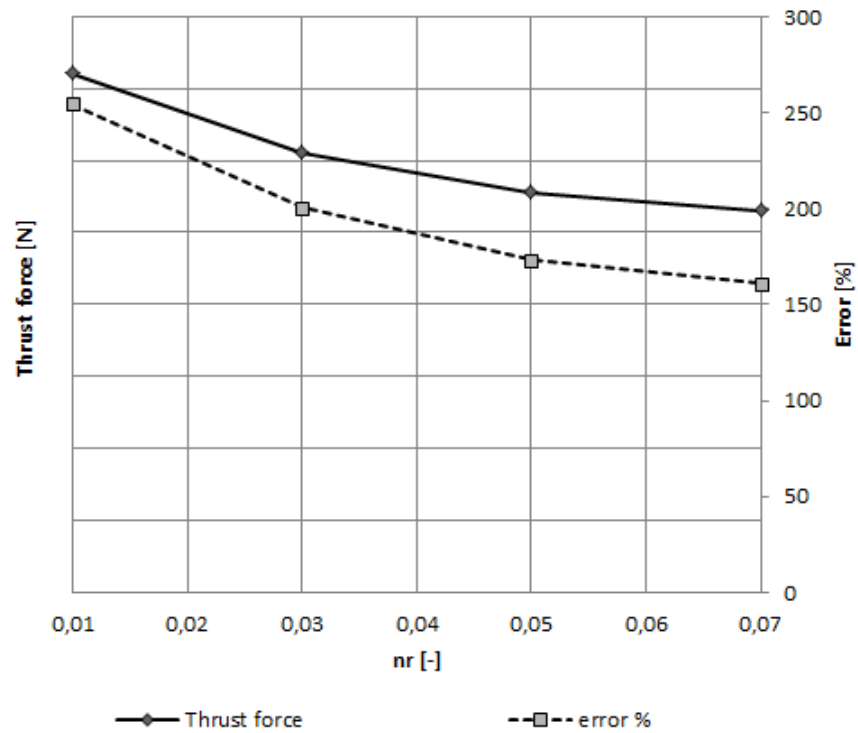


Figure 7.20. The thrust force variation with nr for case B at offset position.

## 7.4. Sensitivity test using different friction-factor models

As seen in section 7.3, the change in friction at the stator shows critical variations for the thrust force and the leakage. Unfortunately the data for different friction factors for the stator are limited, for that reason there was needed a sensitivity test using different models for the friction factor. Observing figure 7.21, the friction factor for most of the models seemed to be functions of the Reynolds number. There are other models like Ha & Childs (1994) that do not depend on that parameter and the model from D'Souza & Childs (2002) is a function of the clearance.

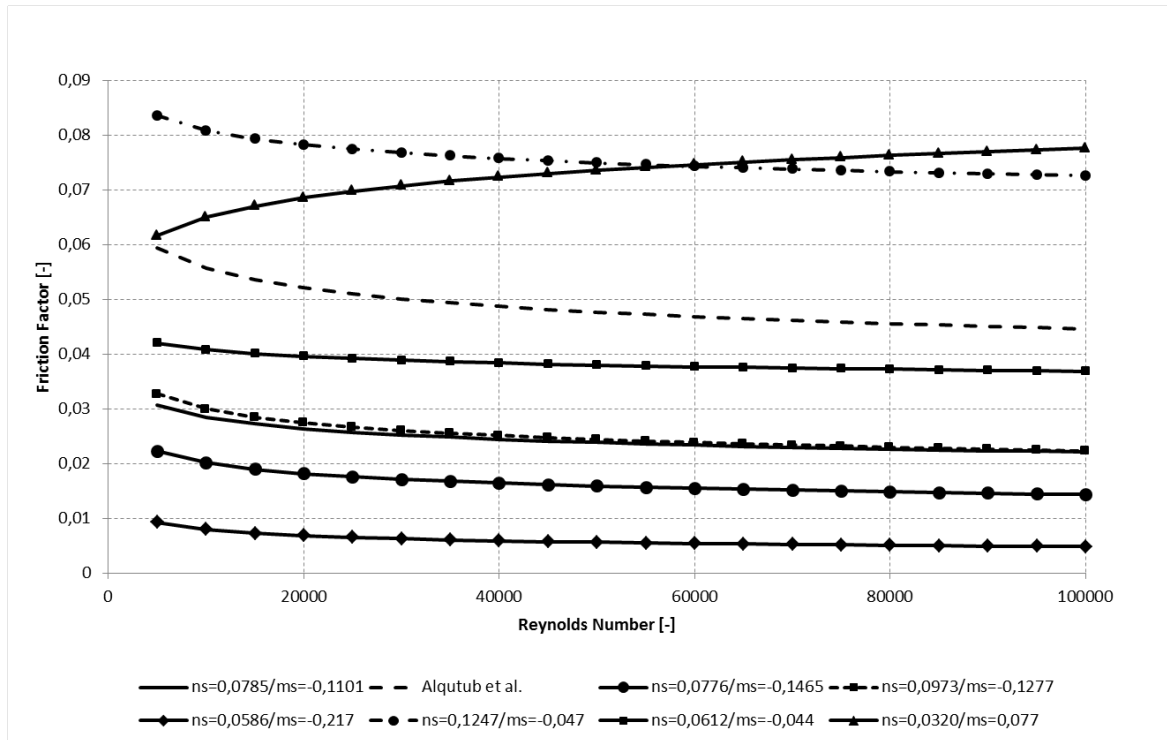


Figure 7.21. Friction factor for the different models that depend on the Reynolds number.

### 7.4.1 Case A

For case A figures 7.22 and 7.23 show that for  $ns=0,0973/ms=-0,1277$  the error of the leakage is the lowest. The first three models show higher levels of accuracy, corresponding to three of the lowest friction factors according to figure 7.21. But the model with the lowest friction-factor is at  $ns=0,0586/ms=-0,217$  shows the highest value for leakage, and this model is used for smooth surfaces.

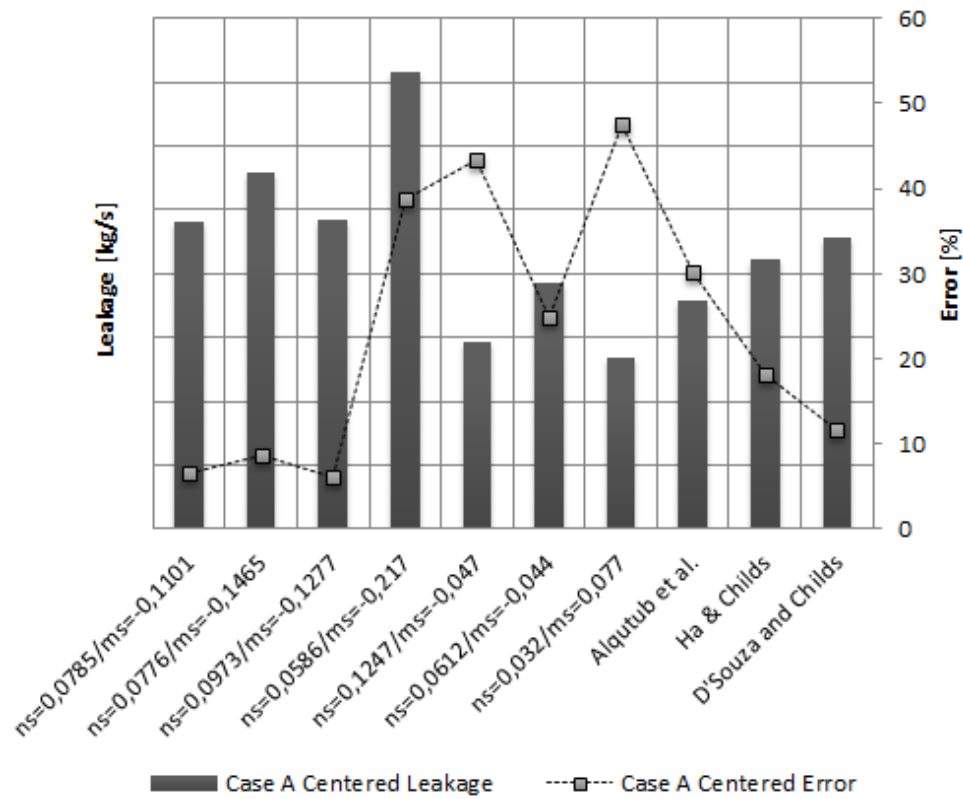


Figure 7.22. Leakage and the errors for case A at centered position.

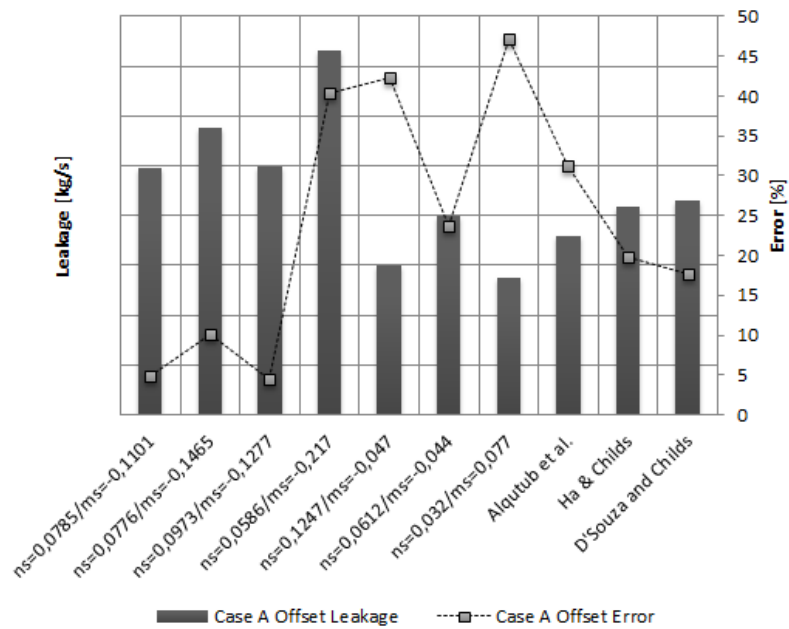


Figure 7.23. Leakage and the errors for case A at offset position.

On the other hand, lower friction assures high thrust force and for that reason low errors. These values correspond to the model for smooth surfaces.

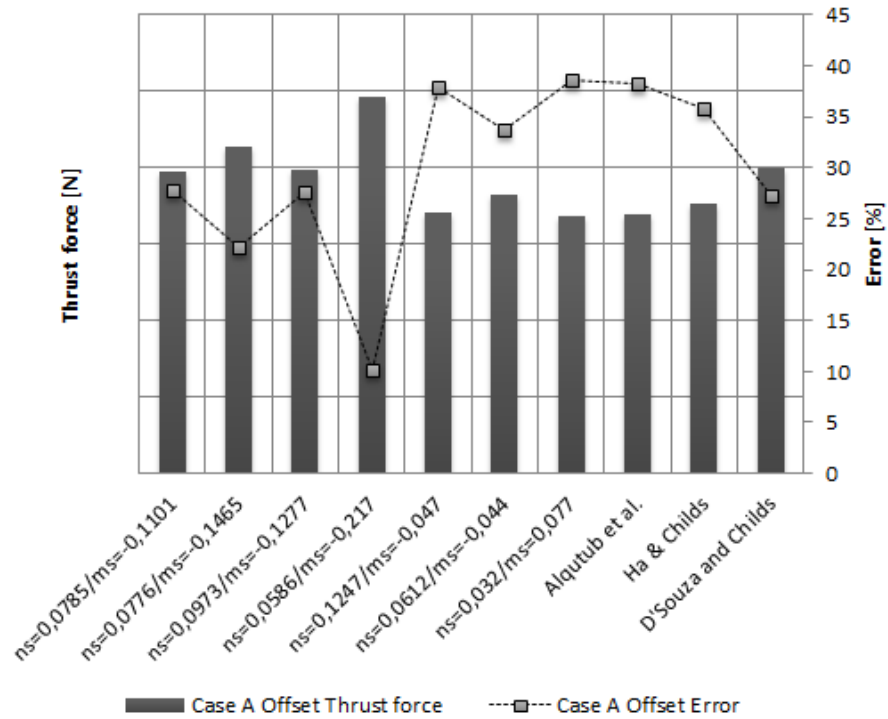


Figure 7.24. Thrust force and the errors for case A at offset position.

#### 7.4.2 Case B

For case B, it seems that the models for Ha & Childs (2000) and D'Souza & Childs (2002) give better approximations for the leakage than most of the other cases, consistently giving errors lower than 10% for centered and offset configurations. In figure 7.27 the errors are above 100%, especially D'Souza & Childs (2002) which gives the less accurate results for thrust force.



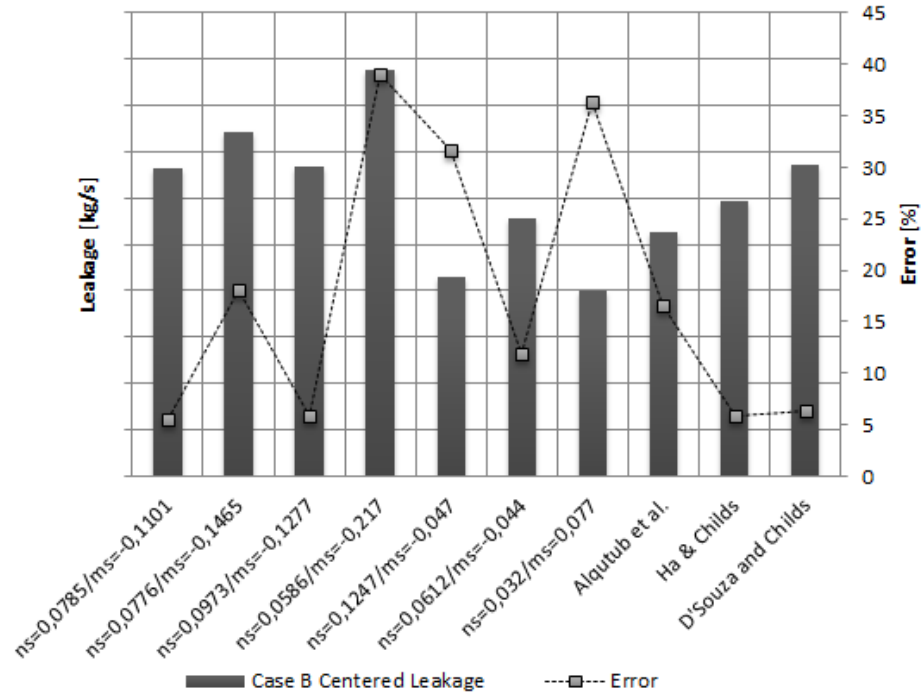


Figure 7.25. Leakage and the errors for case B at centered position.

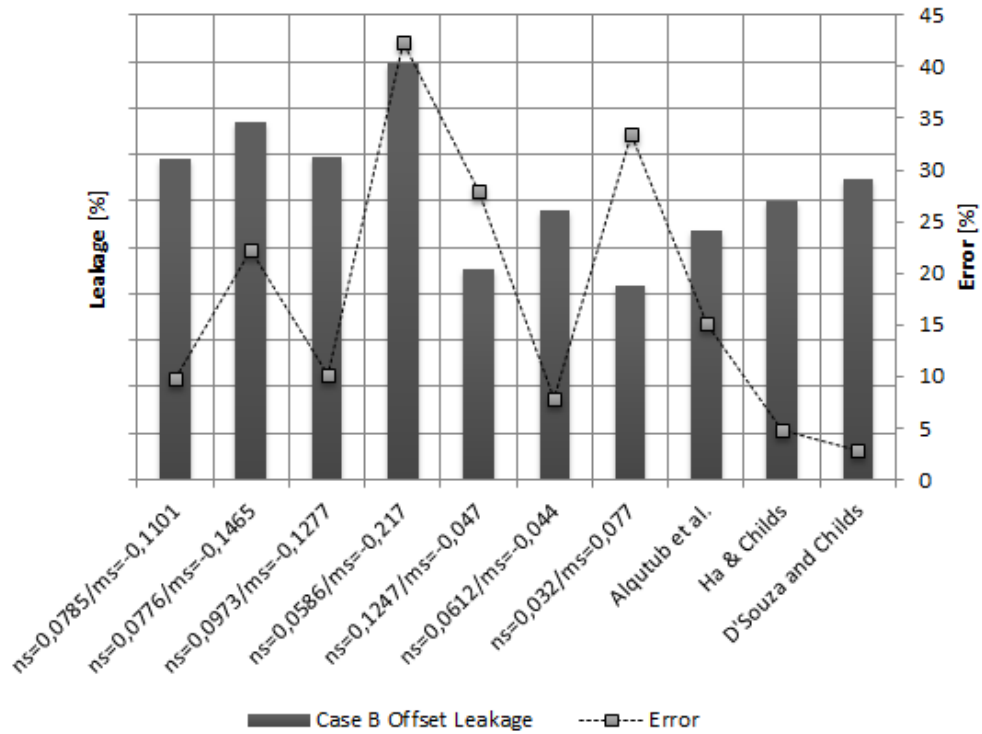


Figure 7.26. Leakage and the errors for case B at offset position.

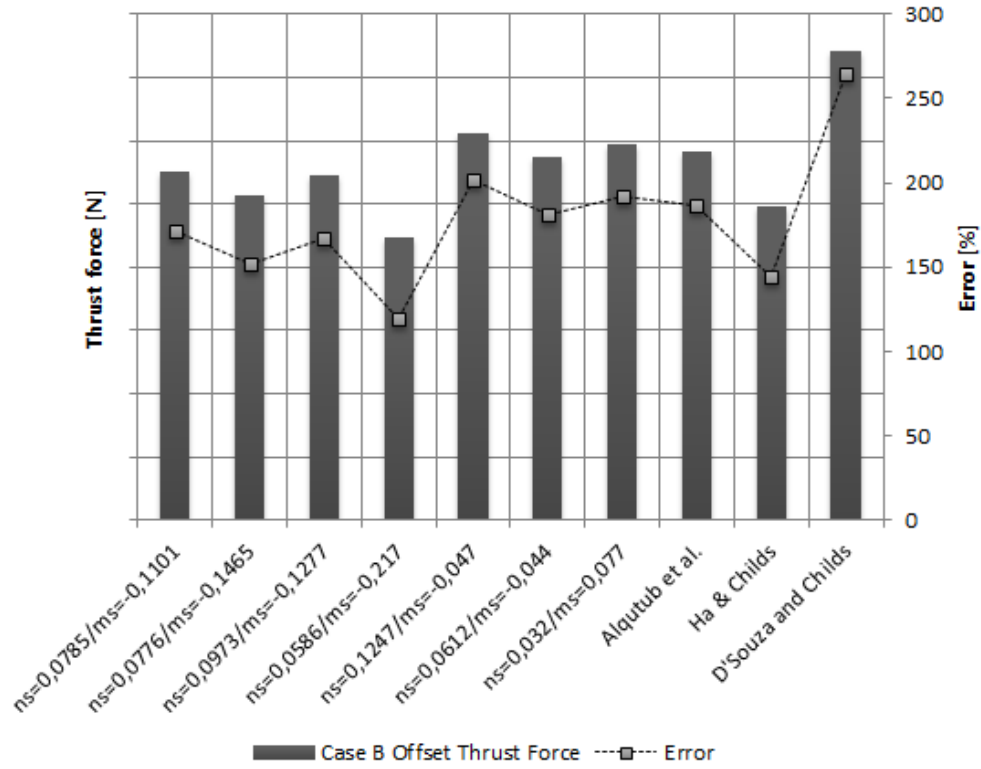


Figure 7.27. Thrust force and the errors for case B at offset position.

## 7.5 Simulations for diverse cases

Using different cases from Appendix D, the error in leakage and thrust force are shown in figure 7.28 and 7.29. For case 8, leakage and thrust force shown to get values higher than the average.

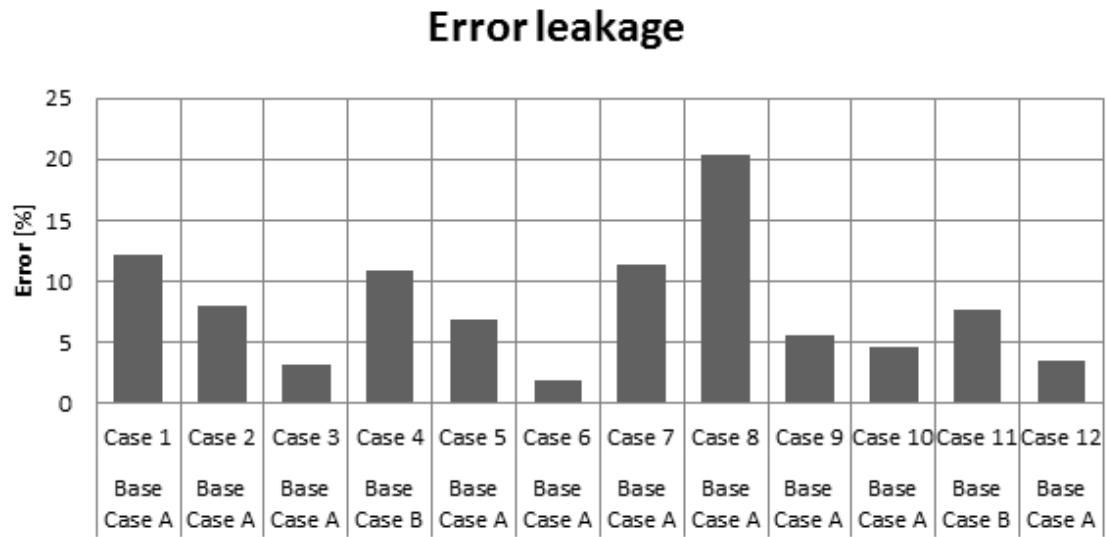


Figure 7.28. Error for leakage at different cases.

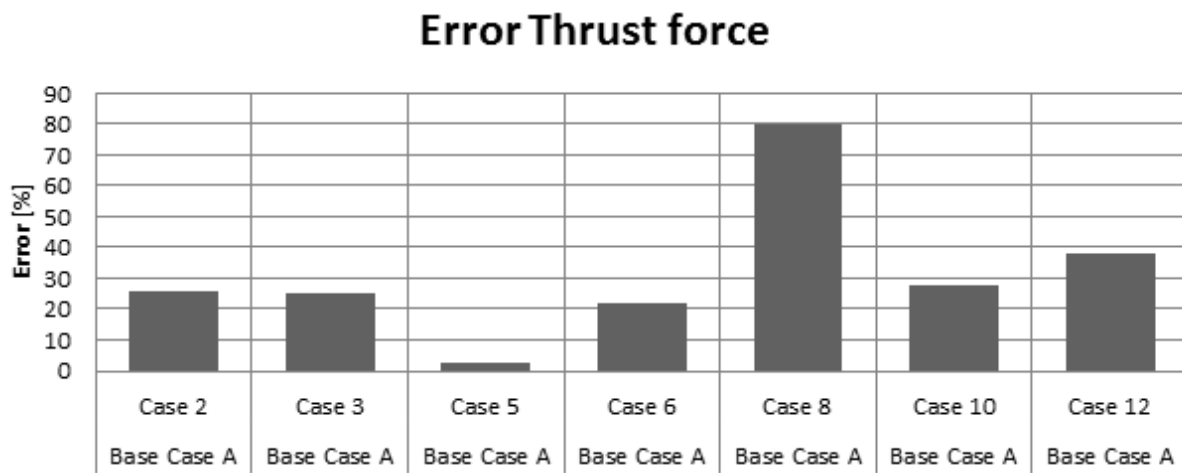


Figure 7.29. Errors for thrust force at different configurations.



## Chapter 8

### Results using First-Order equations

In order to compare the results for stiffness and damping from the analytical tool to the results from the CFD simulations, it is necessary to use the same axial frequency values: 10 Hz, 41,7 Hz, 83,3 Hz, 125 Hz and 166 Hz.

#### 8.1 Case A: Centered position

Figures 8.01 and 8.02 show the values for stiffness at the centered position for case A at different area ratios. It seems that decreasing the area ratio improves the result for models with higher friction factors. This trend is shown in appendix E.

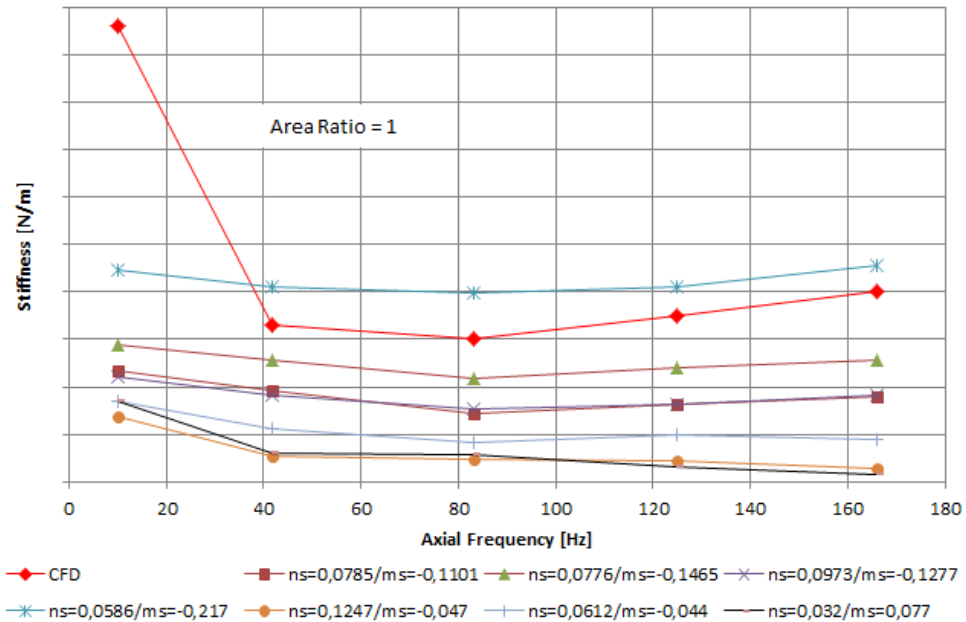


Figure 8.01. Stiffness of the bearing when the area ratio 1 for case A at centered position.

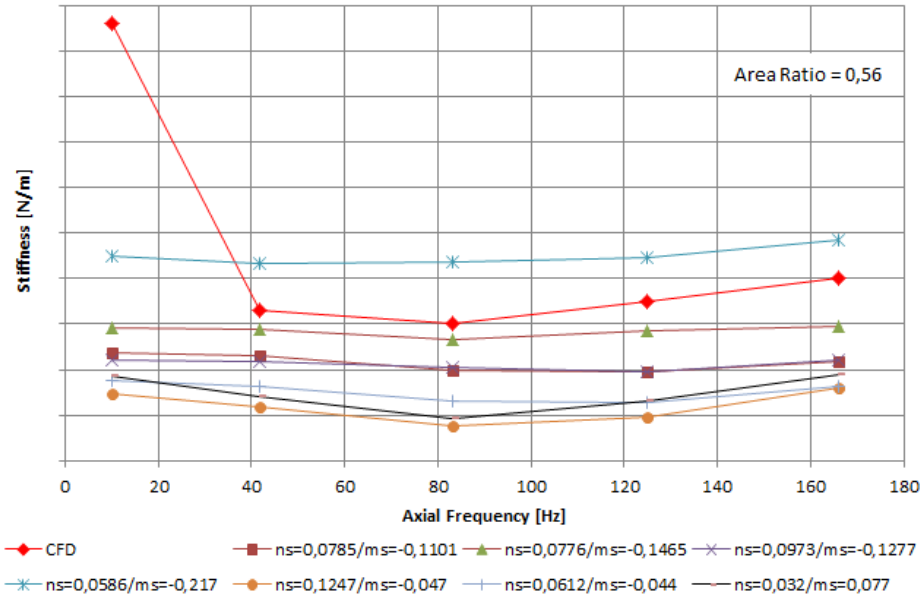


Figure 8.02 Stiffness of the bearing when the area ratio 0,56 for case A at centered position.

Figures 8.03 and 8.04 show the effect of the area ratio on the damping. They cannot be compared to the results from the CFD simulations because these values are not available. However, it has been noted that for the CFD results there should be a crossover in the damping between 125 hz and 166 hz. Both graphs show that unlike the performance for the stiffness, the results for damping for the different frequencies are similar but they differ greatly as the axial frequency lowers.

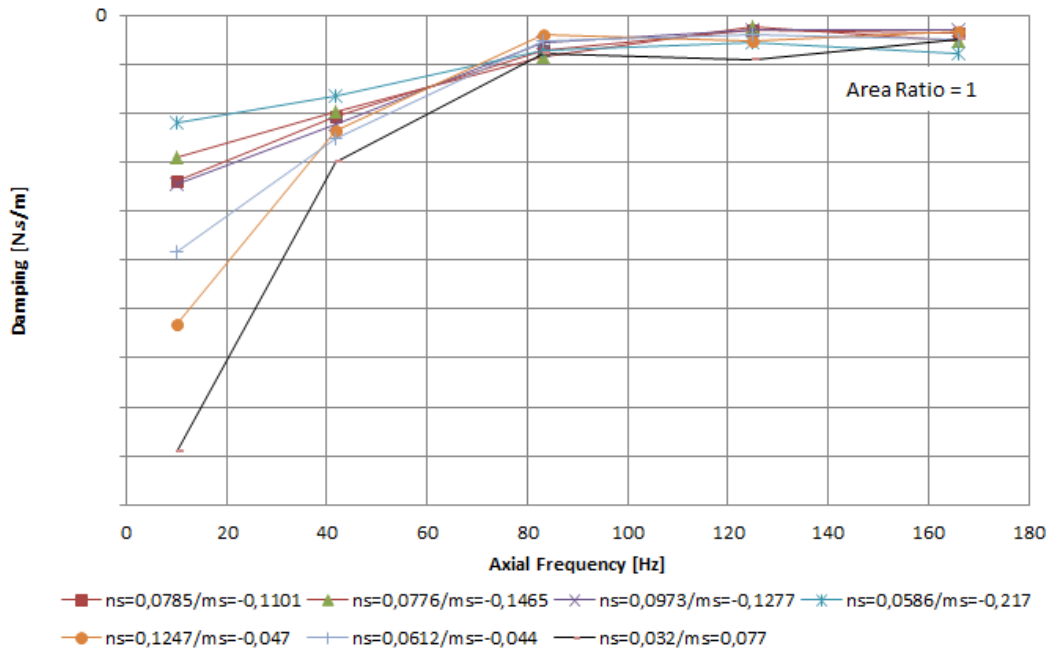


Figure 8.03. Damping of the bearing when the area ratio 1 for case A at centered position.

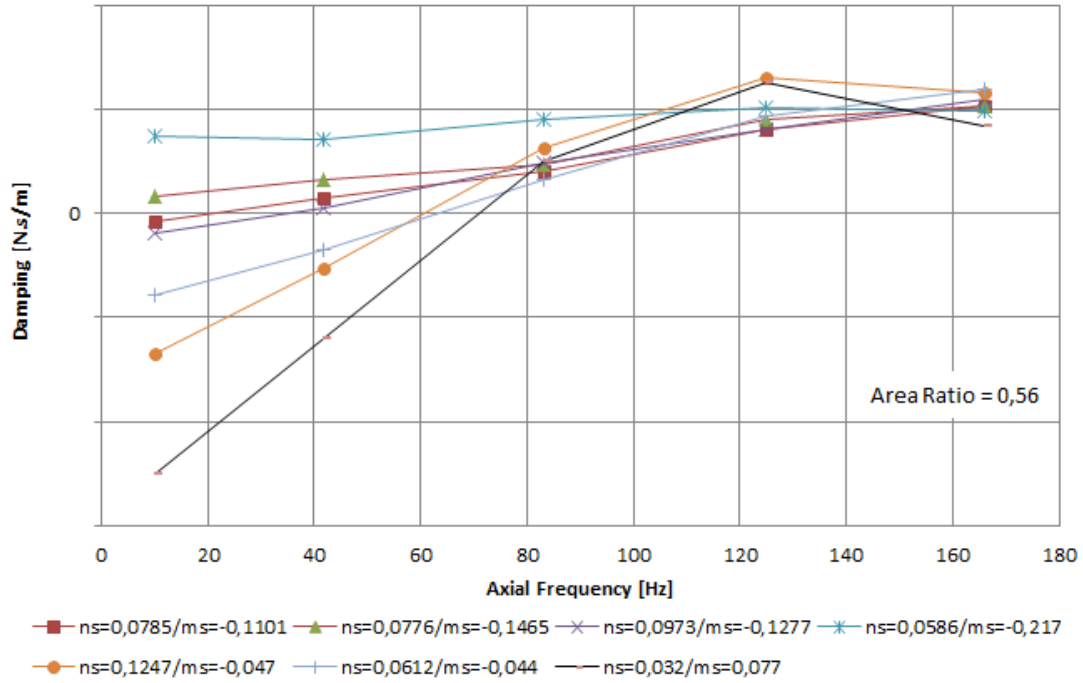


Figure 8.04. Damping of the bearing when the area ratio 0,56 for case A at centered position.

## 8.2 Case A: Offset position

Figures 8.05 and 8.06 show the effect of the area ratio on the stiffness for the offset case. Results show that reducing the area ratio makes the stiffness for models with higher friction factor than the smooth case get closer to the CFD results.

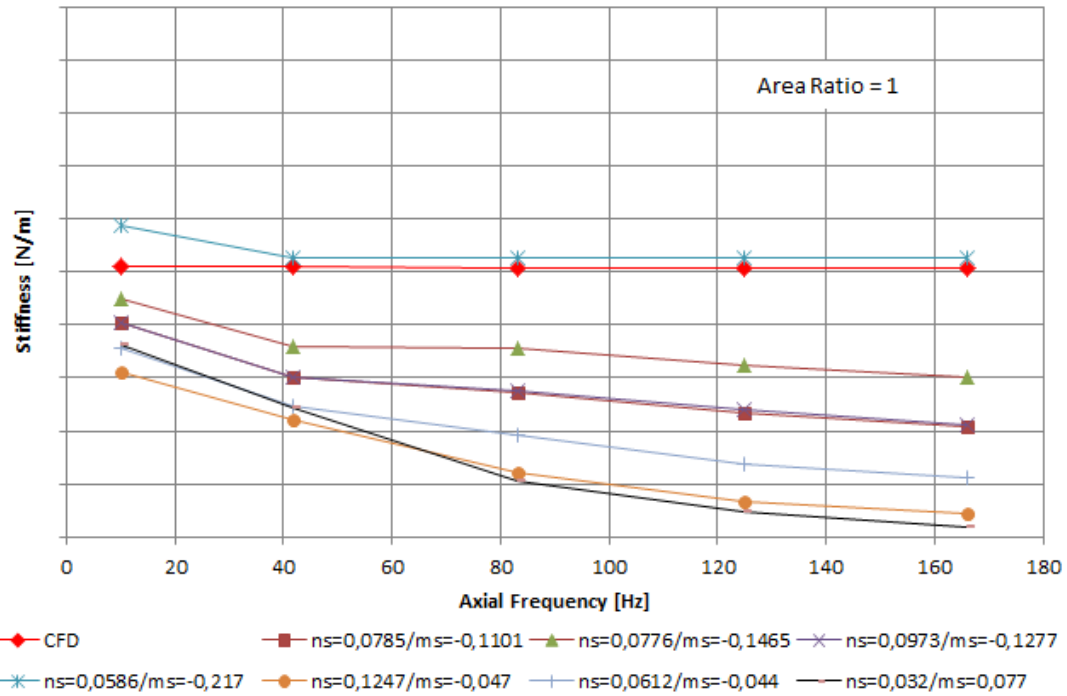


Figure 8.05. Stiffness of the bearing when the area ratio 1 for case A at offset position.

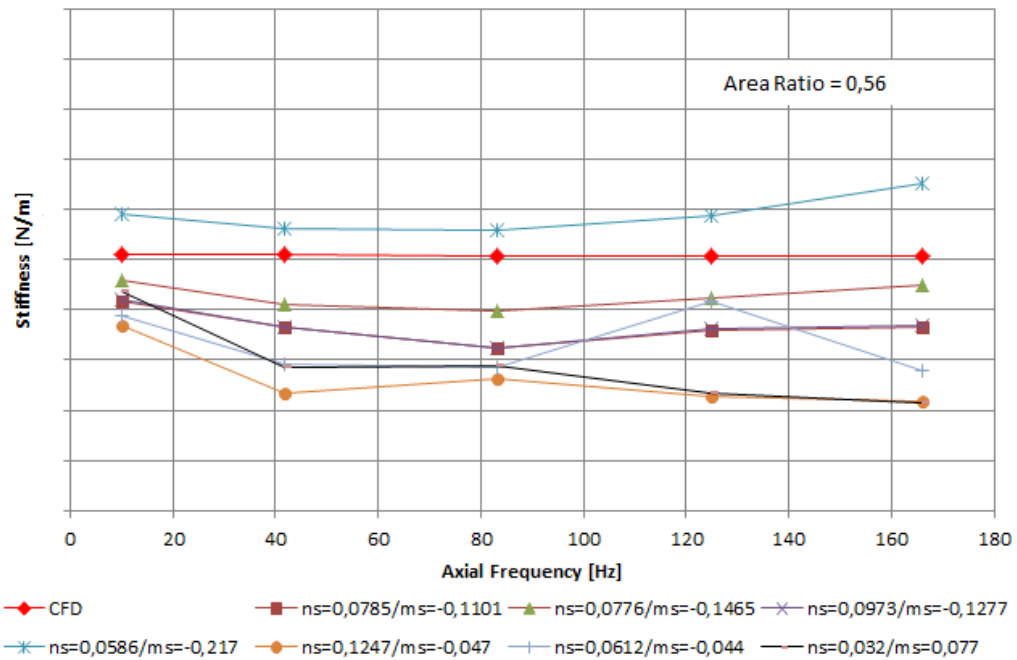


Figure 8.06. Stiffness of the bearing when the area ratio 0,56 for case A at offset position.

The results for damping for the case A at offset position figures 8.07 and 8.08. For an area ratio of 1, some of the results show a crossover between 10 hz and 41.7 hz while for an area ratio of 0,56



another behavior happens. For higher frequencies for both cases the results seem to be closer to the CFD results.

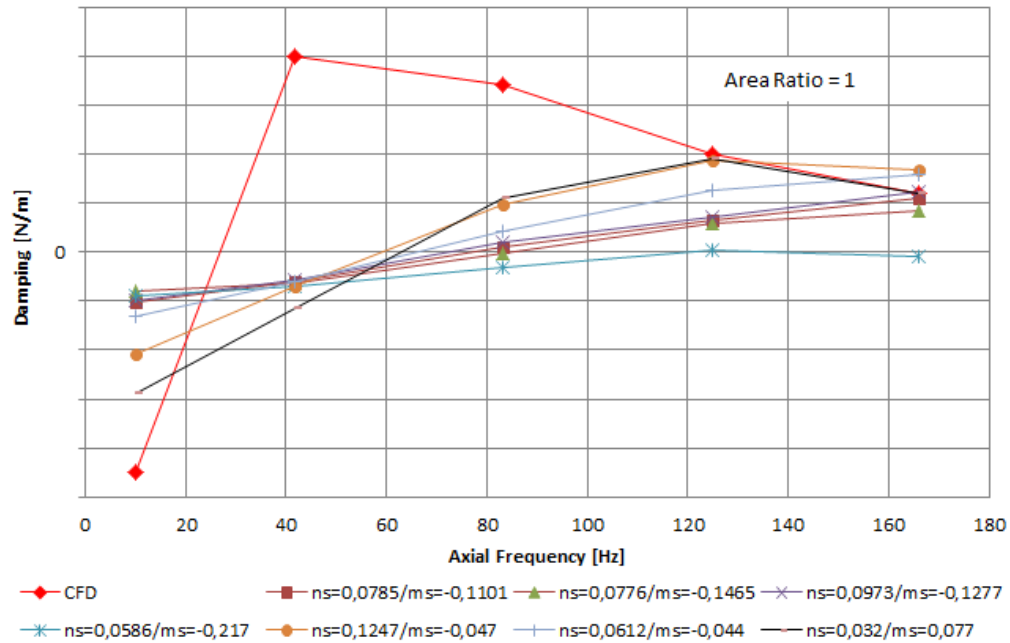


Figure 8.07. Damping of the bearing when the area ratio 1 for case A at offset position.

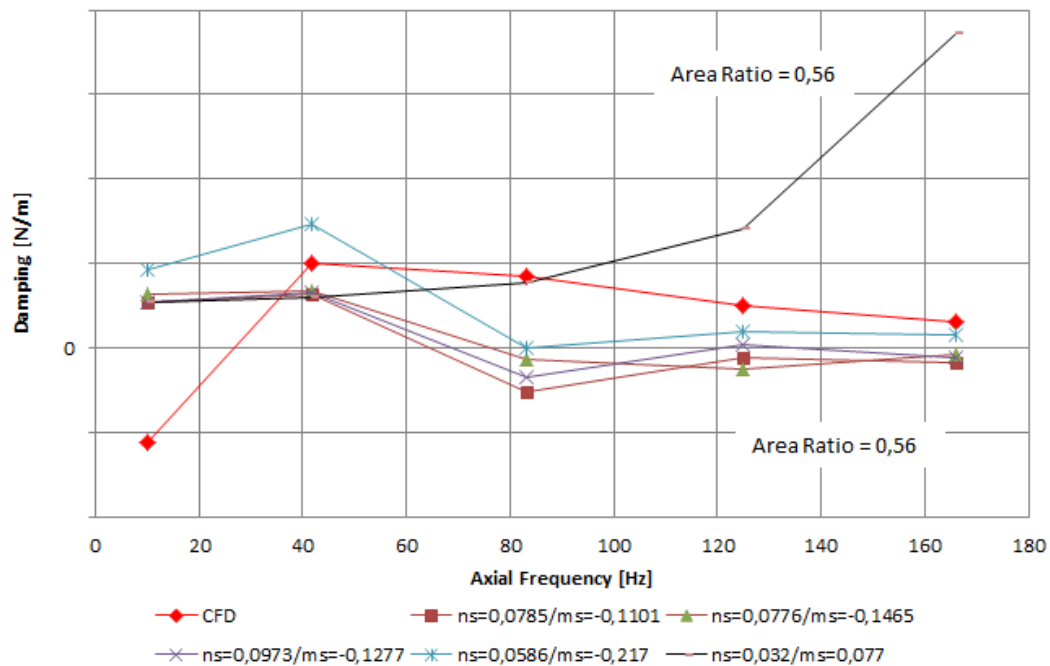


Figure 8.08. Damping of the bearing when the area ratio 0,56 for case A at offset position.

### 8.3 Case B: Centered position

For case B at centered position figures 8.09 and 8.10 show the results for stiffness at different area ratios while figures 8.11 and 8.12 show the results for damping. In general it seems that the stiffness is overestimated while damping is underestimated for different friction models.

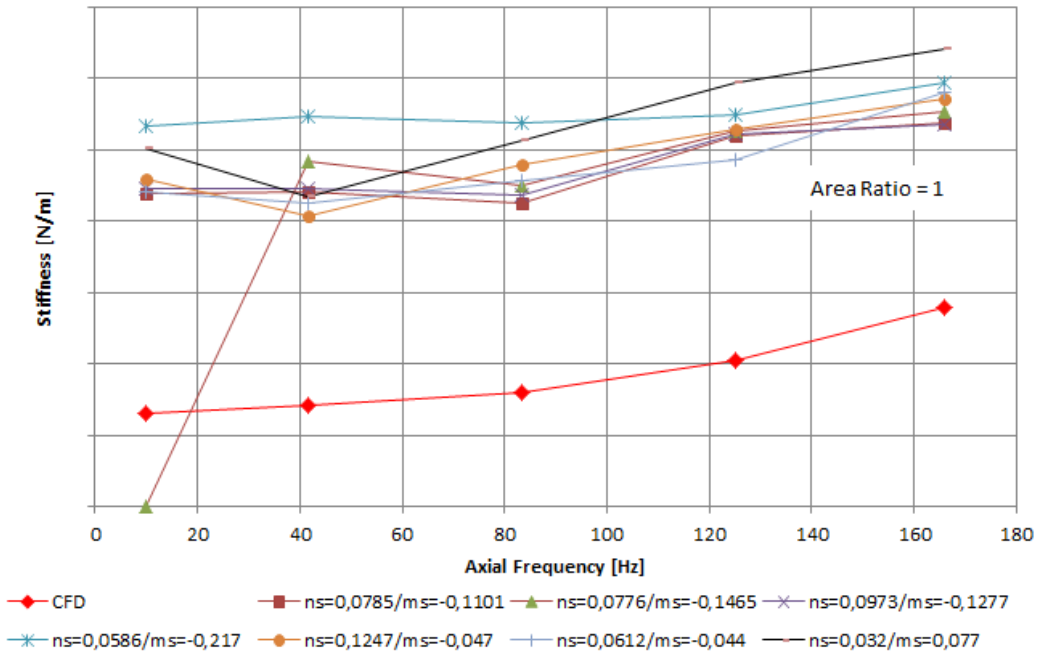


Figure 8.09. Stiffness of the bearing when the area ratio 1 for case B at centered position.

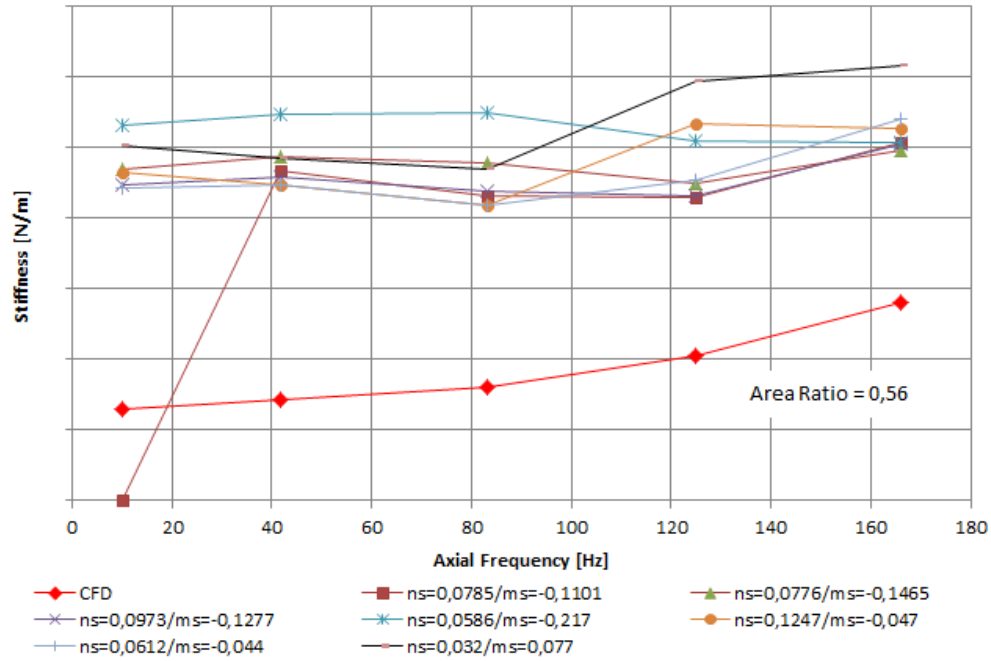


Figure 8.10. Stiffness of the bearing when the area ratio 0,56 for case B at centered position.

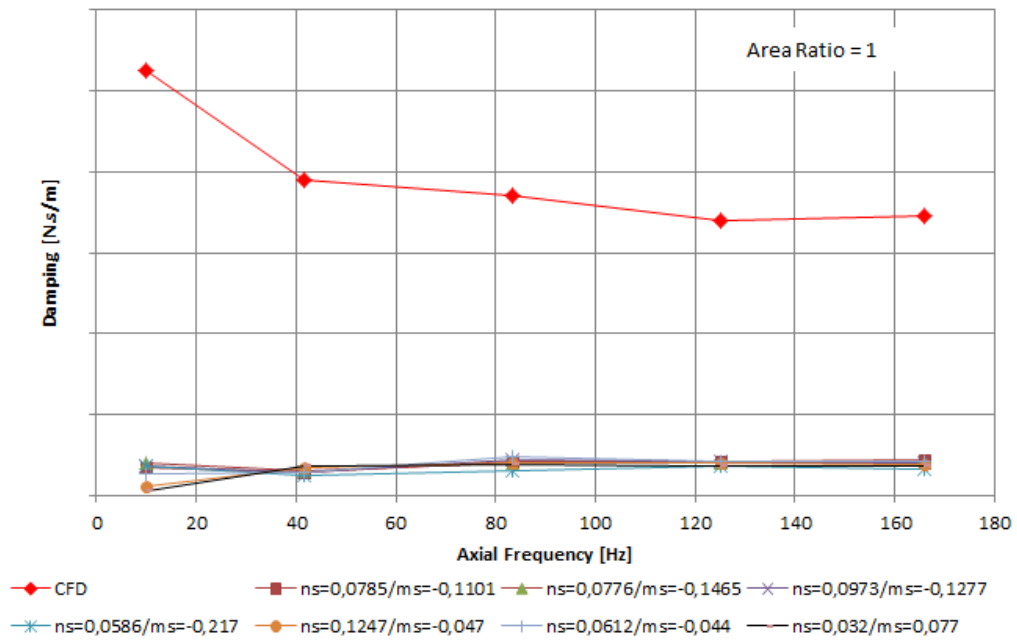


Figure 8.11. Damping of the bearing when the area ratio 1 for case B at centered position.

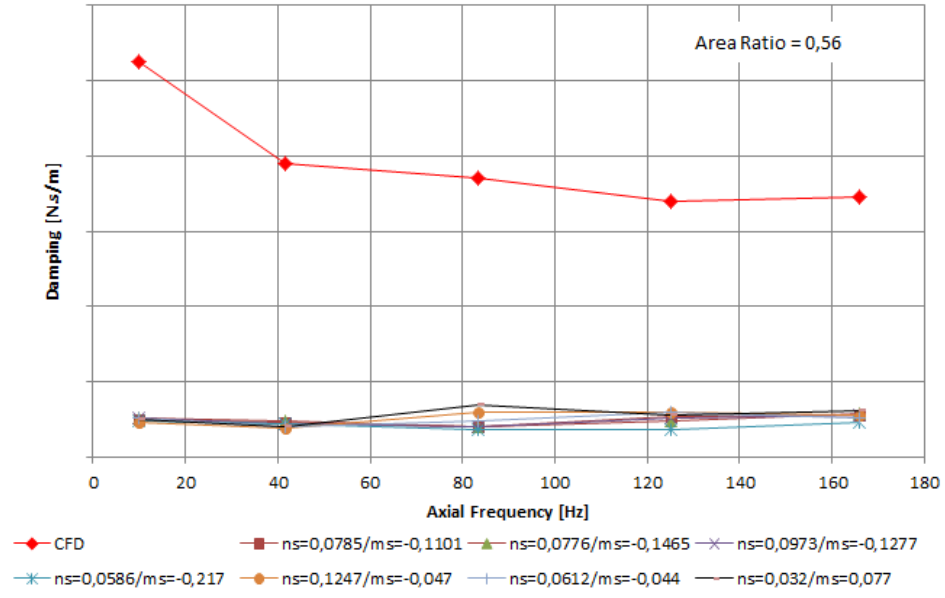


Figure 8.12. Damping of the bearing when the area ratio 0,56 for case B at centered position.

#### 8.4. Case B: Offset position

For case B at offset position, figures 8.13 and 8.14 reflect the overestimation of the stiffness and figures 8.15 and 8.16 reflect the underestimation of the damping, following the trend for the centered position.

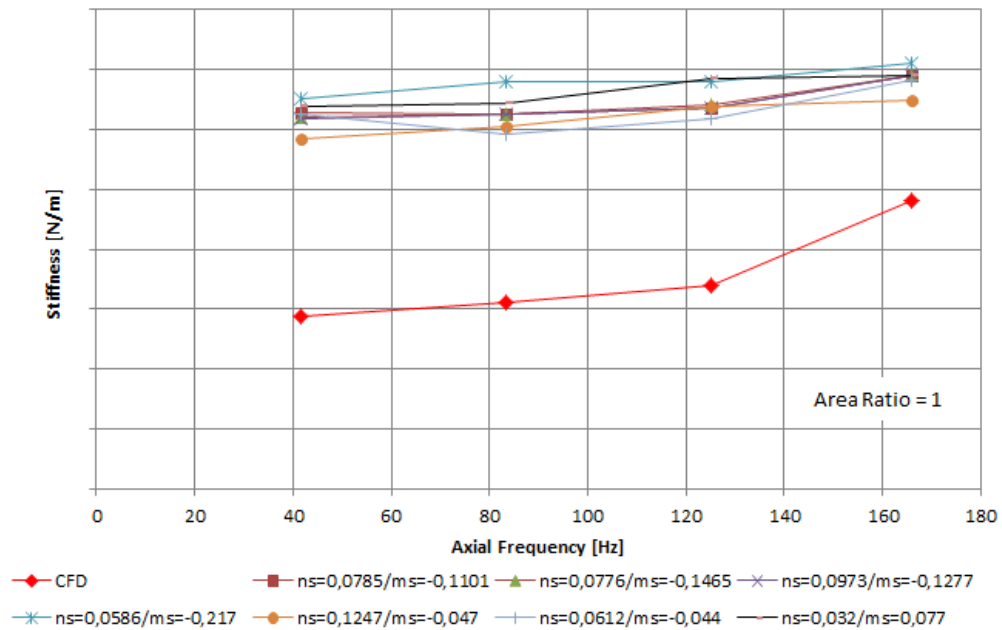


Figure 8.13. Stiffness of the bearing when the area ratio 1 for case B at offset position.

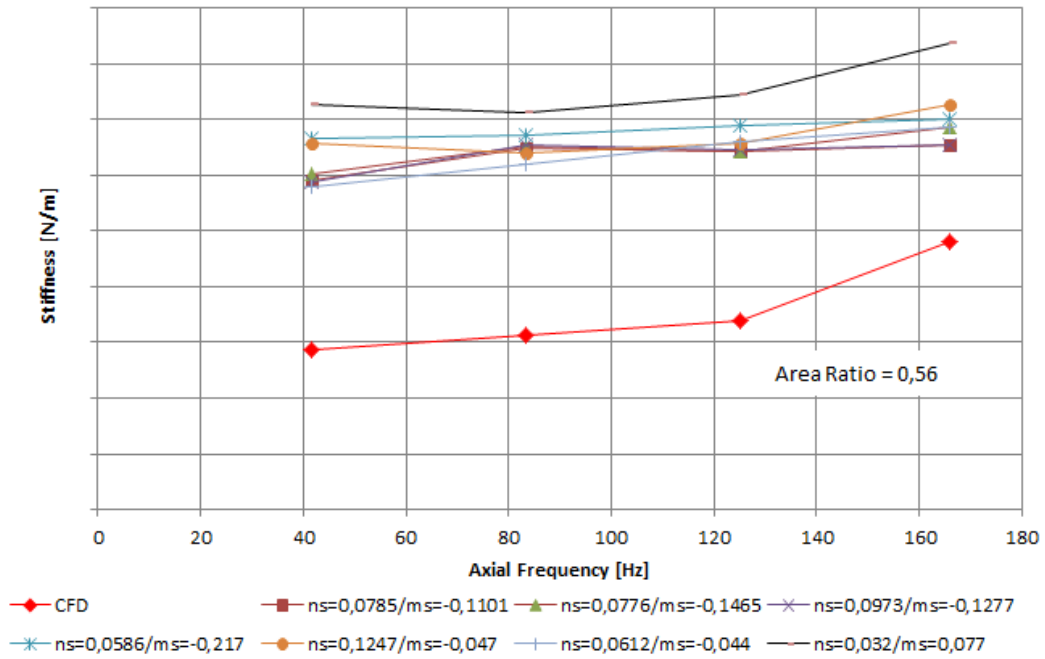


Figure 8.14. Stiffness of the bearing when the area ratio 0,56 for case B at offset position.

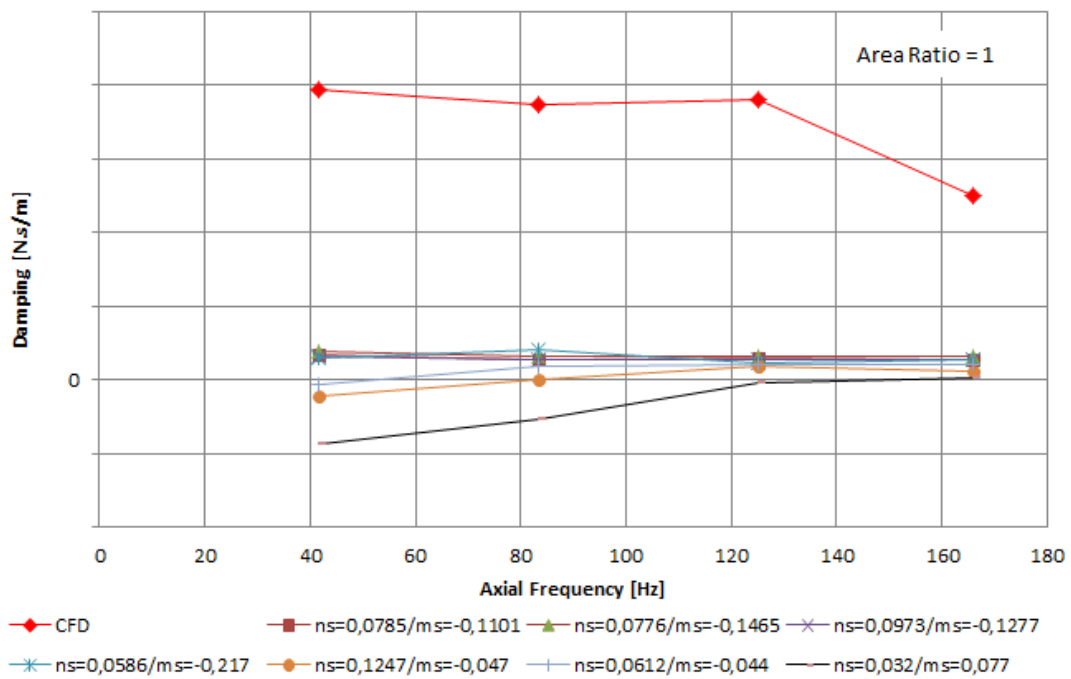


Figure 8.15. Damping of the bearing when the area ratio 1 for case B at offset position.

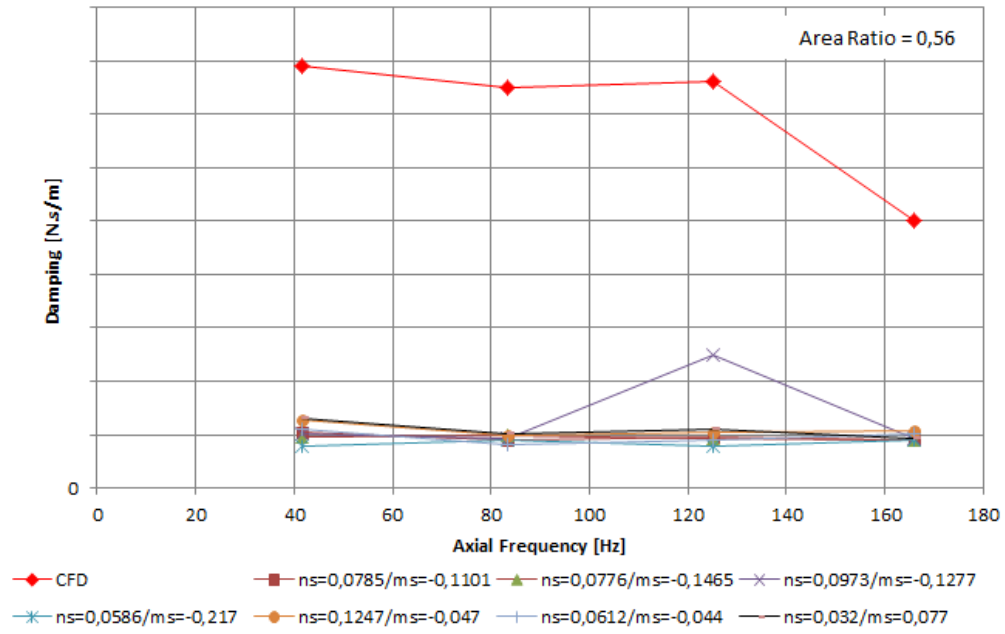


Figure 8.16. Damping of the bearing when the area ratio 0,56 for case B at offset position.

## Chapter 9

### Discussions

#### 9.1 Static Solutions

To calculate the approximate amount of leakage using the bulk-flow theory it was necessary to obtain the radial velocity and density of the fluid at the outlet of the bearing. From results in section 7.2, the leakage has been estimated within 10% of error.

The errors are not acceptable for the thrust force; the deviation seems to represent more than a quarter of the value for case A while Case B displays a deviation of more than twice the value. The thrust force is directly linked to the pressure distribution along the seal and for that reason it is required to analyze the pressure distribution for offset cases in appendix E and, figures 7.01 and 7.05.

For case A at the higher clearance side figure E.01 shows the pressure distribution in the bearing and it shows a large gap between the inlet pressure from the bulk-flow model and the same pressure from the CFD simulations. From the CFD simulation there is an apparent recovery of pressure due to the recirculation at the inlet, and since the bulk flow theory only takes into consideration the average values for the different variables it is not expected to reproduce this recirculation. However, the gap between the two curves is high and that affects the calculation of the thrust force as the mean percent error is about 11%, the same happens with figure E.05, though the mean percent error is less than half of the previous case. And these differences affect the calculation of the thrust force for the offset position.

The effect of higher pressure values for each side is not as strong as the distribution along the radius, this phenomenon is especially appreciated in case B. The mean percent errors for higher and lower clearance cases are lower than for case A, with less than 2,5% but places with high percent error are located at the inlet of the bearing where the inlet diameter is high. Other places with high percent errors are located before the outlet of the bearing like it can be seen in figure E.09. Those factors are responsible for the 171% error in the calculations of the thrust force.

There are different parameters that affect the pressure profile in the algorithm. Figures 7.01, 7.05 and the rest of the figures in Appendix E demonstrate that the pressure at the inlet is higher than the

pressure in the CFD model, thus the boundary conditions must be modified. The entrance loss coefficient which accounts all the losses at the inlet directly affects the pressure and the inlet velocity according to equation 4.18. Furthermore, the friction coefficients also affect the magnitude of the inlet conditions, but in a different way; it affects the development of the variables along the bearing until numerical integration reach, and in chapter 6 it has been discussed that the system of equations is a boundary value problem, meaning the boundary conditions at the outlet will be compared to the results of solving the equations and affecting simultaneously the initial guess values until all the conditions are satisfied.

The pressure at the outlet is also affected by the temperature. Figures 7.02 and 7.06 compared the temperature of the flow along the bearing to the results from the CFD simulations. The inlet temperature is indirectly affected by the entrance loss coefficient and the velocity. Yet along the bearing, the temperature seems to be under 2 different phenomena acting simultaneously, these are the JTE and the friction.

The JTE for gases means that a reduction in the pressure of the fluid carries out a reduction in the temperature whereas acceleration of the fluid increase the friction in the system and this friction increases the temperature. Figure 7.02 shows an increment in the temperature along the bearing for the CFD result and the same happens for the CFD results in figure 7.06, showing that the friction had a stronger effect on the temperature than the JTE. On the contrary, the results from the algorithm showed low increments in temperature at the radii closer to the inlet unlike at the outlet where there is decay in temperature, particularly for case B, indicating that the JTE had stronger influence in the results.

Having such discrepancies between temperature and pressure distributions along the bearing, a sensitivity test was necessary to determine which parameters could improve the calculations. In appendix E, the results for the sensitivity test in the thermodynamic parameters and the preswirl showed that they did not play a role in improving the calculations specifically with the thrust force. However the other variables in section 7.3 showed stronger influence in both the leakage and thrust force.

An increase in entrance loss coefficient means that losses at the entrance are taken into account. For case A the losses are the change in direction of the fluid from axial to radial and incrementing this coefficient in the calculations results in narrowing the gap between the pressure from the algorithm and the CFD and thus incrementing the thrust force, especially for the higher clearance part. For Case B this increments the value for thrust force and therefore increases the errors. For both cases the leakage decreases when incrementing the coefficient, but for case A this result in incrementing the error.

Changing the coefficients  $n_s$  and  $n_r$  to calculate the friction factor also showed relevance for improving the calculations. For case A in figures 7.11 and 7.12 decreasing the  $n_s$  from the value used in ISOTSEAL benefits the calculations for the thrust force that goes from above 25% error to less than 10% error, and simultaneously increasing the leakage. For case B the calculations for leakage



becomes unacceptable while the error for the thrust force decreases but continues to be unacceptable. Meanwhile, decreasing  $nr$  only from 0,0586 in ISOTSEAL decreases the errors for leakage and thrust force (not significantly) for case A and results into negative effects for case B.

As it can be seen in figures 7.22 and 7.23, the first four friction models show higher leakage than the rest and according to figure 7.21 they deliver the smallest friction factors. These results showed that, according to the theory, lower friction means higher leakage; but the model with lower friction factors increased the values for leakage in excess and raised the error. That friction model corresponds to smooth surfaces; the same model is utilized for describing the performance of smooth rotors in ISOTSEAL and according to figure 7.24 delivers the closest result for the thrust force. On the other hand, using this model to describe the friction for honeycomb/hole-patterned areas logically makes no sense. Similar results were obtained in figures 7.25, 7.26 and 7.27 although for the thrust force there was not a significant improvement in the error.

Additionally, section 7.5 shows the results using the same base cases A and B but with different inputs. This last section for the static solutions showed that for the majority of the cases the error for leakage is fewer than 10%, showing that the results for outlet conditions for most of the cases are acceptable. Nevertheless case 8 displayed over 20% error for leakage and at the same time the results for thrust force stood out from the averaged 30% error for the rest of the cases excluding case 12 which does not correspond to the values attributed to a honeycomb/hole-patterned bearing.

These results showed that the algorithm is not able to predict well for small clearances. Small clearances mean nonlinear effects acting on the fluid due to compressibility effects and having an error of 80%, while for other cases is below 30%. These errors showed that there must be nonlinear effects that are disregarded in the equations. The friction model has also an important influence in the results as seen in section 7.3 and 7.4, and the friction model used to calculate the thrust force was determined for clearances of 0,254mm, a quantity that belongs to the range of clearances at 50% offset. For case 8, either the coefficients for friction factors are excessively low for the side with more clearance or excessively high for the side with pinched side.

Results from sections 7.4 and 7.5 showed that changing the coefficients for the friction model improves the results for the thrust force and the leakage, but neither of them accounted the effect of the losses at the inlet and therefore augmenting the loss coefficient could improve the results without using the friction model for smooth seals. These improvements only apply for case A; unfortunately it is not the case for case B, strengthening the hypothesis of the lack of nonlinear effects represented in the equations. Moreover case 8 with smaller clearances exhibited that the algorithm is not capable of calculating the thrust force with the same error as the previous cases and probably is due to the nonlinear effects. The dynamic solutions for the next section will give more hints towards this hypothesis.

Last but not least, the results for cases A and B assuming isothermal flow and adiabatic flow were compared in appendix H, and they show some improvement in leakage but none for thrust force in case A, while for case B there was an improvement in thrust force but it's still above 100% error.

These results show that despite using different assumptions for the energy equation, the results for both cases are similar. It is not accurate to assume isothermal flow when there is a temperature drop or increase, nevertheless it has been used in ISOTSEAL and as already discussed the algorithm is largely used in the industry. The advantage of assuming isothermal flow instead of adiabatic flow is the need of three equations (continuity, radial and circumferential momentum) instead of four equations because the model seems more affected by other parameters like entrance loss coefficients and friction coefficients. To determine which model is correct, experimental data is needed.

## 9.2 Dynamic Solutions

There were two parameters that were varied for the simulations for dynamic variables of damping and stiffness. These two parameters were the coefficients for the calculation of the friction factor using the Blasius model and the ratio of the area of holes to the area of the surface of the bearing, called in the figures as area ratio or  $\gamma_c$ .

- Case A: Centered position. Figures 8.01 and 8.02 show very high stiffness at low axial frequencies while from 41.70 until 166 hz the stiffness is lower. The data for damping is not shown due to the unavailability of data, however it has been reported in (Lloyd's Register, 2013) that negative damping is very high at low frequencies until there is a crossover between 125 hz and 166 hz. The values for stiffness from the algorithm using different area ratios show that for frequencies higher than 10 hz they are in the same order of magnitude than the results from CFD simulations, and figure 8.2 shows that the models using low friction factors get closer values. Using an area ratio of 1 implies that the bearing has extra clearance along the radius. This is true when the flow passes through a gap in the middle of the hole at the surface, but this not true for the gap between holes (see figure 9.01). Hence using the effect of the ratio between areas, this extra clearance is reduced to give a pocket effect on the fluid, rising the stiffness and thus reducing the deviation from the CFD results, but at 10hz the error is high for area ratio. For figures 8.3 and 8.4, the algorithm seems not to predict well at a crossover area for the damping, and this is very important because as noted in chapter 3, negative damping means increasing amplitudes and therefore instabilities in the system. For area ratio of 1 the damping remains negative while for an area ratio of 0,56 there is a crossover, but it is not in the reported range. The damping at low frequencies for both cases is lower than the damping predicted in the CFD simulations and not being able to estimate such rise in the damping and stiffness for low frequencies confirms that the algorithm is not taking into account nonlinear effects.
- Case A: Offset position. Figures 8.05 and 8.06 show better agreement between the CFD simulations and the results from the algorithm. The stiffness does not seem to vary much with the axial frequency, and the trend in area ratio is the same as in case A: results seemed to have improved after adding the effect of the ratio of areas. The friction factor is also relevant for the results, the simulations using lower friction factor deliver better agreement with the curve for CFD than using higher friction factors. For damping the case is the opposite. The

CFD simulations predict a crossover of the damping between 10 hz and 41,7 hz, but neither of figures 8.07 nor 8.08 show that trend. For figure 8.07 at high frequencies the results showed better correspondence for an area ratio of 1 while an area ratio of 0.56 the results for frequencies of 41.7 and 83.3 hz are in better agreement. In contrast the crossover is the most important feature to predict, for it determines at which frequency the system could be unstable.

- Case B: Centered and Offset position. In general, stiffness is overestimated while damping is underestimated for both cases. Reducing the area ratio doesn't seem to improve the results for all the cases. From appendix A, the results from the static simulations were needed to solve the first order equations, as discussed in section 9.1 the results from case B overestimated the thrust force, meaning that the pressure distribution along the radius is not correct as the other variables such as density and velocity which affect the results for the first order equations besides the pressure, causing an overestimation on the stiffness and the underestimation in damping.

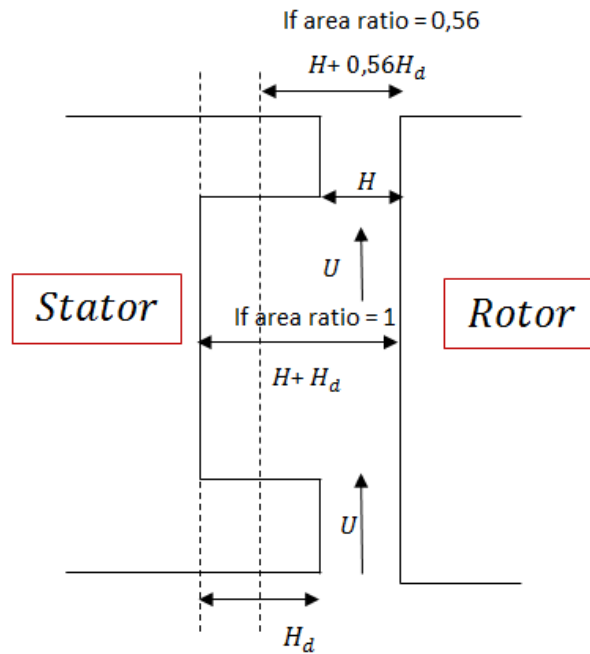


Figure 9.01. Effect of the area ratio in the model for first-order equations.

There are many sources of error that must be considered:

- Boundary conditions. Calculating the boundary conditions is very important to obtain correct values for all the variables. For the sensitivity test it was determined that including the losses at the inlet due to change in direction of the fluid and impact losses leads to improve the results for thrust force because pressure distributions fit better to the CFD results. However,

including these losses did not guarantee errors lesser than 10%, meaning that the entrances loss coefficient was not the only parameter needed to solve the problem, especially for case B.

- Friction model. From the sensitivity test in chapter 7 using different friction models and coefficients may improve the solutions for thrust force and leakage for case A, but reducing friction factors for case B did not solve the problems for thrust force. For case A, the best case for calculating the thrust force was using the friction model for the smooth case at the stator, but these results were not close enough, considering that it led to higher errors for the leakage. Still this model is for smooth cases, which is not physically feasible using this model for honeycomb/ hole-patterned bearings.
- The algorithm. The algorithm could be another source of error. A similar algorithm for the annular seal case was developed in order to compare its results to the ISOTSEAL ones as stated in appendix G. Using the same Matlab® function ode15i, the maximum error was of 0,19%. This result validates the use of ode15i for thrust bearings.
- Gas Law. The use of the average compressibility factor using the data from the CFD simulations could be a source of error. It was argued by Shin (2005) that the results from using ideal gas equations and real gas equations for the annular seal case did not show discrepancies to each other, and validated the use of ideal gas law using the compressibility factor as a good simplification.
- Zeroth-Order and First-Order equations. These equations were based on the analysis for the annular seal case and most of the terms in appendices A, B and C are similar to the equations in Shin (2005) except for adding the centrifugal and Coriolis effect that are not present in the analysis for gas seals. However the results in chapter 7 for different cases and results in chapter 8 showed discrepancies at cases with small clearances and at low axial frequencies, hinting that there are nonlinear effects acting and they are not taken into account in the simulations. The nonlinearities are linked as well to the friction factor and the friction coefficients must be revised for different set of clearances. The models and coefficients for calculating the friction factor are limited to few cases with constant clearances and this thesis used most of them out of their clearance range, giving wrong values for the variables.
- Model. For the thrust bearing case the calculations for stiffness and damping were done by calculating stiffness and damping at each side of the bearing assuming that the variables for one side are not affected by the other side and assuming that at each side there is a spring and damper working in parallel with the set at the other side. The model also assumes that stiffness and damping are lineal. Conversely the geometry of the annular seal allows the model to calculate the stiffness and damping of the seal without recurring to different calculations to another side of the seal. Assuming linearity for the thrust bearing may have affected the results because it is also assumed that the force is linearly proportional to the clearance, while some phenomena i.e. friction are clearly nonlinear. The consequence assuming linearity of the stiffness and damping affected the reliability of this analysis.
- CFD results. The CFD results may also be incorrect. According to the report from Lloyd's Register (2012) the simulations were carried out using a real gas properties table as an input

to the analysis, assuming that density is only a function of pressure instead of a function of pressure and temperature as in the ideal gas law. These simplifications were done in order to solve convergence issues that were present at the beginning of the analysis. However, implying that density is independent of the temperature and vice versa is not accurate and could lead to wrong results. Another issue is related to the analysis for annular seals, Kleynhans & Childs (1997) claimed that there is temperature reduction of less than 5% for annular seals, while for the CFD simulations there was a temperature increment from the inlet to the outlet of the bearing for both sides. Yet these two cases have opposite geometries that could explain the increment in temperature for the axial case, though a further experimental investigation should be conducted and compared with instead of CFD modelling.



## Chapter 10

### Conclusions

The objective of this study was to propose a reliable analytical tool to predict the rotordynamic performance of a thrust bearing using gas as the process fluid. To ensure reliability, results from the algorithm at certain conditions were compared to the results from CFD simulations. To accomplish the objective it was necessary to propose the use of Bulk-Flow theory presented by Hirs (1973) and adapt the governing equations for fluid mechanics to the geometry of axial bearings. Different friction models were also needed to improve the results. The conclusions of this study are discussed below:

- The analytical tool predicted the leakage within a 10% error while the static thrust force was predicted with over 20% error respect to the results from CFD simulations for the case of inflow coming from the inner radius. The same error for the case coming from the outer radius was achieved for the leakage while for the thrust force was over 100%. Lower errors can be obtained by tuning the effect of losses at the inlet (entrance loss coefficient) and changing the friction model, but for thrust force the results were outside the acceptable error margin.
- The analytical tool does not predict properly the thrust force for bearings with smaller clearances than the base cases. Results have proven that there are nonlinear effects that seem not to be considered in the model, therefore results are not reliable.
- The Bulk-flow model for thrust gas bearing highly depends on the friction models, as they can represent the nonlinear effects acting on the flow when the rotor is closer to the stator and especially for honeycomb/hole-patterned bearings. However, data from different friction models are limited and most of them are valid for specific clearances. Extrapolation from available experimental data to the actual model clearances provided even bigger gaps with respect to CFD simulation results.
- Changes in thermodynamic variables such as the compressibility factor and the heat capacity ratio did not affect the results for leakage and thrust force for neither of the cases.
- Modeling the equations for adiabatic flow or isothermal flow did not affect significantly the results for thrust force and leakage. Experiments are needed to determine which assumption is more accurate.

- The calculations for damping and stiffness depend on the friction factor and the ratio of the area of the holes and the area of the surface. The dependency on the friction factor is related to the use of data from the steady state results and dependency on the area ratio is related to the effect of including the cell-depth of the holes in first-order equations.
- The analytical tool did not predict correctly the dependency of damping and stiffness on the axial frequency of the rotor. This dependency refers to magnitude of the variables and crossover. These results are strongly linked to the nonlinear effects on the fluid for smaller clearances.
- The model proposed in this study gives no reliable solutions to the problem. Further attention needs to be given to the friction model and/or including terms to the equations in appendix A to improve the model.

To improve the model, there are some recommendations to follow:

- Including the effects at the inlet of the bearing: it is recommended to assume values higher than zero entrance loss coefficients and simultaneously changing the friction model and compare them to the results from the CFD simulations.
- Investigate more friction models for honeycomb/hole-patterned surface bearings with different clearances, cell-depth and rotational speed of the rotor. These models may significantly improve the results for the model.
- Experiments with thrust bearings are needed to validate the CFD simulations and the performance of the analytical tool. There are some features used on these simulations that are not accurate such as the relationship between temperature, density and pressure that probably impacted the reliability on the results. Additionally, every model either CFD or numerical integration must be validated against experimental data and improved.



## Bibliography

- Al-Qutub, A. Elrod, D. & Coleman, H. (2000). A new Friction factor model and entrance loss coefficient for honeycomb annular gas seals. *ASME Journal of Tribology*. 122(3),pp. 622-627.
- American Petroleum Institute (API).(2010). API Standard Paragraphs Rotordynamic Tutorial: Lateral Critical Speeds, Unbalance Response, Stability, Train Torsional, and Rotor Balancing. Second Edition.
- Ascher, U. & Petzold, L. (1998). Computer Methods for Ordinary Differential Equations and Differential-Algebraic Equations. SIAM.
- Childs (1991). Fluid-structure Interaction forces at pump-impeller-shroud surfaces for axial vibration analysis. *ASME Journal of Vibration and Acoustics*. 113(1), pp. 108-115.
- Cengel, Y. & Boles, M. (1993). Thermodynamics: An Engineering Approach. McGraw-Hill.
- Cambridge Press(2007). Numerical Recipes – The art of scientific computing.
- Crawford, A. (1992). The simplified handbook of vibration analysis. Volume I.
- Childs, D.(1993). Turbomachinery Rotordynamics. Wiley.
- D’Souza, R & Childs, D. (2002). A comparison of rotordynamic-coefficient predictions for annular honeycomb gas seals using three different friction-factor models. *ASME Journal of tribology* 124(3), pp.524-529.
- Gupta, M. (2005). Bulk-flow analysis for force and moment coefficients of a shrouded centrifugal compressor impeller. M.S. thesis, Texas A&M University.
- Hirs, G. (1973). A Bulk-flow theory for turbulence in lubricant films. *ASME Journal of lubrication technology* 95(2), pp. 137-145.
- Ha, T. & Childs, D. (1994). Annular honeycomb-stator turbulent gas seals analysis using a new friction-factor model based on flat plate tests. *ASME Journal of Tribology* 116(2),pp. 352-359.
- Ha, T & Childs, D. (1996). A rotordynamic analysis of an annular honeycomb seal using a two-control volume model. *KSME Journal*10(3), pp. 332-340.
- Hassini, M. & Arghir M. (2013). Phase Change and Choked Flow effects on Rotordynamic coefficients of cryogenic annular seals. *ASME Journal of Tribology* 135(4), 9 pages.

- Kleynhans, G. & Childs, D. (1997). The acoustic influence of cell depth on the rotordynamic characteristics of smooth-rotor/honeycomb-stator annular gas seals. *ASME Journal of Engineering for Gas Turbines and power* 119(4), pp. 949-956.
- Kleynhans, G. (1996). A two-Control-Volume Bulk-Flow Rotordynamic Analysis for Smooth-Rotor/Honeycomb-Stator Gas Annular Seals. Doctoral Thesis. Texas A & M University.
- Lloyd's Register (2012). Hole-pattern seal tilt and axial bearing – Report A. Report no. 12.3496.
- Muszynska, A. (2005). Rotordynamics. CRC Press.
- Nelson, C. (1984). Analysis for leakage and rotordynamic coefficients of surface- roughened tapered annular gas seals. *ASME Journal of Engineering for Gas Turbines and Power* 106(4), pp. 927-934
- Nelson, C. (1985). Rotordynamic coefficients for compressible flow in tapered annular seals. *ASME Journal of tribology* 107(3), pp. 318-325.
- Persson, A. (2005). The Coriolis Effect: Four centuries of conflict between common sense and mathematics, Part I: A history to 1885. *Journal History of Meteorology* 2, pp 1-24.
- Rondon, D. (2013). Estimation of the static performance of honeycomb/holepattern thrust gas bearing using the Bulk-flow theory. Project Work. Norwegian University of Science and Technology.
- Sonntag, R. & Van Wylen, G. (1991). Introduction to Thermodynamics, Classical and Statistical. Wiley & Sons.
- Storsteig, E. (1999). Dynamic characteristics and leakage performance of liquid annular seals in centrifugal pumps. Doctoral Thesis. Norwegian University of Science and Technology.
- Underbakke, H., Kibsgaard, S. & Brenne, L. (2012). Axial gas thrust bearing for rotors in rotating machinery. US Patent 2012/0163742.
- Vanden – Eijnden, E. (n.d.). Introduction to regular perturbation theory. Retrieved from: [http://www.cims.nyu.edu/~eve2/reg\\_pert.pdf](http://www.cims.nyu.edu/~eve2/reg_pert.pdf)
- White, F. (2011). Fluid Mechanics. McGraw Hill.

## Appendix A

### Adiabatic flow

Solution of governing equations

#### A.1. Non-dimensional Governing Equations

Non-dimensionalized parameters for case A are defined as following:

$$\bar{u}_R = \frac{U_R}{R_i \omega} \quad \text{A.01}$$

$$\bar{u}_\theta = \frac{U_\theta}{R_i \omega} \quad \text{A.02}$$

$$r = \frac{R}{R_i} \quad \text{A.03}$$

$$h = \frac{H}{C_r} \quad \text{A.04}$$

$$\tau = t\omega \quad \text{A.05}$$

$$p = \frac{P}{P_R} \quad \text{A.06}$$

$$\bar{\rho} = \frac{\rho}{\rho_R} \quad \text{A.07}$$

$$c = \frac{C_r}{R_i} \quad \text{A.08}$$

$$g = \frac{2\rho_R C_r R_i \omega}{\mu} \quad \text{A.09}$$

And the nondimensionalized parameters for case B are defined as following:

$$\bar{u}_R = \frac{U_R}{R_o \omega} \quad \text{A.10}$$

$$\bar{u}_\theta = \frac{U_\theta}{R_o \omega} \quad \text{A.11}$$

$$r = \frac{R}{R_o} \quad \text{A.12}$$

$$h = \frac{H}{C_r} \quad \text{A.13}$$

$$\tau = t\omega \quad \text{A.14}$$

$$p = \frac{P}{P_r} \quad \text{A.15}$$

$$\bar{\rho} = \frac{\rho}{\rho_R} \quad \text{A.16}$$

$$c = \frac{C_r}{R_o} \quad \text{A.17}$$

$$g = \frac{2\rho_R C_r R_o \omega}{\mu} \quad \text{A.18}$$

For both cases, the average clearance is:

$$C_r = \frac{C_e + C_x}{2} \quad \text{A.19}$$

Non-dimensionalized governing equations for the combined control volume is expressed as:

Continuity:

$$\frac{\partial}{\partial \tau} (\bar{\rho}(h + \gamma_d h_d)) + \frac{1}{r} \frac{\partial}{\partial r} (\bar{\rho} \bar{u}_R h r) + \frac{1}{r} \frac{\partial}{\partial \theta} (\bar{\rho} \bar{u}_\theta h) = 0 \quad \text{A.20}$$

Continuity momentum equation:

$$-\frac{h}{r} \frac{\partial p}{\partial \theta} P_c = \frac{1}{2c} \bar{\rho} (f_r \bar{u}_r (\bar{u}_\theta - r) + f_s \bar{u}_s \bar{u}_\theta) + \bar{\rho} h \bar{u}_R \frac{\partial \bar{u}_\theta}{\partial r} + \frac{\bar{\rho} h \bar{u}_R \bar{u}_\theta}{r} + \bar{\rho} h \frac{\partial \bar{u}_\theta}{\partial \tau} + \frac{\bar{\rho} h \bar{u}_\theta}{r} \frac{\partial \bar{u}_\theta}{\partial \theta} \quad \text{A.21}$$

Radial momentum equation:

$$-h \frac{\partial p}{\partial r} P_c = \frac{1}{2c} \bar{\rho} \bar{u}_R (f_r \bar{u}_r + f_s \bar{u}_s) + \bar{\rho} h \bar{u}_R \frac{\partial \bar{u}_R}{\partial r} - \frac{\bar{\rho} h (\bar{u}_\theta)^2}{r} + \bar{\rho} h \frac{\partial \bar{u}_R}{\partial \tau} + \frac{\bar{\rho} h \bar{u}_\theta}{r} \frac{\partial \bar{u}_R}{\partial \theta} \quad \text{A.22}$$

Energy equation:

$$\begin{aligned} & \frac{P_c}{Z_c(\gamma-1)} \left( \frac{\partial p}{\partial \tau} + \bar{u}_R \frac{\partial p}{\partial r} + \frac{\bar{u}_\theta}{r} \frac{\partial p}{\partial \theta} \right) - \frac{p}{\bar{\rho}} P_c \left( \frac{1}{Z_c(\gamma-1)} + 1 \right) \left( \frac{\partial \bar{\rho}}{\partial \tau} + \bar{u}_R \frac{\partial \bar{\rho}}{\partial r} + \frac{\bar{u}_\theta}{r} \frac{\partial \bar{\rho}}{\partial \theta} \right) + \\ & \frac{\gamma_d h_d}{h} \left[ \frac{P_c}{Z_c(\gamma-1)} \frac{\partial p}{\partial \tau} - \frac{p}{\bar{\rho}} P_c \left( \frac{1}{Z_c(\gamma-1)} + 1 \right) \frac{\partial \bar{\rho}}{\partial \tau} + \bar{\rho} \left( \bar{u}_R \frac{\partial \bar{u}_R}{\partial \tau} + \bar{u}_\theta \frac{\partial \bar{u}_\theta}{\partial \tau} \right) \right] - \frac{\bar{\rho}}{2hc} (\bar{u}_r^3 f_r + \bar{u}_s^3 f_s) = P_c \frac{p}{h} \frac{\partial h}{\partial \tau} \end{aligned} \quad A.23$$

Where

$$P_c = \frac{P_r}{\rho_r (R_i \omega)^2} \quad A.24$$

$$\bar{u}_r = \sqrt{\bar{u}_R^2 + (\bar{u}_\theta - r)^2} \quad A.25$$

$$\bar{u}_s = \sqrt{\bar{u}_R^2 + \bar{u}_\theta^2} \quad A.26$$

Non-dimensional entrance loss and exit recovery equations are:

When the flow goes from the inner radius to the outer radius,

$$1 - p_{(r_i)} = \frac{1 + \varepsilon}{2P_c} \bar{\rho}_{(r_i)} \bar{u}_{R(r_i)}^2 \quad A.27$$

$$p_{(r_i)} = \bar{\rho}_{(r_i)}^\gamma \quad A.28$$

$$p_{(r_o)} - p_s = \frac{1 - \xi}{2P_c} \bar{\rho}_{(r_o)} \bar{u}_{R(r_o)}^2 \quad A.29$$

And when the flow goes from the outer radius to the inner radius,

$$1 - p_{(r_o)} = \frac{1 + \varepsilon}{2P_c} \bar{\rho}_{(r_o)} \bar{u}_{R(r_o)}^2 \quad A.30$$

$$p_{(r_o)} = \bar{\rho}_{(r_o)}^\gamma \quad A.31$$

$$p_{(r_i)} - p_s = \frac{1 - \xi}{2P_c} \bar{\rho}_{(r_i)} \bar{u}_{R(r_i)}^2 \quad A.32$$

## A.2. Perturbation Analysis

Perturbation variables are introduced here,

$$h = h_0 + \epsilon h_1 \quad \text{A.33}$$

$$\bar{u}_R = \bar{u}_{R_0} + \epsilon \bar{u}_{R_1} \quad \text{A.34}$$

$$\bar{u}_\theta = \bar{u}_{\theta_0} + \epsilon \bar{u}_{\theta_1} \quad \text{A.35}$$

$$p = p_0 + \epsilon p_1 \quad \text{A.36}$$

$$\bar{\rho} = \bar{\rho}_0 + \epsilon \bar{\rho}_1 \quad \text{A.37}$$

Where  $\epsilon$  is the perturbed eccentricity ratio, which is a very small value. With the equations A.33-A.37, the governing equations are separated into zeroth and first order perturbation equations.

### A.2.1. Zeroth-Order Equations

For isothermal flow, zeroth-order equations are expressed in appendix H. The following equations are for adiabatic flow.

Continuity equation

$$\bar{u}_{R_0} h_0 r \frac{d\bar{\rho}_0}{dr} + \bar{\rho}_0 h_0 r \frac{d\bar{u}_{R_0}}{dr} + \bar{\rho}_0 \bar{u}_{R_0} r \frac{dh_0}{dr} + \bar{\rho}_0 \bar{u}_{R_0} h_0 = 0 \quad \text{A.38}$$

Circumferential momentum equation

$$\bar{\rho}_0 \bar{u}_{R_0} h_0 \frac{d\bar{u}_{\theta_0}}{dr} + \frac{\bar{u}_{R_0} \bar{u}_{\theta_0} \bar{\rho}_0 h_0}{r} + \frac{\bar{\rho}_0}{2c} [f_{r_0} \bar{u}_{r_0} (\bar{u}_{\theta_0} - r) + f_{s_0} \bar{u}_{s_0} \bar{u}_{\theta_0}] = 0 \quad \text{A.39}$$

Radial momentum equation

$$h_0 P_c \frac{dp_0}{dr} + \frac{\bar{\rho}_0 \bar{u}_{R_0}}{2c} (f_{r_0} \bar{u}_{r_0} + f_{s_0} \bar{u}_{s_0}) + \bar{\rho}_0 h_0 \bar{u}_{R_0} \frac{d\bar{u}_{R_0}}{dr} - \bar{\rho}_0 h_0 \frac{\bar{u}_{\theta_0}^2}{r} = 0 \quad \text{A.40}$$

Energy equation

$$\bar{u}_{R_0} \left( \frac{1}{Z_c(\gamma - 1)} \right) \frac{dp_0}{dr} - \bar{u}_{R_0} \frac{p_0}{\bar{\rho}_0} \left( \frac{1}{Z_c(\gamma - 1)} + 1 \right) \frac{d\bar{\rho}_0}{dr} + \frac{\bar{\rho}_0}{2h_0 P_c} [\bar{u}_{r_0}^3 f_{r_0} + \bar{u}_{s_0}^3 f_{s_0}] = 0 \quad \text{A.41}$$

Where,

$$\bar{u}_{r_0} = \sqrt{\bar{u}_{R_0}^2 + (\bar{u}_{\theta_0} - r)^2} \quad \text{A.42}$$

$$\bar{u}_{s_0} = \sqrt{\bar{u}_{R_0}^2 + \bar{u}_{\theta_0}^2} \quad \text{A.43}$$

$$f_{r_0} = nr(\bar{\rho}_0 h_0 \bar{u}_{r_0} g)^{mr} \quad \text{A.44}$$

$$f_{s_0} = ns(\bar{\rho}_0 h_0 \bar{u}_{s_0} g)^{ms} \quad \text{A.45}$$

## A.2.2. First Order Equations

Continuity equation

$$\begin{aligned} & \bar{\rho}_0 \frac{\partial h_1}{\partial \tau} + (h_0 + \gamma_d h_d) \frac{\partial \bar{\rho}_1}{\partial \tau} + \left( \frac{\bar{\rho}_0 \bar{u}_{R_0}}{r} + \bar{\rho}_0 \frac{\partial \bar{u}_{R_0}}{\partial r} + \bar{u}_{R_0} \frac{\partial \bar{\rho}_0}{\partial r} \right) h_1 + \left( \frac{\bar{\rho}_0 h_0}{r} + \bar{\rho}_0 \frac{\partial h_0}{\partial r} + h_0 \frac{\partial \bar{\rho}_0}{\partial r} \right) \bar{u}_{R_1} + \\ & \left( \frac{\bar{u}_{R_0} h_0}{r} + \bar{u}_{R_0} \frac{\partial h_0}{\partial r} + h_0 \frac{\partial \bar{u}_{R_0}}{\partial r} \right) \bar{\rho}_1 + \bar{\rho}_0 \bar{u}_{R_0} \frac{\partial h_1}{\partial r} + \bar{\rho}_0 h_0 \frac{\partial \bar{u}_{R_1}}{\partial r} + \bar{u}_{R_0} h_0 \frac{\partial \bar{\rho}_1}{\partial r} + \frac{\bar{\rho}_0 \bar{u}_{\theta_0}}{r} \frac{\partial h_1}{\partial \theta} + \frac{\bar{\rho}_0 h_0}{r} \frac{\partial \bar{u}_{\theta_1}}{\partial \theta} + \\ & \frac{h_0 \bar{u}_{\theta_0}}{r} \frac{\partial \bar{\rho}_1}{\partial \theta} = 0 \end{aligned} \quad \text{A.46}$$

Circumferential momentum equation

$$\begin{aligned} & \frac{P_c}{r \bar{\rho}_0} \frac{\partial p_1}{\partial \theta} + \frac{1}{2ch_0} \left[ \bar{u}_{r_0} (\bar{u}_{\theta_0} - r) \left( f_{r_1} - \frac{h_1}{h_0} f_{r_0} \right) + f_{r_0} \bar{u}_{r_0} \bar{u}_{\theta_1} + f_{r_0} \bar{u}_{r_1} (\bar{u}_{\theta_0} - r) + \bar{u}_{r_0} \bar{u}_{\theta_0} \left( f_{s_1} - \frac{h_1}{h_0} f_{s_0} \right) + \right. \\ & \left. f_{s_0} \bar{u}_{s_0} \bar{u}_{\theta_1} + f_{s_0} \bar{u}_{s_1} \bar{u}_{\theta_0} \right] + \bar{u}_{R_0} \frac{\partial \bar{u}_{\theta_1}}{\partial r} + \bar{u}_{R_1} \frac{\partial \bar{u}_{\theta_0}}{\partial r} + \bar{u}_{R_0} \frac{\bar{u}_{\theta_1}}{r} + \bar{u}_{R_1} \frac{\bar{u}_{\theta_0}}{r} + \frac{\partial \bar{u}_{\theta_1}}{\partial \tau} + \frac{\bar{u}_{\theta_0}}{r} \frac{\partial \bar{u}_{\theta_1}}{\partial \theta} = 0 \end{aligned} \quad \text{A.47}$$

Radial momentum equation

$$\begin{aligned} & \frac{P_c}{\bar{\rho}_0} \left( \frac{\partial p_1}{\partial r} - \frac{\bar{\rho}_1}{\bar{\rho}_0} \frac{\partial p_0}{\partial r} \right) + \frac{1}{2ch_0} \left[ \bar{u}_{r_0} \bar{u}_{R_0} \left( f_{r_1} - \frac{h_1}{h_0} f_{r_0} \right) + f_{r_0} \bar{u}_{r_1} \bar{u}_{R_0} + f_{r_0} \bar{u}_{r_0} \bar{u}_{R_1} + \bar{u}_{s_0} \bar{u}_{R_0} \left( f_{s_1} - \frac{h_1}{h_0} f_{s_0} \right) + \right. \\ & \left. f_{s_0} \bar{u}_{s_1} \bar{u}_{R_0} + f_{s_0} \bar{u}_{s_0} \bar{u}_{R_1} \right] + \frac{\partial \bar{u}_{R_1}}{\partial r} \bar{u}_{R_0} + \frac{\partial \bar{u}_{R_0}}{\partial r} \bar{u}_{R_1} + 2 \frac{\bar{u}_{\theta_0} \bar{u}_{\theta_1}}{r} + \frac{\partial \bar{u}_{R_1}}{\partial \tau} + \frac{\bar{u}_{\theta_0}}{r} \frac{\partial \bar{u}_{R_1}}{\partial \theta} = 0 \end{aligned} \quad \text{A.48}$$

Energy equation

$$\begin{aligned} & P_c \frac{p_0}{h_0} \frac{\partial h_1}{\partial \tau} = \frac{P_c}{Z_c(\gamma-1)} \left( \frac{\partial p_1}{\partial \tau} + \bar{u}_{R_0} \frac{\partial p_1}{\partial r} + \bar{u}_{R_1} \frac{\partial p_0}{\partial r} + \frac{\bar{u}_{\theta_0}}{r} \frac{\partial p_1}{\partial \theta} \right) - P_c \frac{p_0}{\bar{\rho}_0} \left( \frac{1}{Z_c(\gamma-1)} + 1 \right) \left[ \frac{\partial \bar{\rho}_1}{\partial \tau} + \bar{u}_{\theta_0} \frac{\partial \bar{\rho}_1}{\partial \theta} + \bar{u}_{R_1} \frac{\partial \bar{\rho}_0}{\partial r} + \right. \\ & \frac{p_1}{p_0} \bar{u}_{R_0} \frac{\partial \bar{\rho}_0}{\partial r} + \bar{u}_{R_0} \frac{\partial \bar{\rho}_1}{\partial r} - \frac{\bar{\rho}_1}{\bar{\rho}_0} \bar{u}_{R_0} \frac{\partial \bar{\rho}_0}{\partial r} \left. \right] + \frac{\gamma_d h_d}{h_0} \left[ \frac{P_c}{Z_c(\gamma-1)} \frac{\partial p_1}{\partial \tau} - P_c \frac{p_0}{\bar{\rho}_0} \left( \frac{1}{Z_c(\gamma-1)} + 1 \right) \frac{\partial \bar{\rho}_1}{\partial \tau} + \bar{\rho}_0 \left( \bar{u}_{R_0} \frac{\partial \bar{u}_{R_1}}{\partial \tau} + \right. \right. \\ & \left. \bar{u}_{\theta_0} \frac{\partial \bar{u}_{\theta_1}}{\partial \tau} \right) \left. \right] - \frac{\bar{\rho}_0}{2ch_0} \left[ \bar{u}_{r_0}^2 (\bar{u}_{r_0} f_{r_1} + 3 \bar{u}_{r_1} f_{r_0}) + \left( \frac{\bar{\rho}_1}{\bar{\rho}_0} - \frac{h_1}{h_0} \right) \bar{u}_{r_0}^3 f_{r_0} + \bar{u}_{s_0}^2 (\bar{u}_{s_0} f_{s_1} + 3 \bar{u}_{s_1} f_{s_0}) + \right. \\ & \left. \left( \frac{\bar{\rho}_1}{\bar{\rho}_0} - \frac{h_1}{h_0} \right) \bar{u}_{s_0}^3 f_{s_0} \right] \end{aligned} \quad \text{A.49}$$

Where,

$$\bar{u}_{s1} = \frac{\bar{u}_{\theta 0} \bar{u}_{\theta 1} + \bar{u}_{R0} \bar{u}_{R1}}{\bar{u}_{s0}} \quad \text{A.50}$$

$$\bar{u}_{r1} = \frac{(\bar{u}_{\theta 0} - r) \bar{u}_{\theta 1} + \bar{u}_{R0} \bar{u}_{R1}}{\bar{u}_{s0}} \quad \text{A.51}$$

And

$$f_{s1} = m s f_{s0} \left( \frac{\bar{\rho}_1}{\bar{\rho}_0} + \frac{h_1}{h_0} + \frac{\bar{u}_{s1}}{\bar{u}_{s0}} \right) \quad \text{A.52}$$

$$f_{r1} = m r f_{r0} \left( \frac{\bar{\rho}_1}{\bar{\rho}_0} + \frac{h_1}{h_0} + \frac{\bar{u}_{r1}}{\bar{u}_{r0}} \right) \quad \text{A.53}$$

These equations can be rearranged as following:

$$[A_{(r)}] \frac{\partial \vec{X}_1}{\partial \tau} + [B_{(r)}] \frac{\partial \vec{X}_1}{\partial r} + [C_{(r)}] \frac{\partial \vec{X}_1}{\partial \theta} + [D_{(r)}] \vec{X} + [E_{(r)}] \frac{\partial h_1}{\partial \tau} + [F_{(r)}] \frac{\partial h_1}{\partial r} + [G_{(r)}] \frac{\partial h_1}{\partial \theta} + [L_{(r)}] h_1 = 0 \quad \text{A.54}$$

Where vector  $\vec{X}_1$  is represented as,

$$\vec{X}_1 = \begin{Bmatrix} \bar{u}_{R1} \\ p_1 \\ \bar{u}_{\theta 1} \\ \bar{\rho}_1 \end{Bmatrix} \quad \text{A.55}$$

The matrices A,B,C,D and vectors E,F,G,L are given in appendix B.

As in Childs (1993) assuming that the clearance function is

$$h = h_0 - d e^{i\phi t} \quad \text{A.56}$$

with  $\phi$  as the frequency of the axial motion of the rotor. Introducing f as,

$$f = \frac{\phi}{\omega} \quad \text{A.57}$$

f is the frequency ratio.

$$h = h_0 - d e^{i f \tau} \quad \text{A.58}$$

With

$$\epsilon h_1 = -d e^{i f \tau} \quad \text{A.59}$$



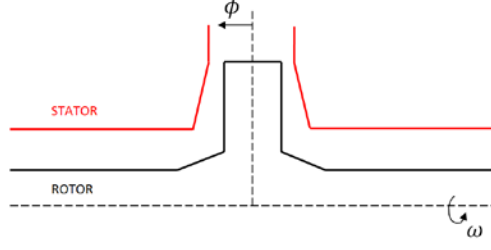


Figure A.01 Different frequencies acting on the rotor.

Assuming the dependent perturbation variables as,

$$\bar{\mathbf{u}}_{R1} = \bar{u}_{R1(r)} e^{if\tau} \quad \text{A.60}$$

$$\mathbf{p}_1 = p_{1(r)} e^{if\tau} \quad \text{A.61}$$

$$\bar{\mathbf{u}}_{\theta 1} = \bar{u}_{\theta 1(r)} e^{if\tau} \quad \text{A.62}$$

$$\bar{\rho}_1 = \bar{\rho}_{1(r)} e^{if\tau} \quad \text{A.63}$$

Applying equation A.60 through A.63 on the equation A.54 the first order equations are expressed in matrix form:

$$[M_{(r)}] \frac{\partial \vec{X}_1}{\partial r} + [N_{(r,f)}] \vec{X}_1 = \frac{d}{\epsilon} [\vec{g}_{(r,f)}] \quad \text{A.64}$$

The components for the matrix M, N and vector g are given in the Appendix C. Four boundary conditions are required to solve equation A.64, equations A.65 and A.66 are conditions for cases A and B:

$$\bar{u}_{\theta 1(r_i)} = 0 \quad \text{A.65}$$

$$\bar{u}_{\theta 1(r_o)} = 0 \quad \text{A.66}$$

And from equations A.27 to A.32, the following equations are the boundary conditions for case A:

$$p_{1(r_i)} = -\frac{1+\epsilon}{2P_c} \left( \bar{\rho}_{1(r_i)} \bar{u}_{R0(r_i)}^2 + 2\bar{\rho}_{0(r_i)} \bar{u}_{R0(r_i)} \bar{u}_{R1(r_i)} \right) \quad \text{A.67}$$

$$p_{1(r_i)} = \gamma \bar{\rho}_{0(r_i)}^{\gamma-1} \bar{\rho}_{1(r_i)} \quad \text{A.68}$$

$$p_{1(r_o)} = -\frac{1-\xi}{2P_c} \left( \bar{\rho}_{1(r_o)} \bar{u}_{R0(r_o)}^2 + 2\bar{\rho}_{0(r_o)} \bar{u}_{R0(r_o)} \bar{u}_{R1(r_o)} \right) \quad \text{A.69}$$

And for case B:

$$p_{1(r_o)} = -\frac{1+\varepsilon}{2P_c} \left( \bar{\rho}_{1(r_o)} \bar{u}_{R0(r_o)}^2 + 2\bar{\rho}_{0(r_o)} \bar{u}_{R0(r_o)} \bar{u}_{R1(r_o)} \right) \quad \text{A.70}$$

$$p_{1(r_o)} = \gamma \bar{\rho}_{0(r_o)}^{\gamma-1} \bar{\rho}_{1(r_o)} \quad \text{A.71}$$

$$p_{1(r_i)} = -\frac{1-\xi}{2P_c} \left( \bar{\rho}_{1(r_i)} \bar{u}_{R0(r_i)}^2 + 2\bar{\rho}_{0(r_i)} \bar{u}_{R0(r_i)} \bar{u}_{R1(r_i)} \right) \quad \text{A.72}$$

To solve the system, Childs (1993) used a transition-matrix approach. It was proposed the homogeneous version of equation A.64 successively with the initial conditions (1,0,0,0), (0,1,0,0), (0,0,1,0) and (0,0,0,1) to obtain the transition matrix  $[\Phi_{(f,r)}]$ . As Childs (1993) remarked, a particular solution is solved for initial conditions (0,0,0,0) with  $\frac{d}{\epsilon} = 1$ , yielding a vector  $\{\vec{\Psi}_{(f,r)}\}$  as the vector non homogeneous solutions, so the complete solution for case A is:

$$\vec{X}_{1(f,r)} = [\Phi_{(f,r)}] \vec{X}_{1(r_i)} + \frac{d}{\epsilon} \vec{\Psi}_{(f,r)} \quad \text{A.73}$$

And for case B:

$$\vec{X}_{1(f,r)} = [\Phi_{(f,r)}] \vec{X}_{1(r_o)} + \frac{d}{\epsilon} \vec{\Psi}_{(f,r)} \quad \text{A.74}$$

Following the procedure from Childs (1993) the equations must be solved for specific frequency ratios. To solve the unknown initial conditions, equations A.73 and A.74 can be rewritten for case A as:

$$\bar{u}_{R1(f,r_o)} = \Phi_{1,1(f,r_o)} \bar{u}_{R1(r_i)} + \Phi_{1,2(f,r_o)} p_{1(r_i)} + \Phi_{1,4(f,r_o)} \bar{\rho}_{1(r_i)} + \frac{d}{\epsilon} \Psi_{1(f,r_o)} \quad \text{A.75}$$

$$p_{1(f,r_o)} = \Phi_{2,1(f,r_o)} \bar{u}_{R1(r_i)} + \Phi_{2,2(f,r_o)} p_{1(r_i)} + \Phi_{2,4(f,r_o)} \bar{\rho}_{1(r_i)} + \frac{d}{\epsilon} \Psi_{2(f,r_o)} \quad \text{A.76}$$

$$\bar{\rho}_{1(f,r_o)} = \Phi_{4,1(f,r_o)} \bar{u}_{R1(r_i)} + \Phi_{4,2(f,r_o)} p_{1(r_i)} + \Phi_{4,4(f,r_o)} \bar{\rho}_{1(r_i)} + \frac{d}{\epsilon} \Psi_{4(f,r_o)} \quad \text{A.77}$$

And for case B:

$$\bar{u}_{R1(f,r_i)} = \Phi_{1,1(f,r_i)} \bar{u}_{R1(r_o)} + \Phi_{1,2(f,r_i)} p_{1(r_o)} + \Phi_{1,4(f,r_i)} \bar{\rho}_{1(r_o)} + \frac{d}{\epsilon} \Psi_{1(f,r_i)} \quad \text{A.78}$$

$$p_{1(f,r_i)} = \Phi_{2,1(f,r_i)} \bar{u}_{R1(r_o)} + \Phi_{2,2(f,r_i)} p_{1(r_o)} + \Phi_{2,4(f,r_i)} \bar{\rho}_{1(r_o)} + \frac{d}{\epsilon} \Psi_{2(f,r_i)} \quad \text{A.79}$$

$$\bar{\rho}_{1(f,r_i)} = \Phi_{4,1(f,r_i)} \bar{u}_{R1(r_o)} + \Phi_{4,2(f,r_i)} p_{1(r_o)} + \Phi_{4,4(f,r_i)} \bar{\rho}_{1(r_o)} + \frac{d}{\epsilon} \Psi_{4(f,r_i)} \quad \text{A.80}$$

Then equations A.75-A.77 are substituted into A.69 for the final equation, the matrix form of the three substituted equations A.67-A.69 is:

$$[\Lambda] \begin{Bmatrix} \bar{u}_{R1(r_i)} \\ p_{1(r_i)} \\ \bar{\rho}_{1(r_i)} \end{Bmatrix} = \frac{d}{\epsilon} W \quad \text{A.81}$$

Where  $\Lambda$  is a 3x3 matrix,

$$\begin{aligned} \Lambda_{1,1} &= \frac{1+\epsilon}{P_c} \left( \bar{\rho}_{0(r_i)} \bar{u}_{R0(r_i)} \right) \\ \Lambda_{1,2} &= 1 \\ \Lambda_{1,3} &= \frac{1+\epsilon}{2P_c} \left( \bar{u}_{R0(r_i)}^2 \right) \\ \Lambda_{2,1} &= 0 \\ \Lambda_{2,2} &= 1 \\ \Lambda_{2,3} &= -\gamma \bar{\rho}_{0(r_i)}^{\gamma-1} \\ \Lambda_{3,1} &= \Phi_{2,1(f,r_o)} + \left( \frac{1-\xi}{2P_c} \right) \left( \Phi_{4,1(f,r_o)} \bar{u}_{R0(r_o)}^2 + 2\bar{\rho}_{0(r_o)} \bar{u}_{R0(r_o)} \Phi_{1,1(f,r_o)} \right) \\ \Lambda_{3,2} &= \Phi_{2,2(f,r_o)} + \left( \frac{1-\xi}{2P_c} \right) \left( \Phi_{4,2(f,r_o)} \bar{u}_{R0(r_o)}^2 + 2\bar{\rho}_{0(r_o)} \bar{u}_{R0(r_o)} \Phi_{1,2(f,r_o)} \right) \\ \Lambda_{3,3} &= \Phi_{2,4(f,r_o)} + \left( \frac{1-\xi}{2P_c} \right) \left( \Phi_{4,4(f,r_o)} \bar{u}_{R0(r_o)}^2 + 2\bar{\rho}_{0(r_o)} \bar{u}_{R0(r_o)} \Phi_{1,4(f,r_o)} \right) \\ W_1 &= 0 \\ W_2 &= 0 \\ W_3 &= -\Psi_{2(f,r_o)} - \left( \frac{1-\xi}{2P_c} \right) \left( \Psi_{4(f,r_o)} \bar{u}_{R0(r_o)}^2 + 2\bar{\rho}_{0(r_o)} \bar{u}_{R0(r_o)} \Psi_{1(f,r_o)} \right) \end{aligned}$$

And equations A.78-A.80 are substituted into A.72 for the final equation for case B, the matrix form of the three substituted equations A.70-A.72 is:

$$\Lambda \begin{Bmatrix} \bar{u}_{R1(r_o)} \\ p_{1(r_o)} \\ \bar{\rho}_{1(r_o)} \end{Bmatrix} = \frac{d}{\epsilon} W \quad \text{A.82}$$

Where,

$$\begin{aligned} \Lambda_{1,1} &= \frac{1 + \epsilon}{P_c} \left( \bar{\rho}_{0(r_o)} \bar{u}_{R0(r_o)} \right) \\ \Lambda_{1,2} &= 1 \\ \Lambda_{1,3} &= \frac{1 + \epsilon}{2P_c} \left( \bar{u}_{R0(r_o)}^2 \right) \\ \Lambda_{2,1} &= 0 \\ \Lambda_{2,2} &= 1 \\ \Lambda_{2,3} &= -\gamma \bar{\rho}_{0(r_o)}^{\gamma-1} \\ \Lambda_{3,1} &= \Phi_{2,1(f,r_i)} + \left( \frac{1 - \xi}{2P_c} \right) \left( \Phi_{4,1(f,r_i)} \bar{u}_{R0(r_i)}^2 + 2\bar{\rho}_{0(r_i)} \bar{u}_{R0(r_i)} \Phi_{1,1(f,r_i)} \right) \\ \Lambda_{3,2} &= \Phi_{2,2(f,r_i)} + \left( \frac{1 - \xi}{2P_c} \right) \left( \Phi_{4,2(f,r_i)} \bar{u}_{R0(r_i)}^2 + 2\bar{\rho}_{0(r_i)} \bar{u}_{R0(r_i)} \Phi_{1,2(f,r_i)} \right) \\ \Lambda_{3,3} &= \Phi_{2,4(f,r_i)} + \left( \frac{1 - \xi}{2P_c} \right) \left( \Phi_{4,4(f,r_i)} \bar{u}_{R0(r_i)}^2 + 2\bar{\rho}_{0(r_i)} \bar{u}_{R0(r_i)} \Phi_{1,4(f,r_i)} \right) \\ W_1 &= 0 \\ W_2 &= 0 \\ W_3 &= -\Psi_{2(f,r_i)} - \left( \frac{1 - \xi}{2P_c} \right) \left( \Psi_{4(f,r_i)} \bar{u}_{R0(r_i)}^2 + 2\bar{\rho}_{0(r_i)} \bar{u}_{R0(r_i)} \Psi_{1(f,r_i)} \right) \end{aligned}$$

After the equations are solved, the Stiffness and Damping are obtained by integrating the function of the first-order pressure:

$$K = -\frac{\epsilon}{d} \iint Re(P_1) dA \quad \text{A.83}$$

$$C = -\frac{\epsilon}{d\phi} \iint \text{Im}(P_1) dA$$

A.84



## Appendix B

Matrix A, as a 4x4 matrix:

$$A_{1,4} = h_0 + h_d \quad \text{B.01}$$

$$A_{2,3} = 1 \quad \text{B.02}$$

$$A_{3,1} = 1 \quad \text{B.03}$$

$$A_{4,1} = \frac{h_d}{h_0} \bar{\rho}_0 \bar{u}_{R0} \quad \text{B.04}$$

$$A_{4,2} = P_c \frac{1}{Z_c(\gamma - 1)} \left( 1 + \frac{h_d}{h_0} \right) \quad \text{B.05}$$

$$A_{4,3} = \frac{h_d}{h_0} \bar{\rho}_0 \bar{u}_{\theta 0} \quad \text{B.06}$$

$$A_{4,4} = -P_c \frac{p_0}{\bar{\rho}_0} \left( \frac{1}{Z_c(\gamma - 1)} + 1 \right) \left( 1 + \frac{h_d}{h_0} \right) \quad \text{B.07}$$

Matrix B, as a 4x4 matrix:

$$B_{1,1} = \bar{\rho}_0 h_0 \quad \text{B.08}$$

$$B_{1,4} = h_0 \bar{u}_{R0} \quad \text{B.09}$$

$$B_{2,3} = \bar{u}_{R0} \quad \text{B.10}$$

$$B_{3,1} = \bar{u}_{R0} \quad \text{B.11}$$

$$B_{3,2} = P_c \frac{1}{\bar{\rho}_0} \quad \text{B.12}$$

$$B_{4,2} = P_c \frac{1}{Z_c(\gamma - 1)} \bar{u}_{R0} \quad \text{B.13}$$

$$B_{4,4} = -P_c \frac{p_0}{\bar{\rho}_0} \left( \frac{1}{Z_c(\gamma - 1)} + 1 \right) \bar{u}_{R0} \quad \text{B.14}$$

Matrix C, as a 4x4 matrix:

$$C_{1,3} = \frac{\bar{\rho}_0 h_0}{r} \quad \text{B.15}$$

$$C_{1,4} = \frac{\bar{u}_{\theta 0} h_0}{r} \quad \text{B.16}$$

$$C_{2,2} = \frac{1}{r} P_c \frac{p_0}{\bar{\rho}_0} \quad \text{B.17}$$

$$C_{2,3} = \frac{\bar{u}_{\theta 0}}{r} \quad \text{B.18}$$

$$C_{3,1} = \frac{\bar{u}_{\theta 0}}{r} \quad \text{B.19}$$

$$C_{4,2} = P_c \frac{1}{Z_c(\gamma - 1)} \frac{\bar{u}_{\theta 0}}{r} \quad \text{B.20}$$

$$C_{4,4} = -P_c \frac{p_0}{\bar{\rho}_0} \left( \frac{1}{Z_c(\gamma - 1)} + 1 \right) \frac{\bar{u}_{\theta 0}}{r} \quad \text{B.21}$$

Matrix D, as a 4x4 matrix:

$$D_{1,1} = \frac{\bar{\rho}_0 h_0}{r} + \bar{\rho}_0 \frac{dh_0}{dr} + h_0 \frac{d\bar{\rho}_0}{dr} \quad \text{B.22}$$

$$D_{1,4} = \frac{\bar{u}_{R0} h_0}{r} + \bar{u}_{R0} \frac{dh_0}{dr} + h_0 \frac{d\bar{u}_{R0}}{dr} \quad \text{B.23}$$

$$D_{2,1} = \frac{\bar{u}_{R0}}{2ch_0} \left[ \frac{(\bar{u}_{\theta 0} - r)}{\bar{u}_{r0}} f_{r0}(m_r + 1) + \frac{\bar{u}_{\theta 0}}{\bar{u}_{s0}} f_{s0}(m_s + 1) \right] + \frac{\bar{u}_{\theta 0}}{r} + \frac{d\bar{u}_{\theta 0}}{dr} \quad \text{B.24}$$

$$D_{2,3} = \frac{1}{2ch_0} \left[ \frac{1}{\bar{u}_{r0}} f_{r0} \left( (m_r + 1)(\bar{u}_{\theta 0} - r)^2 + \bar{u}_{r0}^2 \right) + \frac{1}{\bar{u}_{s0}} f_{s0} \left( (m_s + 1)\bar{u}_{\theta 0}^2 + \bar{u}_{s0}^2 \right) \right] + \frac{\bar{u}_{R0}}{r} \quad \text{B.25}$$

$$D_{2,4} = \frac{1}{2c\bar{\rho}_0 h_0} [\bar{u}_{r0} f_{r0} m_r (\bar{u}_{\theta 0} - r) + \bar{u}_{s0} f_{s0} \bar{u}_{\theta 0} m_s] \quad \text{B.26}$$

$$D_{3,1} = \frac{\bar{u}_{R0}^2}{2ch_0} \left[ \frac{1}{\bar{u}_{r0}} f_{r0} \left( m_r + 1 + \left( \frac{\bar{u}_{r0}}{\bar{u}_{R0}} \right)^2 \right) + \frac{1}{\bar{u}_{s0}} f_{s0} \left( m_s + 1 + \left( \frac{\bar{u}_{s0}}{\bar{u}_{R0}} \right)^2 \right) \right] + \frac{d\bar{u}_{R0}}{dr} \quad \text{B.27}$$

$$D_{3,3} = \frac{\bar{u}_{R0}}{2ch_0} \left[ \frac{(\bar{u}_{\theta 0} - r)}{\bar{u}_{r0}} f_{r0}(m_r + 1) + \frac{\bar{u}_{\theta 0}}{\bar{u}_{s0}} f_{s0}(m_s + 1) \right] + 2 \frac{\bar{u}_{\theta 0}}{r} \quad \text{B.28}$$



$$D_{3,4} = -P_c \frac{1}{\bar{\rho}_0^2} \frac{\partial p_0}{\partial r} + \frac{\bar{u}_{R0}}{2c\bar{\rho}_0 h_0} [\bar{u}_{r0} f_{r0} m_r + \bar{u}_{s0} f_{s0} m_s] \quad \text{B.29}$$

$$D_{4,1} = P_c \frac{1}{Z_c(\gamma - 1)} \frac{\partial p_0}{\partial r} - P_c \frac{p_0}{\bar{\rho}_0} \left( \frac{1}{Z_c(\gamma - 1)} + 1 \right) \frac{d\bar{\rho}_0}{dr} - \frac{\bar{\rho}_0 \bar{u}_{R0}}{2ch_0} [\bar{u}_{r0} f_{r0} (m_r + 3) + \bar{u}_{s0} f_{s0} (m_s + 3)] \quad \text{B.30}$$

$$D_{4,2} = -P_c \frac{1}{\bar{\rho}_0} \left( \frac{1}{Z_c(\gamma - 1)} + 1 \right) \frac{d\bar{\rho}_0}{dr} \quad \text{B.31}$$

$$D_{4,3} = -\frac{\bar{\rho}_0}{2ch_0} [\bar{u}_{r0} f_{r0} (\bar{u}_{\theta 0} - r) (m_r + 3) + \bar{u}_{s0} f_{s0} \bar{u}_{\theta 0} (m_s + 3)] \quad \text{B.32}$$

$$D_{4,4} = P_c \frac{p_0}{\bar{\rho}_0^2} \bar{u}_{R0} \left( \frac{1}{Z_c(\gamma - 1)} + 1 \right) \frac{d\bar{\rho}_0}{dr} - \frac{1}{2ch_0} [\bar{u}_{r0}^3 f_{r0} (m_r + 1) + \bar{u}_{s0}^3 f_{s0} (m_s + 1)] \quad \text{B.33}$$

Vector E, column vector of 4 rows:

$$E_1 = \bar{\rho}_0 \quad \text{B.34}$$

$$E_4 = -P_c \frac{p_0}{h_0} \quad \text{B.35}$$

Vector F, column vector of 4 rows:

$$F_1 = \bar{\rho}_0 \bar{u}_{R0} \quad \text{B.36}$$

Vector G, column vector of 4 rows:

$$G_1 = \frac{\bar{\rho}_0 \bar{u}_{\theta 0}}{r} \quad \text{B.37}$$

Vector L, column vector of 4 rows:

$$L_1 = \frac{\bar{u}_{R0} \bar{\rho}_0}{r} + \bar{u}_{R0} \frac{d\bar{\rho}_0}{dr} + \bar{\rho}_0 \frac{d\bar{u}_{R0}}{dr} \quad \text{B.38}$$

$$L_2 = \frac{1}{2ch_0^2} [\bar{u}_{r0} f_{r0} (m_r - 1) (\bar{u}_{\theta 0} - r) + \bar{u}_{s0} f_{s0} \bar{u}_{\theta 0} (m_s - 1)] \quad \text{B.39}$$

$$L_3 = \frac{\bar{u}_{R0}}{2ch_0^2} [\bar{u}_{r0} f_{r0} (m_r - 1) + \bar{u}_{s0} f_{s0} (m_s - 1)] \quad \text{B.40}$$

$$L_4 = -\frac{\bar{\rho}_0}{2ch_0^2} [\bar{u}_{r_0}{}^3 f_{r_0}(m_r - 1) + \bar{u}_{s_0}{}^3 f_{s_0}(m_s - 1)] \quad \text{B.41}$$

## Appendix C

Matrix M, as a 4x4 matrix:

$$M_{1,1} = \bar{\rho}_0 h_0 \quad \text{C.01}$$

$$M_{1,4} = h_0 \bar{u}_{R0} \quad \text{C.02}$$

$$M_{2,3} = \bar{u}_{R0} \quad \text{C.03}$$

$$M_{3,1} = \bar{u}_{R0} \quad \text{C.04}$$

$$M_{3,2} = P_c \frac{1}{\bar{\rho}_0} \quad \text{C.05}$$

$$M_{4,2} = P_c \frac{1}{Z_c(\gamma - 1)} \bar{u}_{R0} \quad \text{C.06}$$

$$M_{4,4} = -P_c \frac{p_0}{\bar{\rho}_0} \left( \frac{1}{Z_c(\gamma - 1)} + 1 \right) \bar{u}_{R0} \quad \text{C.07}$$

Matrix N, as a 4x4 matrix:

$$N_{1,1} = \frac{\bar{\rho}_0 h_0}{r} + \bar{\rho}_0 \frac{dh_0}{dr} + h_0 \frac{d\bar{\rho}_0}{dr} \quad \text{C.08}$$

$$N_{1,4} = \frac{\bar{u}_{R0} h_0}{r} + \bar{u}_{R0} \frac{dh_0}{dr} + h_0 \frac{d\bar{u}_{R0}}{dr} + f j (h_0 + h_d) \quad \text{C.09}$$

$$N_{2,1} = \frac{\bar{u}_{R0}}{2ch_0} \left[ \frac{(\bar{u}_{\theta 0} - r)}{\bar{u}_{r0}} f_{r0} (m_r + 1) + \frac{\bar{u}_{\theta 0}}{\bar{u}_{s0}} f_{s0} (m_s + 1) \right] + \frac{\bar{u}_{\theta 0}}{r} + \frac{d\bar{u}_{\theta 0}}{dr} \quad \text{C.10}$$

$$N_{2,3} = \frac{1}{2ch_0} \left[ \frac{1}{\bar{u}_{r0}} f_{r0} \left( (m_r + 1)(\bar{u}_{\theta 0} - r)^2 + \bar{u}_{r0}^2 \right) + \frac{1}{\bar{u}_{s0}} f_{s0} \left( (m_s + 1)\bar{u}_{\theta 0}^2 + \bar{u}_{s0}^2 \right) \right] + \frac{\bar{u}_{R0}}{r} + f j \quad \text{C.11}$$

$$N_{2,4} = \frac{1}{2c\bar{\rho}_0 h_0} [\bar{u}_{r0} f_{r0} m_r (\bar{u}_{\theta 0} - r) + \bar{u}_{s0} f_{s0} \bar{u}_{\theta 0} m_s] \quad \text{C.12}$$

$$N_{3,1} = \frac{\bar{u}_{R0}^2}{2ch_0} \left[ \frac{1}{\bar{u}_{r0}} f_{r0} \left( m_r + 1 + \left( \frac{\bar{u}_{r0}}{\bar{u}_{R0}} \right)^2 \right) + \frac{1}{\bar{u}_{s0}} f_{s0} \left( m_s + 1 + \left( \frac{\bar{u}_{s0}}{\bar{u}_{R0}} \right)^2 \right) \right] + \frac{d\bar{u}_{R0}}{dr} + fj \quad C.13$$

$$N_{3,3} = \frac{\bar{u}_{R0}}{2ch_0} \left[ \frac{(\bar{u}_{\theta 0} - r)}{\bar{u}_{r0}} f_{r0} (m_r + 1) + \frac{\bar{u}_{\theta 0}}{\bar{u}_{s0}} f_{s0} (m_s + 1) \right] + 2 \frac{\bar{u}_{\theta 0}}{r} \quad C.14$$

$$N_{3,4} = -P_c \frac{1}{\bar{\rho}_0^2} \frac{\partial p_0}{\partial r} + \frac{\bar{u}_{R0}}{2c\bar{\rho}_0 h_0} [\bar{u}_{r0} f_{r0} m_r + \bar{u}_{s0} f_{s0} m_s] \quad C.15$$

$$N_{4,1} = P_c \frac{1}{Z_c(\gamma - 1)} \frac{\partial p_0}{\partial r} - P_c \frac{p_0}{\bar{\rho}_0} \left( \frac{1}{Z_c(\gamma - 1)} + 1 \right) \frac{d\bar{\rho}_0}{dr} - \frac{\bar{\rho}_0 \bar{u}_{R0}}{2ch_0} [\bar{u}_{r0} f_{r0} (m_r + 3) + \bar{u}_{s0} f_{s0} (m_s + 3)] \\ + fj \frac{h_d}{h_0} \bar{\rho}_0 \bar{u}_{R0} \quad C.16$$

$$N_{4,2} = -P_c \frac{1}{\bar{\rho}_0} \left( \frac{1}{Z_c(\gamma - 1)} + 1 \right) \frac{d\bar{\rho}_0}{dr} + fj P_c \frac{1}{Z_c(\gamma - 1)} \left( 1 + \frac{h_d}{h_0} \right) \quad C.17$$

$$N_{4,3} = -\frac{\bar{\rho}_0}{2ch_0} [\bar{u}_{r0} f_{r0} (\bar{u}_{\theta 0} - r) (m_r + 3) + \bar{u}_{s0} f_{s0} \bar{u}_{\theta 0} (m_s + 3)] + fj \frac{h_d}{h_0} \bar{\rho}_0 \bar{u}_{\theta 0} \quad C.18$$

$$N_{4,4} = P_c \frac{p_0}{\bar{\rho}_0^2} \bar{u}_{R0} \left( \frac{1}{Z_c(\gamma - 1)} + 1 \right) \frac{d\bar{\rho}_0}{dr} - \frac{1}{2ch_0} [\bar{u}_{r0}^3 f_{r0} (m_r + 1) + \bar{u}_{s0}^3 f_{s0} (m_s + 1)] \\ - fj P_c \frac{p_0}{\bar{\rho}_0} \left( \frac{1}{Z_c(\gamma - 1)} + 1 \right) \left( 1 + \frac{h_d}{h_0} \right) \quad C.19$$

Vector  $\vec{g}$ , column vector of 4 rows:

$$g_1 = \frac{\bar{u}_{R0} \bar{\rho}_0}{r} + \bar{u}_{R0} \frac{d\bar{\rho}_0}{dr} + \bar{\rho}_0 \frac{d\bar{u}_{R0}}{dr} + fj \bar{\rho}_0 \quad C.20$$

$$g_2 = \frac{1}{2ch_0^2} [\bar{u}_{r0} f_{r0} (m_r - 1) (\bar{u}_{\theta 0} - r) + \bar{u}_{s0} f_{s0} \bar{u}_{\theta 0} (m_s - 1)] \quad C.21$$

$$g_3 = \frac{\bar{u}_{R0}}{2ch_0^2} [\bar{u}_{r0} f_{r0} (m_r - 1) + \bar{u}_{s0} f_{s0} (m_s - 1)] \quad C.22$$

$$g_4 = -\frac{\bar{\rho}_0}{2ch_0^2} [\bar{u}_{r0}^3 f_{r0} (m_r - 1) + \bar{u}_{s0}^3 f_{s0} (m_s - 1)] - P_c \frac{p_0}{h_0} fj \quad C.23$$

## Appendix D

This appendix shows the different cases that were taken into account when analyzing the different cases for each case with different settings than the base cases A and B.

### Case 1:

Parameter	Value	Unit
Inlet Diameter	300	mm
Outlet Diameter	560	mm
Inlet Clearance	0,6	mm
Outlet Clearance	0,3	mm
Inlet Pressure	60	bara
Outlet Pressure	45	bara
Inlet Temperature	120	C
Speed	10000	rpm

Base case: A

Offset: 0%

**Case 2:**

Parameter	Value	Unit
Inlet Diameter	300	mm
Outlet Diameter	560	mm
Inlet Clearance	0,6	mm
Outlet Clearance	0,3	mm
Inlet Pressure	60	bara
Outlet Pressure	45	bara
Inlet Temperature	120	C
Speed	10000	rpm

Base case: A

Offset: 50%

**Case 3:**

Parameter	Value	Unit
Inlet Diameter	300	mm
Outlet Diameter	560	mm
Inlet Clearance	0,6	mm
Outlet Clearance	0,3	mm
Inlet Pressure	30	bara
Outlet Pressure	15	bara
Inlet Temperature	120	C
Speed	10000	rpm

Base case: A

Offset: 50%

**Case 4:**

Parameter	Value	Unit
Inlet Diameter	560	mm
Outlet Diameter	300	mm
Inlet Clearance	0,3	mm
Outlet Clearance	0,3	mm
Inlet Pressure	120	bara
Outlet Pressure	60	bara
Inlet Temperature	120	C
Speed	10000	rpm

Base case: B

Offset: 0%

**Case 5:**

Parameter	Value	Unit
Inlet Diameter	300	mm
Outlet Diameter	560	mm
Inlet Clearance	0,6	mm
Outlet Clearance	0,3	mm
Inlet Pressure	120	bara
Outlet Pressure	60	bara
Inlet Temperature	120	C
Speed	10000	rpm

Base case: A

Offset: 0%

Comment: It only features one side of the bearing, the other side is assumed of presenting constant pressure of 60 bara.

**Case 6:**

Parameter	Value	Unit
Inlet Diameter	300	mm
Outlet Diameter	450	mm
Inlet Clearance	0,6	mm
Outlet Clearance	0,3	mm
Inlet Pressure	120	bara
Outlet Pressure	60	bara
Inlet Temperature	120	C
Speed	10000	rpm

Base case: A

Offset: 50%

**Case 7:**

Parameter	Value	Unit
Inlet Diameter	300	mm
Outlet Diameter	560	mm
Inlet Clearance	0,4	mm
Outlet Clearance	0,2	mm
Inlet Pressure	120	bara
Outlet Pressure	60	bara
Inlet Temperature	120	C
Speed	10000	rpm

Base case: A

Offset: 0%



**Case 8:**

Parameter	Value	Unit
Inlet Diameter	300	mm
Outlet Diameter	560	mm
Inlet Clearance	0,4	mm
Outlet Clearance	0,2	mm
Inlet Pressure	120	bara
Outlet Pressure	60	bara
Inlet Temperature	120	C
Speed	10000	rpm

Base case: A

Offset: 50%

**Case 9:**

Parameter	Value	Unit
Inlet Diameter	300	mm
Outlet Diameter	560	mm
Inlet Clearance	0,6	mm
Outlet Clearance	0,3	mm
Inlet Pressure	120	bara
Outlet Pressure	60	bara
Inlet Temperature	120	C
Speed	6000	rpm

Base case: A

Offset:0%

**Case 10:**

<b>Parameter</b>	<b>Value</b>	<b>Unit</b>
<b>Inlet Diameter</b>	300	mm
<b>Outlet Diameter</b>	560	mm
<b>Inlet Clearance</b>	0,6	mm
<b>Outlet Clearance</b>	0,3	mm
<b>Inlet Pressure</b>	120	bara
<b>Outlet Pressure</b>	60	bara
<b>Inlet Temperature</b>	120	C
<b>Speed</b>	6000	rpm

Base case: A

Offset: 50%

**Case 11:**

<b>Parameter</b>	<b>Value</b>	<b>Unit</b>
<b>Inlet Diameter</b>	560	mm
<b>Outlet Diameter</b>	300	mm
<b>Inlet Clearance</b>	0,6	mm
<b>Outlet Clearance</b>	0,3	mm
<b>Inlet Pressure</b>	120	bara
<b>Outlet Pressure</b>	60	bara
<b>Inlet Temperature</b>	120	C
<b>Speed</b>	6000	rpm

Base case: B

Offset: 0%

**Case 12:**

<b>Parameter</b>	<b>Value</b>	<b>Unit</b>
<b>Inlet Diameter</b>	300	mm
<b>Outlet Diameter</b>	560	mm
<b>Inlet Clearance</b>	0,6	mm
<b>Outlet Clearance</b>	0,3	mm
<b>Inlet Pressure</b>	120	bara
<b>Outlet Pressure</b>	60	bara
<b>Inlet Temperature</b>	120	C
<b>Speed</b>	6000	rpm

Base case: A

Offset: 50%

Comment: Smooth seal.



## Appendix E

### Results for Zeroth Order Equation

#### E.1 Offset cases

Case A: Higher clearance

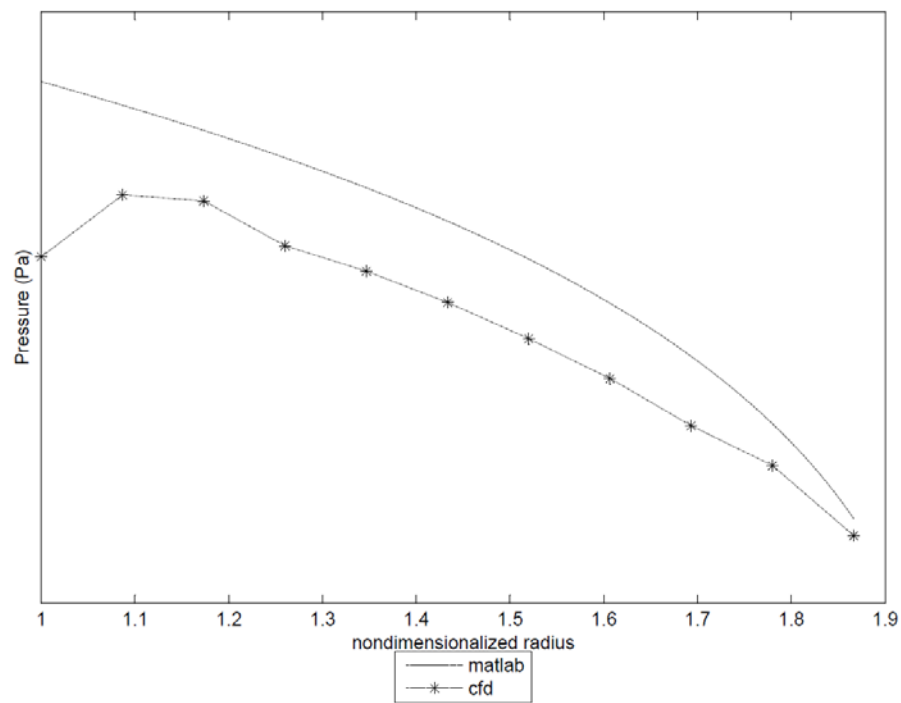


Figure E.01. Pressure of the flow along the radius for case A at the higher clearance side with 11,02% mean percentage error.

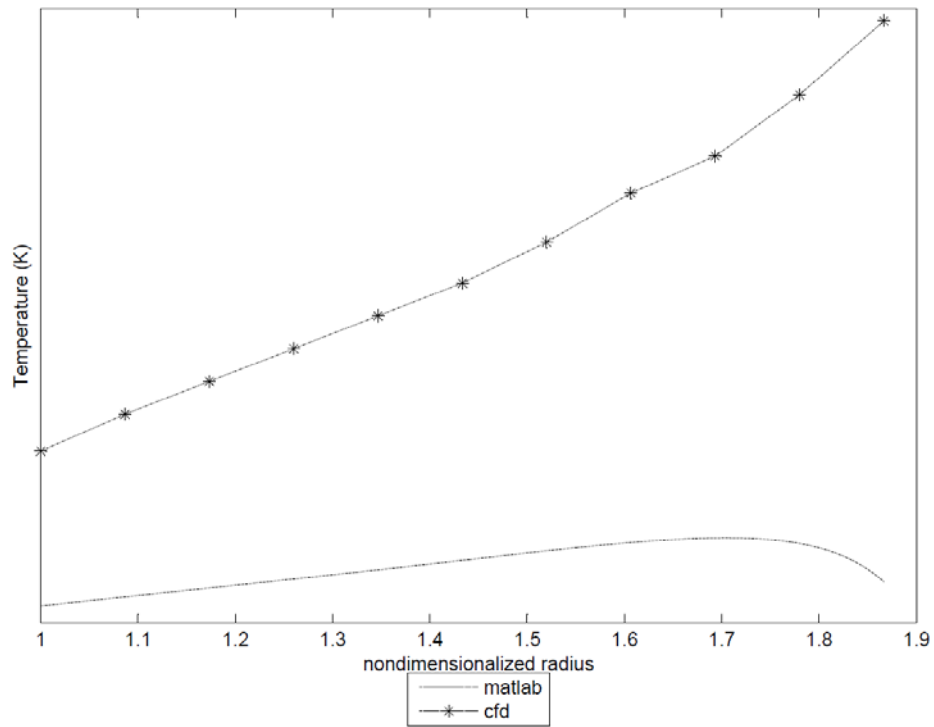


Figure E.02. Temperature of the flow along the radius for case A at the higher clearance side with 5,94% mean percentage error.

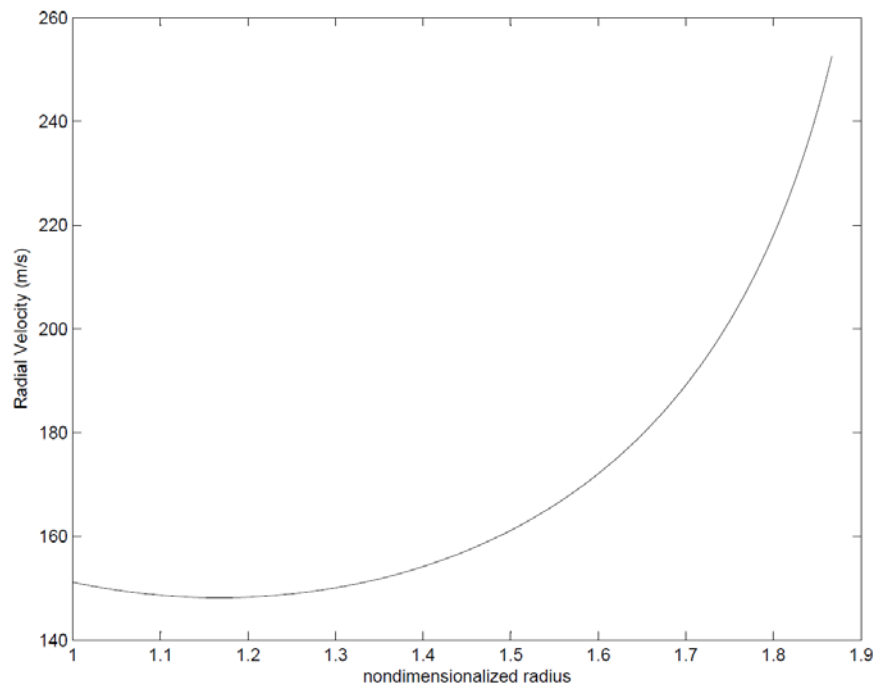


Figure E.03. Radial Velocity of the flow along the radius for case A at the higher clearance side.

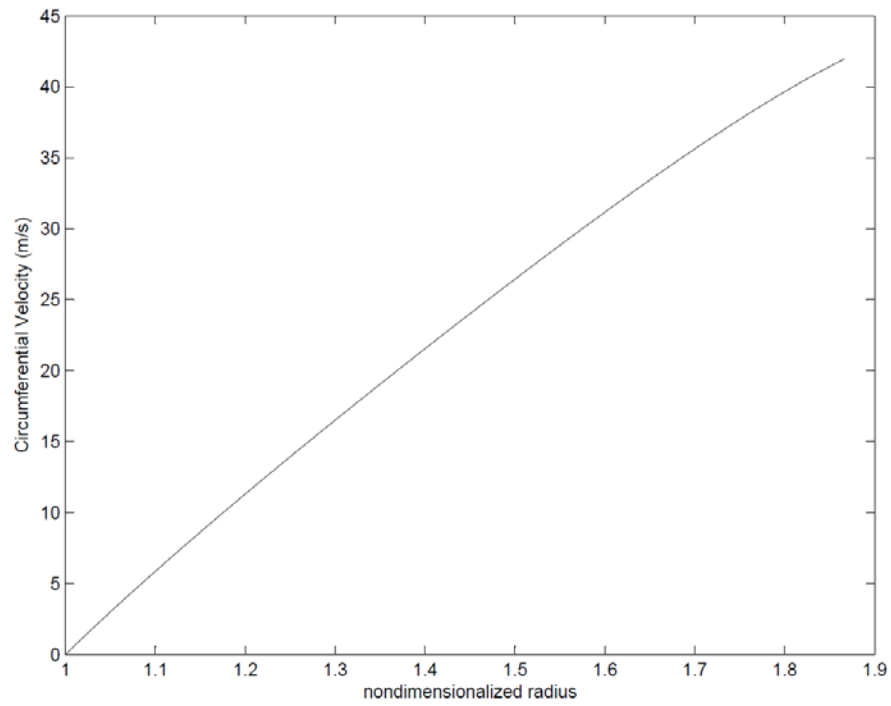


Figure E.04. Circumferential velocity of the flow along the radius for case A at the higher clearance side.

### Case A: Lower Clearance

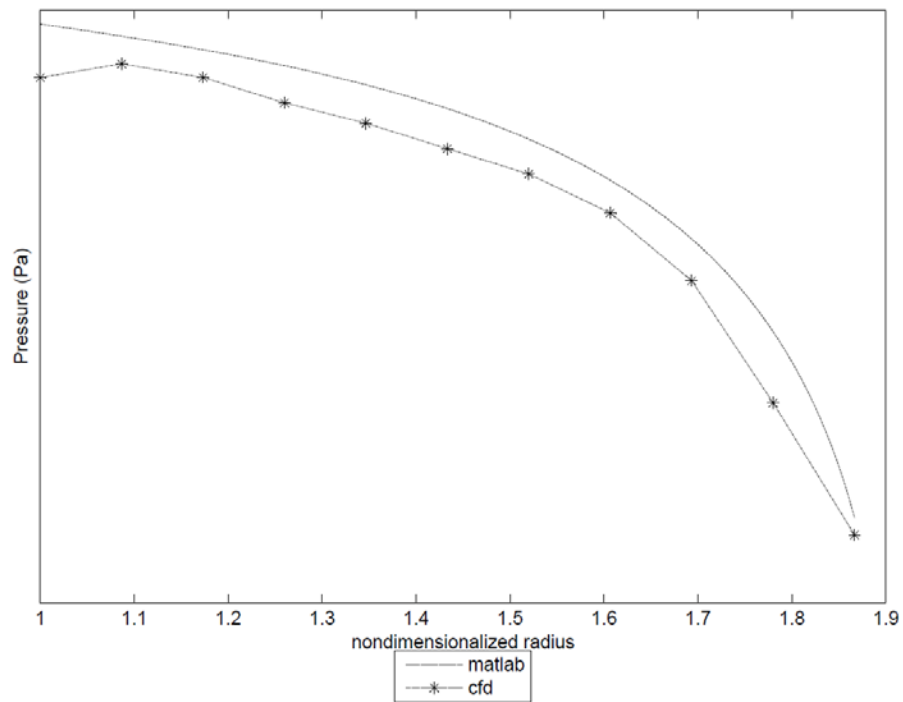


Figure E.05. Pressure of the flow along the radius for case A at the lower clearance side with 4,81% mean percentage error.

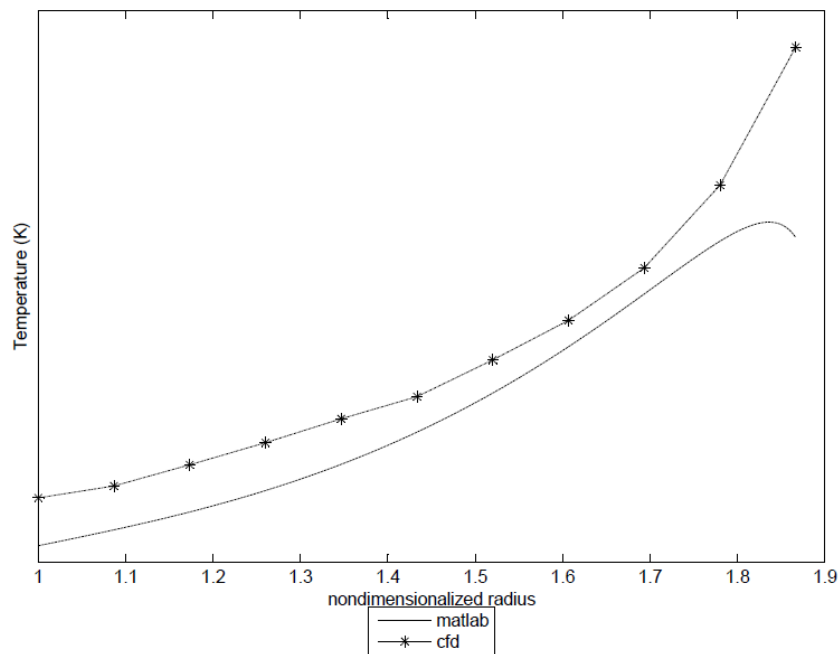


Figure E.06. Temperature of the flow along the radius for case A at the lower clearance side with 1,41% mean percentage error.



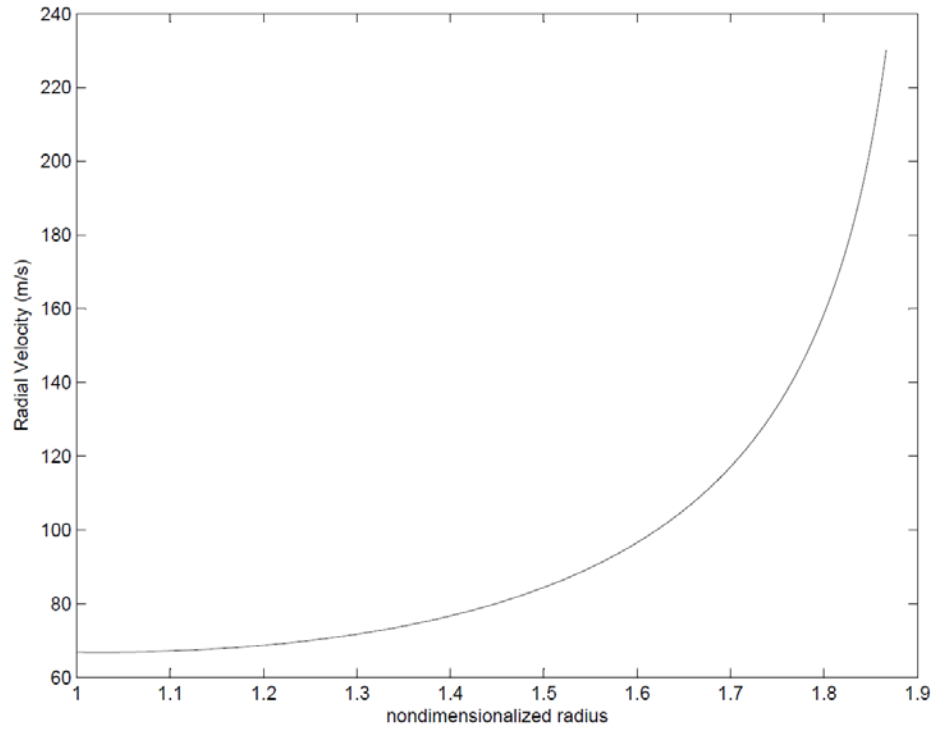


Figure E.07. Radial Velocity of the flow along the radius for case A at the lower clearance side.

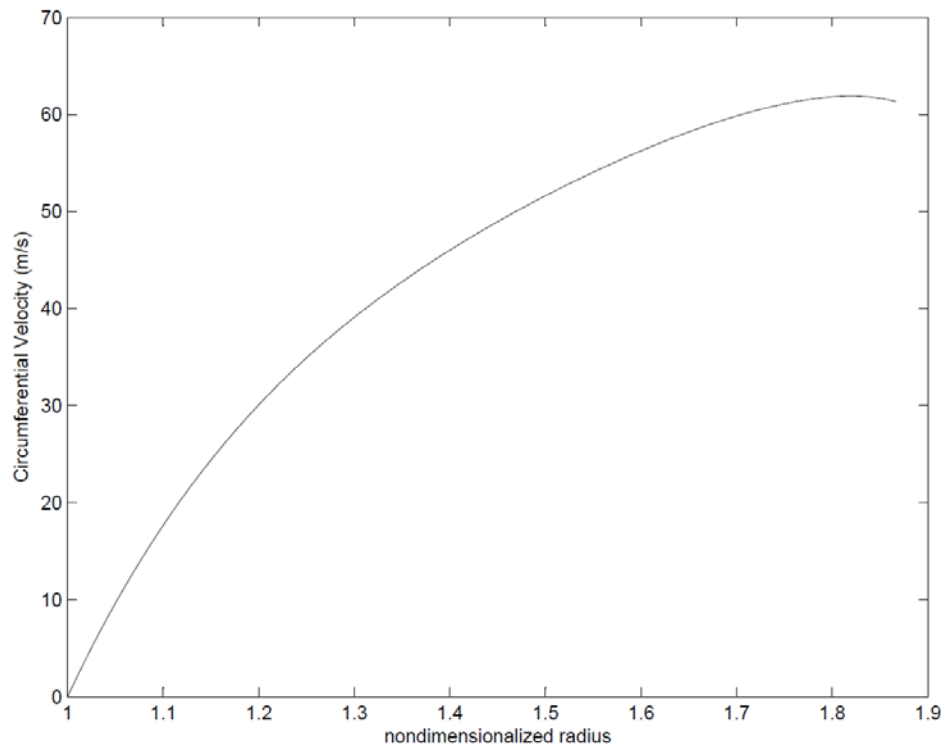


Figure E.08. Circumferential velocity of the flow along the radius for case A at the lower clearance side.

### Case B: Higher Clearance

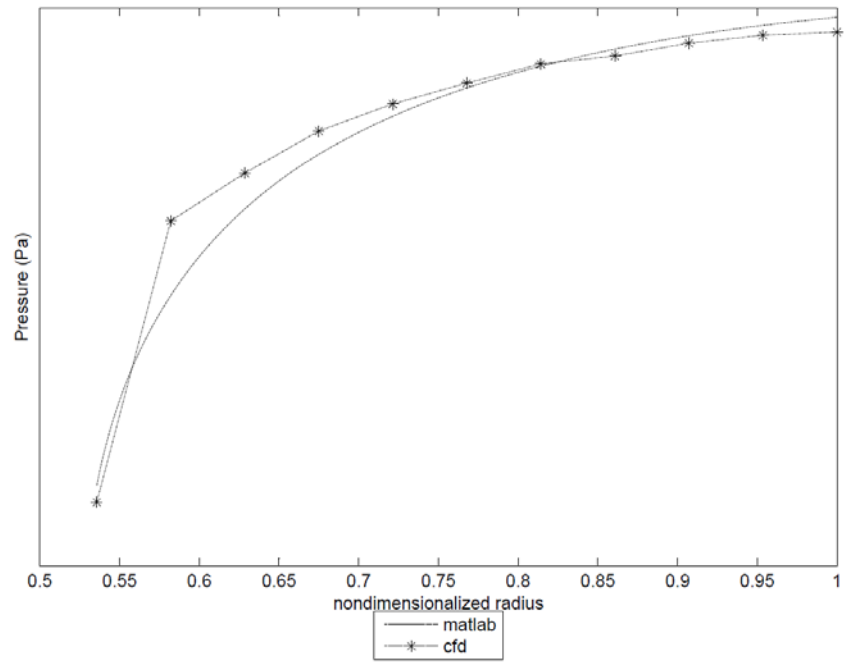


Figure E.9. Pressure of the flow along the radius for case B at the higher clearance side with 2,48% mean percentage error.

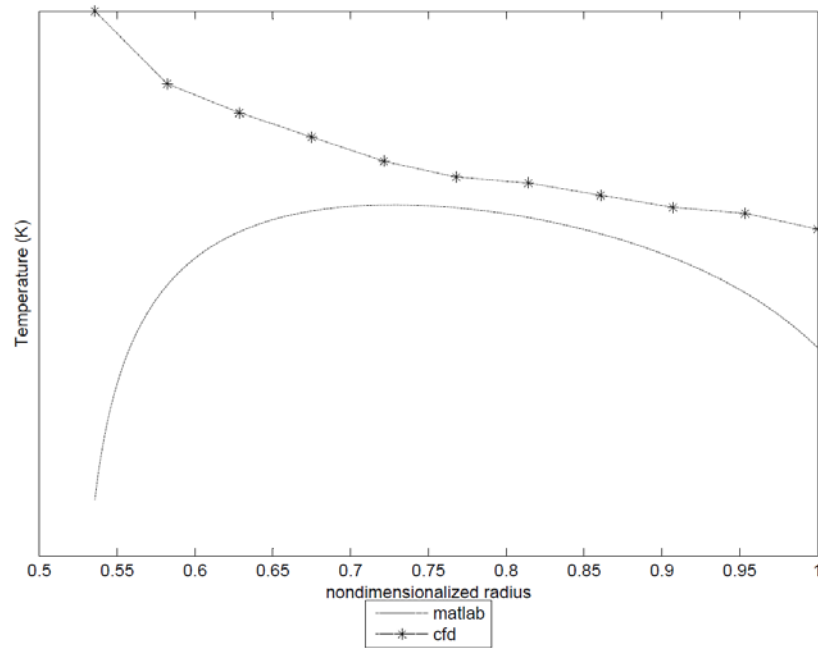


Figure E.10. Temperature of the flow along the radius for case B at the higher clearance side with 2,33% mean percentage error.

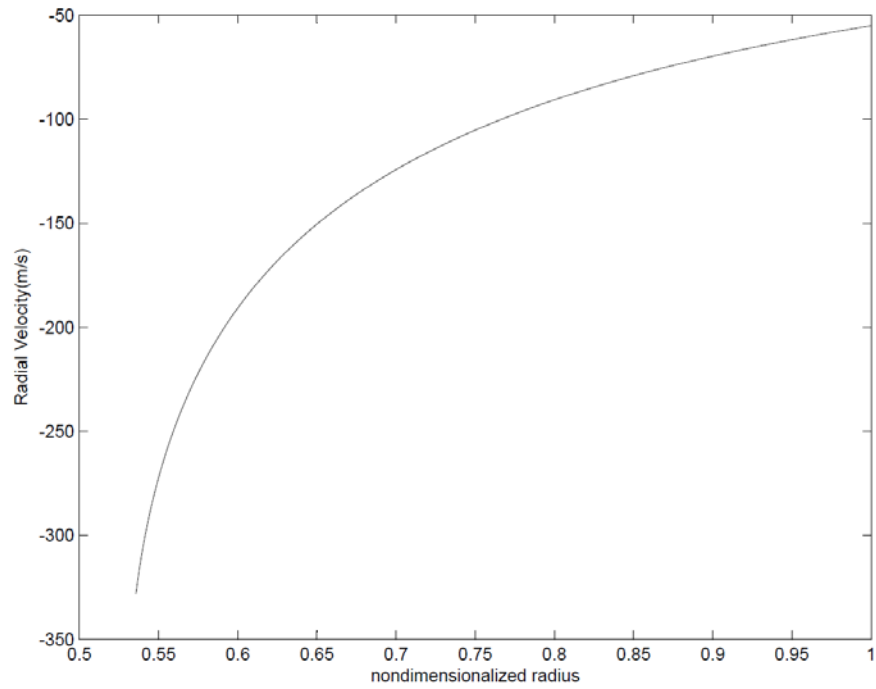


Figure E.11. Radial Velocity of the flow along the radius for case B at the higher clearance side.

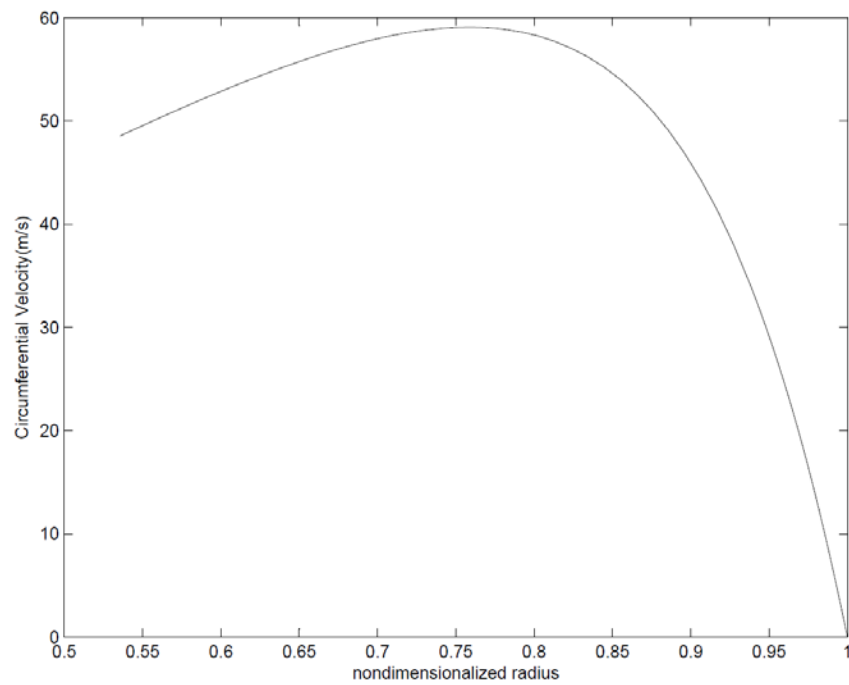


Figure E.12. Circumferential velocity of the flow along the radius for case B at the higher clearance side.

### Case B: Higher Clearance

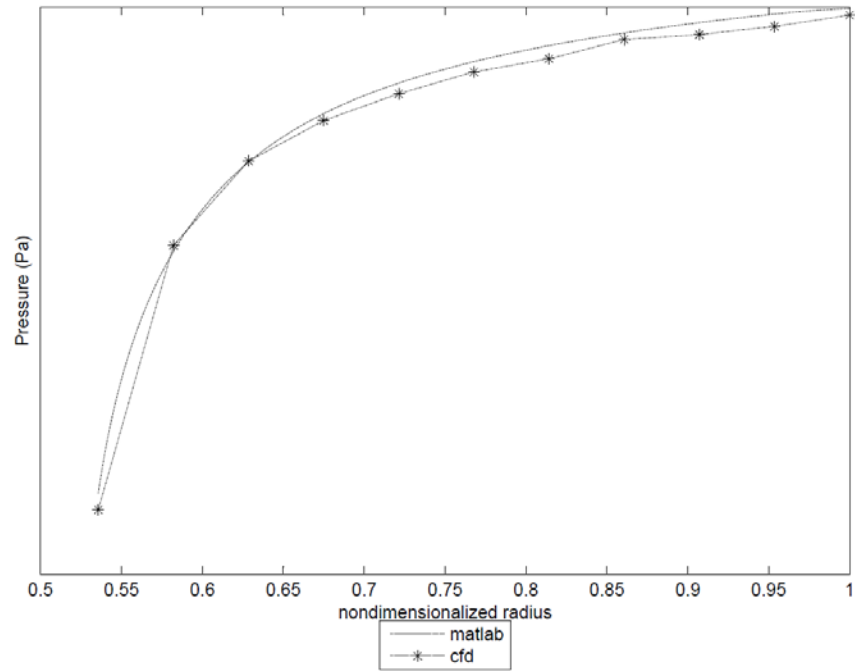


Figure E.13. Pressure of the flow along the radius for case B at the lower clearance side with 1,1763% mean percentage error.

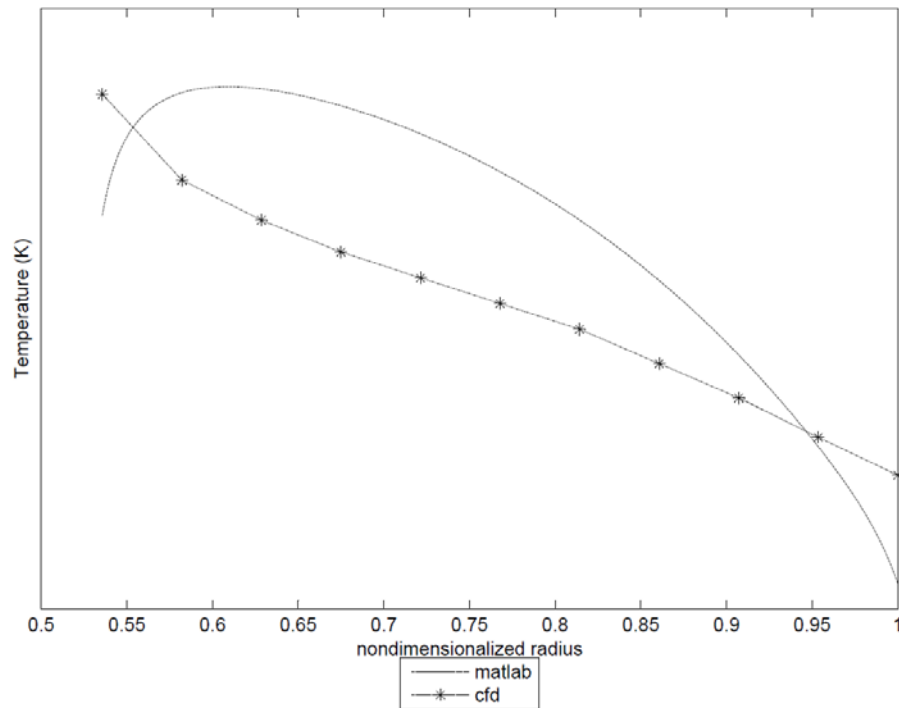


Figure E.14. Temperature of the flow along the radius for case B at the lower clearance side with 2,76% mean percentage error.

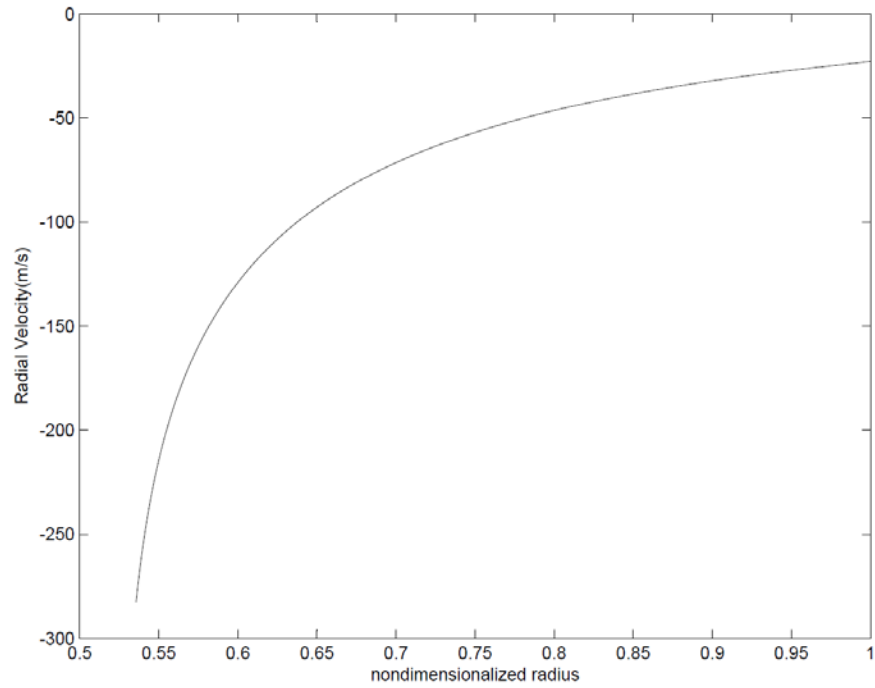


Figure E.15. Radial velocity of the flow along the radius for case B at the lower clearance side.

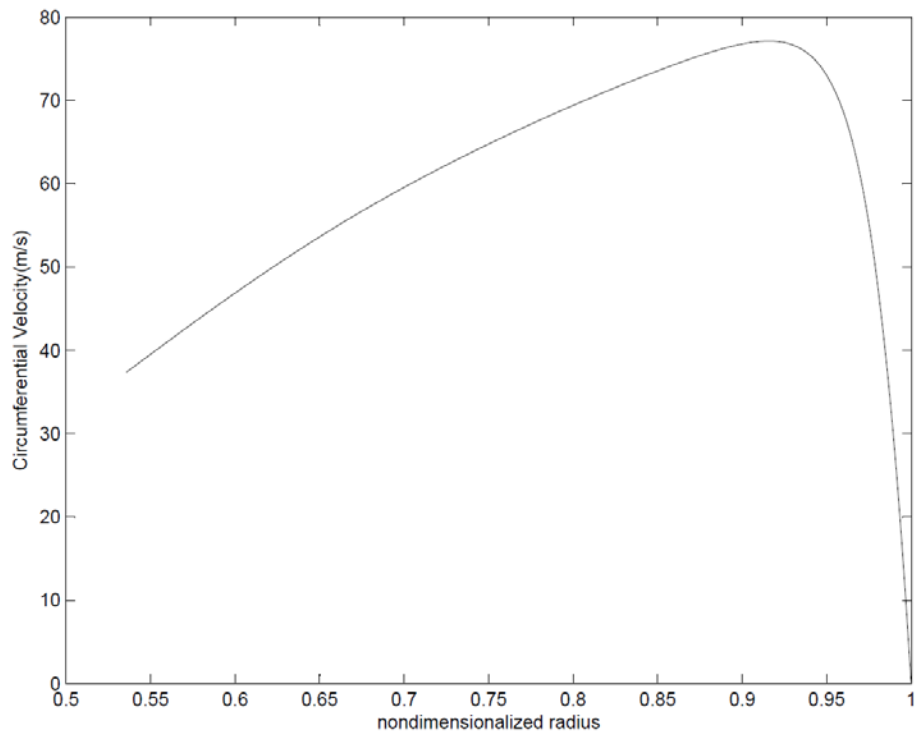


Figure E.16. Circumferential Velocity of the flow along the radius for case B at the lower clearance side.

## E.2 Sensitivity test for case A

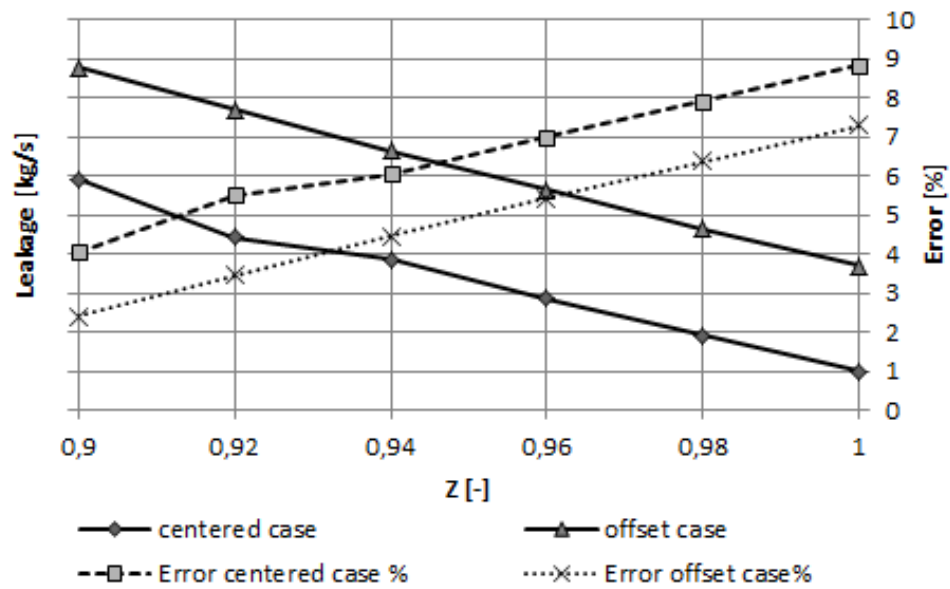


Figure E.17. The leakage variation with compressibility factor for case A for centered and offset position.

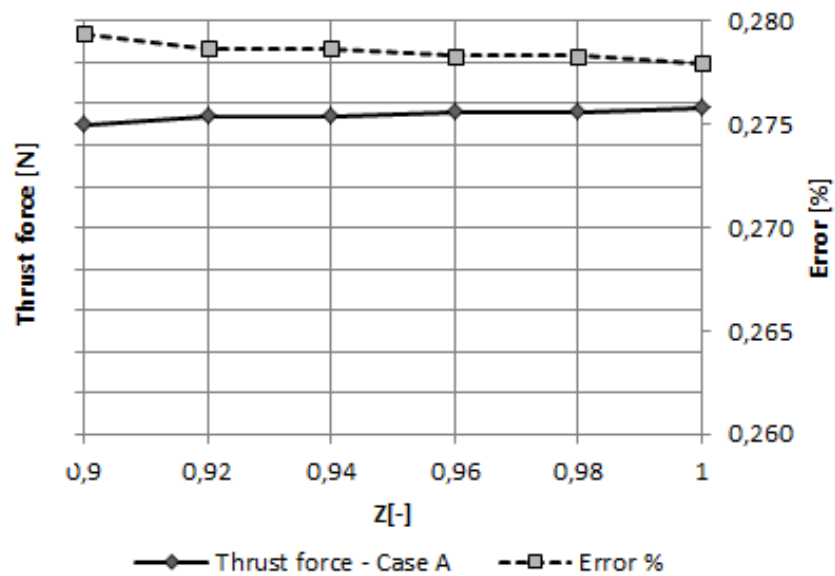


Figure E.18. The thrust force variation with compressibility factor for case A for offset position.

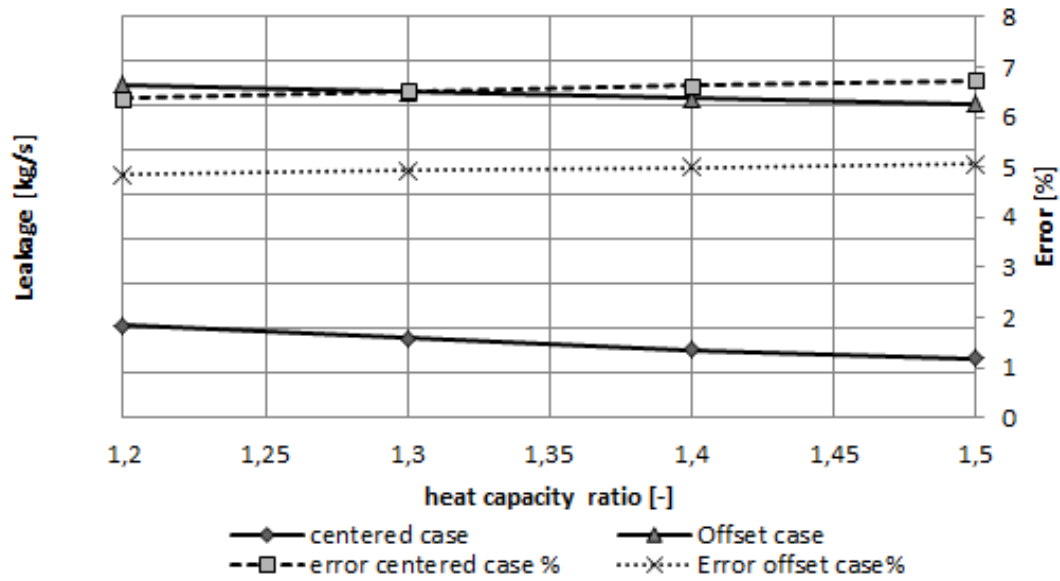


Figure E.19. The leakage variation with heat capacity ratio for case A for centered and offset position.

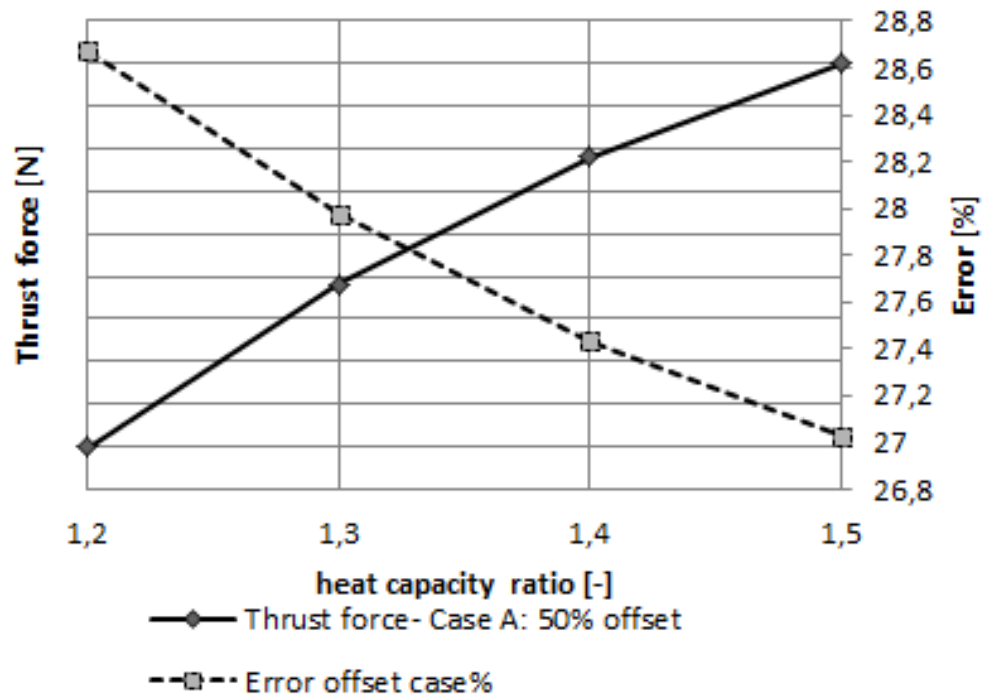


Figure E.20. The thrust force variation with heat capacity ratio for case A for offset position.

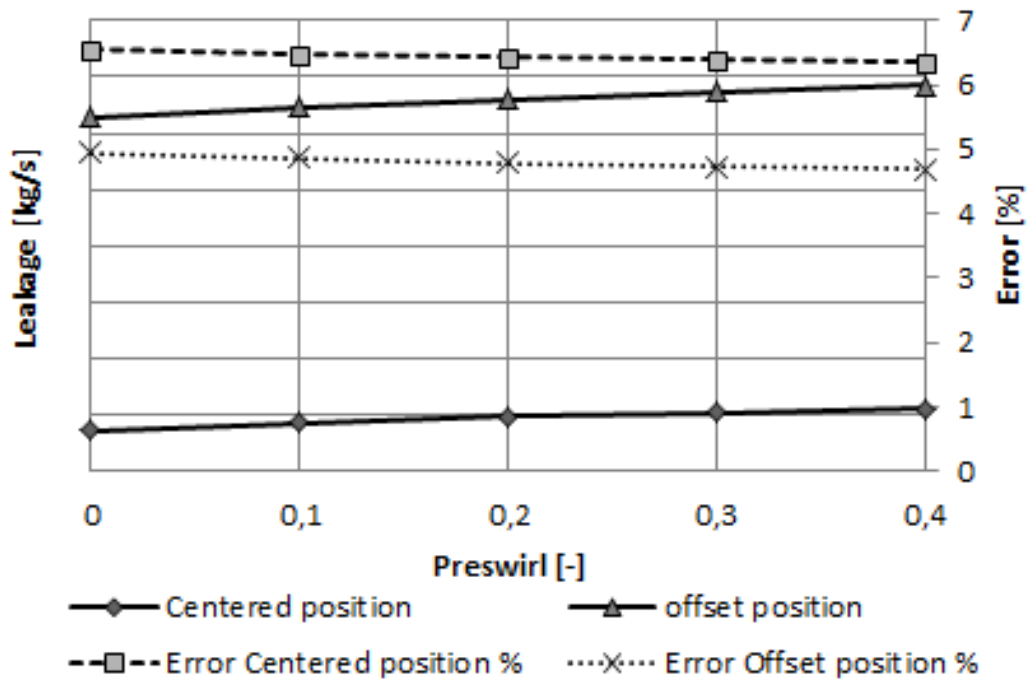


Figure E.21. The leakage variation with preswirl ratio for case A for centered and offset position.

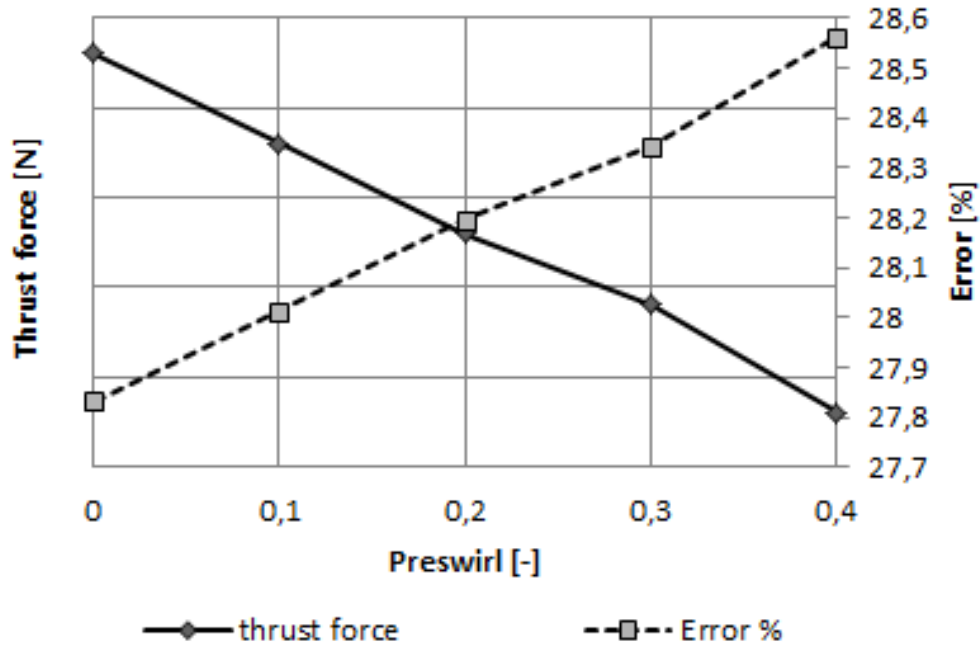


Figure E.22. The thrust force variation with preswirl ratio for case A for offset position.



### E.3 Sensitivity test for case B

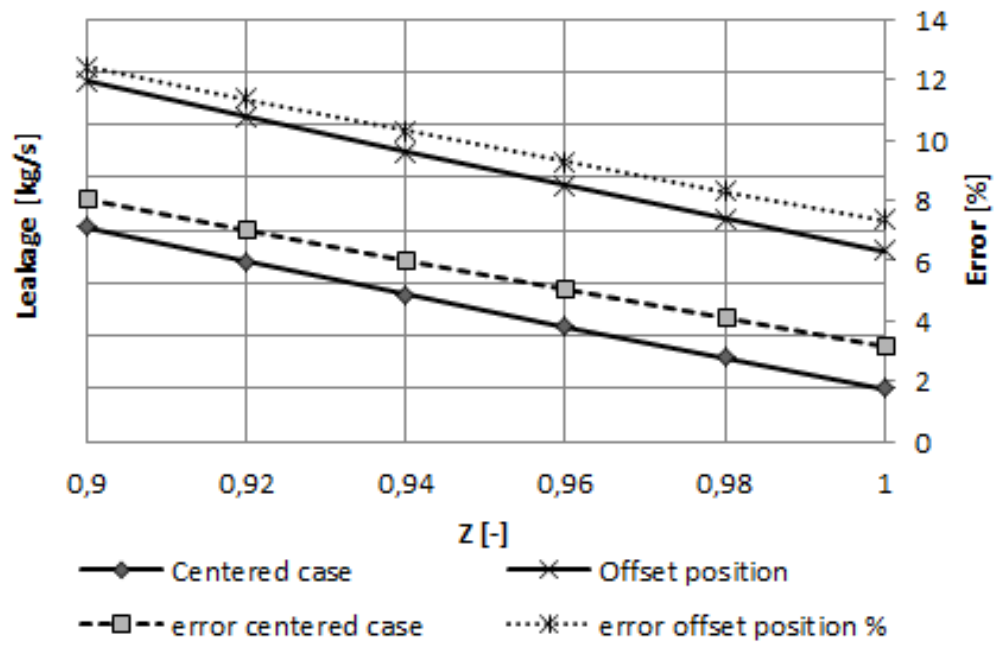


Figure E.23. The leakage variation with compressibility factor for case B for centered and offset position.

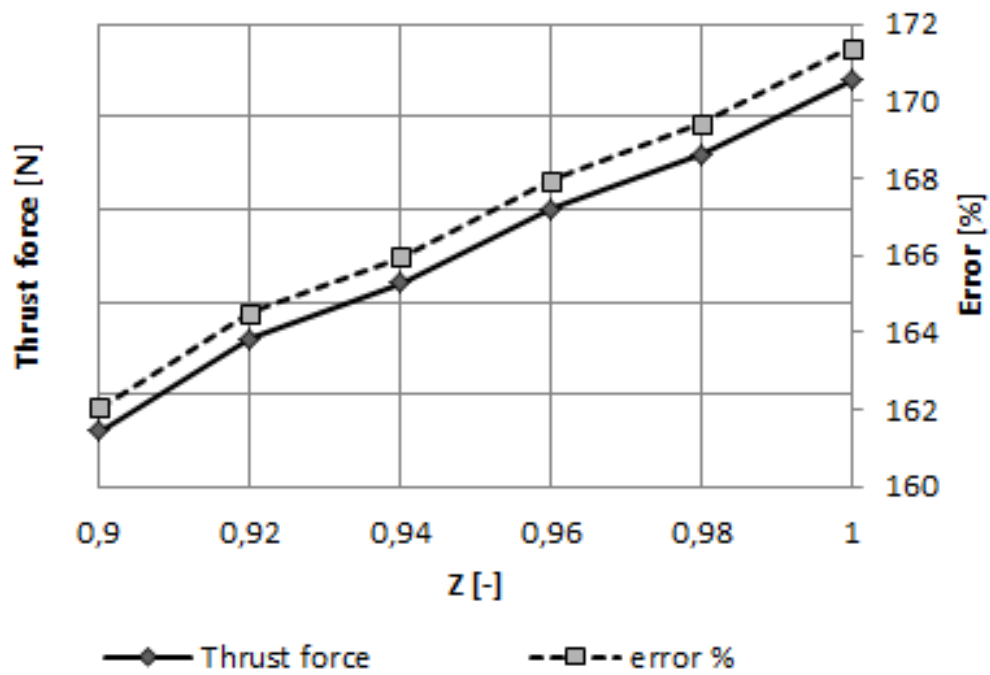


Figure E.24. The Thrust force variation with compressibility factor for case B for offset position.

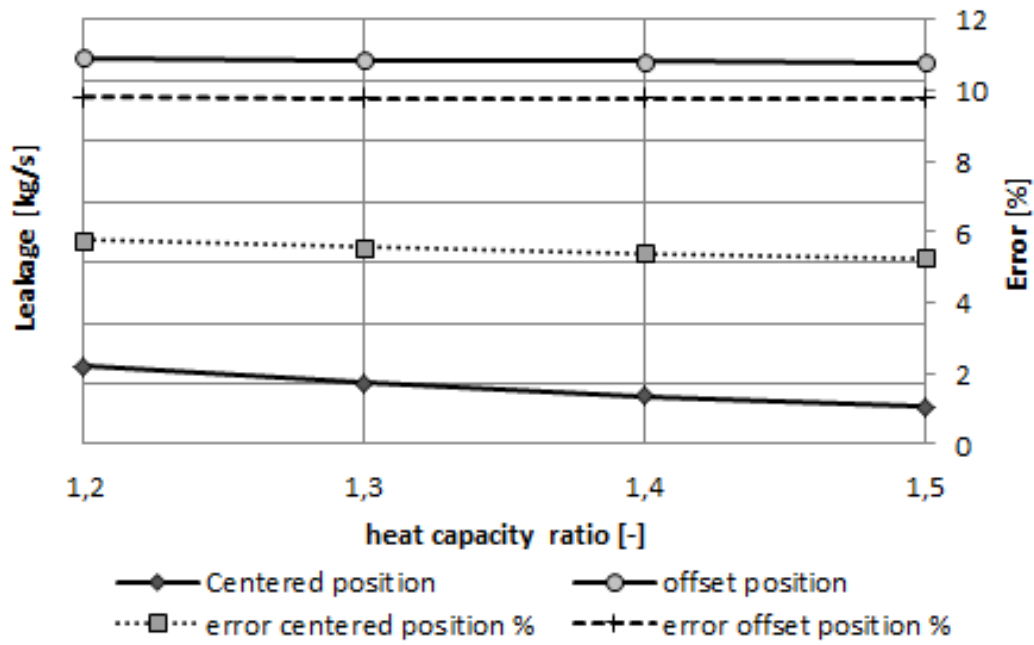


Figure E.25. The leakage variation with heat capacity ratio for case B for centered and offset position.

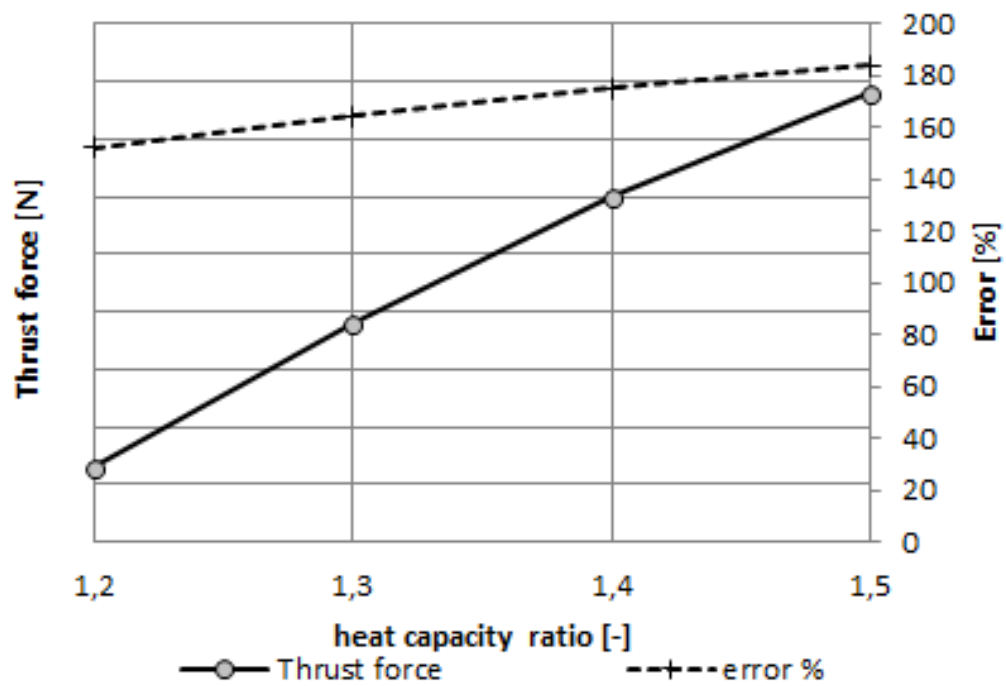


Figure E.26. The Thrust force variation with heat capacity ratio for case B for offset position.

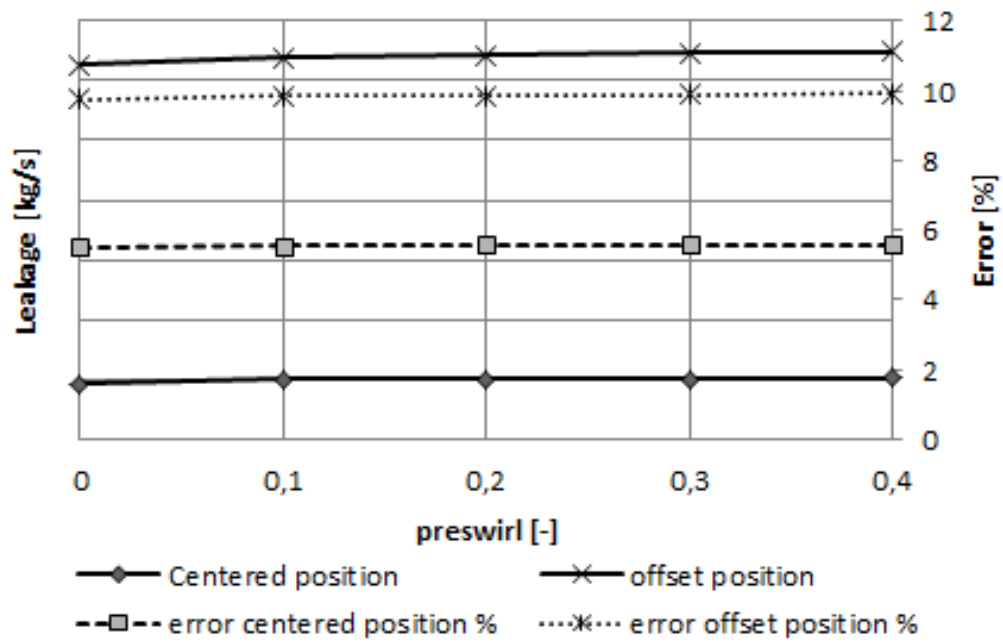


Figure E.27. The leakage variation with preswirl ratio for case B for centered and offset position.

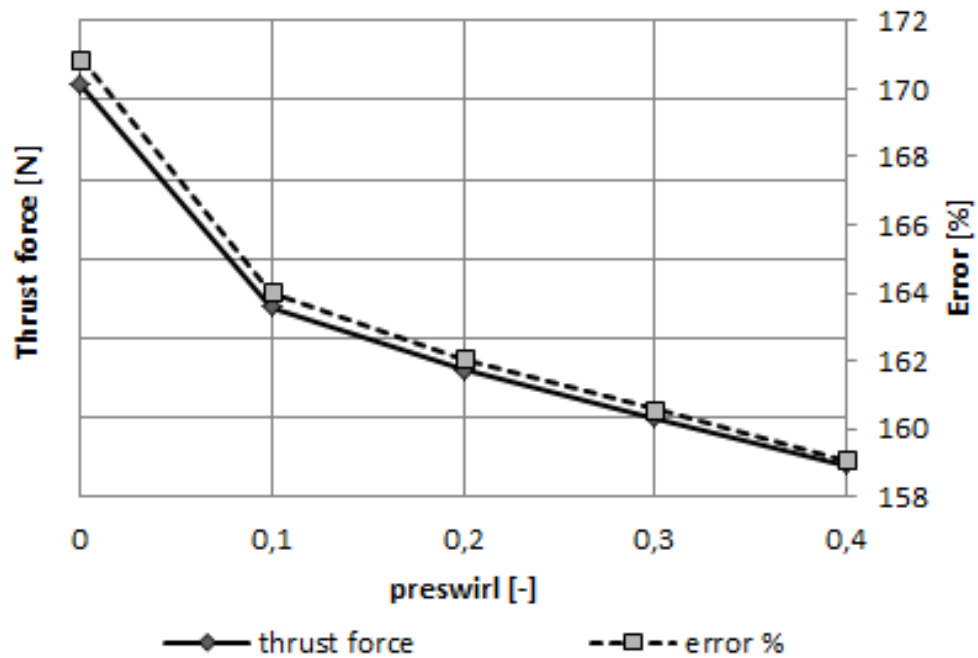


Figure E.28. The Thrust force variation with preswirl ratio for case B for offset position.



Appendix F

Case A: Centered

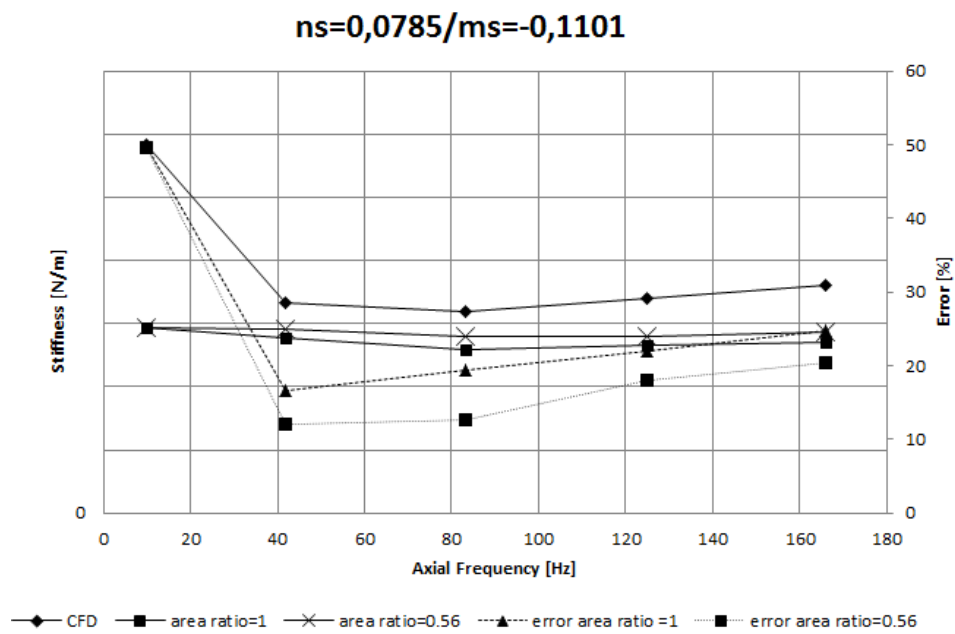


Figure F.01. Stiffness vs axial frequency at  $ns=0,0785/ms=-0,1101$  for case A centered position.

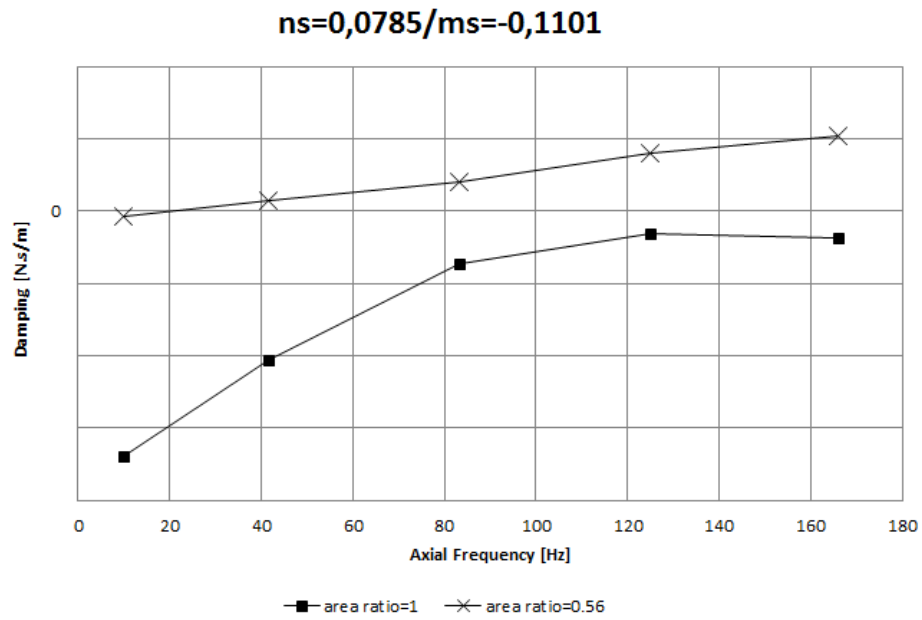


Figure F.02. Damping vs axial frequency at ns=0,0785/ms=-0,1101 for case A centered position.

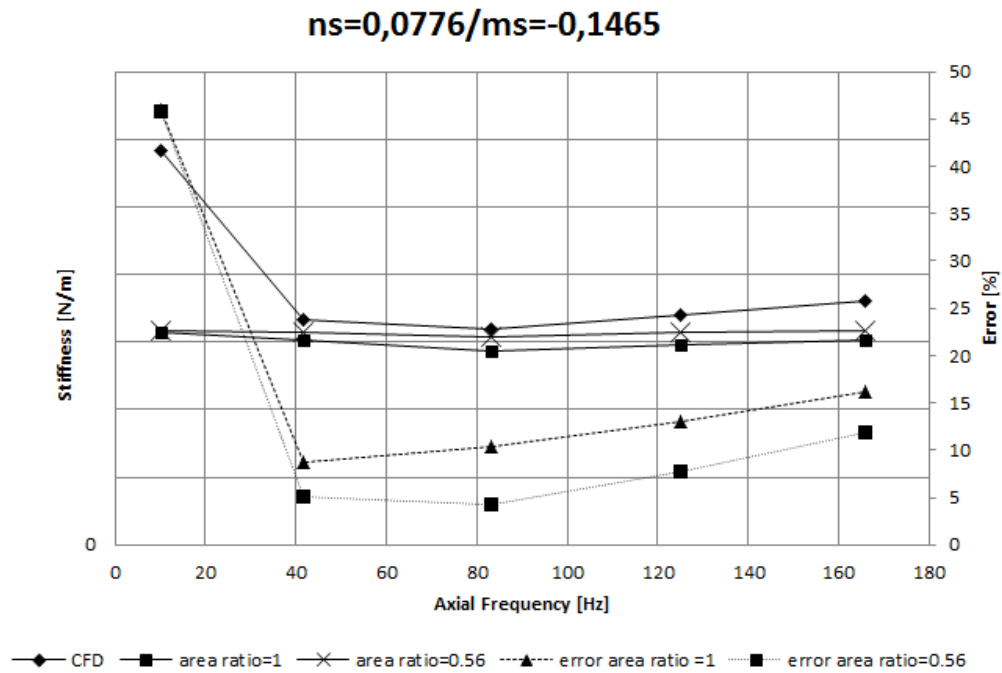


Figure F.03. Stiffness vs axial frequency at ns=0,0776/ms=-0,1465 for case A centered position.

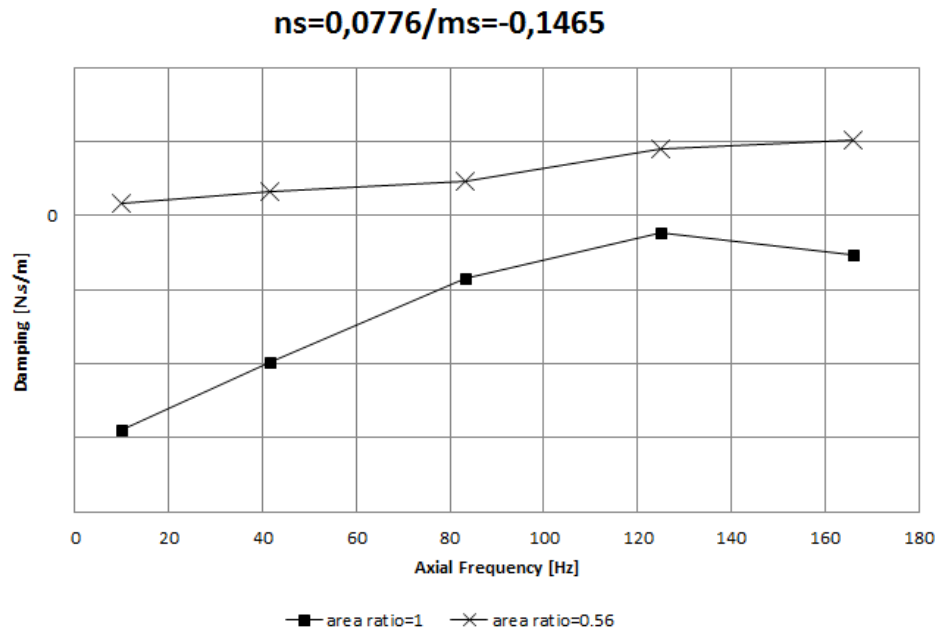


Figure F.04. Damping vs axial frequency at ns=0,0776/ms=-0,1465 for case A centered position.

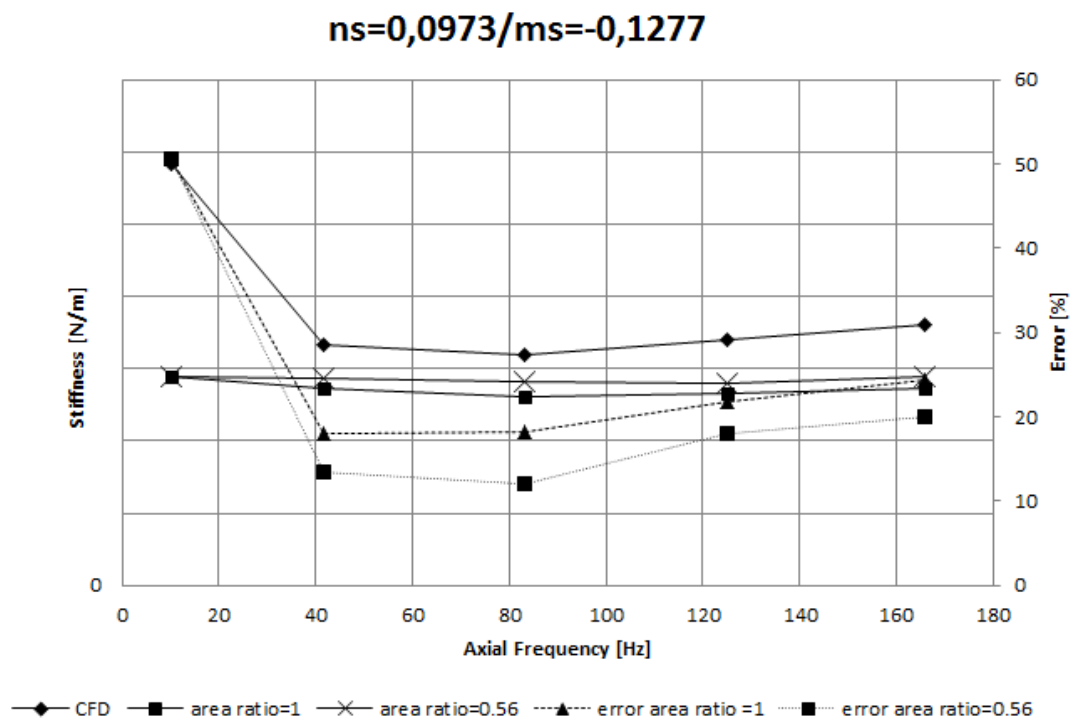


Figure F.05. Stiffness vs axial frequency at ns=0,0973/ms=-0,1277 for case A centered position.

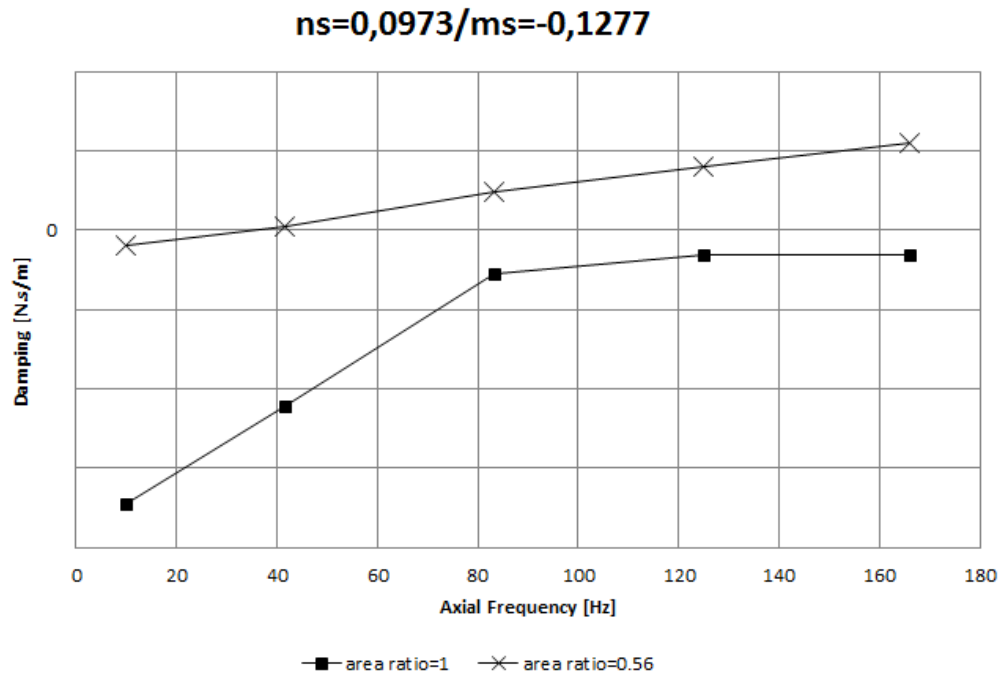


Figure F.06. Damping vs axial frequency at  $ns=0,0973/ms=-0,1277$  for case A centered position.

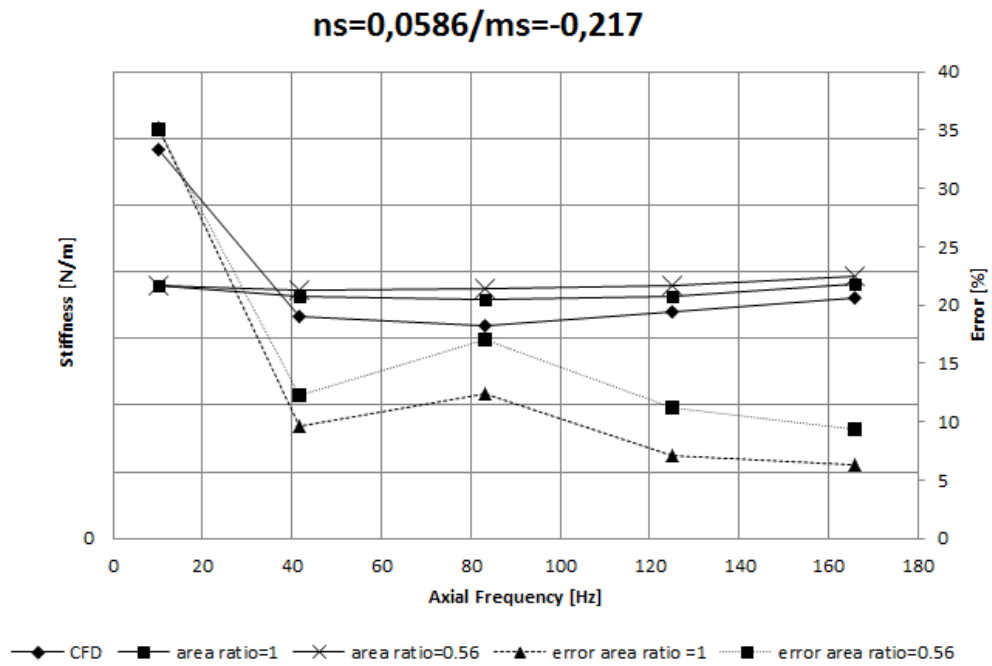


Figure F.07. Stiffness vs axial frequency at  $ns=0,0586/ms=-0,217$  for case A centered position.



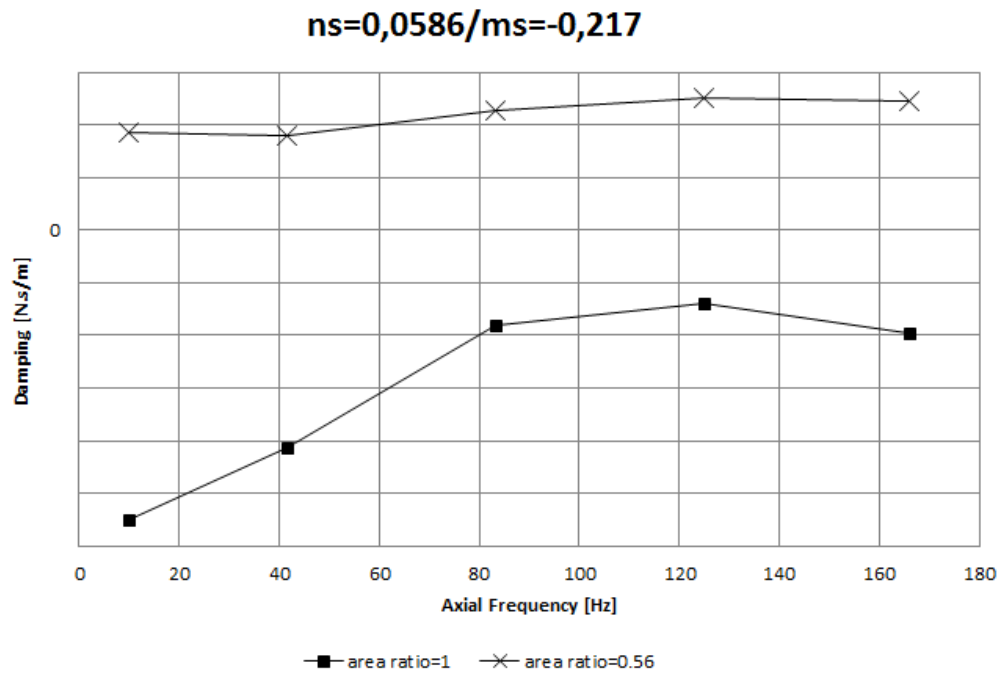


Figure F.08. Damping vs axial frequency at  $ns=0,0586/ms=-0,217$  for case A centered position.

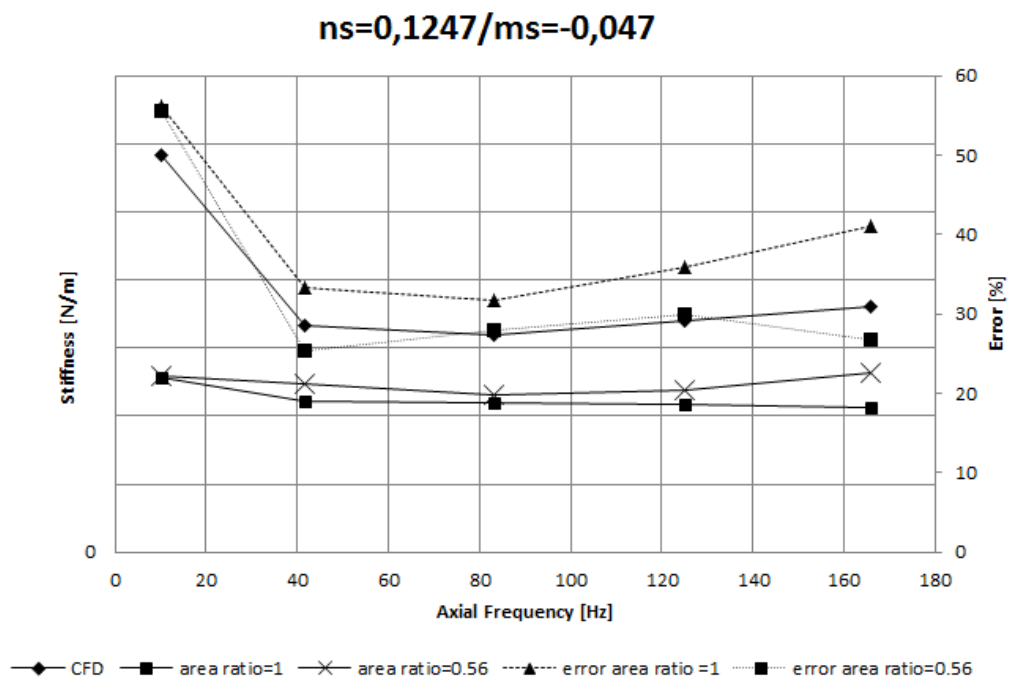


Figure F.09. Stiffness vs axial frequency at  $ns=0,1247/ms=-0,047$  for case A centered position.

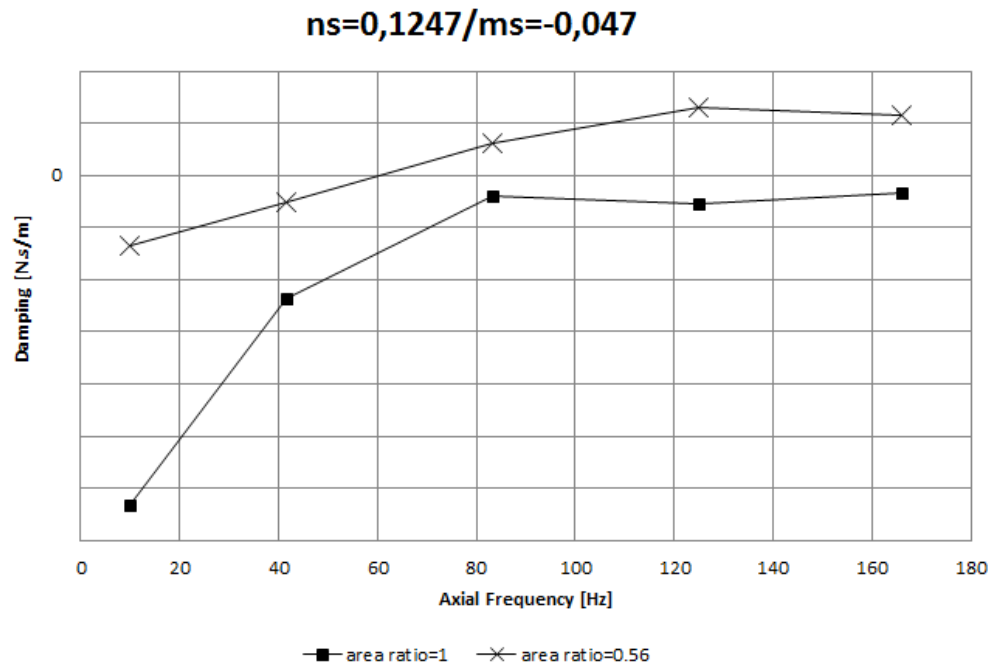


Figure F.10. Damping vs axial frequency at  $ns=0,1247/ms=-0,047$  for case A centered position.

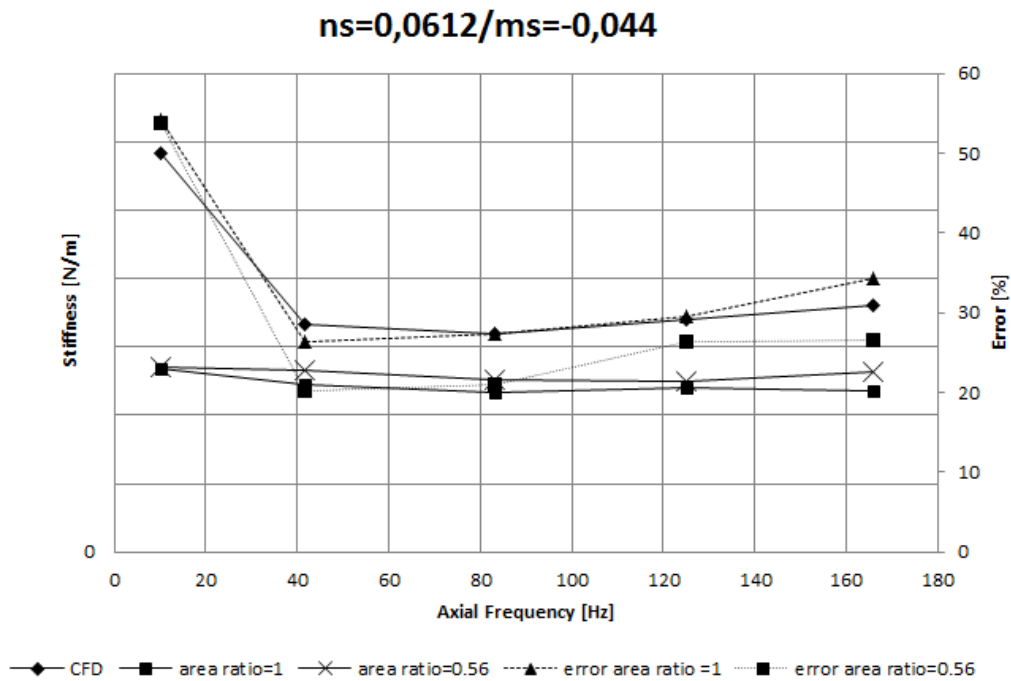


Figure F.11. Stiffness vs axial frequency at  $ns=0,0612/ms=-0,044$  for case A centered position.

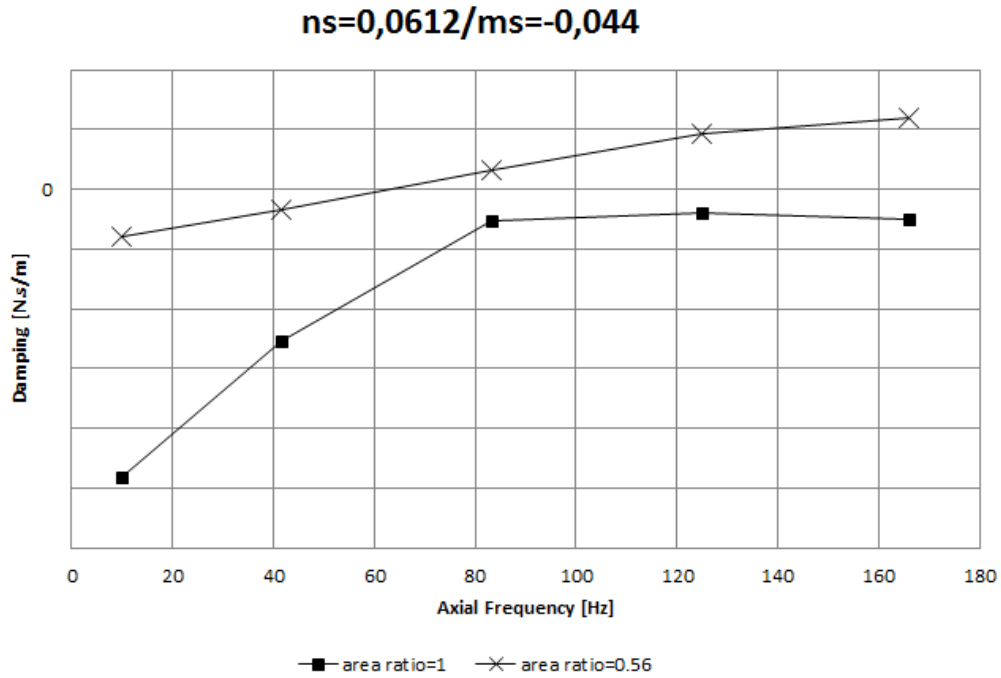


Figure F.12. Damping vs axial frequency at  $ns=0,0612/ms=-0,044$  for case A centered position.

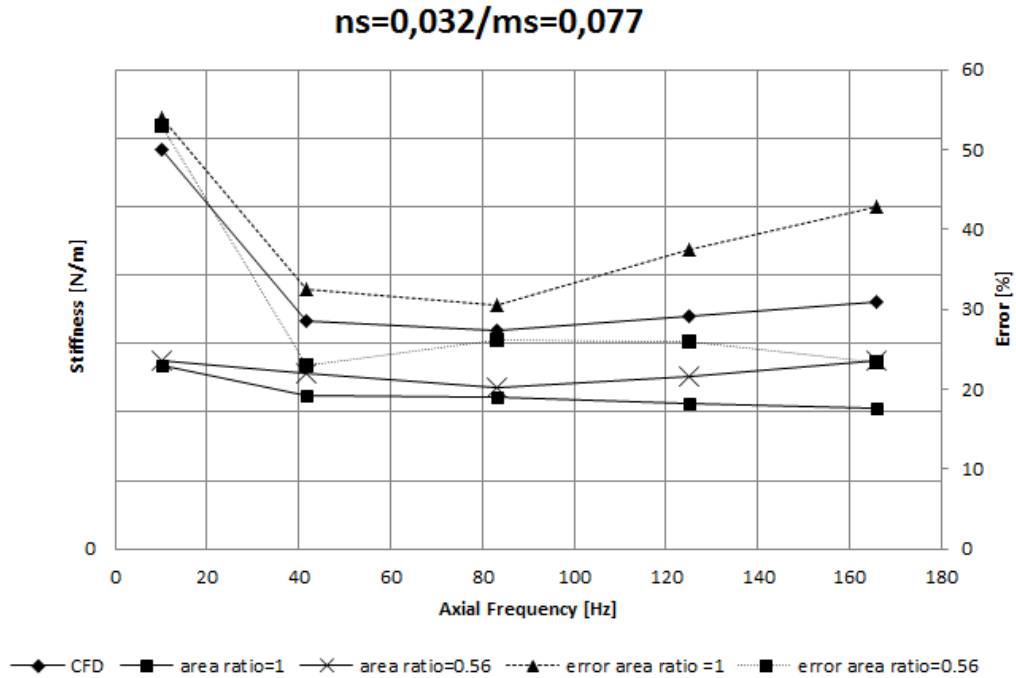


Figure F.13. Stiffness vs axial frequency at  $ns=0,032/ms=0,077$  for case A centered position.

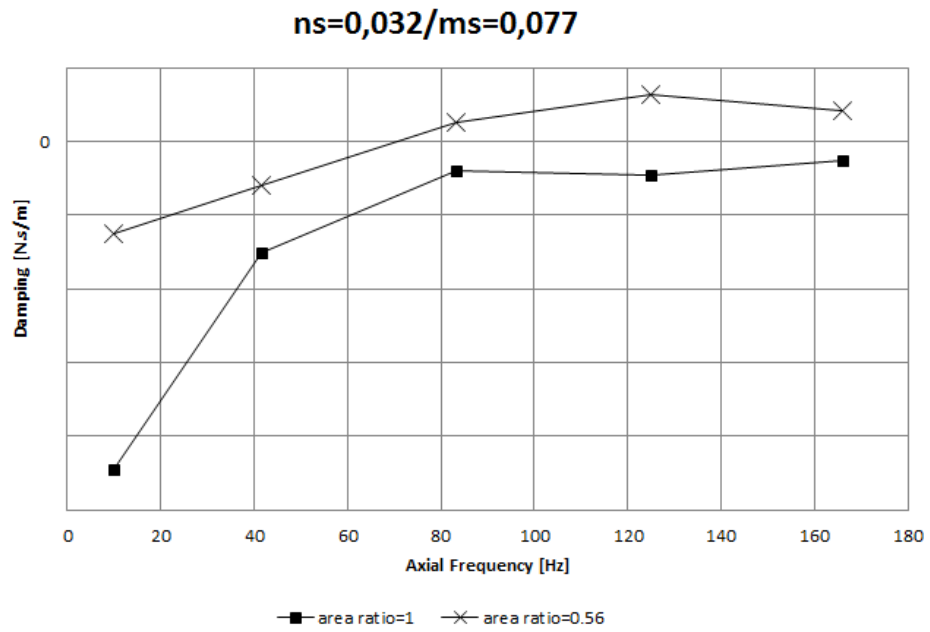


Figure F.14. Damping vs axial frequency at ns=0,032/ms=-0,077 for case A centered position.

**Case A: Offset**

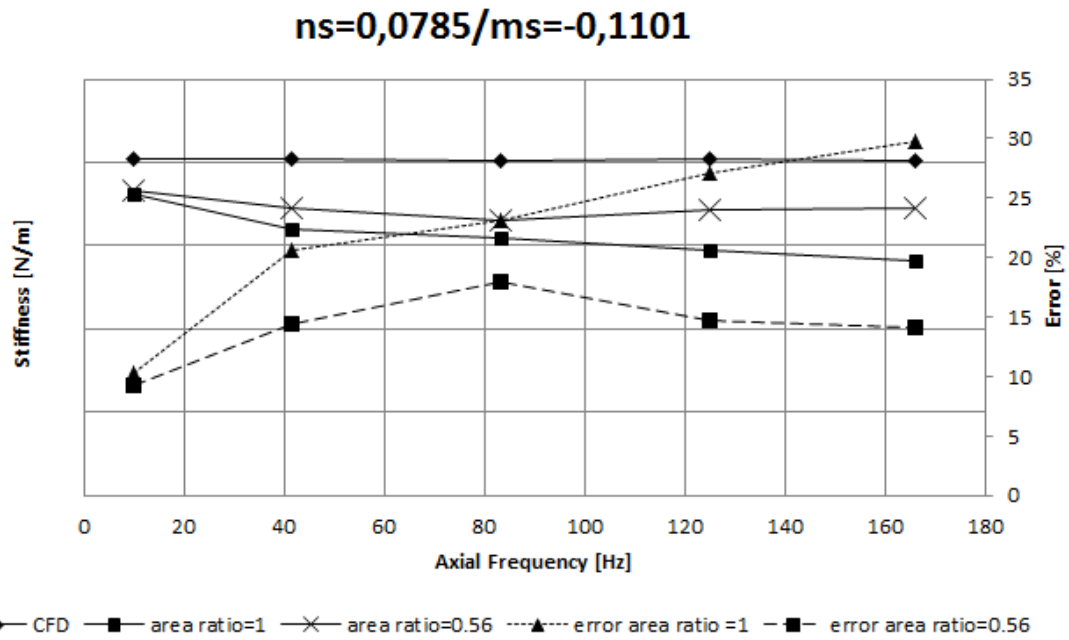


Figure F.15. Stiffness vs axial frequency at ns=0,0785/ms=-0,1101 for case A 50% offset position.

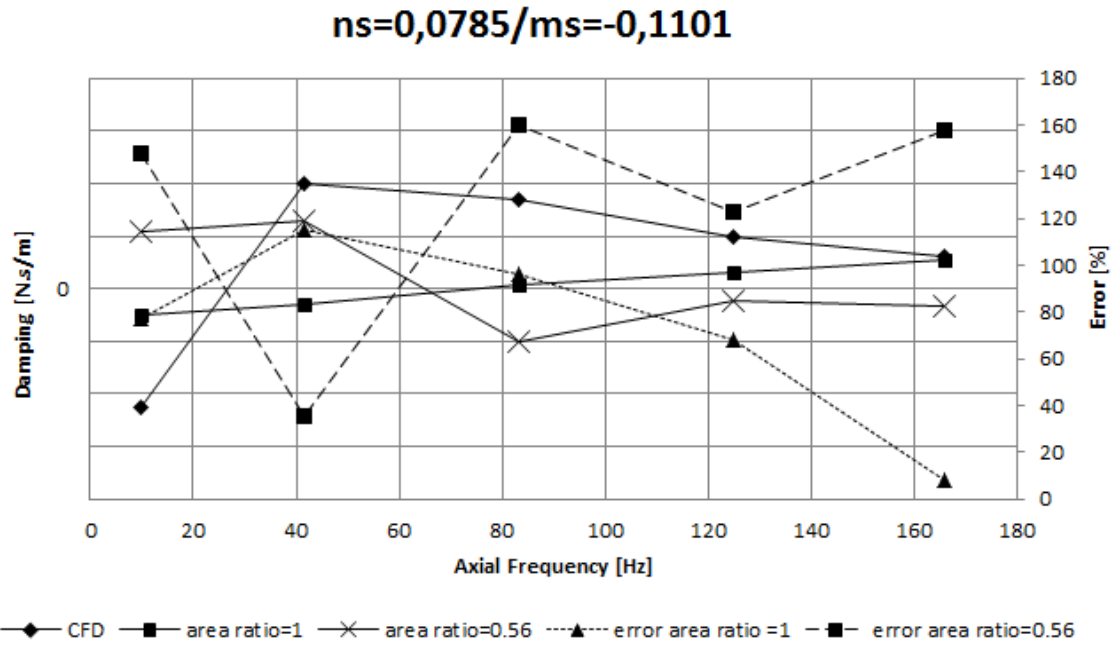


Figure F.16. Damping vs axial frequency at ns=0,0785/ms=-0,1101 for case A 50% offset position.

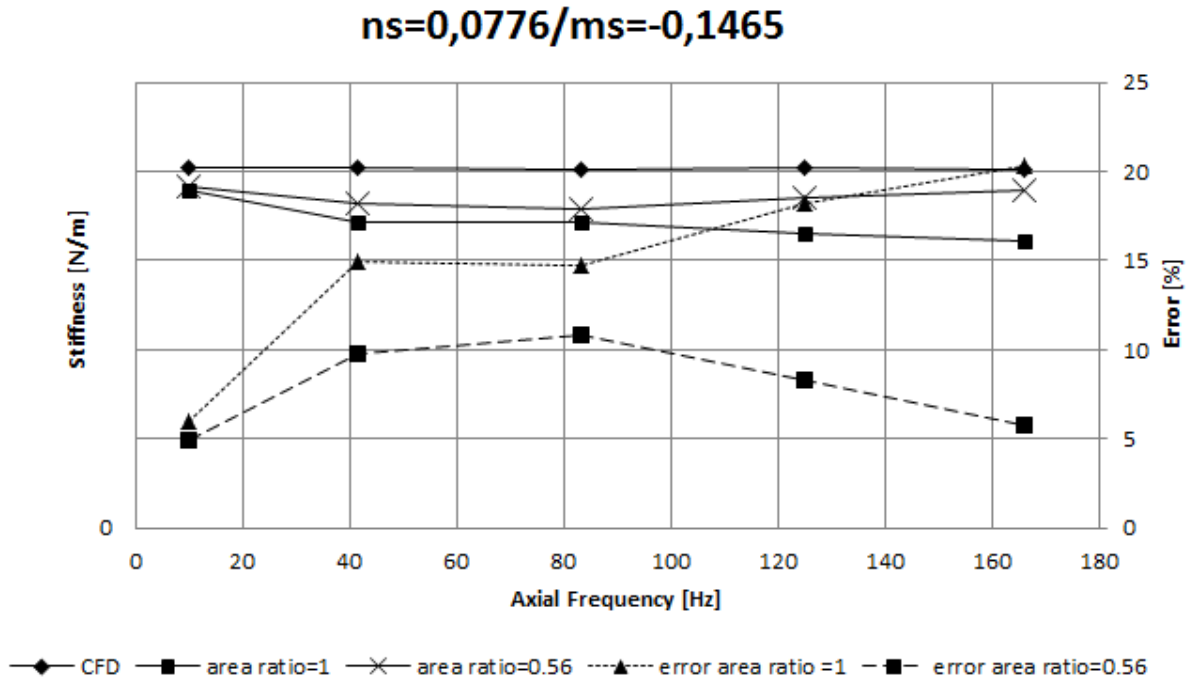


Figure F.17. Stiffness vs axial frequency at ns=0,0776/ms=-0,1465 for case A 50% offset position.

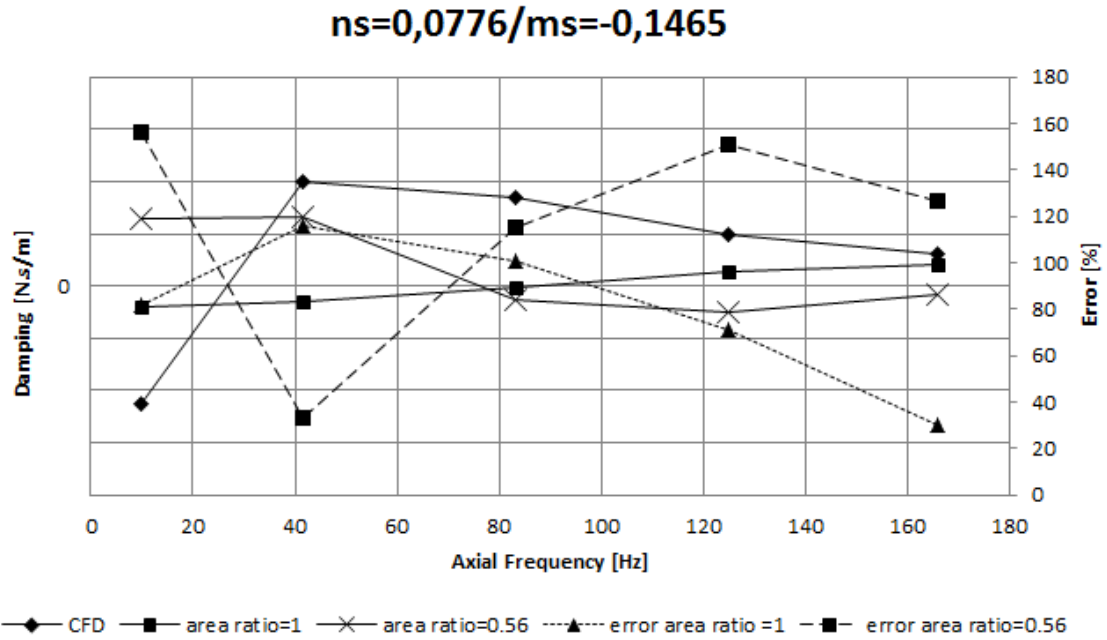


Figure F.18. Damping vs axial frequency at  $ns=0,0776/ms=-0,1465$  for case A 50% offset position.

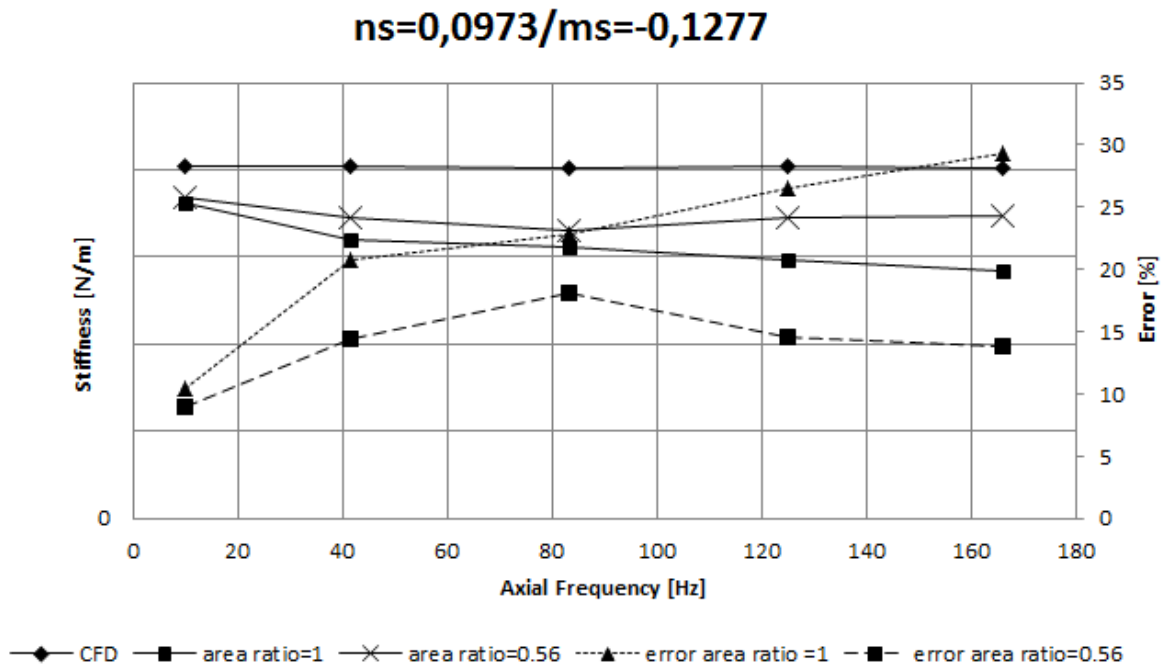


Figure F.19. Stiffness vs axial frequency at  $ns=0,0973/ms=-0,1277$  for case A 50% offset position.

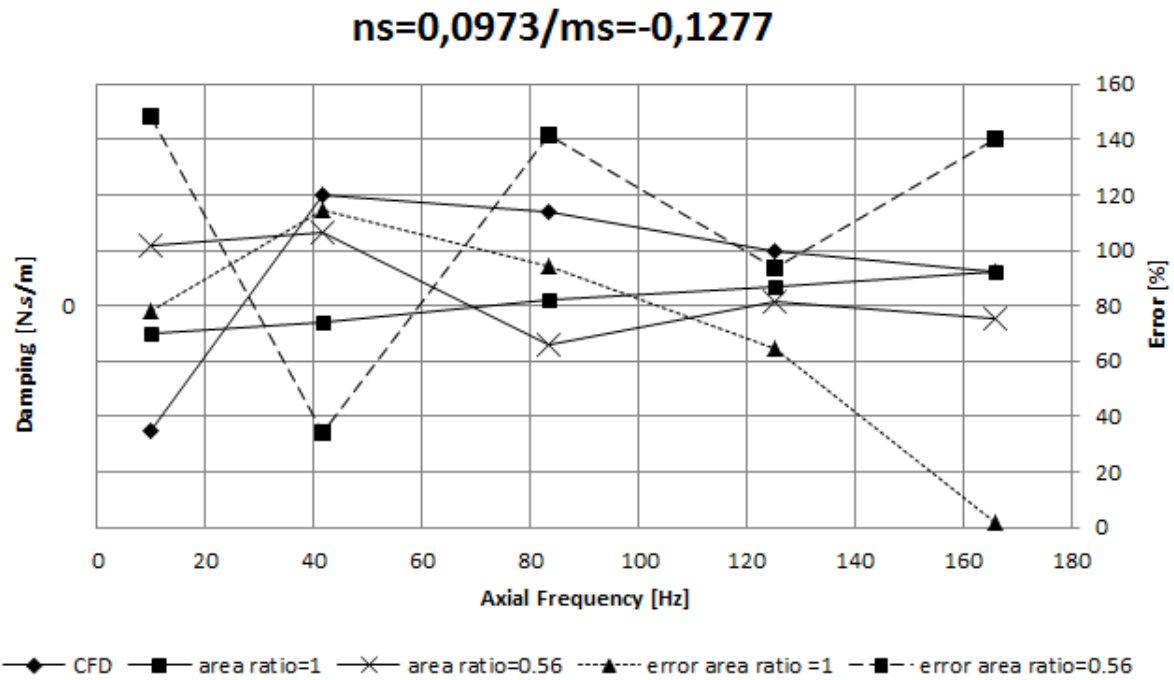


Figure F.20. Damping vs axial frequency at  $ns=0,0973/ms=-0,1277$  for case A 50% offset position.

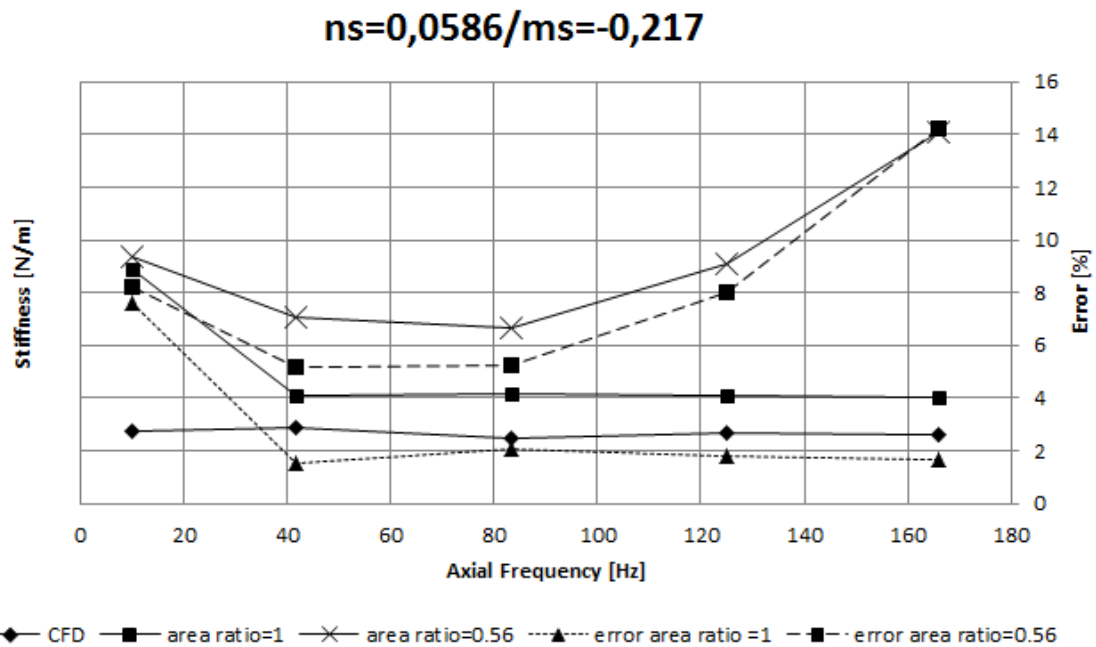


Figure F.21. Stiffness vs axial frequency at  $ns=0,0586/ms=-0,217$  for case A 50% offset position.

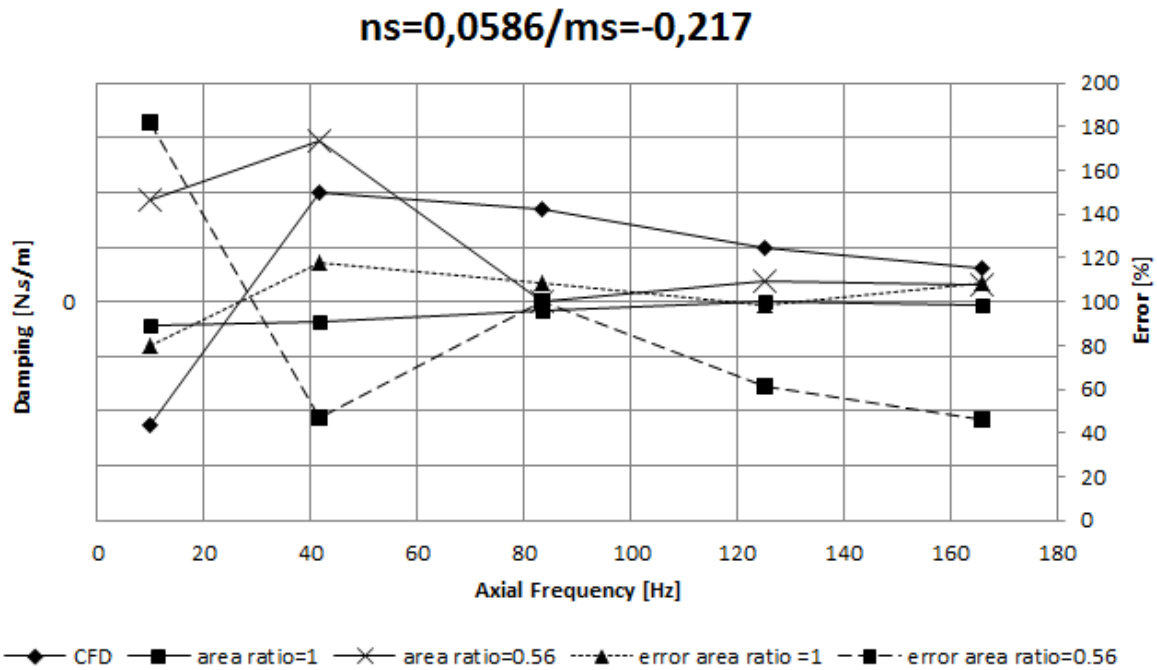


Figure F.22. Damping vs axial frequency at  $ns=0,0586/ms=-0,217$  for case A 50% offset position.

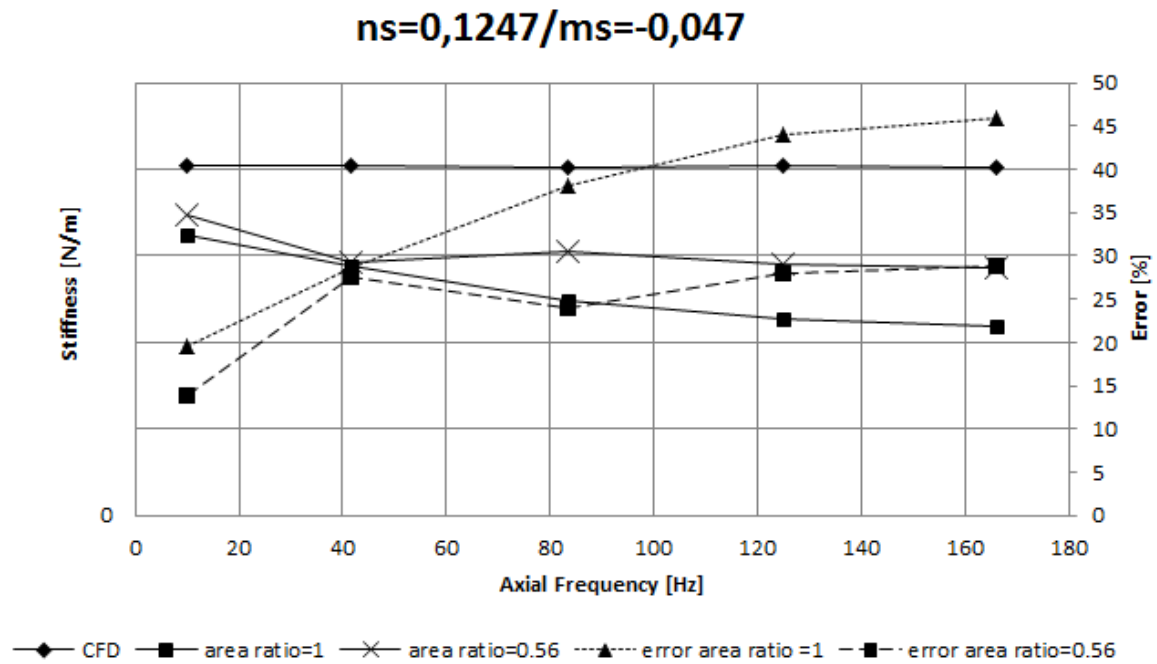


Figure F.23. Stiffness vs axial frequency at  $ns=0,1247/ms=-0,047$  for case A 50% offset position.



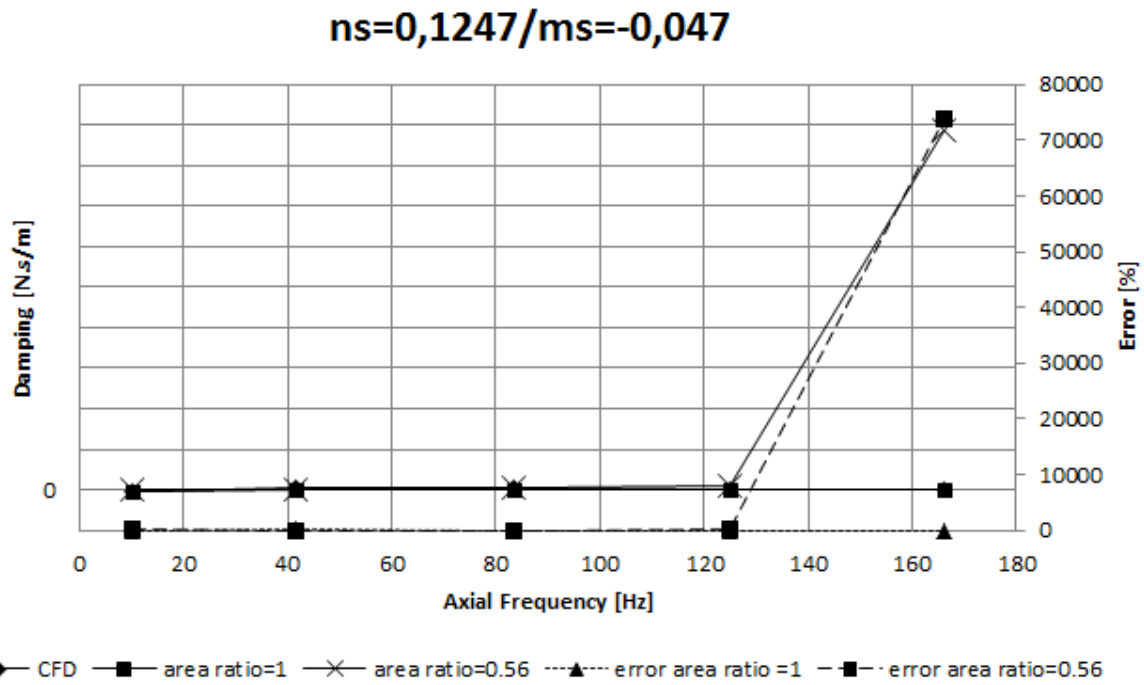


Figure F.24 Damping vs axial frequency at  $ns=0,1247/ms=-0,047$  for case A 50% offset position.

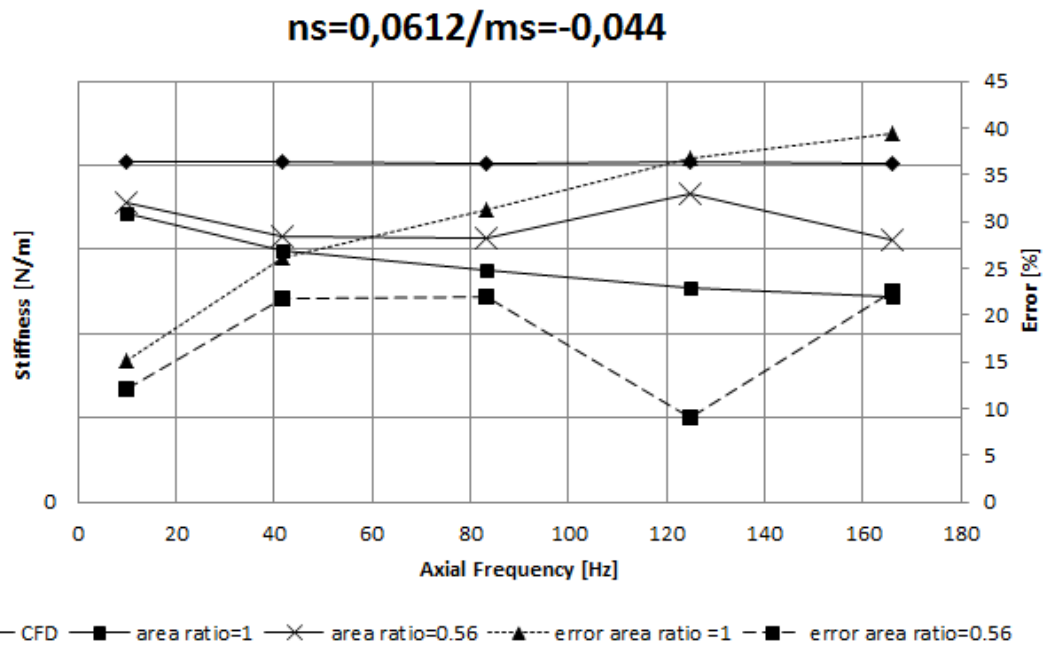


Figure F.25. Stiffness vs axial frequency at  $ns=0,0612/ms=-0,044$  for case A 50% offset position.

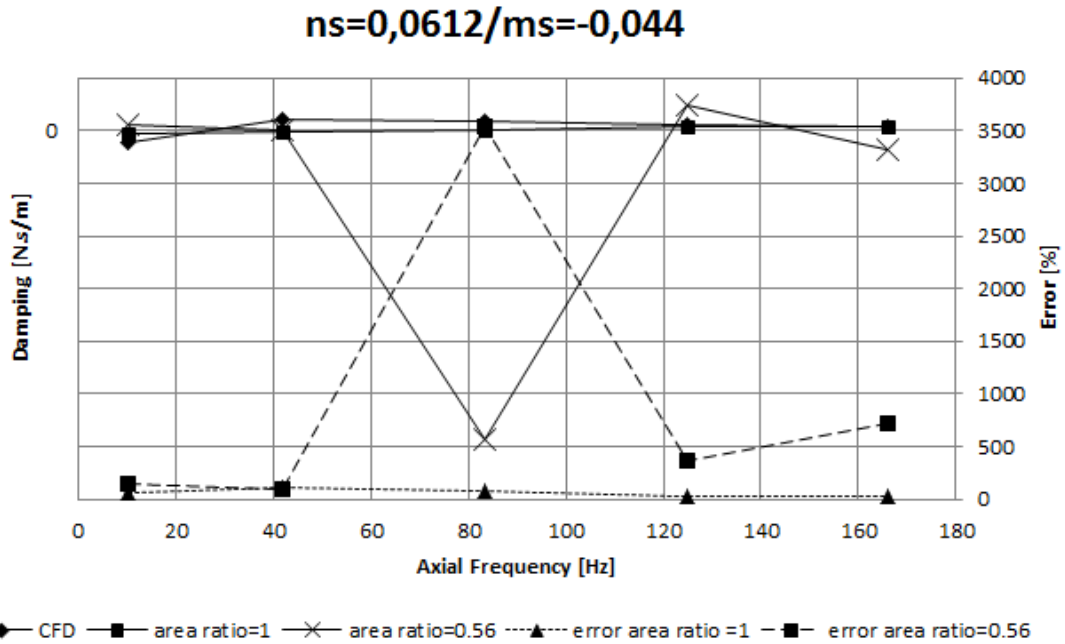


Figure F.26. Damping vs axial frequency at  $ns=0,0612/ms=-0,044$  for case A 50% offset position.

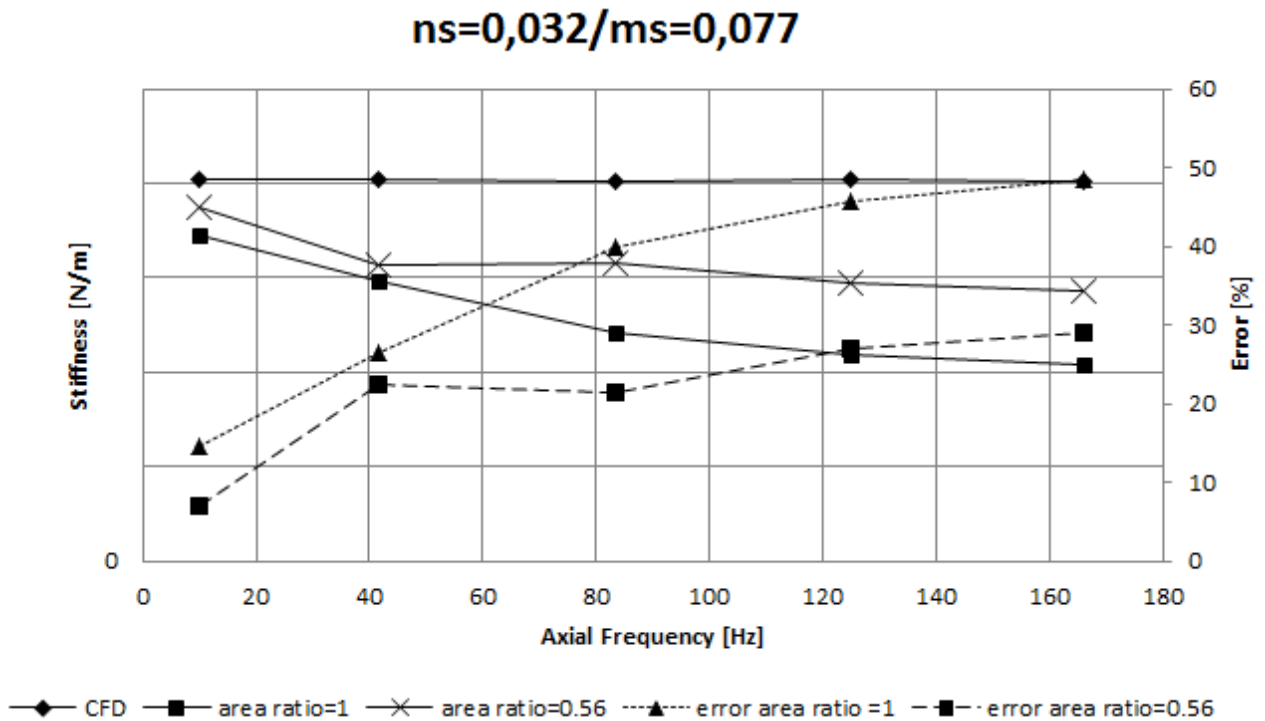


Figure F.27. Stiffness vs axial frequency at  $ns=0,032/ms=0,077$  for case A 50% offset position.

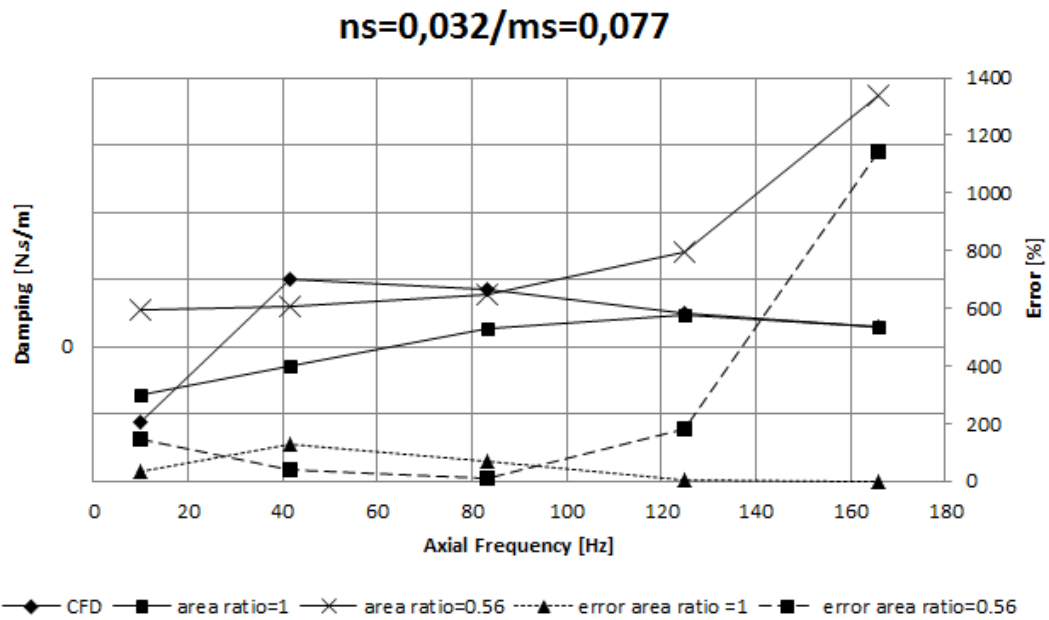


Figure F.28. Damping vs axial frequency at  $ns=0,032/ms=0,077$  for case A 50% offset position.

**Case B: centered**

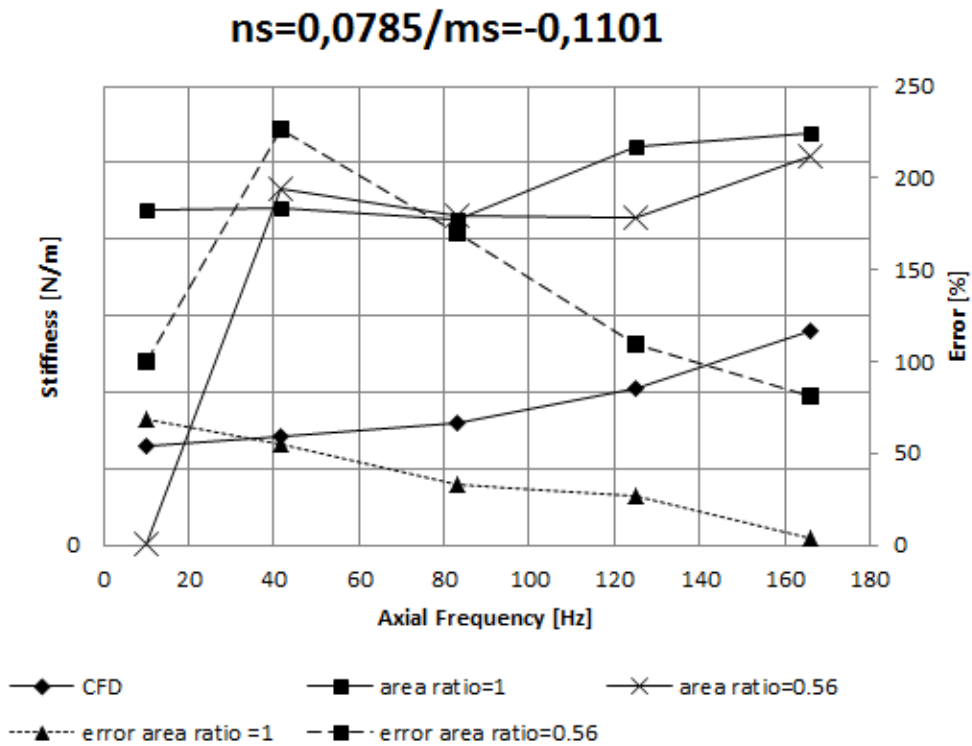


Figure F.29. Stiffness vs axial frequency at  $ns=0,0785/ms=-0,1101$  for case B centered position.

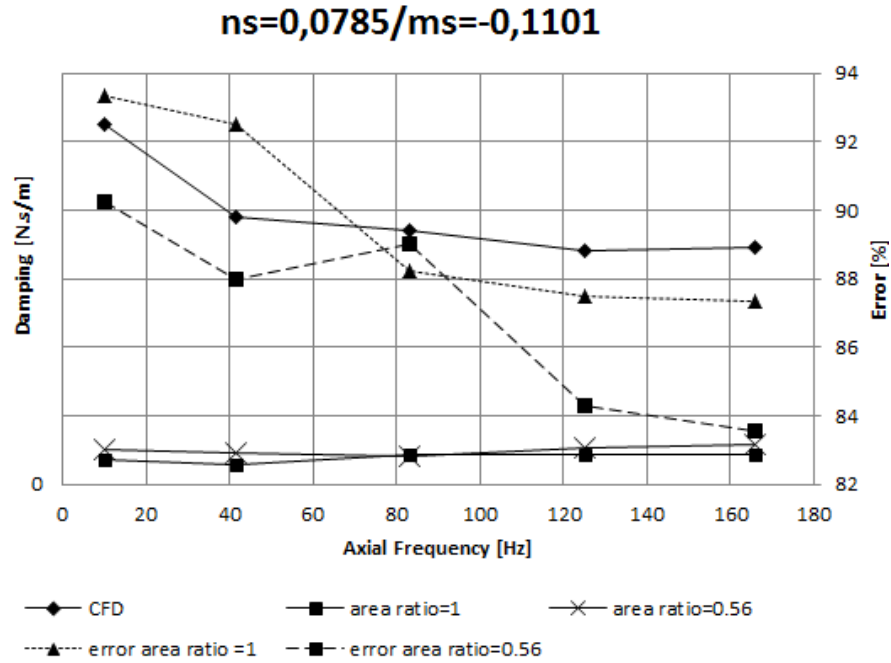


Figure F.30. Damping vs axial frequency at ns=0,0785/ms=-0,1101 for case B centered position.

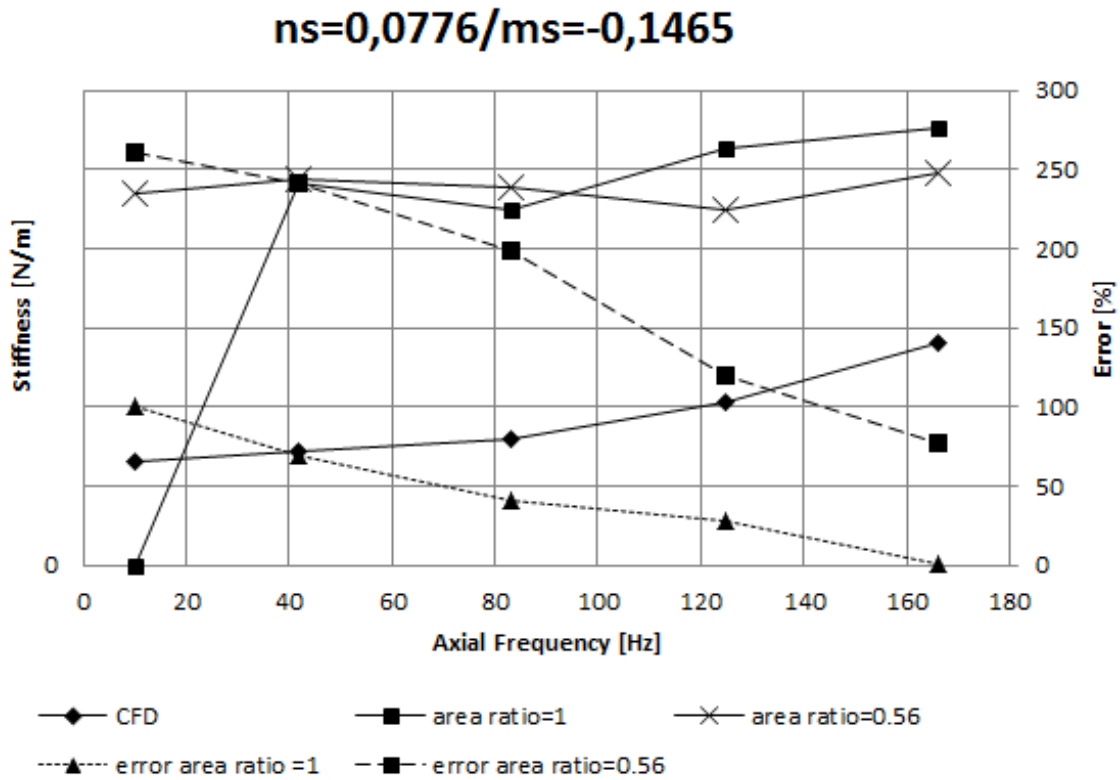


Figure F.31. Stiffness vs axial frequency at ns=0,0776/ms=-0,1465 for case B centered position.

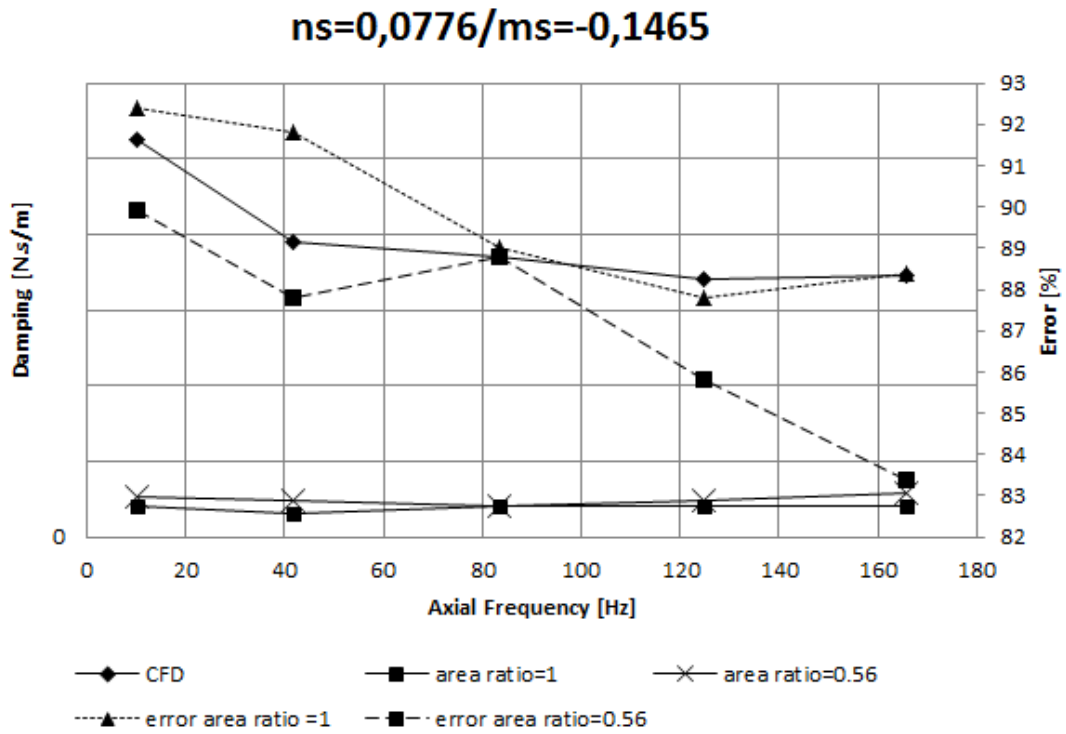


Figure F.32. Damping vs axial frequency at  $ns=0,0776/ms=-0,1465$  for case B centered position.

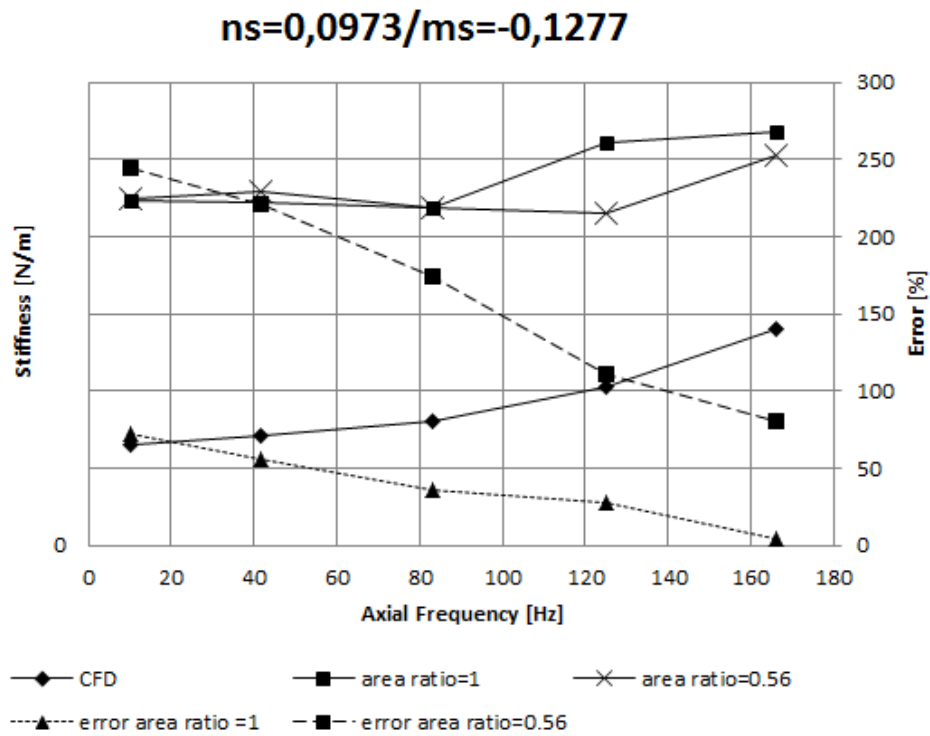


Figure F.33. Stiffness vs axial frequency at  $ns=0,0973/ms=-0,1277$  for case B centered position.

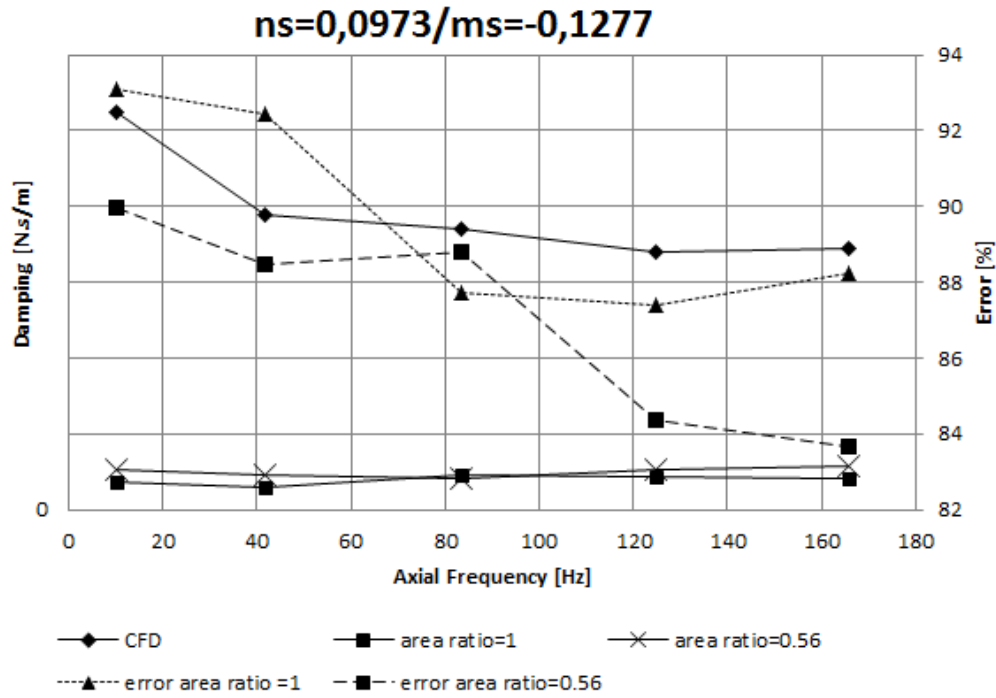


Figure F.34. Damping vs axial frequency at  $ns=0,0973/ms=-0,1277$  for case B centered position.

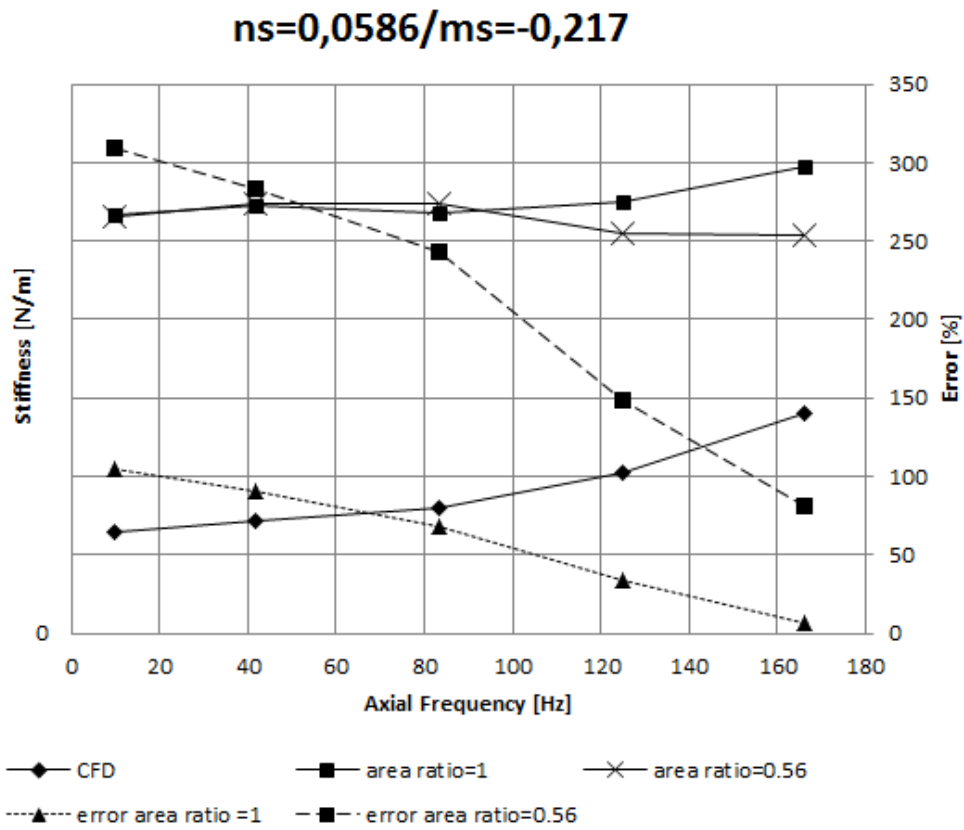


Figure F.35. Stiffness vs axial frequency at  $ns=0,0586/ms=-0,217$  for case B centered position.

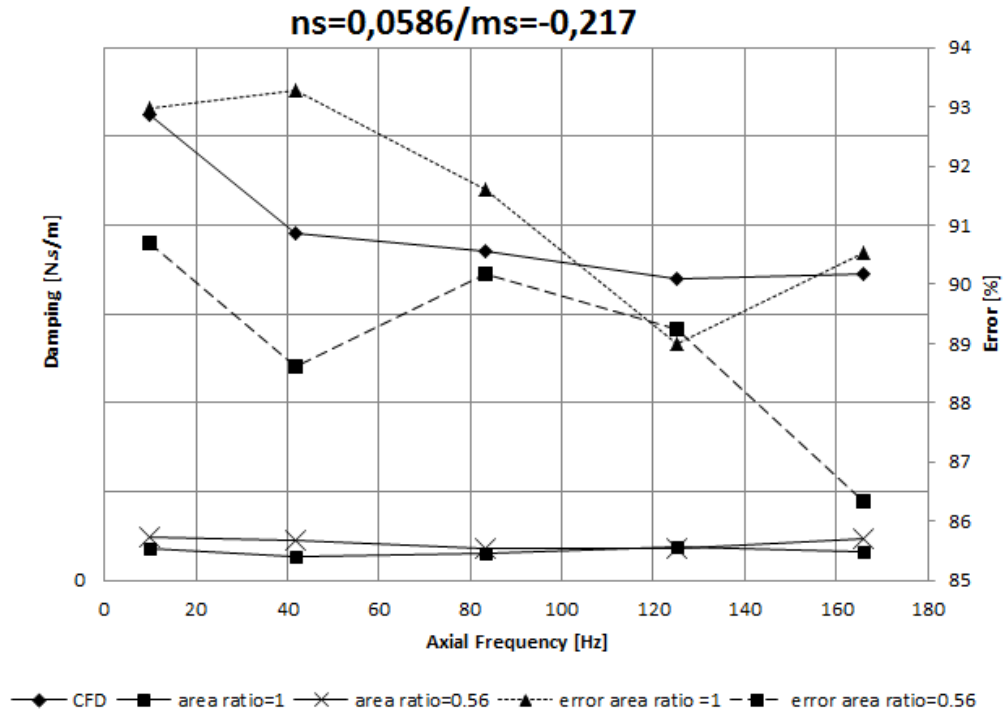


Figure F.36. Damping vs axial frequency at  $ns=0,0586/ms=-0,217$  for case B centered position.

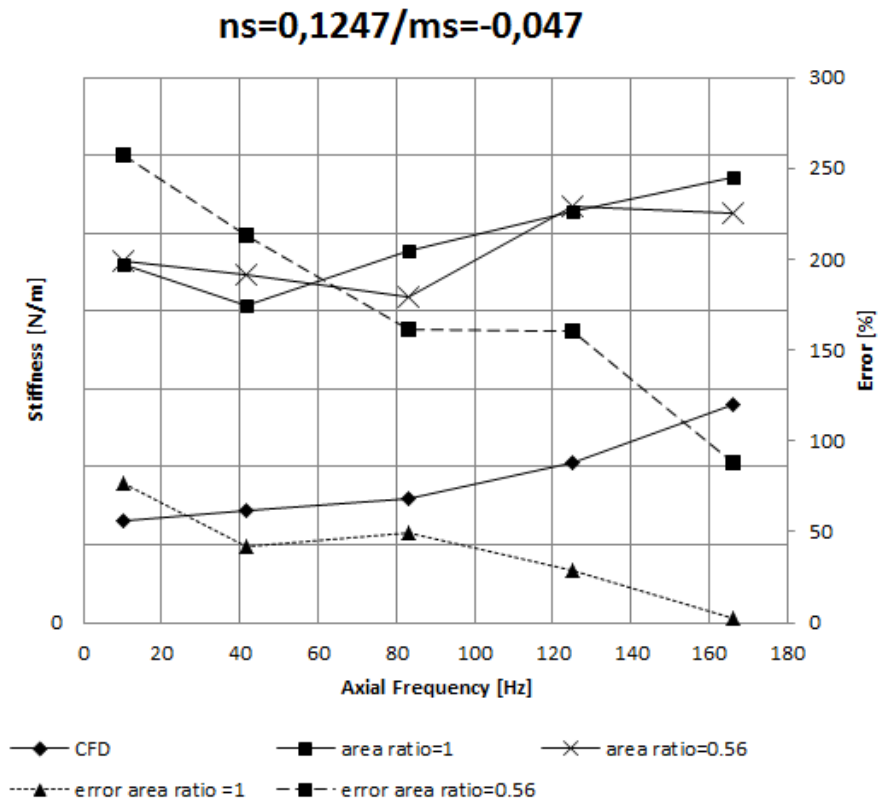


Figure F.37. Stiffness vs axial frequency at  $ns=0,1247/ms=-0,047$  for case B centered position.

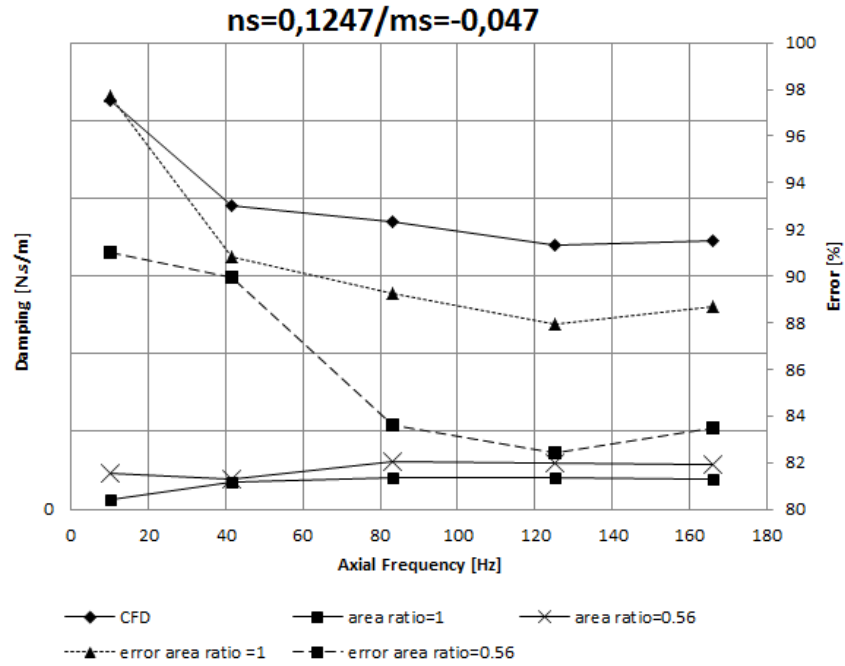


Figure F.38. Damping vs axial frequency at  $ns=0,1247/ms=-0,047$  for case B centered position.

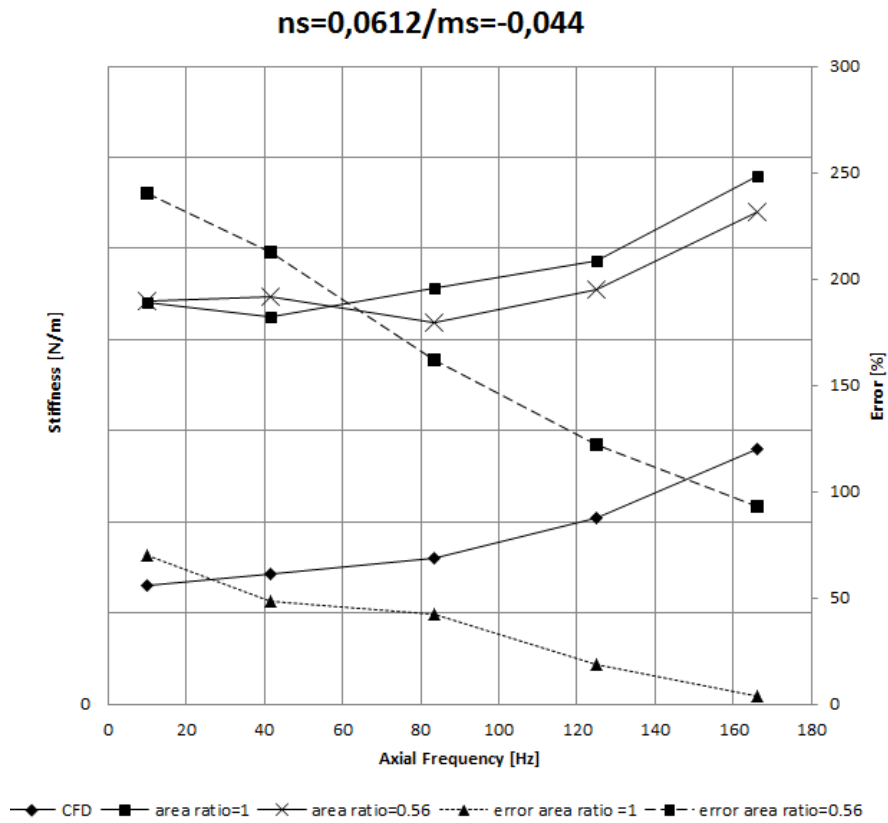


Figure F.39. Stiffness vs axial frequency at  $ns=0,0612/ms=-0,044$  for case B centered position.



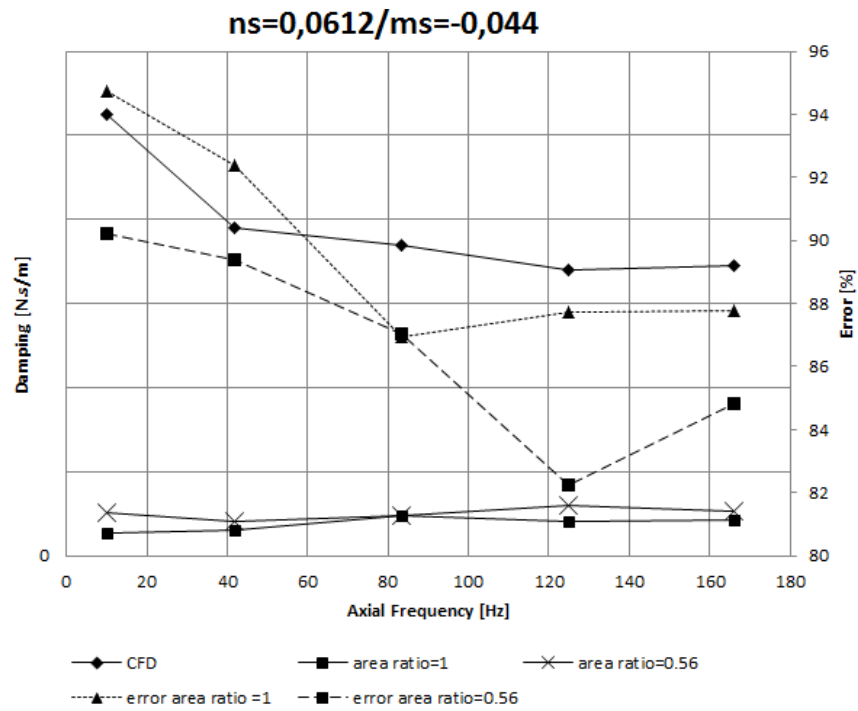


Figure F.40. Damping vs axial frequency at  $ns=0,0612/ms=-0,044$  for case B centered position.

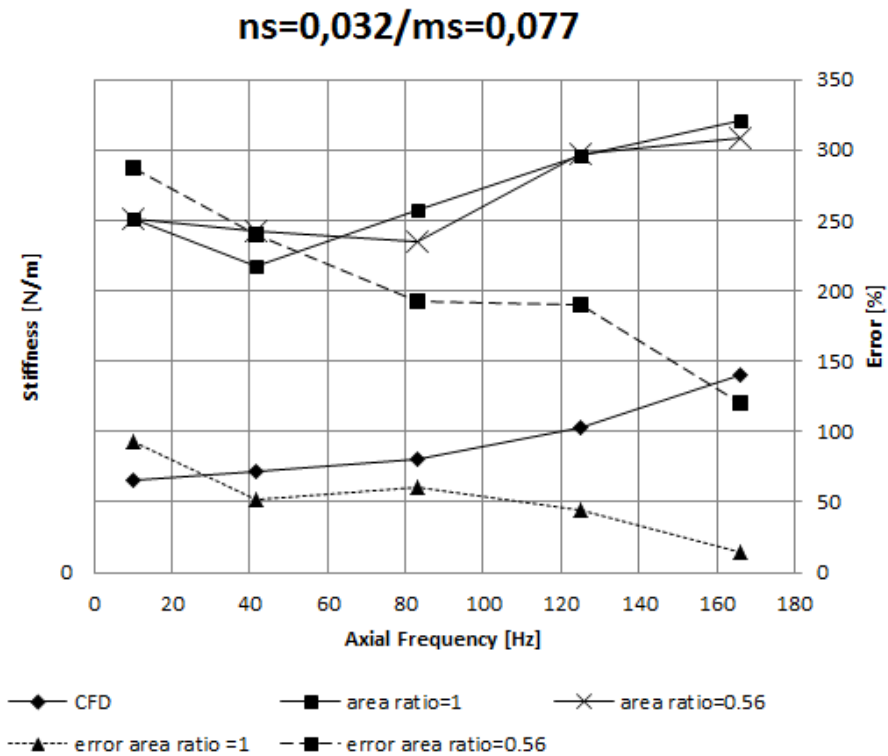


Figure F.41. Stiffness vs axial frequency at  $ns=0,032/ms=0,077$  for case B centered position.

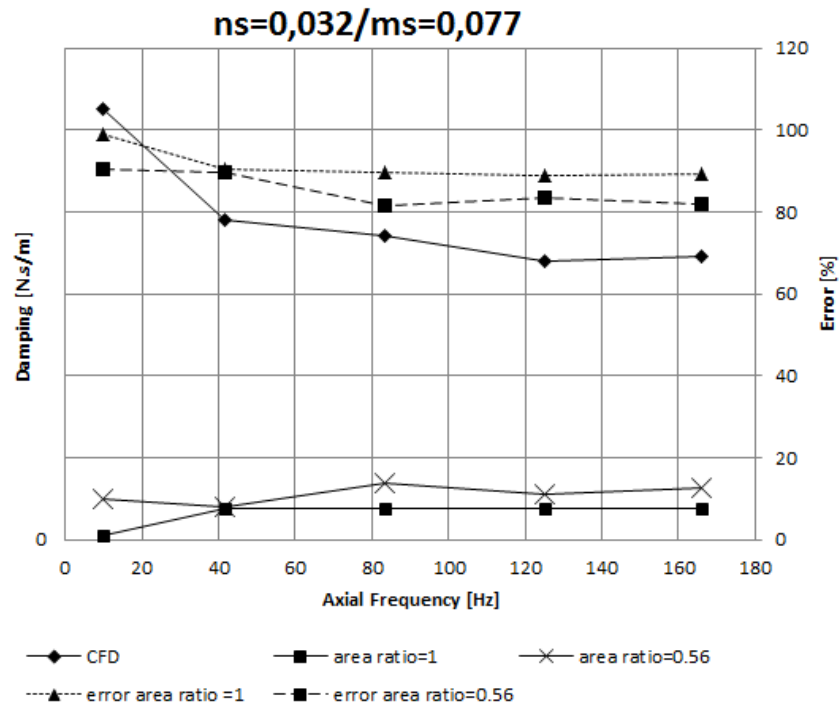


Figure F.42. Damping vs axial frequency at ns=0,032/ms=0,077 for case B centered position.

#### Case B: Offset

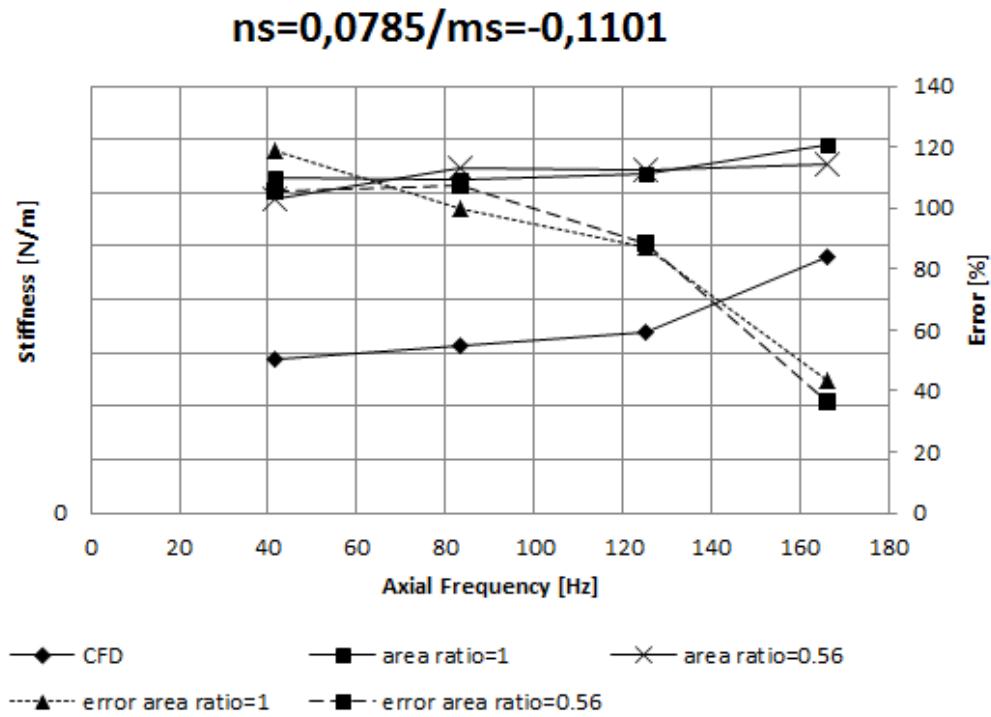


Figure F.43. Stiffness vs axial frequency at ns=0,0785/ms=-0,1101 for case B 50% offset position.

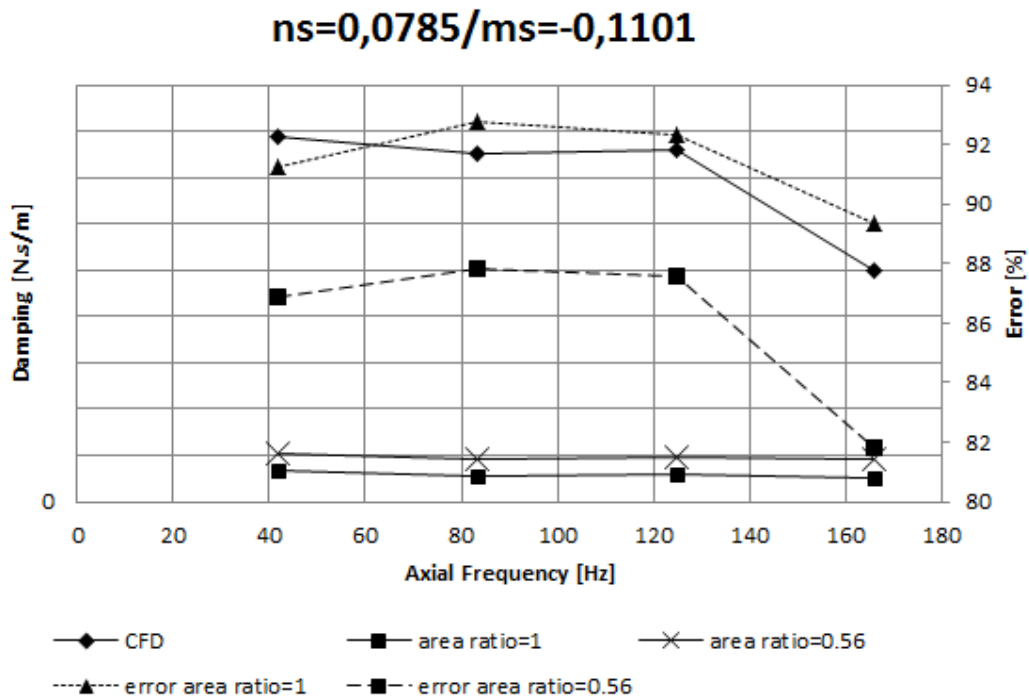


Figure F.44. Damping vs axial frequency at ns=0,0785/ms=-0,1101 for case B 50% offset position.

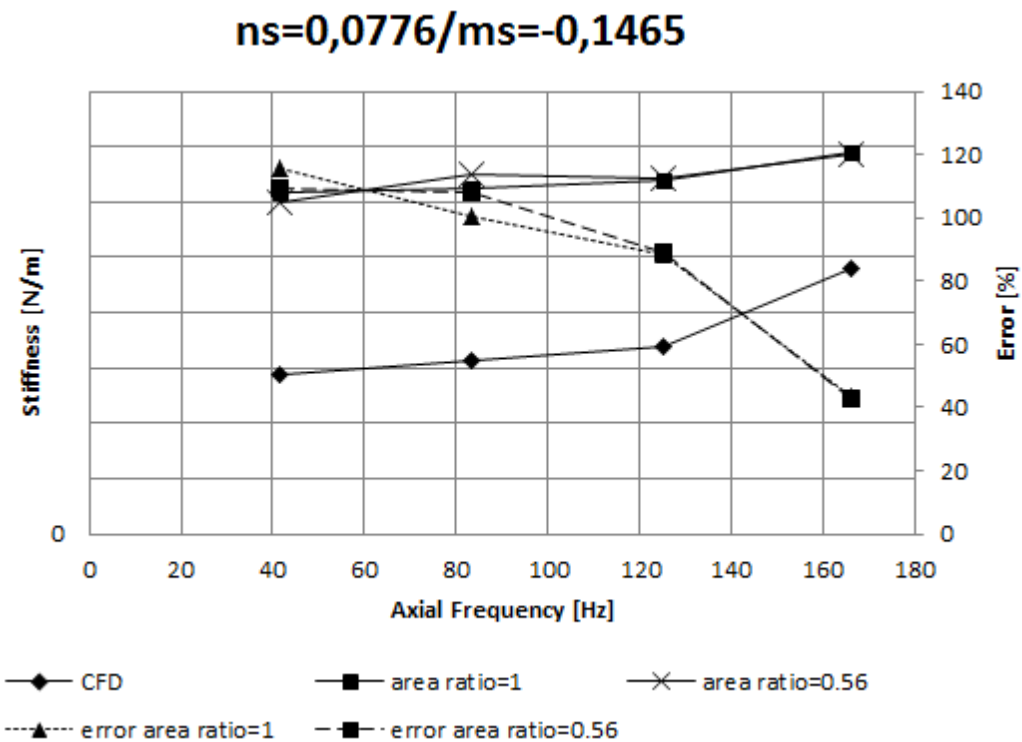


Figure F.45. Stiffness vs axial frequency at ns=0,0776/ms=-0,1465 for case B 50% offset position.

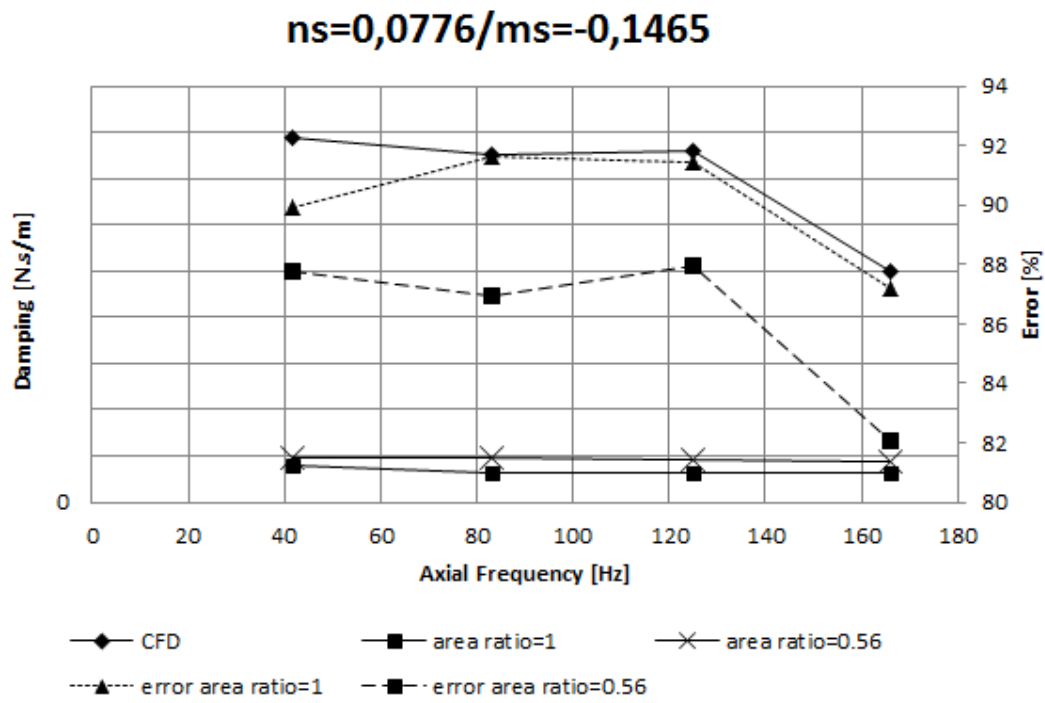


Figure F.46. Damping vs axial frequency at  $ns=0,0776/ms=-0,1465$  for case B 50% offset position.

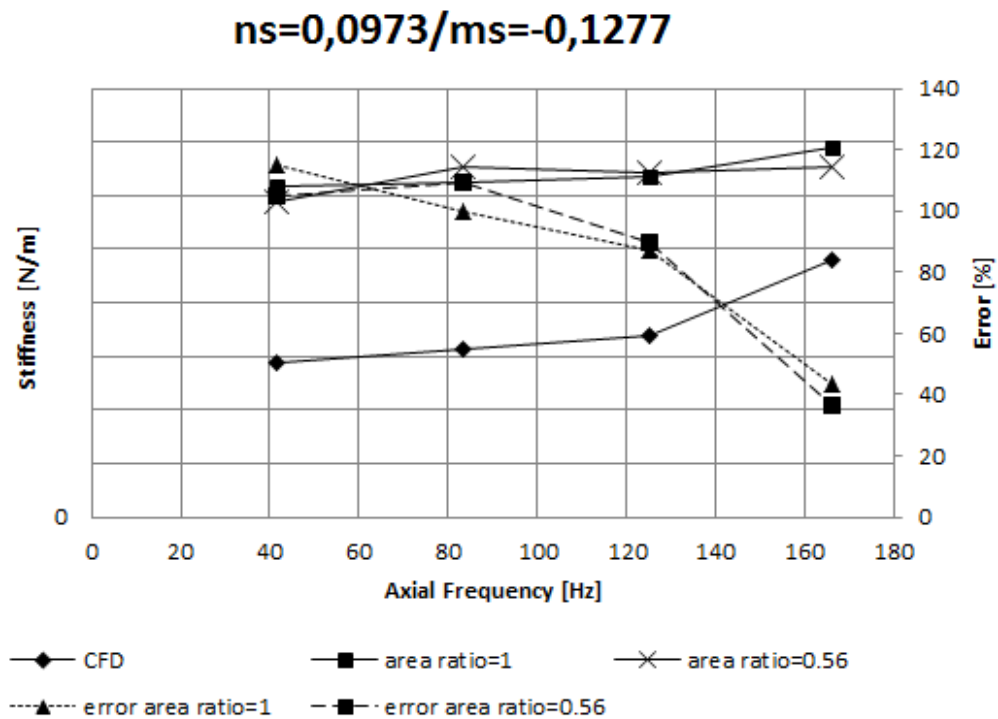


Figure F.47. Stiffness vs axial frequency at  $ns=0,0973/ms=-0,1277$  for case B 50% offset position.

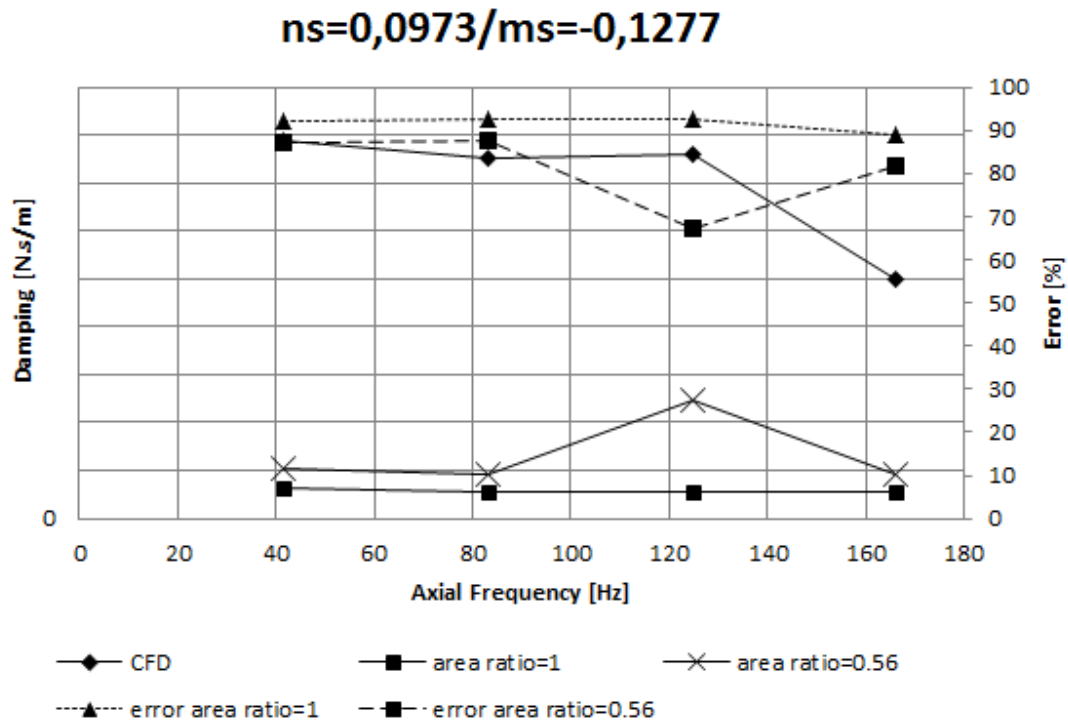


Figure F.48. Damping vs axial frequency at  $ns=0,0973/ms=-0,1277$  for case B 50% offset position.

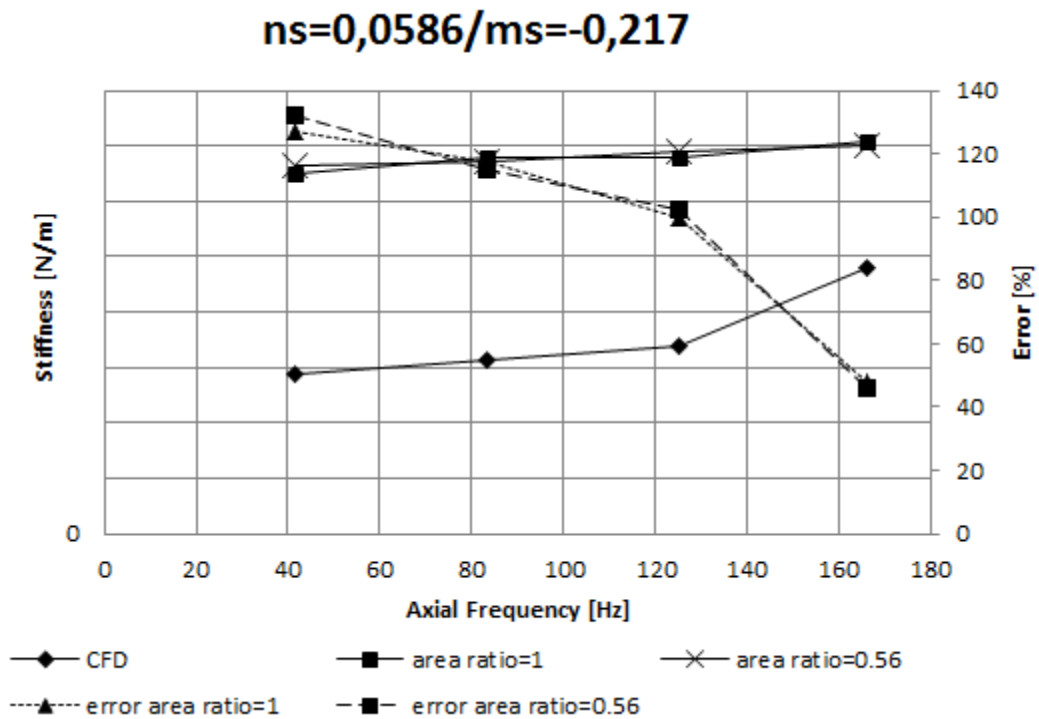


Figure F.49. Stiffness vs axial frequency at  $ns=0,0586/ms=-0,217$  for case B 50% offset position.

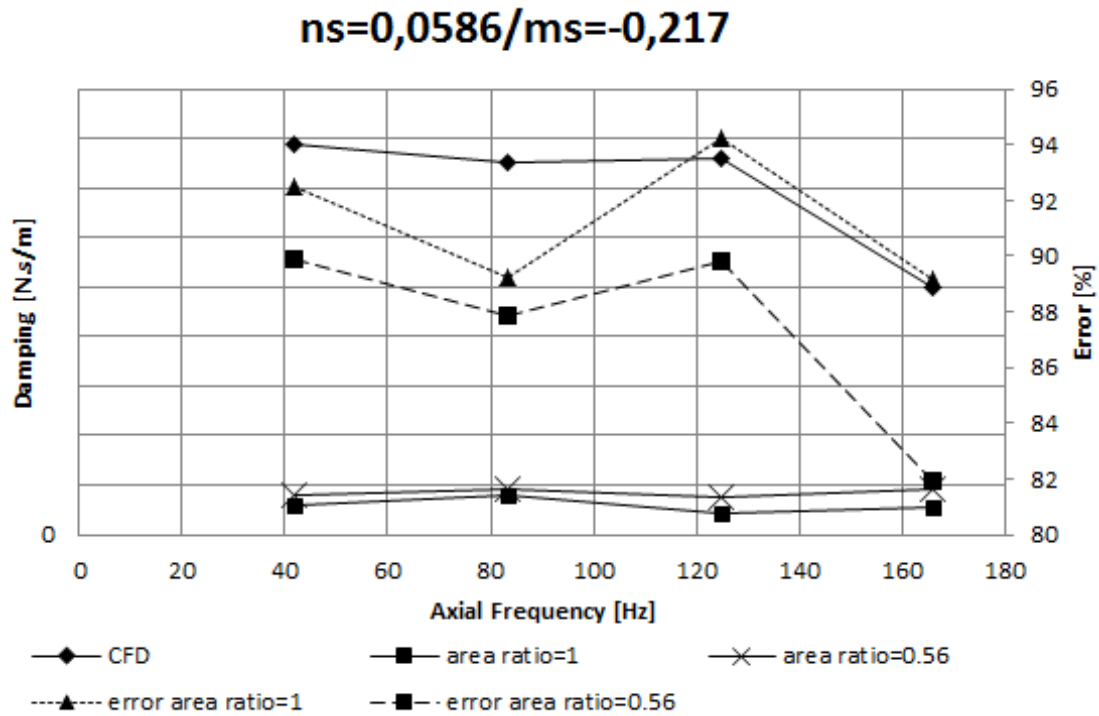


Figure F.50. Damping vs axial frequency at  $ns=0,0586/ms=-0,217$  for case B 50% offset position.

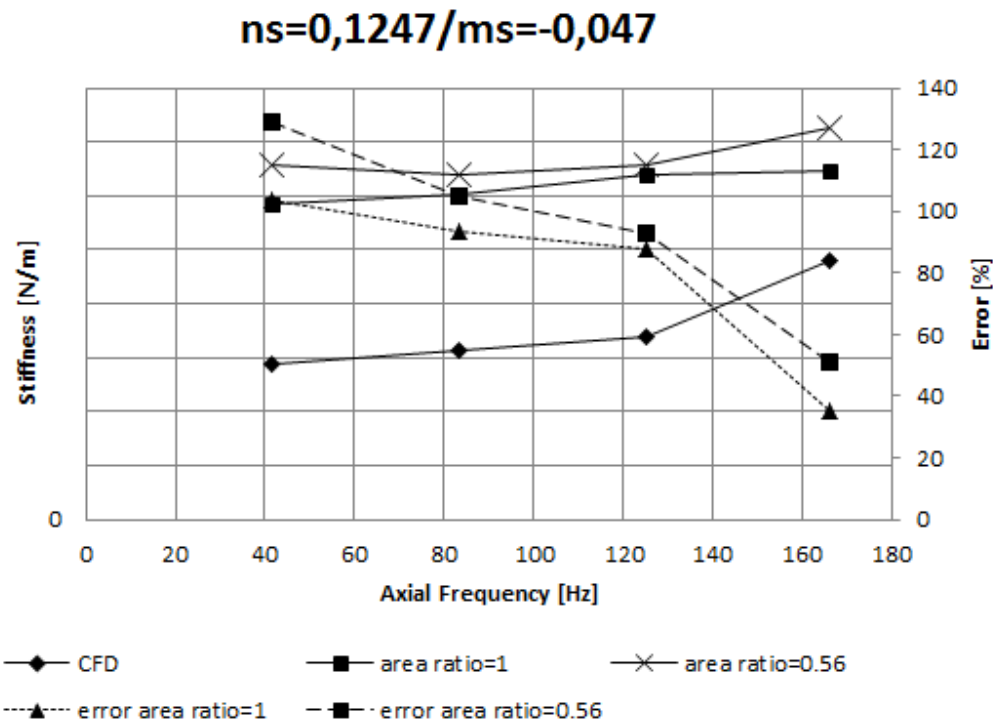


Figure F.51. Stiffness vs axial frequency at  $ns=0,1247/ms=-0,047$  for case B 50% offset position.

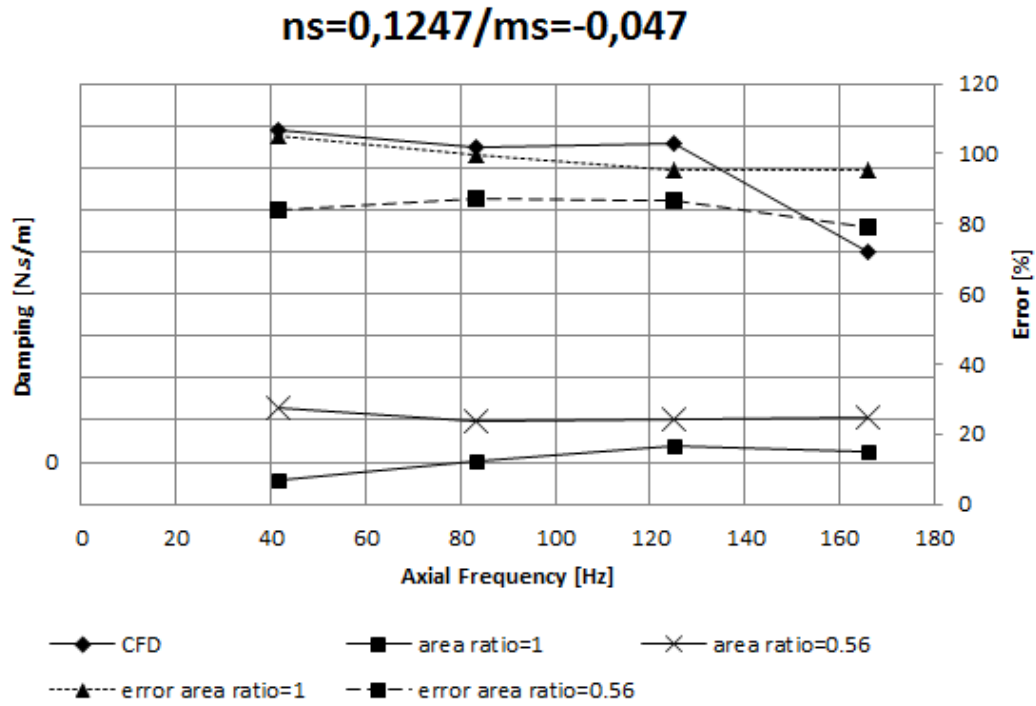


Figure F.52. Damping vs axial frequency at  $ns=0,1247/ms=-0,047$  for case B 50% offset position.

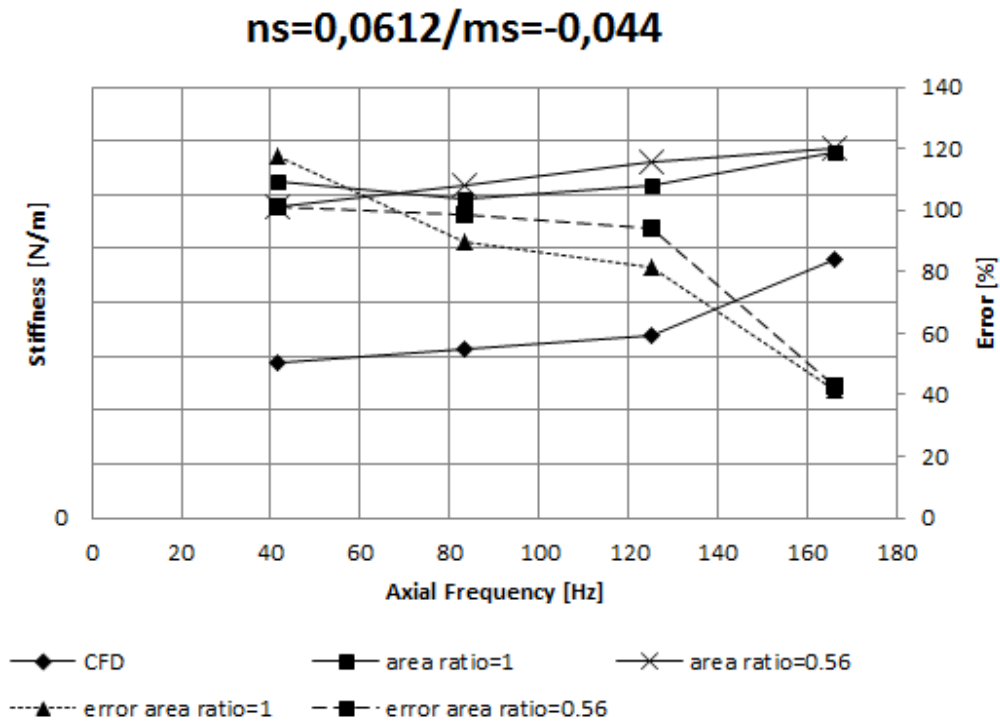


Figure F.53. Stiffness vs axial frequency at  $ns=0,0612/ms=-0,044$  for case B 50% offset position.

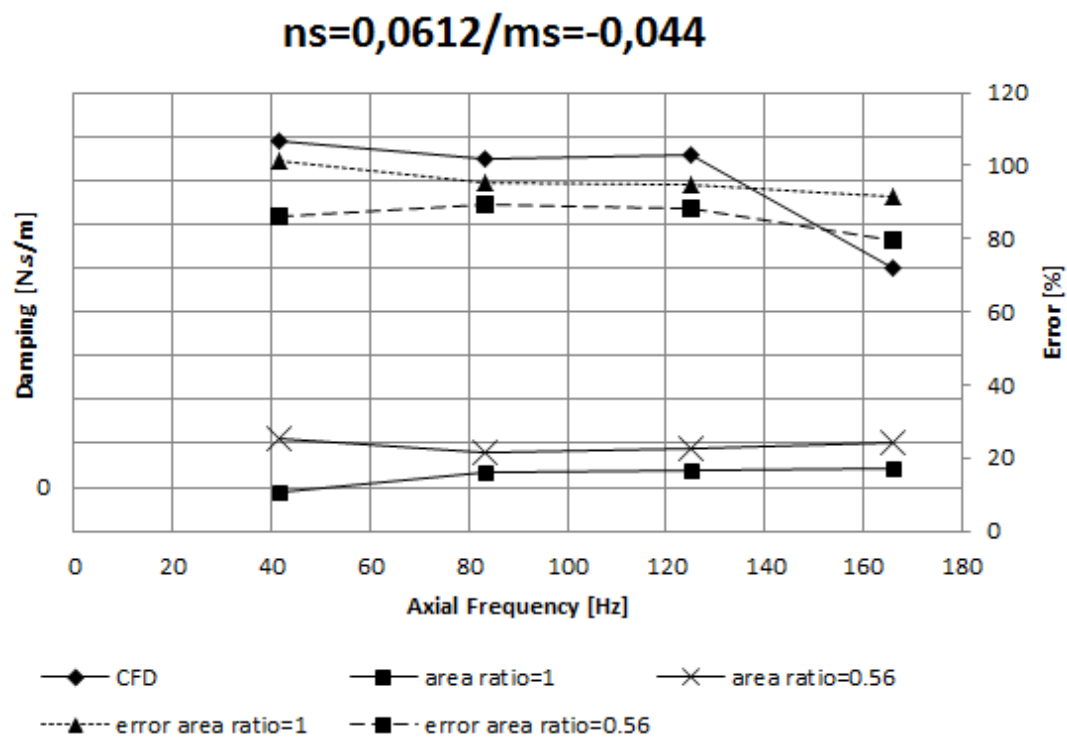


Figure F.54. Damping vs axial frequency at  $ns=0,0612/ms=-0,044$  for case B 50% offset position.

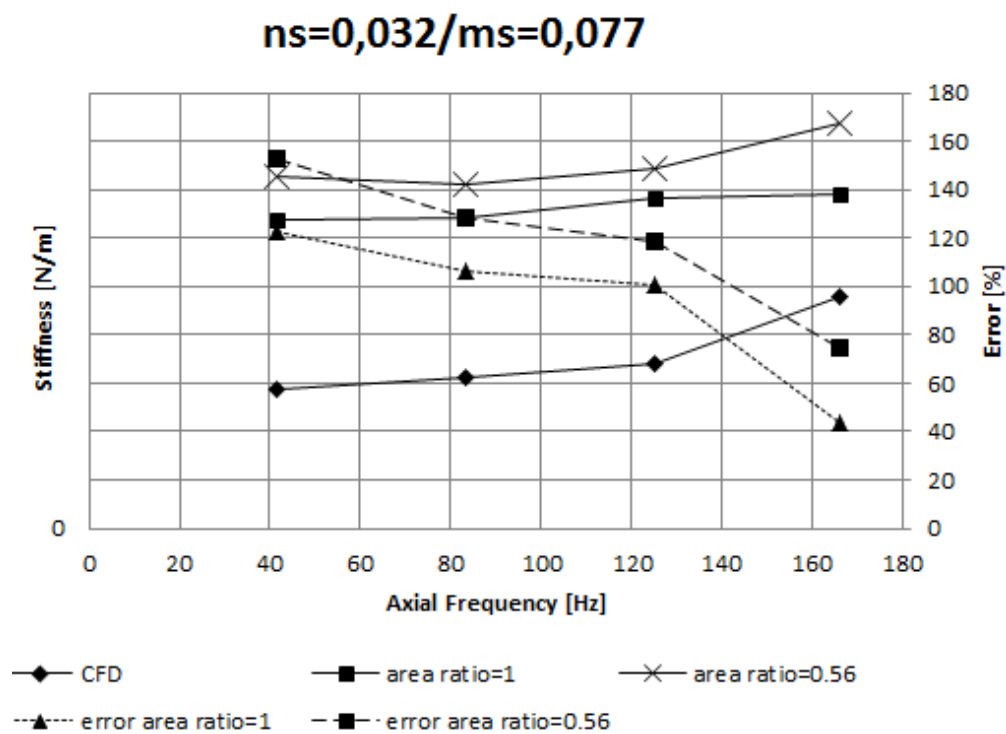


Figure F.55. Stiffness vs axial frequency at  $ns=0,032/ms=0,077$  for case B 50% offset position.



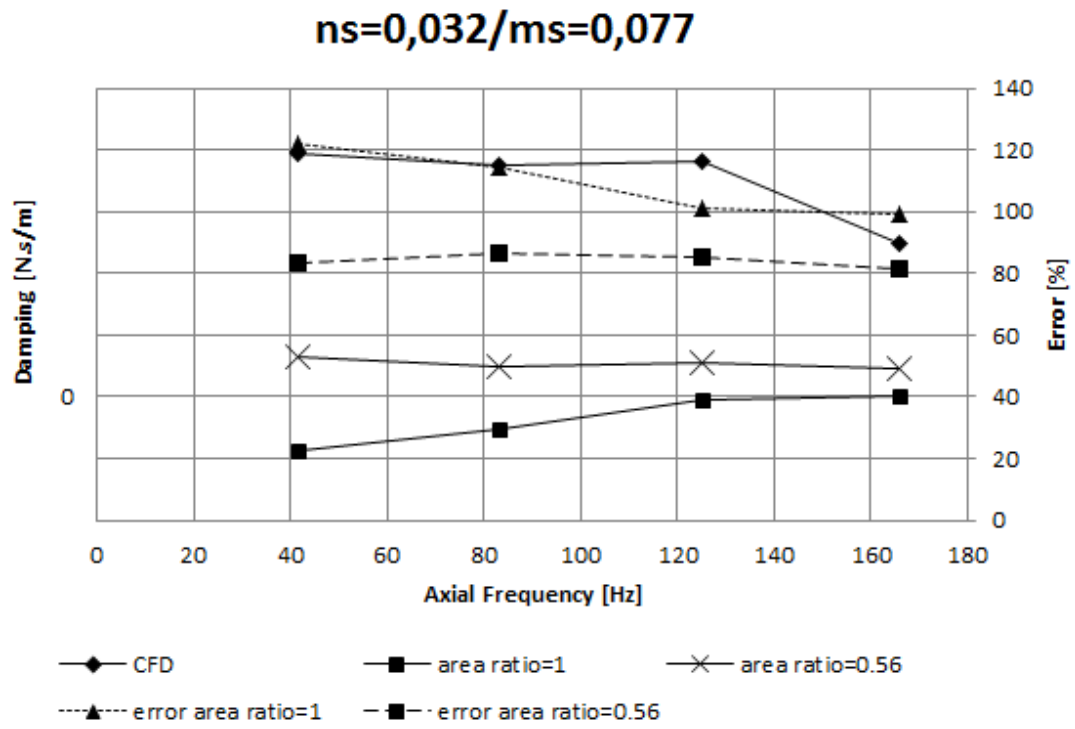


Figure F.56. Damping vs axial frequency at  $ns=0,032/ms=0,077$  for case B 50% offset position.



## Appendix G

Table G.01. Comparison in results using ISOTSEAL and the algorithm in Matlab for annular gas seals.

Parameter	units	Case I	Case II	Case III	Case IV
Reservoir Pressure	bar	70	70	70	70
Sump Pressure	bar	31,50	31,50	31,50	50,00
Reservoir Temperature	C	17,40	17,40	17,40	17,40
Rotational speed	rpm	6000	20200	20200	20200
seal diameter	mm	114,74	114,74	160	114,74
seal length	mm	85,7	85,7	85,7	85,7
Inlet clearance	mm	0,4745	0,35	0,4745	0,4745
Exit clearance	mm	0,2102	0,2102	0,2102	0,2102
entrance loss coefficient	-	0	0	0	0
exit recovery factor	-	1	1	1	1
absolute viscosity	Ns/m <sup>2</sup>	1,88E-05	1,88E-05	1,88E-05	1,88E-05
Molecular weight	kg/kmol	28,96	28,96	28,96	28,96
Z	-	1	1	1	1
Leakage (ISOTSEAL)	kg/s	0,7063	0,5986	0,9488	0,5683
Leakage (MATLAB)	kg/s	0,7059	0,6006	0,9501	0,5694
Error	%	0,06	0,33	0,14	0,19



## Appendix H

### Isothermal flow

The zeroth-order equations for isothermal flow are:

Continuity equation

$$p_0 h_0 r \frac{d\bar{\rho}_0}{dr} + p_0 h_0 r \frac{d\bar{u}_{R0}}{dr} + p_0 \bar{u}_{R0} r \frac{dh_0}{dr} + p_0 \bar{u}_{R0} h_0 = 0 \quad \text{H.01}$$

Circumferential momentum equation

$$\bar{u}_{R0} h_0 \frac{d\bar{u}_{\theta 0}}{dr} + \frac{\bar{u}_{R0} \bar{u}_{\theta 0} h_0}{r} + \frac{1}{2c} [f_{r0} \bar{u}_{r0} (\bar{u}_{\theta 0} - r) + f_{s0} \bar{u}_{s0} \bar{u}_{\theta 0}] = 0 \quad \text{H.02}$$

Radial momentum equation

$$h_0 P_c \frac{dp_0}{dr} + \frac{p_0 \bar{u}_{R0}}{2c} (f_{r0} \bar{u}_{r0} + f_{s0} \bar{u}_{s0}) + p_0 h_0 \bar{u}_{R0} \frac{d\bar{u}_{R0}}{dr} - p_0 h_0 \frac{\bar{u}_{\theta 0}^2}{r} = 0 \quad \text{H.03}$$

Three equations are needed because it has been assumed that temperature is constant and therefore density is a function of the pressure.

The following tables show the comparison in errors for the isothermal and adiabatic cases.

Table H.01. Errors for leakage at case A centered

Error (ISOTHERMAL)	Error (ADIABATIC)
[%]	[%]
$\pm 5,35$	$\pm 6,53$

Table H.02. Errors for leakage at case A 50% offset.

Error (ISOTHERMAL)	Error (ADIABATIC)
[%]	[%]

$\pm 4,22$	$\pm 4,95$
------------	------------

Table H.03. Errors for Thrust force at case A 50% offset.

<b>Error (ISOTHERMAL)</b>	<b>Error (ADIABATIC)</b>
[%]	[%]
$\pm 27,83$	$\pm 27,83$

Table H.04. Errors for leakage at case B centered.

<b>Error (ISOTHERMAL)</b>	<b>Error (ADIABATIC)</b>
[%]	[%]
$\pm 7,51$	$\pm 5,50$

Table H.05. Errors for leakage at case B 50% offset.

<b>Error (ISOTHERMAL)</b>	<b>Error (ADIABATIC)</b>
[%]	[%]
$\pm 11,14$	$\pm 9,73$

Table H.06. Errors for Thrust force at case B 50% offset.

<b>Error (ISOTHERMAL)</b>	<b>Error (ADIABATIC)</b>
[%]	[%]
$\pm 120$	$\pm 171$